Molecular and structural investigation of assembly, maturation and heterogeneity of inner hair cell ribbon synapses

Dissertation
for the award of the degree
”Doctor rerum naturalium” (Dr.rer.nat.)
of the Georg-August-Universität Göttingen

within the doctoral program GAUSS Basic program in Biology
of the Georg-August University School of Science (GAUSS)

Submitted by
Susann Michanski

Born in
Perleberg, Germany

Göttingen, 2018

Members of the Thesis Committee:

Prof. Dr. Tobias Moser
Institute for Auditory Neuroscience & InnerEarLab, University Medical Center Göttingen

Prof. Dr. André Fiala
Schwann-Schleiden Research Center, Georg-August University Göttingen

Prof. Dr. Carolin Wichmann
Institute for Auditory Neuroscience & InnerEarLab, University Medical Center Göttingen

Members of the Examination Board:

First Reviewer: **Prof. Dr. Tobias Moser**
Institute for Auditory Neuroscience & InnerEarLab,
University Medical Center Göttingen

Second Reviewer: **Prof. Dr. André Fiala**
Schwann-Schleiden Research Center,
Georg-August University Göttingen

Further members of the Examination Board:

Prof. Dr. Carolin Wichmann
Institute for Auditory Neuroscience & InnerEarLab, University Medical Center Göttingen
Prof. Dr. Stefan Jakobs
Department of NanoBiophotonics, Max Planck Institute for Biophysical Chemistry, Göttingen
PD Dr. Michael Hoppert
Department of General Microbiology, Georg-August University Göttingen
Prof. Dr. Thomas Dresbach
Center for Anatomy and Embryology, University Medical Center Göttingen

Date of the oral examination: October 15^{th}, 2018

Declaration

I hereby declare that this dissertation ”Molecular and structural investigation of assembly, maturation and heterogeneity of inner hair cell ribbon synapses” is written independently with no other sources and aids than quoted.

_____

Susann Michanski

Göttingen, Germany

Contents

List of Figures

List of Tables

Abbreviations

2D	Two Dimension
3D	Three Dimension
Aff	Afferent fiber
AP	Action potential
AMPA	A-amino-3-hydroxy-5-methyl-4-isoxazolepropionic acid
ATP	Adenosin Tri Phosphat
AZ	Active zone
BDNF	Brain-derived neurotrophic factor
BK channel	Big potassium ($^{+}$) channel
BSA	Bovine serum albumin
Ca^{2+}	Calcium
Ca_v	Voltage-dependent calcium channel
$CaCl_2$	Calcium chloride
$CaCO_3$	Calcium carbonat
CAST	(Cytomatrix of Active Zone)-Associated Structural Protein
C_m	Membrane capacitance
CNS	Central nervous system
CO_2	Carbon dioxide
CtBP2	C-terminal binding protein 2
dB	Decibel
DCV	Dense-core vesicle
DFNB9	Deafness, autosomal recessive 9
DSDB	Donkey serum dilution buffer
E	Embryonic day
EDTA	Ethylene diamine tetraacetic acid
Eff	Efferent fiber
EGTA	Ethylene glycol tetraacetic acid
ELKS	Glutamate (E), Leucin (L), Lysine (K) and Serine (S) rich Protein
EM	Electron microscopy
EPSC	Excitatory Postsynaptic Current
EtOH	Ethanol
FIB-SEM	Focused ion beam - scanning electron microscopy
GSDB	Goat serum dilution buffer
HC	Hair cell
Hz	Hertz

HEPES	4-(2-hydroxyethyl)-1-piperazineethanesulfonic acid
HEPES-HANKS	HEPES-HANKS Balanced Salt Solution
IHC	Inner hair cell
K^+	Potassium
KCl	Potassium chloride
KH_2PO_4	Monopotassium phosphate
KFeCn	Potassium ferrocyanide
KO	Knockout
KW	Kruskal-Wallis
MeOH	Methanol
MET	Mechanoelectrical transduction
$MgCl_2$	Magnesium chloride
$MgCl_2$-$6H_2O$	Magnesium chloride hexahydrate
$MgSO_4$-$7H_2O$	Magnesium sulfate heptahydrate
MP	Membrane-proximal
Munc13	Mammalian Homologue of Unc(uncoordinated)-13
NaCl	Sodium chloride
Na^+	Sodium
NADH	Nicotinamide adenine dinucleotide
Na_2HPO_4	Disodium phosphate
NaOH	Sodium hydroxide
NHS	Normal horse serum
NPMC	Non-parametric multiple comparison
n.s.	Not significant
NT-3	Neurotrophin-3
Nuc	Nucleus
OHC	Outer hair cell
OsO_4	Osmium tetroxide
P	Postnatal day
PBS	Phosphate buffered saline
PD	Presynaptic density
PDA	Presynaptic density associated
PIPES	1,4-Piperazinediethanesulfonic acid
PSD	Postsynaptic density
PTV	Piccolo-bassoon transport vesicle
R	Ribbon
RA	Ribbon-associated
RBE	RIBEYE
RIM	Rab3-interacting molecule
RRP	Readily releasable pool
SBF-SEM	Serial block face - scanning electron microscopy

SEM	Standard error of the mean
SGN	Spiral ganglion neuron
SNARE	N-ethylmaleimide-sensitive factor attachment protein receptor
SR	Spike rate
STED	Stimulated emission depletion
SV	Synaptic vesicle
TCH	Thiocarbohydrazite solution
TEM	Transmission electron microscopy
Vglut	Vesicular glutamate transporter
v/v	Volume/volume
WT	Wild-type
w/v	Weight/volume

Abstract

Age-related hearing and balance impairments represent the most common sensory deficits in humans. Both senses rely on hair cell ribbon synapses, which are highly specialized to sustain continuous release of neurotransmitter filled synaptic vesicles mediating indefatigable signal transmission. Disruption of their complex structural features are associated with disorders. However, their developmental aspects including the time course of ribbon synapse assembly, ribbon material targeting to active zones and their morphological maturation remain elusive.

To address these questions, I first attempted to characterize the nanostructure of the auditory ribbon-type synapse by using electron microscopy and electron-tomography. The morphology of the inner hair cell (IHC) ribbon synapse was investigated in the mouse cochlea from late embryonic stages into adulthood. I could show that afferent synaptic contacts are established before floating spherical ribbon precursors arrive at immature active zones. Furthermore, pre-embedding immunogold labelings revealed two of the ribbon precursor constituents, namely RIBEYE and piccolino. The close proximity of floating ribbon precursors to cytoskeletal structures indicates active transport mechanisms to target them towards active zones. Moreover, ribbon fusion events around the onset of hearing serve as one key mechanism to transform multiple small ribbons per synaptic contact in IHCs of pre-hearing mice to a predominantly single and large synaptic ribbon in hearing animals. A similar structural confinement was found for the postsynaptic density. The employment of large 3D volume imaging techniques exhibited a morphological spatial gradient of active zones within individual IHCs, which is already established prior to hearing onset. Synapses of the modiolar side exhibited more frequently multiple ribbons per contact with generally larger sized ribbons, whereas pillar sides revealed a lower synapse density with contacts comprising a single and smaller ribbon.

In the second part of this thesis, I studied the loss of the ribbon specific protein RIBEYE and its impact on the ultrastructural organization of cochlear IHC active zones. Multiple conventional-like active zones were present at each ribbonless synaptic contact of IHCs in RIBEYE knockout mice, which implies a partial compensation. Exploring older mature animals excluded a developmental delay in these knockout mice.

In the third part, I compared my developmental results from auditory IHCs with the two different types of vestibular hair cells from the utricle. While developmental processes have been studied extensively in the auditory pathway, much less is reported for the vestibular system. Utricular hair cells can be divided into type I and type II cells. In contrast to cochlear IHCs, they do not exhibit a change in size or number of synaptic ribbons per synapse or in the number of synaptic vesicles upon maturation. Unexpectedly, floating ribbons were present even in 11 months old mice arguing against a pure precursor function as described for immature IHCs. The number of floating

ribbons increased during development in type I cells forming clusters, but decreased in type II cells. I propose that the large number of floating ribbons in type I hair cell could be the result of a secondary detachment of synaptic ribbons, which indicates a distinct maturation compared to type II and cochlear HCs. Type II hair cells showed a sequence of maturational events, which was more comparable to cochlear IHCs.

In conclusion, mapping hair cell synapses during development resulted in the discovery of structural modifications, which correlate to functional maturation processes of the active zone. If also occurring in mature hair cells, the observed fusion or detachment events of ribbon material might represent a mechanism to modulate the ribbon size and number, which might influence the respective synaptic strength in cochlear and vestibular hair cells.

1. Introduction

1.1. Overview of the mammalian ear

Hearing is the perception of sound via pressure waves that carry information about pitch (frequency) and intensity (sound pressure). Humans, for example, have the ability to perceive sound frequencies from 20 to 20,000 Hertz (Hz), while intensities can be encoded in a range between 0 and 120 dB sound pressure level. These sound pressure waves are first captured by the external ear (auricle) (Figure 1.1A), which focuses them onto the elastic tympanic membrane (also referred to as eardrum). These vibrations are then further conveyed onto the three smallest bones in the human body - the so-called ossicles - malleus, incus and stapes, which are localized within the middle ear. The stapes passes on the vibrations onto the oval window of the inner ear and subsequently causes the movement of the extracellular fluid inside the cochlea, named perilymph (Figure 1.1A). In order to ensure proper sound transmission, the middle ear increases the pressure by around 200-fold. This effect arises from different diameters between the tympanic membrane and the oval window combined with the leverage effect of the ossicles (Purves, 2004). The movements of the cochlear perilymph are transmitted to the endolymph inside the cochlear duct, where the organ of Corti transduce the acoustic information via the cochlear nuclei to the auditory cortex of the brain for further processing (Figure 1.1B, C).

In addition to the sense of hearing, the mammalian inner ear carries five sensory organs that detect spatial orientation and balance: sacculus, utriculus and three semicircular canals (Figure 1.4A). Similar to the cochlea, the vestibular apparatus is filled with perilymph and endolymph whose movements, due to changes in head and body position, transduce the motion information into electrical signals for the vestibular centers of the brain. Both senses, hearing and balance, rely on mechanosensory hair cells (HCs), which are specialized for converting mechanical stimuli into electrical signals and will be discussed in more detail in the following sections.

1.2. Functional anatomy of the cochlea

1.2.1. Sound transduction

The snail-shaped cochlea is divided by a membranous cochlear duct into three fluid-filled compartments: the scala vestibuli, scala tympani and scala media (Figure 1.1B). The scala media is located in between the other two chambers, where it is separated by the Reissner's membrane from the upper scala vestibuli and by the basilar membrane from the lower scala tympani. In contrast to the scala vestibuli and scala tympani, which are filled with high Na^+ ($\sim$ 140 mM) and low K^+ ($\sim$ 5 mM) perilymph, the scala media contains endolymph (high concentration of $\sim$ 160/150 mM

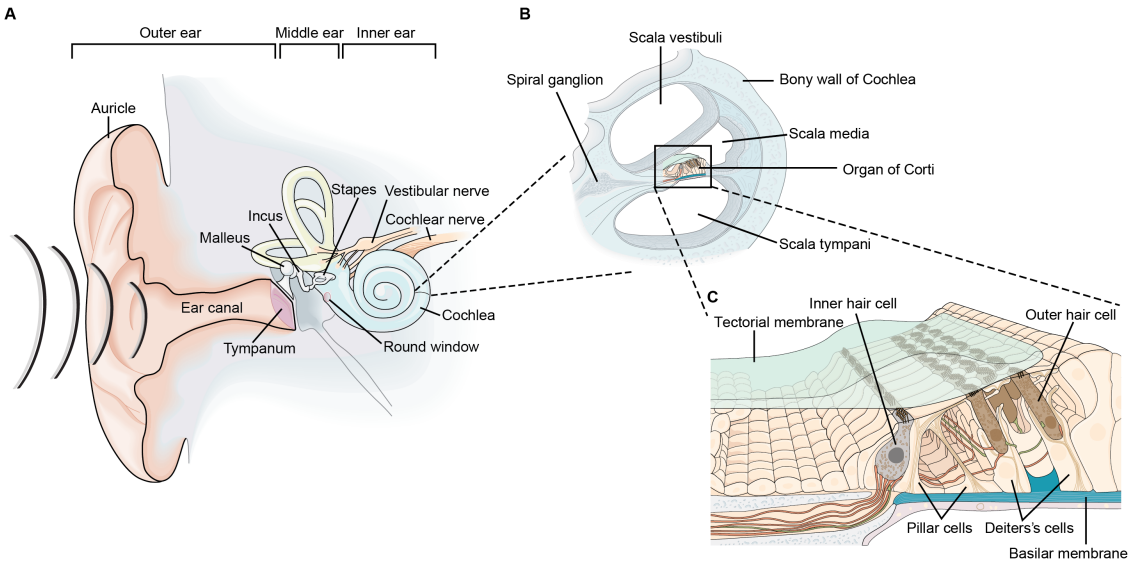

Figure 1.1.: Anatomy of the human ear
(A) The human ear consists of: (i) the outer ear focusing sound pressure waves into the ear canal; (ii) the middle ear, which further transmits the vibrations of the tympanum via the ossicles (malleus, incus, stapes); and (iii) the inner ear. **(B)** Cross-section through the hearing receptor organ of the inner ear, the cochlea, shows three fluid-filled compartments: the scala vestibuli, scala tympani, and the scala media containing the organ of Corti. **(C)** The organ of Corti comprises three rows of OHCs acting as cochlear amplifiers, a single row of sensory IHCs, and various types of supporting cells. Sound induced displacement of IHC stereocilia causes a depolarization of the cell with resulting neurotransmitter release onto the afferent terminals contacting the basal part of IHCs. Figure modified from Kandel et al. (2012).

K^+ and low concentration of $\sim$ 1 mM Na^+) and harbors the sensory epithelium, the organ of Corti (Peter Dallos et al., 1996; Moller, 2006). As a result, an electrochemical gradient exists, which is essential for hair cell depolarization (Wan et al., 2013).

Sound induced movements of the perilymph lead to vibrations of the basilar membrane, which ultimately results in the activation of the auditory pathway (Figure 1.1C). Separation of sound waves according to their frequency - so-called tonotopy - is achieved by the uneven structure of the basilar membrane. The membrane is narrower and more stiff at the base but wider and more flexible at the apex of the cochlea (Oghalai, 2004). Due to these features, high frequencies lead to vibrations at the base of the cochlea and low frequencies lead to vibrations at the apex. In humans, the cochlea is about 33 mm long with 2.5 turns and in mice it is 11 mm long with 1.75 turns (Ashmore, 2008; Kandel et al., 2012; Fritzsch et al., 2015), where it contains different types of cells such as roughly 1,000 inner hair cells (IHCs), 2,600 outer hair cells (OHCs) and several supporting cells (pillar-, phalangeal-, Deiter's-, and Hensen's cells) (Keithley and Feldman, 1982; Burda and Branis, 1988; Niparko, 1993; Pujol et al., 1998). OHCs are arranged in three rows along the basilar membrane and have been described to act as cochlear amplifiers due to their electromotility, which is driven by the motor protein prestin (Dallos, 2008). Their stereocilia are embedded in the tectorial membrane causing a deflection of the stereocilia at every displacement of the basilar

membrane. Based on the OHC depolarization, prestin undergoes a voltage-sensitive conformational change that results in voltage-dependent elongation and contraction of OHCs (Russell and Kössl, 1992; Liberman, 2017). These mechanical motions feed back to the basilar membrane vibration, thereby enhancing the sound evoked movement relative to the tectorial membrane leading to stronger deflection of the IHC stereocilia (Zheng et al., 2000). The various types of supporting cells serve as structural support for inner and outer HCs, but they also seem to play a crucial role in cochlear homeostasis by regulating glutamate uptake and recycling K^+ from HCs to the endolymph (Ramrírez-Camacho et al., 2006; Wan et al., 2013).

In contrast to OHCs, IHCs are arranged in a single row and are the actual sensory receptors encoding sound at their afferent synapses with type I spiral ganglion neurons (Figure 1.1C). Stereocilia deflection leads to cell depolarization and neurotransmission by interconnected filamentous tip links composed of cadherin 23 and protocadherin 15 (Müller, 2008). It is proposed that they serve as tethers or gating springs directly linked to mechanoelectrical transduction (MET) channels. A displacement of the basilar membrane then increases the tension in the tip links and consequently opens MET channels to mediate K^+ influx from the endolymph (Corey and Hudspeth, 1979). The resulting depolarization of IHCs opens presynaptic voltage-gated L-type Ca^{2+}-channels ($Ca_v1.3$) and the incoming Ca^{2+} triggers the fusion of glutamate filled synaptic vesicles (SVs) with the plasma membrane (exocytosis) to release their neurotransmitter into the synaptic cleft. This chemical neurotransmitter binds to postsynaptic AMPA-type glutamate receptors and elicits action potentials firing in the associated spiral ganglion neuron (SGN). In mice, 90 - 95 % represent type I SGNs sending their bouton-like terminal contacts to single IHCs and a myelinated axon towards the cochlear nucleus, which receives all the acoustic information and relays it further to the central auditory system (Spoendlin, 1969; Delacroix and Malgrange, 2015). Mature type I SGNs form 10 - 20 monosynaptic contacts with one IHC and are therefore each receiving input from a single presynaptic ribbon (Meyer et al., 2009). On the contrary, unmyelinated type II SGNs constitute 5 - 10 %, cross the tunnel of Corti and innervate multiple OHCs (Spoendlin, 1972; Simmons and Liberman, 1988).

1.2.2. The IHC ribbon-type active zone

The presynaptic ribbon is a highly specialized electron-dense organelle between IHCs and SGNs (Figure 1.2A, B) that is anchored to the active zone (AZ) and tethers a large pool of synaptic vesicles (Lenzi et al., 1999; Nouvian et al., 2006; Moser and Starr, 2016). Ribbon-type synapses can be as well found in vestibular HCs, photoreceptors, retinal bipolar cells, lateral line in fish, and the pineal gland (Hopsu and Arstila, 1965; Lenzi and von Gersdorff, 2001; Fuchs et al., 2003; Sterling and Matthews, 2005; Eatock and Songer, 2011; Wichmann and Moser, 2015). Depending on the species and organ, synaptic ribbons vary in size and shape from ribbon-like to round (Melchionda et al., 2001; Yu and Goodrich, 2014; Wong et al., 2014) structures. A typical ribbon, in mature mice, has an ellipsoid shape (in cross-section) with tens to hundreds of vesicles tethered to it (Moser et al., 2006; Wong et al., 2014) (Figure 1.2C). The precise ribbon function is still not understood, but it is thought that ribbons act as nanomachines (Lenzi and von Gersdorff, 2001; Rutherford and Pangršič, 2012) by providing a large readily releasable pool (RRP) of vesicles

for synchronous and sustained signaling (Kikuchi and Hilding, 1965; Khimich et al., 2005; Frank et al., 2009; Buran et al., 2010; Safieddine et al., 2012).

Ribbon synapses achieve rapid and indefatigable afferent transmission at high rates of hundreds of Hz with sub-millisecond precision (Moser and Beutner, 2000; Moser and Starr, 2016). One hypothesis suggests that this unique property is obtained by clustering Ca^{2+}-channels at the release sites, thereby promoting the association with fusion-competent vesicles (Dick et al., 2003; Khimich et al., 2005; Hull et al., 2006; Frank et al., 2010; Sheets et al., 2011; Wong et al., 2014; Maxeiner et al., 2016). Indeed, immunohistochemical stainings in mature IHCs revealed a co-localization of Ca^{2+}-channels with ribbon synapses (Brandt et al., 2005; Frank et al., 2010; Wong et al., 2014). Another, not mutually exclusive, hypothesis suggests that the ribbon functions as a conveyor belt where SVs are transported along the ribbon to the AZ membrane (von Gersdorff et al., 1996; Muresan et al., 1999; Graydon et al., 2014). Disruption of the ribbon as well as repeated stimulation that causes synaptic depression revealed an impairment of the RRP leading to reduced fast and sustained exocytosis (von Gersdorff and Matthews, 1997; Moser and Beutner, 2000; Spassova et al., 2004; LoGiudice et al., 2008; Frank et al., 2010; Snellman et al., 2011). Consequently, this supports the assumption that ribbons provide release sites by organizing Ca^{2+}-channels as well as SVs and promote SV replenishment.

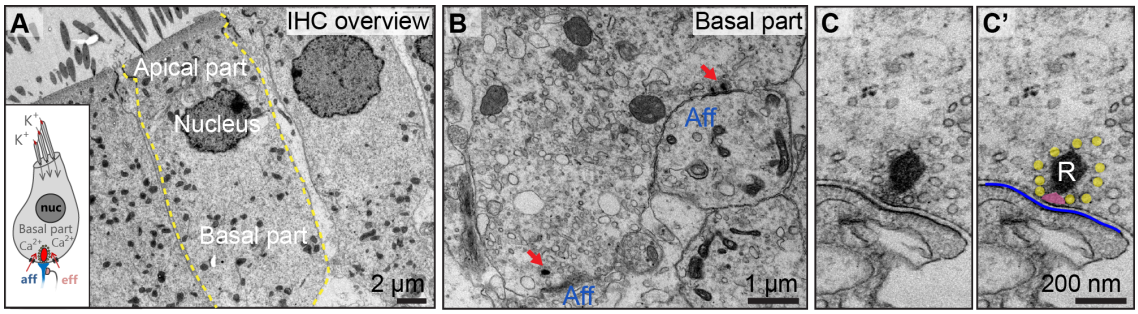

Figure 1.2.: Ultrastructure of murine IHCs and corresponding ribbon synapses
(A) Electron micrograph of an IHC row visualizing the nucleus, apical, and basal part. For simplification, schematic illustration highlights the main components of an IHC. The yellow dashed line indicates the IHC plasma membrane. **(B)** At the IHC base, synaptic ribbons (red arrows) are found opposing to afferent nerve fiber boutons (aff). **(C, C')** Representative electron micrographs depicting a cross-section of the proteinaceous electron-dense ribbon (R), which is attached to the AZ membrane by a presynaptic density (magenta) and tethers several SVs (yellow). Blue line highlights the postsynaptic density.

1.2.3. The type I SGNs

Mice have around 20,000 type I SGNs (from now on termed 'SGNs' for simplicity as type II SGNs will not be further discussed) forming AZ contacts with IHCs in order to carry the acoustical signal from the inner ear to the brainstem. It has been shown that the amplitude as well as the shape of their excitatory postsynaptic currents (EPSC) are highly variable (mono-phasic versus multi-phasic EPSCs) despite similar frequency characteristics (Chen et al., 2007; Grant et al.,

2010; Chapochnikov et al., 2014). The current explanation for this observation may lay in the SV release mechanism, which remains controversially discussed in the field. On one side, a multi-vesicular (or multi-quantal) release mode has been proposed (Glowatzki and Fuchs, 2002; Parsons and Sterling, 2003; Neef et al., 2007; Matthews and Fuchs, 2010) in which two or more SVs fuse in a synchronized manner (Fuchs et al., 2003). Thus, depending on the total number and synchronicity of the released SVs, variably sized and shaped EPSCs would occur. On the other side, an alternative uni-quantal release mode may also cause the diversity in EPSCs. In this scenario, a single SV can either open and close via dynamic fusion pore flickering (i.e. multi-phasic events) or can fuse completely and collapse (monophasic events) (Chapochnikov et al., 2014). Support for this latter hypothesis stems from the observation that the charge of both, multi- and monophasic EPSCs did not differ significantly, which suggests that both events may indeed derive from a single SV with diverging release kinetics.

In addition to heterogeneous EPSCs, there are also major differences in postsynaptic SGN firing. Some SGNs, for instance, are more sensitive to sound (low threshold neurons) and have a high spontaneous spike rate (SR) whereas others activate at higher sound intensities (high threshold neurons) and have a low SR (Liberman, 1982; Winter et al., 1993; Taberner and Liberman, 2005; Liberman et al., 2011). A correlation between the size as well as the location of presynaptic ribbons and the auditory afferent responses was already demonstrated in cats and mice (Merchan-Perez and Liberman, 1996; Liberman et al., 2011). Here, SGNs with middle and low SR are predominantly found at the modiolar (neural) side of the IHCs, where larger ribbons are localized (Figure 1.3). On the contrary, smaller ribbons are mainly localized at the pillar (abneural) side of IHCs innervated by high SR SGNs (Figure 1.3). Moreover, the fiber diameter of high SR SGNs is thicker with a higher amount of mitochondria compared to low SR SGNs. As a consequence, the spatial gradient in ribbon size is a proxy for the AZ size in IHCs, which might have an influence on the AZ function. However, how and when the spatial gradient is established is still enigmatic.

1.3. Functional anatomy of vestibular HCs

1.3.1. Sensory transduction

The vestibular system consists of: (i) three semicircular canals (lateral-, superior-, and inferior canal), each containing a crista ampullaris detecting rotational acceleration; and (ii) the otolith organs (saccule and utricle) detecting linear accelerations and head tilt (Figure 1.4A). In this thesis, I will focus on the utricle.

Similar to the IHCs of the auditory system, utricular HCs transform mechanical signals of their stereocilia displacement into receptor potentials triggering glutamate release onto the terminals of afferent neurons. The resulting action potentials are finally conveyed to central neural structures in the brain that control eye movements, balance and posture. Stereocilia of utricular HCs are anchored in a gelatinous structure, the otolithic membrane, which carries otoliths or otoconia. The otoliths are calcium carbonate ($CaCO_3$) crystals that evoke the movement of the otolithic membrane in response to head movements. In this way, stereocilia get deflected and cause the stimulation of utricular HCs (Eatock and Lysakowski, 2006).

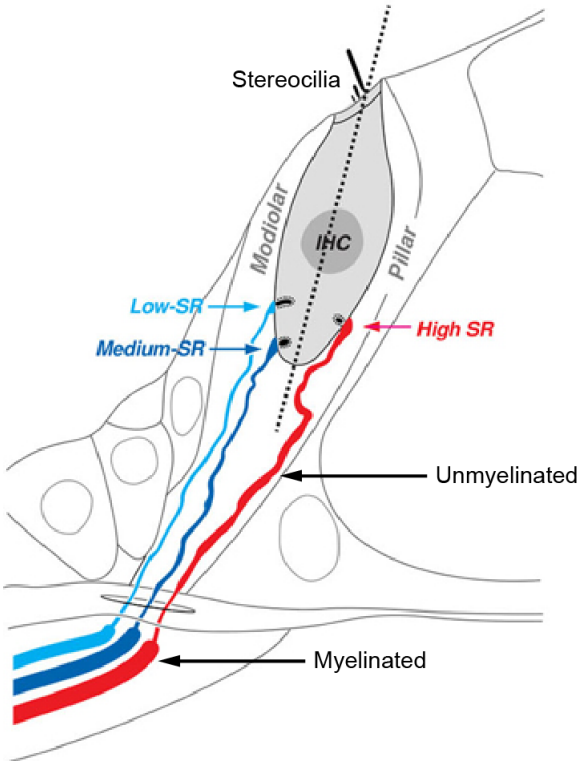

Figure 1.3.: Spatial gradient in IHCs and heterogeneous response properties of SGNs
In cats, a differentiated innervation of SGNs in relation to the IHC topography has been observed (Liberman, 1980, 1982; Kawase and Liberman, 1992). The pillar side (facing OHCs) of IHCs possess smaller ribbons, which are characteristically innervated by high SR SGNs (highlighted in red) that tend to have lower auditory thresholds and a narrow dynamic range. On the other hand, middle and low SR SGNs (represented in blue) innervate the modiolar side (facing incoming afferent fibers) of IHCs, oppose larger synaptic ribbons and have high auditory thresholds with a broader dynamic range. Image modified from Bharadwaj et al. (2014).

Wersall (1956) described two types of vestibular HCs: type I and type II (Figure 1.4C). The flask shaped type I cells have larger mitochondria (Rüsch et al., 1998) and are enclosed by a calyceal afferent terminal (Figure 1.5A, A') whereas the cylindric type II cells are innervated by several individual afferent fibers forming round (bouton) contacts (Figure 1.5B, B'). In addition, a third type of afferents contacts the vestibular HCs, named the dimorphic afferents. They branch to form contacts on type I and type II HCs (Holstein et al., 2004; Eatock and Songer, 2011).

The utricle is morphologically and physiologically organized into two different zones (Figure 1.4B). The central, striolar zone is occupied predominantly by type I cells and complex calyces, surrounding up to a few vestibular HCs. The peripheral extrastriolar zone contains numerous type II and type I HCs with simple calyces (Lindeman, 1969; Eatock and Lysakowski, 2006) (Figure 1.4C). The two types of vestibular HCs differ in their ionic K^+-selective conductances: the type II cells show outwardly rectifying conductances with a positive activation; the type I cells, on the other hand, possess conventional outwardly rectifying currents with an unusually large and negatively activating conductance (Correia and Lang, 1990; Eatock and Hutzler, 1992; Rennie and Correia, 1994; Rusch and Eatock, 1996; Chen and Eatock, 2000). The larger currents in type

I cells are supposed to result in greater metabolic and buffering needs (Eatock and Lysakowski, 2006), which in turn might explain the occurrence of larger mitochondria (Rüsch et al., 1998). Furthermore, the exocytosis in type I cells seems to have faster kinetics as compared to type II cells (Dulon et al., 2009).

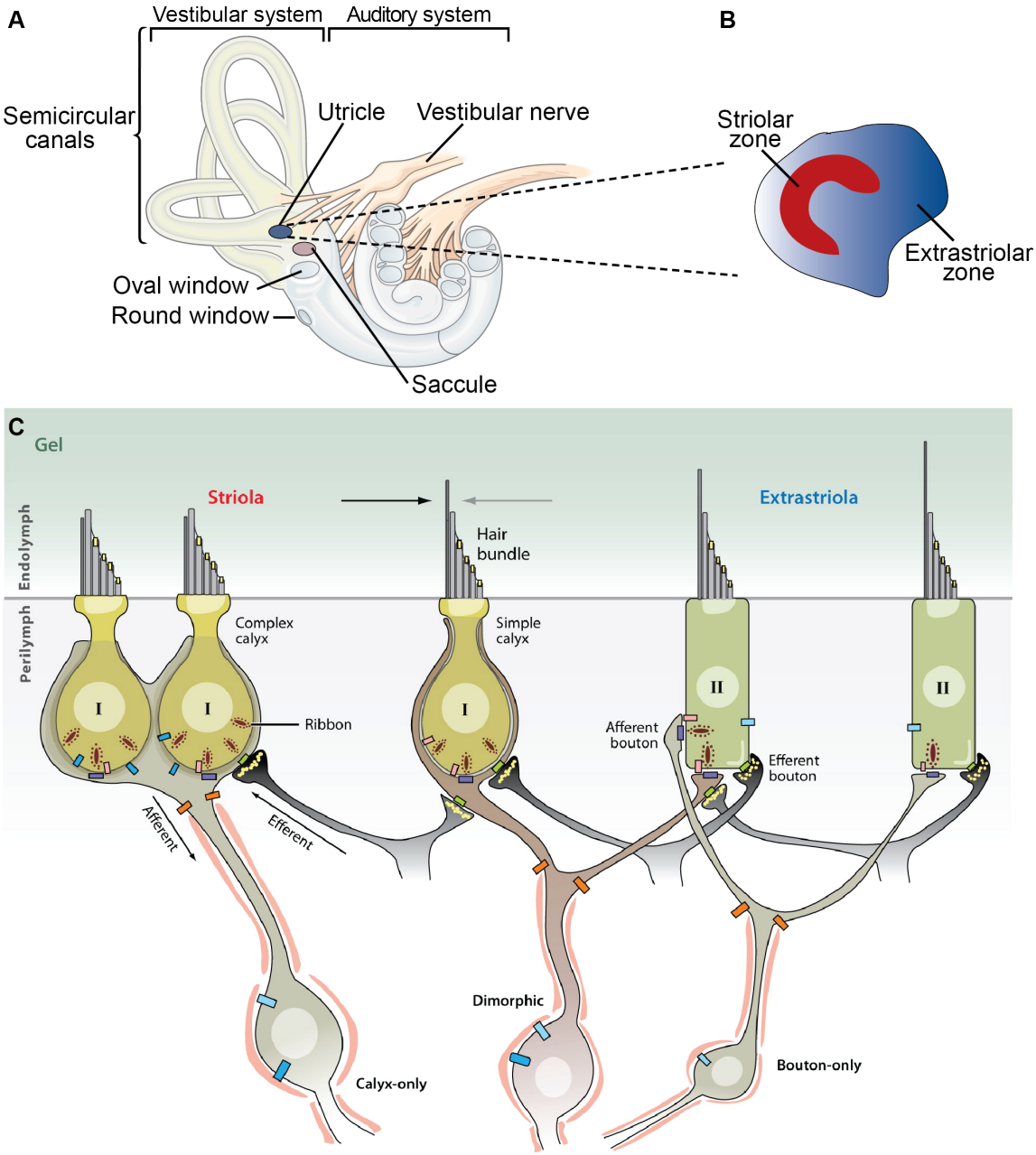

Figure 1.4.: The structure of the peripheral vestibular sensory organs highlighting the two different types of HCs
(A) The mammalian vestibular system comprises five sensory organs, the three cristae ampullaris, located in the ampullae of the semicircular canals, and the two otolith organs, utricle and saccule, located in the vestibular sacs.

Figure 1.4 ***(previous page)*****: (B)** The utricle can be divided into the central striolar zone and the peripheral extrastriolar zone. Along this axis, two different HC types and three different types of afferent innervation have been reported. **(C)** Vestibular HCs transduce mechanical signals about head movements and tilts to central neural structures controlling eye, head and body position. In the striolar zone, calyx-only afferents predominantly innervate type I utricular HCs, while dimorphic afferents contact HCs in both zones. Type II utricular HCs in the extrastriolar zone are contacted by bouton-only afferent nerve fibers. Figure adapted from Eatock and Songer (2011) and Kandel et al. (2012).

1.3.2. The vestibular HC synaptic ribbon

Vestibular HCs harbor synaptic ribbons (Figure 1.5A-B'), which are highly variable in size, shape and number depending on the species, HC type or epithelial zone (Eatock and Lysakowski, 2006). In the crista of adult chinchillas, the abundance of ribbons in central type II HCs is comparable to peripheral type II HCs, but the afferent innervation is sparser in the central zone (Lysakowski and Goldberg, 1997). This may be explained by: (i) a tendency towards more ribbon synapses per afferent bouton; and (ii) higher numbers of ribbon synapses on the outer faces of neighboring calyces (Lysakowski and Goldberg, 1997). Regarding the ribbon size and shape, larger and more complex shaped ribbons were found in type II cells, which likely recruit more Ca^{2+}-channels and tether more SVs (Lysakowski and Goldberg, 1997). Although, some regional and morphological data are available for vestibular HCs of different organs and species, relatively little is known about the structure of murine utricular synaptic ribbons and its potential impact on the vestibular HC physiology.

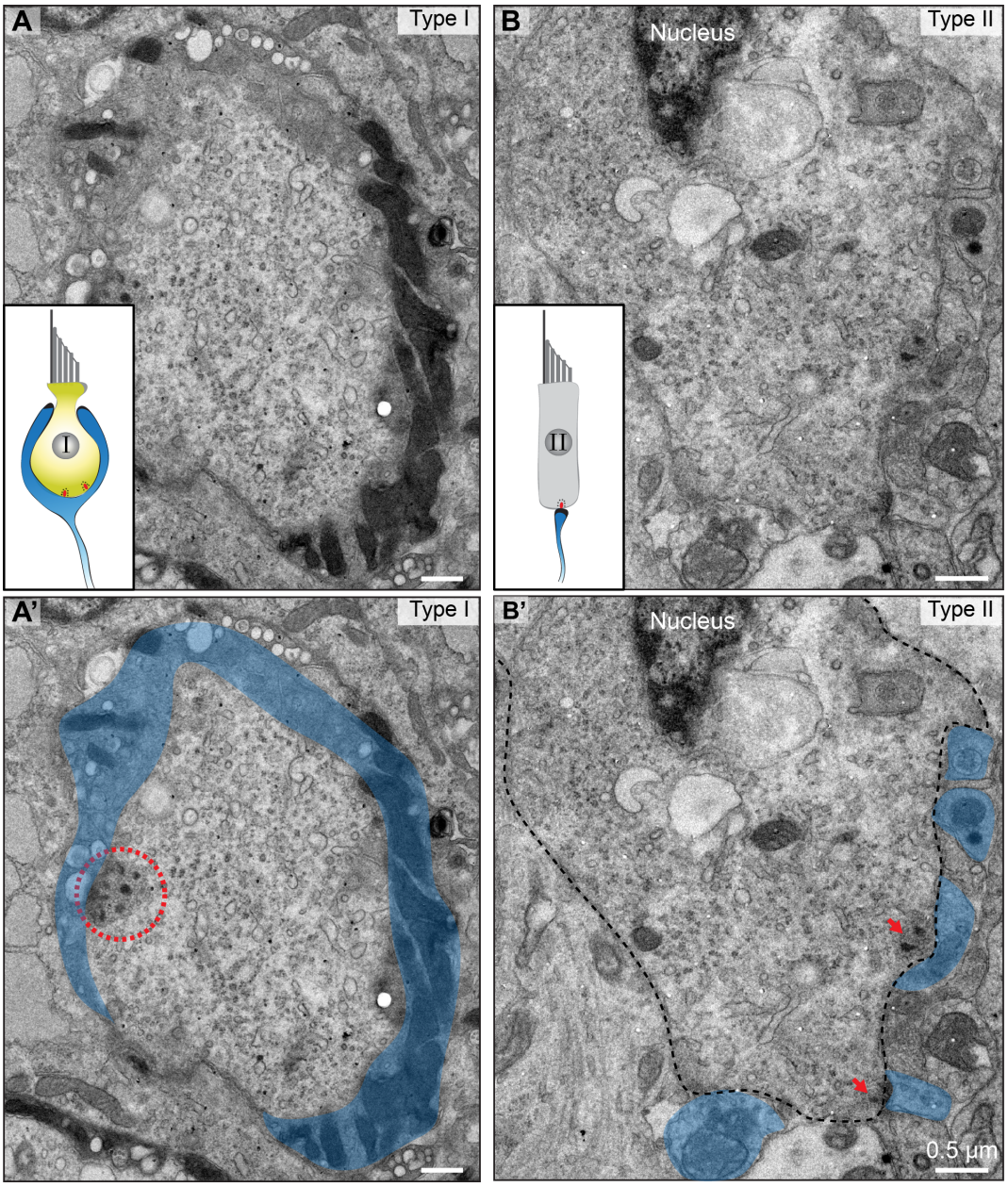

Figure 1.5.: Microanatomy of type I and type II utricular HCs
Electron microscopic overview of a type I utricular HC **(A, A')** compared to a type II utricular HC **(B, B')**. **(A)** Type I cells can be differentiated from type II cells by the mitochondria rich calyceal afferent endings (highlighted with blue in **A'**) surrounding the type I cells. In close proximity to the cell membrane, synaptic ribbons (encircled in red) with a halo of SVs can be found. **(B)** In contrast, type II cells are contacted by several afferent boutons, which are illustrated in blue **(B')** and opposed to presynaptic ribbons (red arrows). Schematic drawings demonstrate the main differences between the two HC types.

1.4. Molecular key players of cochlear and utricular HC AZs

In the central nervous system, proteins of the AZ maintain morphological and physiological integrity of SVs and Ca^{2+}-channels in order to organize fast and synchronous release, thereby regulating synaptic strength (Torres et al., 2017). The molecules of the ribbon AZs and synaptic machinery are partially preserved and partially unique at ribbon synapses. IHC ribbon-type AZs use specialized synaptic proteins, such as RIBEYE (Schmitz et al., 2000; Maxeiner et al., 2016), otoferlin (Yasunaga et al., 1999; Roux et al., 2006) and $Ca_v1.3$ L-type Ca^{2+}-channels (Platzer et al., 2000; Brandt et al., 2003) and seem to operate only partially with conventional synaptic proteins (Pangršič et al., 2012, reviewed in Wichmann, 2015). Several synaptic proteins involved in neurotransmission at conventional synapses appear to be absent from HC ribbon synapses or are not functionally required such as synapsins and synaptophysins (Safieddine and Wenthold, 1999), complexins (Strenzke et al., 2009; Uthaiah and Hudspeth, 2010), synaptotagmin 1 and 2 (Safieddine and Wenthold, 1999; Beurg et al., 2010; Reisinger et al., 2011), and neuronal SNARE (soluble NSF attachment protein receptors) proteins (Nouvian et al., 2011). There are also additional differences between ribbon synapses in different cell types. For instance, the auditory ribbon synapse composition is distinct from the visual system by the absence of Rab3-interacting molecule 1 (RIM1), Munc13s, synaptotagmin 1 and 2, and neuronal SNAREs from IHC AZs (Strenzke et al., 2009; Uthaiah and Hudspeth, 2010; Beurg et al., 2010; Reisinger et al., 2011; Nouvian et al., 2011; Jung et al., 2015b; Vogl et al., 2015).

RIBEYE

The main protein component of the ribbon is RIBEYE, a protein unique to synaptic ribbons (Schmitz et al., 2000). It consists of two domains, a ribbon specific A domain and a B domain that is identical to the transcriptional co-repressor named C-terminal binding protein 2 (CtBP2) (Schmitz et al., 2000). The A domain is essential for the structural organization of the ribbon due to the assembly of RIBEYE molecules into a large complex, while the B domain is assumed to facilitate tethering of SVs to the ribbon (Schmitz et al., 2000; Schmitz, 2009; Schwarz et al., 2011). Maxeiner and colleagues recently reported that the deletion of RIBEYE leads to a complete loss of retinal ribbons from photoreceptors and bipolar cells (Maxeiner et al., 2016). Thus, they could confirm the necessity of RIBEYE to form ribbons in the retina and in addition they demonstrated an impairment of glutamate release by a severe reduction of the fast and sustained components of exocytosis. Maxeiner et al. (2016) concluded that ribbons are required to couple voltage-gated Ca^{2+}-channels to vesicular release sites in order to enable tight control of vesicle fusion (also known as Ca^{2+}-nanodomain coupling), which had already been described by various studies in the ear and eye (Brandt et al., 2005; Bartoletti et al., 2011; Graydon et al., 2011; Wong et al., 2014; Pangršič et al., 2015; Johnson et al., 2017).

Bassoon and piccolo

The two large scaffolding proteins bassoon and piccolo (also termed aczonin) have been described in conventional and ribbon-type synapses (for overview Gundelfinger et al., 2016; Wichmann and Moser, 2015). In conventional synapses, bassoon is structurally related to piccolo (Wang et al., 1999; Fenster et al., 2000). Synaptic ribbons are anchored to the AZ via the presynaptic density at

the base of the ribbon containing the protein bassoon (Dick et al., 2003; Khimich et al., 2005; tom Dieck et al., 2005; Frank et al., 2010; Jing et al., 2013; Wong et al., 2014). In bassoon-deficient mice, retinal and cochlear ribbon synapses are not properly anchored to the AZ, which results in floating ribbons (Dick et al., 2003; tom Dieck et al., 2005; Khimich et al., 2005; Frank et al., 2010; Jing et al., 2013). Moreover, the organization of Ca^{2+}-channels is impaired and the size of the RRP is decreased, which in turn reduce Ca^{2+}-currents and the fast component of exocytosis at IHCs causing a hearing impairment (Khimich et al., 2005; Frank et al., 2010; Jing et al., 2013). Thus, bassoon is essential for the synaptic architecture and neurotransmitter release in ribbon synapses. The lack of bassoon in central synapses reveal no structural changes, but an impaired replenishment of SVs as well as a decline in the RRP size was detected and more silent synapses were observed (Altrock et al., 2003; Hallermann et al., 2010; Mendoza Schulz et al., 2014). The homologous scaffolding protein piccolo is another large AZ protein in conventional synapses (Gundelfinger and Fejtova, 2012; Südhof, 2012). In ribbon-type synapses, the short isoform of piccolo is expressed, named piccolino, which is a C-terminal truncated piccolo variant (Limbach et al., 2011; Regus-Leidig et al., 2013, 2014). Immunogold electron microscopy using an antibody that recognizes the short and the long isoform revealed that piccolino is localized across the whole ribbon area in photoreceptors (Limbach et al., 2011). In contrast to conventional synapses, piccolino does not colocalize with bassoon (Limbach et al., 2011). In vivo piccolino knockdown experiments in photoreceptors resulted in an impairment of the synaptic ribbon morphology (Regus-Leidig et al., 2014) indicating a potential involvement in the structural organization and/or maturation of synaptic ribbons. At conventional synapses, piccolo interacts with several other AZ proteins indicating functions in vesicle trafficking, adhesion, cytoskeletal organization and SV docking and fusion (Fenster et al., 2000; Kim et al., 2003; Gundelfinger et al., 2016, reviewed in Torres et al., 2017). Western blot data associated piccolo as well as bassoon with cytoskeletal structures demonstrating that both proteins organize the AZ (tom Dieck et al., 1998).

In bassoon- and piccolo-deficient conventional synapses, clustering, docking, and density of SVs were reduced, whereas synapses lacking only piccolo showed an increase in short-term synaptic depression and decreased vesicle reloading (Mukherjee et al., 2010; Butola et al., 2017). Piccolo may also be involved in regulating the assembly of presynaptic F-actin, which is known to be important for the SV cycle (Waites et al., 2011; Wagh et al., 2015). Since piccolino in ribbon-type synapses lacks the interaction sites of the long isoform for various AZ proteins like RIM, Munc13, bassoon, CAST/ELKS, and Ca^{2+}-channels (Regus-Leidig et al., 2013), it is highly probable that the long and short isoforms exhibit distinct functions. To date, no data are available about the expression of bassoon and piccolino in vestibular HCs. Therefore, the role of bassoon and piccolino in HCs of the vestibular system remains to be elucidated.

Otoferlin

The protein otoferlin belongs to the ferlin family and is essential for exocytosis in vestibular HCs and mature cochlear IHCs and thus has been proposed to exhibit a multi-functional role, including Ca^{2+} sensing to trigger SV fusion and SV replenishment (Roux et al., 2006; Johnson and Chapman, 2010; Michalski et al., 2017). Importantly, otoferlin seems not to be functionally required

during the early first postnatal week, where IHC transiently express the neuronal Ca^{2+} sensors synaptotagmin 1 and 2 (Safieddine and Wenthold, 1999; Uthaiah and Hudspeth, 2010; Beurg et al., 2010; Reisinger et al., 2011). Mutations in this otoferlin gene have been identified to cause a neurosensory non-syndromic recessive form of human deafness (DFNB9) (Yasunaga et al., 1999). In otoferlin-deficient cochlear IHCs, Roux et al. (2006) observed a nearly complete abolished exocytosis, however, ribbon synapse morphogenesis, numbers of docked SVs, and Ca^{2+}-currents were not affected in the profoundly deaf mice. Further studies could confirm the involvement of otoferlin in the last steps of IHC exocytosis such as SV tethering and priming (Pangršič et al., 2010; Vogl et al., 2015) as well as AZ clearance (Pangršič et al., 2010; Jung et al., 2015a). In contrast to cochlear IHCs, vestibular HCs transmit lower frequency head motion stimuli, however, they also operate with high temporal precision in the millisecond range (Huterer and Cullen, 2002). Interestingly, fast kinetics of exocytosis with higher Ca^{2+} sensitivity is characteristic for type I utricular HCs, while type II cells show slower kinetics and reduced Ca^{2+} efficiency (Dulon et al., 2009). Similar differences in exocytosis have also been reported for cones and rods of the retina (Rabl et al., 2005) as well as in immature vs. mature cochlear IHCs (Johnson et al., 2005). Otoferlin knockout (KO) experiments in utricular HCs suggested that otoferlin is a high affinity Ca^{2+} sensor essential for exocytosis in type I but not type II HCs, which implies an additional unidentified Ca^{2+} sensing mechanism in type II HCs (Dulon et al., 2009).

Ca^{2+}-channels

Hair cell exocytosis also depends on Ca^{2+}-channels that regulate neurotransmitter release and interact with otoferlin (Ramakrishnan et al., 2009). In contrast to conventional synapses that mostly express P/Q-, N-, or R-type channels (Catterall, 2011), the predominant Ca^{2+}-channel isoform mediating excitation-secretion coupling at IHC synapses is the L-type $Ca_v1.3$ (Platzer et al., 2000; Brandt et al., 2003). Ca_v1 (or L-type) Ca^{2+}-channels are characterized by non-inactivating currents with large amplitudes and are mostly found in muscle cells. Using confocal and stimulated emission depletion (STED) microscopy, $Ca_v1.3$-channels could be localized at AZs where they form a stripe-like pattern in mature cochlear IHCs (Brandt et al., 2005; Frank et al., 2010; Wong et al., 2014). When $Ca_v1.3$ Ca^{2+}-channels are absent from IHCs, exocytosis is completely abolished causing deafness (Platzer et al., 2000). On the other hand, exocytosis in vestibular HCs only partially relies on $Ca_v1.3$-channels (Bao et al., 2003; Dou et al., 2004). The lack of $Ca_v1.3$-channels leads to deafness, but no obvious vestibular defect has been reported (Dou et al., 2004). Vestibular HCs, in addition, likely possess the T-type Ca^{2+}-channel $Ca_v3.1$ (Nie et al., 2008).

Fundamental understanding of the ultrastructural morphology of AZ proteins and their developmental changes at cochlear and vestibular HC ribbon synapses is still insufficient. To decipher the role of ribbons in the presynaptic HC function, it is important to gain more knowledge on the molecular structure and precise topology of presynaptic proteins. This can give new insights into the functions played by particular synaptic proteins and how they work together to reliably transmit sensory input.

1.5. Current status of postnatal synaptic ribbon development

1.5.1. Cochlear ribbon synapses

To date, the available data demonstrate that upon maturation, ribbon synapses of auditory HCs undergo dramatic structural and functional changes. Before the onset of hearing, around postnatal day (P)12 (Mikaelian and Ruben, 1965; Mikaelian, 1979), immature IHCs fire spontaneous Ca^{2+}-mediated action potentials (Kros et al., 1998; Marcotti et al., 2003; Johnson et al., 2011, 2013), which causes glutamate release (Beutner and Moser, 2001) and drives bursting activity in SGNs (Tritsch et al., 2007). Similar immature spontaneous activities were found in the retina, spinal cord, hippocampus, and cerebellum where they are assumed to be required for adequate neuronal development (Blankenship and Feller, 2010). In contrast, functional mature IHCs generate graded receptor potentials in response to sound stimuli (Kros et al., 1998). While small Ca^{2+}-currents and exocytosis are found in IHCs up to three days after birth, the increased clustering and synaptic confinement of Ca^{2+}-channels at IHC AZs causes an increase in current density with advancing maturation (Beutner and Moser, 2001; Brandt et al., 2005; Johnson et al., 2005; Sendin et al., 2007; Johnson et al., 2009; Zampini et al., 2010; Beurg et al., 2010; Wong et al., 2013, 2014, reviewed in Bulankina and Moser, 2012). In parallel, the amplitude of Ca^{2+}-currents increases during the first postnatal week generating sufficient Ca^{2+} influx to trigger exocytosis at immature synaptic ribbons (Beutner and Moser, 2001; Johnson et al., 2005) and induce action potentials in SGNs (Tritsch and Bergles, 2010; Bulankina and Moser, 2012). Later upon maturation, the number of Ca^{2+}-channels reduces (Brandt et al., 2003) and the number of K^{+}-channels is upregulated preventing regenerative depolarizations (Kros et al., 1998). Moreover, the Ca^{2+} efficiency of exocytosis rises in mature IHCs due to a tighter spatial Ca^{2+}-channel release site coupling (Wong et al., 2014). After the onset of hearing: (i) ribbon synapses mature by likely merging several small presynaptic AZs and apposed postsynaptic densities (PSD) to one large AZ/PSD complex per SGN bouton; (ii) Ca^{2+}-channels form stripe-like clusters rather than the small and round clusters observed before onset of hearing; (iii) extrasynaptic Ca^{2+}-channels are selectively pruned; and (iv) the relationship of Ca^{2+} influx to release during sequential blockade of Ca^{2+}-channels linearizes (Figure 1.6C) (Wong et al., 2014). As a consequence, mature IHCs are capable of evoking similar amounts of exocytosis in response to short stimuli with smaller Ca^{2+} influx (Beutner and Moser, 2001; Brandt et al., 2005; Johnson et al., 2005; Sendin et al., 2007, reviewed in Bulankina and Moser, 2012).

Previous studies showed an involvement of different synaptic proteins in the exocytosis process during the transition from otoferlin-independent to otoferlin-dependent exocytosis (Beurg et al., 2010). At immature IHCs, the Ca^{2+} sensors synaptotagmin 1 and 2 are found (Beurg et al., 2010), while mature IHCs appear to operate without these proteins (Safieddine and Wenthold, 1999; Uthaiah and Hudspeth, 2010; Reisinger et al., 2011). Here, the hair-cell specific protein otoferlin is required for Ca^{2+}-dependent SV fusion (Roux et al., 2006; Dulon et al., 2009; Reisinger et al., 2011). Although the high immature activity is well described in murine cochlear IHCs, the mechanisms behind are not fully clarified. It is assumed that the early activity of the auditory pathway

is essential for the maturation of the Ca^{2+}-sensitivity, IHC innervation and maintenance as well as refinement of the tonotopic organization of the pathway (Friauf et al., 1999; Kandler et al., 2009; Kennedy, 2012; Safieddine et al., 2012; Johnson et al., 2013). However, it is still not understood whether immature IHCs are depolarized either sufficiently at rest (Johnson et al., 2011, 2013) or by external adenosine triphosphate (ATP) stimuli from supporting cells (Tritsch et al., 2007; Tritsch and Bergles, 2010) in order to trigger action potentials.

These observed physiological maturation coincides with a number of morphological changes (reviewed in Yu and Goodrich, 2014). First SGNs fibers start contacting cochlear IHCs already before birth (Koundakjian et al., 2007; Appler and Goodrich, 2011) whereafter they increase in number during the first postnatal week similar to the number of ribbon synapses (Lenoir et al., 1980; Shnerson et al., 1981). Up to the second postnatal week, SGNs undergo a reorganization from forming contacts with both IHCs and OHCs to predominantly forming contacts with IHCs, while OHC connections are eliminated (Huang et al., 2012). During this process, IHC afferent contacts enlarge over the development with increased numbers of mitochondria (Stamataki et al., 2006). Pruning of immature fibers is supposed to reduce the number of SGNs leading to an approximately 50 % decrease in PSD and presynaptic ribbon number (Sobkowicz et al., 1986; Stamataki et al., 2006; Huang et al., 2007; Meyer et al., 2009; Huang et al., 2012; Bulankina and Moser, 2012) (Figure 1.6B). Despite of fewer synaptic ribbons and PSDs, an increase in size was reported for both where multiple small PSD appositions are assumed to merge to one large PSD (Wong et al., 2014). Moreover, immature IHCs mostly possess multiple round ribbons that are anchored at a single AZ via two rootlets (Figure 1.6A, B) (Sobkowicz et al., 1982, 1986; Stamataki et al., 2006; Wong et al., 2014). In contrast, floating ribbon precursors, another typical immature characteristic, disappear over development. Interestingly, such ribbon precursors are present as well in the cytoplasm of retinal photoreceptors where they consist not only of RIBEYE, but also other synaptic proteins like bassoon, piccolo, and RIM1 (Regus-Leidig et al., 2009). Mature AZs reveal an 1:1 ratio with predominantly ellipsoid ribbon synapses, which are all connected to the AZ membrane by a mainly single continuous presynaptic density containing the protein bassoon (Sobkowicz et al., 1986; Khimich et al., 2005; Stamataki et al., 2006; Wong et al., 2014) (Figure 1.6A, B). Currently, we still do not understand the processes and pathways that initiate and coordinate ribbon synapse assembly, maturation and targeting ribbon precursors to the AZ. The described structural refinements are associated with the above mentioned developmental functional changes as well as changes in the molecular composition. Thyroid hormone, for example, appears to be essential for normal ribbon development (Rüsch et al., 1998; Sendin et al., 2007). Mature IHCs that lack the thyroid hormone reveal an immature phenotype with high numbers of ribbon synapses, the occurrence of multiple ribbons and large Ca^{2+}-currents with low release efficiency (Sendin et al., 2007). Secondly, myosin VI - an actin based motor protein that is present at the IHC AZ membrane and interacts with otoferlin - has been shown to be involved in ribbon synapse development (Heidrych et al., 2009; Roux et al., 2009). Myosin VI mutant mice at the age of P15 and P21 exhibit a delay in IHC maturation as shown by: (i) the impairment of BK channel transport to the membrane; (ii) immature spontaneous action potential generation and exocytic Ca^{2+} efficiency; and (iii) a reduction in the ribbon number by 30 % with the rest demonstrating immature round

shapes (Heidrych et al., 2009; Roux et al., 2009). Finally, SGNs are presumed to influence the formation and maturation of ribbon synapses based on the research of Sobkowicz et al. (1986) where the removal of afferent SGNs results into an impairment of the ribbon localization to the basal part of the IHCs. Neurotrophins have been reported to be critical for axonal pathfinding and survival as well as synapse formation (Ernfors et al., 1995; Michael et al., 1997; Fariñas et al., 2001; Luo et al., 2001; Wu et al., 2004; Kersigo and Fritzsch, 2015, reviewed in Rubel and Fritzsch, 2002). Deletion of the neurotrophins brain-derived neurotrophic factor (Bdnf) and neurotrophin-3 (Ntf-3) eliminates afferent innervation, which in turn causes a loss of ribbons in cochlear HCs implying a role in ribbon synapse formation and maintenance (Fritzsch et al., 2004; Wan et al., 2014; Fritzsch et al., 2015). Moreover, the disruption of ribbons causes a decrease of SGNs as shown in zebrafish HCs (Sheets et al., 2011).

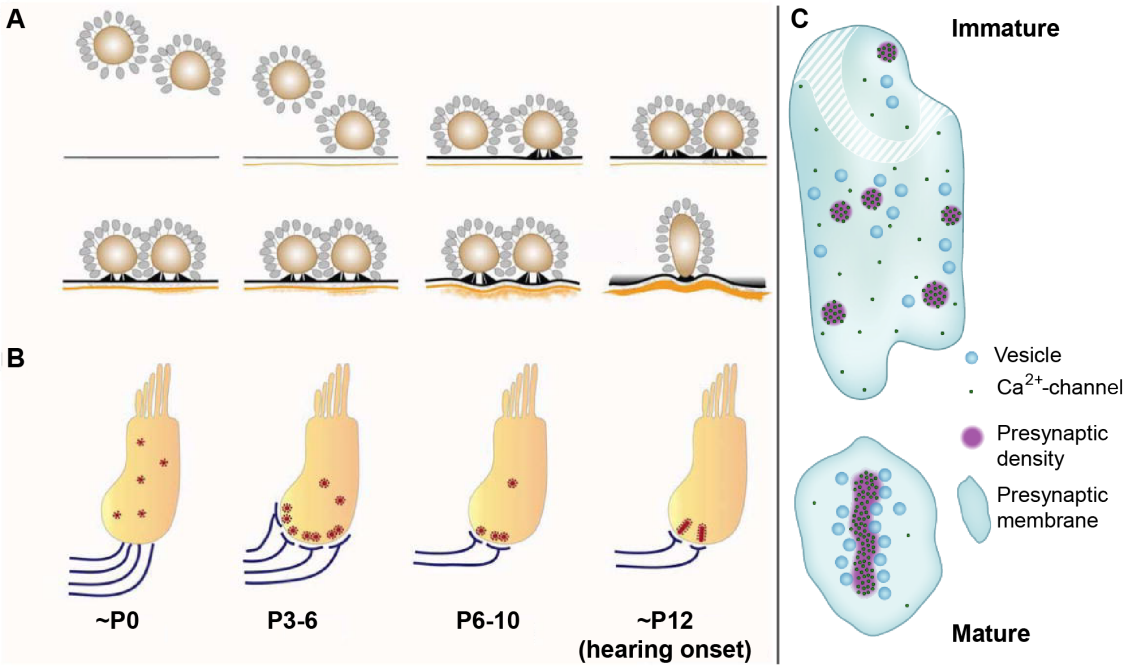

Figure 1.6.: Timeline of mouse IHC ribbon synapse development according to the current knowledge
(A) In pre-hearing mice, multiple cytoplasmically floating ribbon precursors are localized towards the basal cell membrane where PSDs begin to assemble opposing to presynaptic AZs (Sobkowicz et al., 1986). Immature and round ribbons are first anchored to the presynaptic membrane via two rootlets, while during maturation synaptic ribbons become more elliptic in shape and are attached to the AZ by a single presynaptic density (Sobkowicz et al., 1982). **(B)** During development ribbons are targeted to the basolateral membrane of IHCs in response to the innervation of SGNs (blue). Further development of afferent nerve fibers such as pruning, retraction, and refinement leads to a degradation of ribbon synapses and consequently to the establishment of a monosynaptic contact between IHCs and SGNs.

Figure 1.6 ***(previous page)*****: (C)** In line with synaptic ribbons also Ca^{2+}-channels undergo developmental alterations from small clusters with less organized SVs at immature AZs to a more confined stripe-like Ca^{2+}-channel cluster at the mature AZ with evenly distributed SVs in close proximity (Wong et al., 2014). Figure adapted from Yu and Goodrich (2014) and Wong et al. (2014).

The described refinements in ribbon number (first increase during the first week and then decrease after the onset of hearing) and size (enlargement) upon maturation lead to the question which mechanisms are involved and how exactly the ribbon structure reorganizes. Two mechanisms are intensively discussed: (i) pruning of ribbons via unknown mechanisms to eliminate surplus ribbons (Spoendlin, 1972; Sobkowicz et al., 1986; Simmons and Liberman, 1988; Spiwoks-Becker et al., 2004; Wong et al., 2014). In this case, the remaining synaptic ribbon undergoes the final structural maturation. The other possibility is (ii) fusion of synaptic ribbons (Spiwoks-Becker et al., 2004; Regus-Leidig et al., 2009; Wong et al., 2014). Recent evidence in pre-hearing cochlear IHCs and retinal photoreceptors rather favors the fusion hypothesis, as floating ribbon precursors have been found in close proximity to AZs (Regus-Leidig et al., 2009; Wong et al., 2014). However, a clear indication for either one of these two scenarios is lacking as well as the mechanisms involved. Further, it is not understood what kind of signals are necessary between IHCs and SGNs to induce the attachment of ribbons at the AZ membrane along with the PSD assembly and the coordination between the size of synaptic ribbons and PSDs.

1.5.2. Utricular ribbon synapses

Utricular HCs acquire functional transduction channels (Holt et al., 1997) as well as voltage-gated Na^+, Ca^{2+} and K^+ (fast inwardly and outwardly rectifying) channels (Rüsch et al., 1998) between the embryonic days (E)14 and E21 (Géléoc and Holt, 2003; Géléoc et al., 2004). These channels might be involved in the spiking activity of immature HCs, which could influence afferent synaptogenesis and differentiation by two mechanisms. Either indirectly by facilitating neurotrophin release or directly by glutamatergic transmission (Eatock and Hurley, 2003). It has been proposed that the outwardly rectifying K^+-channels increase in number and become more versatile, while the other channels decline upon maturation causing a reduction in the spontaneous spiking activity of vestibular HCs (Eatock and Hurley, 2003). Additional developmental differences between the extrastriolar and striolar zone were observed. During the first postnatal week, most HCs in the striolar zone show a more negative inactivating conductance, whereas more HCs in the extrastriolar zone show a less negative inactivating conductance (Chabbert et al., 2003). The latter disappears by P20 speaking for an immature state of the extrastriolar zone that develops more slowly than the central striolar zone (Sans and Chat, 1982; Rüsch et al., 1998; Chabbert et al., 2003). Similar to the above mentioned cochlear IHC development (see Section 1.5.1), the functional changes of vestibular HCs may coincide with a structural reorganization of synaptic contacts in order to establish mature vestibular HC synapses and generate graded receptor potentials only in response to mechanical input. Compared to cochlear IHCs even less is known about the morphological maturation of vestibular HCs. The number of ribbon synapses of type I vestibu-

lar HCs in crista decreases dramatically after birth in cats, while no change in the ribbon number could be observed in type II HCs (Favre and Sans, 1979). As described earlier, pruning and/or ribbon fusion could possibly explain the decline of synaptic ribbons in type I HCs. According to Favre and Sans (1979), this decline may reflect a reduced requirement of SV transmission. In contrast to type I HCs in cats, constant ribbon counts are maintained in both utricular HC types of mature mice (Eatock and Lysakowski, 2006). Furthermore, differences in the establishment of afferent fiber contacts on cochlear and utricular HCs have been found. In the cochlea, afferent fibers form contacts on IHCs already before birth (Koundakjian et al., 2007; Appler and Goodrich, 2011), whereas first complete calyces occur after birth at P4 (Rüsch et al., 1998). Thus, also other developmental processes may differ in the utricle compared to the cochlea. Much more detailed research is needed in mouse utricular HCs in order to relate structural with functional changes upon maturation.

1.6. Aim of the study

Deafness and vestibular disorders can be divided into congenital and acquired forms whereby the acquired forms (e.g. due to increasing age) represent the most common ones. Indeed, the reduction in the balancing ability is associated with aging as older adults have a higher risk to fall. According to the World Health Organization, more than 5 % of the world's population has a disabling hearing loss from which 34 million are children suffering from a severe impact on their development and education (http://www.who.int/deafness/en/, 24.04.2018). Hearing impairments may arise as developmental defects in the immature ear (Kopecky et al., 2012). Hence, prevention of hearing and balance loss as well as future therapies require more fundamental research in model organisms in order to improve the understanding of the developmental timeline when essential synaptic features arise or change upon maturation. Further, a detailed overview of cellular mechanisms is crucial for comprehending the development of sound and head motion encoding.

The first aim of this study was thus to perform a comprehensive ultrastructural analysis of cochlear and utricular HC AZ development using the laboratory mouse (*Mus musculus*) model organism. Because of similar cell pathologies as noted for humans, their high reproducibility and fast achievement of sexual maturity, the mouse represents an applicable model for hearing and balance research in order to elucidate age-related alterations. In this thesis, I combined high resolution transmission electron microscopy (TEM) and electron tomography with serial block face- and focused ion beam-scanning electron microscopy to first investigate the temporal sequence and underlying molecular mechanisms of AZ assembly, ribbon formation and maintenance as well as ribbon position upon cochlear IHC and utricular HC maturation. Along with these objectives, the question about the transport mechanism of synaptic components arises since floating ribbon precursors have been observed in cochlear IHCs (Wong et al., 2014). Accordingly, the next objective of my thesis was to figure out the molecular composition of IHC ribbon precursors. Moreover, very little is known about the protein composition in utricular HCs. For this reason, I aspired to elucidate the presence of synaptic proteins that are known to be expressed at cochlear ribbon synapses. Therefore, pre-embedding immunogold labelings followed by TEM were utilized in cochlear and

utricular HCs. Studying immature HC synaptic ribbons and compare them with juvenile and adult HCs enabled a broad quantification of morphological AZ parameters and their molecular components, which simultaneously aimed to provide a link between structural and functional presynaptic AZ properties.

The second aim was to characterize the role of the synaptic ribbon for sound encoding in the cochlea by exploring morphological effects of genetic disruption in the major constituent of the ribbon, RIBEYE. In spite of decades of research, the functional importance of the synaptic ribbon has remained elusive. Therefore, electron microscopic imaging of random single sections and serial sections intended to assess the molecular anatomy of presynaptic AZs at mature RIBEYE knockout mice ($RBE^{KO/KO}$) on an ultrastructural level.

2. Materials and Methods

2.1. Animals

For this thesis, mice ranging in age from the embryonic day (E)14 to the postnatal day (P)48 were used for studying cochlear inner hair cell (IHC) development. Utricular hair cell (HC) development was investigated using mice from P9 to 11 months, while for the characterization of RIBEYE knockout (KO) IHC ribbon synapses, mice ranging from P21 to 8 months were examined. All experiments complied with national animal care guidelines and were approved by the University of Göttingen Board for Animal Welfare and the Animal Welfare Office of the State of Lower Saxony. Different mouse lines, used in this study, are listed below in Table 2.1.

Mouse line	Age	Reference
C57BL/6J mice (wild-type)	cochlea: E14, E16, E18, P0, P1, P2, P4, P9, P11, P12, P14, P15, P19, P20, P21, P48; utricle: P9, P14, P15, P20, P93, 11 months	available at The Jackson Laboratory
RIBEYE knockout mice ($RBE^{KO/KO}$) and littermate control mice ($RBE^{WT/KO}$; $RBE^{WT/WT}$)	P21, P43, 8 months	published in Maxeiner 2016 (*The EMBO Journal*)
CBA (wild-type)	P189	available at The Jackson Laboratory

Table 2.1.: Investigated mouse lines

2.2. Materials

Chemical and reagent details:

Product	Company	Cat. No
Acetone	Carl Roth	5025.5
Bovine serum albumin (BSA)	Aurion	900099
Calcium chloride ($CaCl_2$)	Sigma Aldrich	793639
Chloroform	Merck & Co.	1.024.451.000
Copper 100 mesh grids	Plano	G2410C
Copper slot grid 3.05 mm	Plano	G2500C
Durcupan ACM Fluka	Sigma Aldrich	44610
Embedding moulds	Agar Scientific	G3533
EPON pre-mix kit	Agar Scientific	R1140

Continued on next page

Table 2.2 – continued from previous page

Product	Company	Cat. No
Epoxy Conductive Adhesive (EPO-TEK EE 129-4)	Electron microscopy sciences	12670-EE
Ethanol	Sigma Aldrich	32205
Ethylene glycol-bis(β-aminoethyl ether)-N,N,N',N'-tetraacetic acid (EGTA)	Sigma Aldrich	E3889
FIB-SEM pins (standard SEM stub; 12.7 mm, slotted head, 3.1 mm tapered end pin)	Science services GmbH	MT75220
Glass slides	VWR	630-1986
Glucose	Sigma-Aldrich	G8270-1KG
Glutaraldehyde (GA)	Sigma-Aldrich	G7651
Goat serum	Merck	S26-100ml
Grid boxes	Plano	B801003080
4-(2-hydroxyethyl)-1-piperazineethanesulfonic acid (HEPES)	Sigma Aldrich	H3375
HQ Silver-enhancement kit (Nanoprobes)	Biotrend GmbH	N-2012
insect pins (apex diameter 0.0125 mm)	Fine Science Tools	26002-10
L-Glutamine	Sigma Aldrich	G3126-100g
Lead(II)nitrate ($Pb(NO_3)_2$)	Carl Roth	HN32.1
Magnesium chloride hexahydrate ($MgCl_2$-$6H_2O$)	Sigma Aldrich	M2670
Magnesium sulfate ($MgSO_4$)	Sigma Aldrich	746452
Micro curette 1.5 mm	Fine Science Tools	10082-15
Mowiol 4-88	Carl Roth	0713.1
Normal horse serum (NHS)	Biozol GmbH	VEC-S-200
Osmium tetroxide liquid	Sigma Aldrich	75632.5ml
Paraformaldehyde (PFA)	Carl Roth	0335.1
Petri dishes (35 x 10 mm)	Greiner Bio-One	627160
Petri dishes (94 x 16 mm)	Greiner Bio-One	633180
Phosphate buffered saline (PBS) tablet	Sigma Aldrich	P4417
PIPES (1,4-Piperazinediethanesulfonic acid)	Sigma Aldrich	P1851-500g
Potassium chloride (KCl)	Sigma Aldrich	746436
Potassium ferrocyanide (KFeCn)	EMS	25154-10
Protein A 10 nm gold	CMC Utrecht	PAG 10 nm/S
Proteinase XXIV	Th. Geyer	P 8038-100MG
Saponin	Carl Roth	4185.1
SBF-SEM pins	Workshop at Georg August University of Göttingen	Custom made
Sodium cacodylate trihydrate	Sigma Aldrich	CO250.10g
Sodium chloride (NaCl)	Sigma Aldrich	746398
Sodium citrate dihydrate ($Na_3C_6H_5O_7$-$2H_2O$)	Merck & Co.	567446
Sodium hydroxide (NaOH) pellets	Carl Roth	6771.1
Sodium phosphate (dibasic, Na_2HPO_4)	UMG pharmacy	1029598
Steriplan glass petri dishes 15 x 60 mm	Duran group	237554008
Sylgard	GE Healthcare Bayer	RTV615-A+B-1LBS-2-Silikon
Triton X-100	Sigma Aldrich	X100-500ml
Uranyl acetate	Merck	8473
Uranyl acetate replacement	EMS	22405
Vinylec E (Formvar®) Resin	TED Pella, inc.	19222

Table 2.2.: Products used for the experiments

Equipment details:

Product	Company
AxioCam ERc 5s	Zeiss

Continued on next page

Table 2.3 – continued from previous page

Product	Company
Binocular Stemi 2000-C	Zeiss
Centrifuge 5414	Eppendorf
Crossbeam 540 dual-beam scanning microscope	Zeiss
Cryotrim 45°	Diatome
Cryotrim 90°	Diatome
Digital incubator INCU-Line IL10	VWR
JEM-1011	JEOL
JEM-2100	JEOL
Magnetic stirrer including hot plate (IKA-COMBIMAG RCT)	Janke & Kunkel KG
Micro scale LA230S	Sartorius
Orius SC1000 CCD camera	GATAN
pH-meter 1000L	VWR
Quanta 250 FEG scanning electron microscope	FEI
Reichert Ultracut E	Leica Microsystems
Rotating wheel	Workshop at University Medical Center Göttingen
Separatory glass funnel ϕ 34 x 90 mm	Glasgerätebau Ochs
Sputter coating machine EM ACE600 (for FIB-SEM)	Leica
Sputter coating machine SCD 050 (for SBF-SEM)	Balzers
TCS SP2	Leica Microsystems
Ultra 35° diamond knife	Diatome
Vapor pressure osmometer 5520	WESCOR
3View automatic microtome	GATAN Inc., Pleasonton, USA

Table 2.3.: Equipment utilized in this study

Solution details:

Solution	Concentration and treatment condition
Block contrast (for enhanced en bloc staining)	2.5 % uranyl acetate (v/v) in distilled water (under the hood at room temperature, in dark on a shaker)
Blocking solution (for Saponin pre-embedding	2 % BSA (v/v) / 3 % NHS (v/v) in PBS (under the hood at room temperature)
Blocking solution (for Triton X pre-embedding)	2 % BSA (v/v) / 3 % NHS (v/v) in 0.2 % PBST (under the hood at room temperature)
Fixative 1 (for conventional embedding)	4 % (v/v) PFA and 0.5 % (v/v) GA in PBS (under the hood on ice)
Fixative 2 (for conventional embedding)	2 % glutaraldehyde (v/v) in 0.1 M cacodylate buffer (under the hood on ice)
Fixative (for Saponin pre-embedding)	4 % paraformaldehyde (v/v) in PBS (under the hood on ice)
Fixative (Triton X pre-embedding)	2 % paraformaldehyde (v/v) with 0.06 % glutaraldehyde (v/v) in 1 x PEM (under the hood on ice)
Formvar solution	1 % in water free chloroform (w/v), light protected (under the hood at room temperature)
Goat serum dilution buffer (GSDB)	16 % normal goat serum, 450 mM NaCl, 0.3 % Triton X-100, 20 mM phosphate buffer, pH 7.4
HEPES-Hanks' balanced salt solution	KCl 5.36 mM, NaCl 141.7 mM, $MgCl_2$-$6H_2O$ 1 mM, $MgSO_4$-$7H_2O$ 0.5 mM, HEPES 10 mM, glucose 2 mg/ml, L-glutamine 0.5 mg/ml (pH was adjusted to 7.2 with NaOH, osmolarity about 300 mmol/kg)
Osmium tetroxide (OsO_4)	2 % (v/v) in sodium cacodylate buffer (for pre-embedding; under the hood) and 1 % (v/v) in cacodylate (for conventional embedding; under the hood)
Osmium tetroxide (OsO_4) - potassium ferrocyanide solution (KFeCn) (for enhanced en bloc staining)	2 % OsO_4 (v/v) and 1.5 % (KFeCn) (v/v) in cacodylate buffer (under the hood on ice)

Continued on next page

Table 2.4 – continued from previous page

Solution	Concentration and treatment condition
PBST (for Triton X pre-embedding)	0.1 % or 0.2 % Triton X-100 (v/v) in PBS
PEM	0.1 M PIPES, 2 mM EGTA, 1 mM $MgSO_4$ x $7H_2O$ in distilled water
Phosphate buffer 240 mM	27.52 g Na_2HPO_4, 5.52 g NaH_2PO_4, add H_2O up to 1 liter
Post-fixative (for Triton X and Saponin pre-embedding)	2 % glutaraldehyde (v/v) in PBS (under the hood at room temperature)
Proteinase XXIV	50 μg/ml in ice-cold HEPES-Hanks' balanced salt solution (w/v)
Reynold's lead citrate	1.33 g $Pb(NO_3)_2$ and 1.76 g $Na_3C_6H_5O_7$-$2H_2O$ (w/v) in 92 ml distilled water (dissolved upon heating, with constant stirring and in the end 8 ml 1 M NaOH was added). Usable after filtering and stored airtight at 4°C (applied under the hood after centrifugation for 10 min, respectively).
Sodium cacodylate buffer	0.1 M in distilled water, pH 7.2-7.4 (under the hood)
Thiocarbohydrazide solution (TCH)	0.1 g TCH (w/v) in 10 ml distilled water (under the hood; incubate at 60°C for 60 min and mix carefully every 10 min). Usable after cooling and filtering.
Uranyl acetate	4 % (v/v) in distilled water (under the hood)
Wash buffer	450 mM NaCl, 0.3 % Triton X-100, 20 mM phosphate buffer
Water free chloroform	500 ml glass bottle filled up to the level mark of 100 ml with $CaCl_2$ powder and till the level mark of 500 ml with Chloroform (w/v), stirred once well (stored airtight and light protected under the hood at room temperature; undisturbed)

Table 2.4.: Solutions used in this study

2.3. Methods

2.3.1. Dissection procedures

Sample preparations of organs of Corti and utricles were performed around noon time to reduce a putative impact of circadian changes (Hull et al., 2006).

2.3.1.1. Dissection of the organ of Corti

Mice were anesthetized with CO_2 and sacrificed by decapitation. After removing the skin from the head, the skull was sagittally cut in half (Figure 2.1A) and placed into ice-cold phosphate buffered saline solution (PBS). The brain was removed and the inner ear labyrinth was twisted out carefully from the skull (Figure 2.1B, C). Next, a small opening at the cochlear apex was made with Dumont #5 forceps. Nearly the complete bony wall of the cochlea was removed afterwards starting from the apical opening (Figure 2.1D, E). The exposed organ of Corti was first separated from the central axis, named modiolus, to finally cut its apical turn using Dumont #5 - fine forceps (Figure 2.1F). The tissue was transferred for further processing with a micro curette.

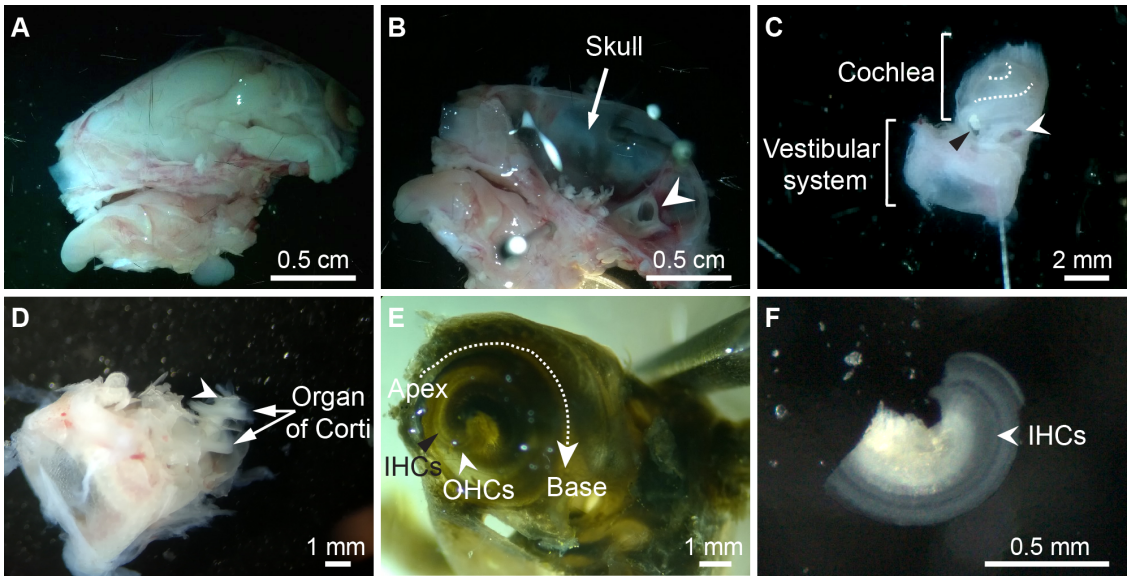

Figure 2.1.: Apical turn preparation of the organ of Corti
Dissected skull after sagittal cut with **(A)** and without **(B)** the right brain hemisphere. The arrowhead highlights the inner ear. **(C)** Separated inner ear with the apical bony wall surrounding the cochlea. White arrowhead: round window, black arrowhead: oval window, dotted line: cochlea turns. **(D)** After removing the bone tissue, the cochlear coil turned around the modiolus (arrowhead) is visible. **(E)** Top view onto the apical turn after fixation and contrasting steps. **(F)** Dissected apical turn of the organ of Corti containing IHCs.

2.3.1.2. Dissection of the organ of Corti in young (E14 - P4) mice

Organs of Corti from embryonic mice and mice shortly after birth were prepared following Driver and Kelley (2010). For the dissection, inner ears were exposed in the same way as for older

animals. In short, animals were decapitated and the skull was sagittally cut in half (Figure 2.2A-C). The isolated inner ears (Figure 2.2D) were pinned down onto PBS filled sylgard coated glass petri dishes by placing minutien pins through the vestibular region. Using Dumont #5 - fine forceps the cartilage was opened and cut parallel to the duct (Figure 2.2E). Before the cartilage was removed, the underlying cochlea was detached with closed forceps. The same procedure was performed to separate the cochlea also from the underlying cartilage. Afterwards, the cochlea was cut at the base and delicately taken out of the inner ear (Figure 2.2F). Beginning from the base, the upper half of the duct was removed to expose the developing sensory epithelium (Figure 2.2G), which was next transferred with a micro curette for further handling.

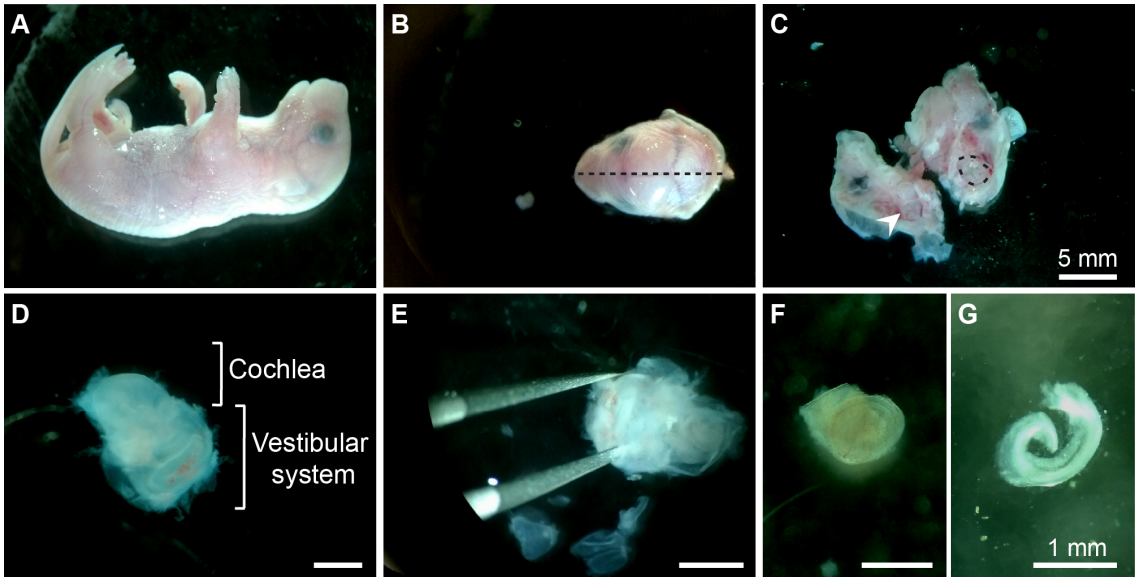

Figure 2.2.: Isolation of the developing organ of Corti
(A, B) After decapitation of the embryo, the skull was cut into halves **(C)** to expose the inlying inner ears. The right inner ear is highlighted with a black dotted line and the left inner ear with a white arrowhead. **(D)** Isolated inner ear displaying two distinguishable parts, the cochlea and the vestibular system. **(E)** After removing the cartilage and excising the cochlea **(F)**, the ventral half of the cochlea duct can be separated so that the epithelium located on the dorsal side of the duct is visible **(G)**.

2.3.1.3. Dissection of the utricle

Utricle preparations were performed in ice-cold HEPES-HANKS solution. The inner ear was dissected in the same way as described before for the organ of Corti (Section 2.3.1.1) and transferred into a new petri dish containing ice-cold HEPES-HANKS solution (Figure 2.3A). After carefully removing the vestibular bone tissue above the utricle (Figure 2.3B), the pigmented epithelium was opened and gently pulled apart using Dumont #5 - fine forceps (Figure 2.3C). To facilitate the removal of the otolithic membrane overlying hair bundles of the utricle, the organ was placed into a petri dish filled with proteinase XXIV solution (50 μg/ml in HEPES-HANKS solution, w/v) for 5 min at room temperature. In fresh HEPES-HANKS solution, the otolithic membrane was then removed with an eyelash and the exposed utricle was cut out with Dumont #5 - fine forceps and a

microscissor (Figure 2.3D). Using a micro curette, the explanted utricle was transferred for further treatments.

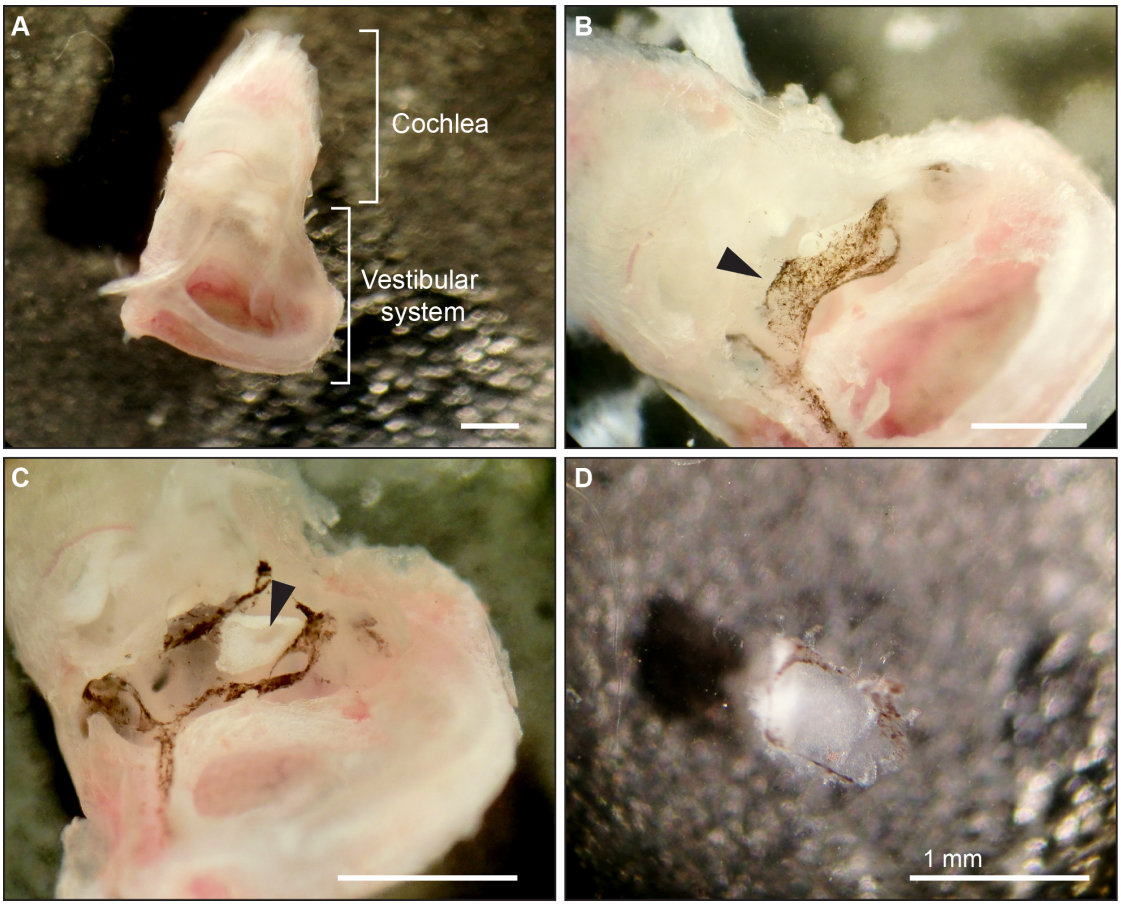

Figure 2.3.: Utricle preparation from the vestibular system
(A) Medial view of the exposed inner ear with cochlea and vestibular system. **(B)** View of the pigmented epithelium (black arrowhead) after bone removal. **(C)** Opened pigmented epithelium revealing the otolithic membrane (black arrowhead) underneath. After removal of the otolithic membrane, the utricle is accessible and can be excised **(D)**.

2.3.2. Immunohistochemistry

Dissected organs of Corti were fixed in 4 % formaldehyde and 0.5 % glutaraldehyde containing PBS for 1 h on ice. After washing (three times for 10 min each, at room temperature) in PBS, samples were blocked with goat serum dilution buffer (GSDB) at room temperature in a wet chamber for 1 h. Next, the following primary antibodies were applied overnight at 4°C in a wet chamber: mouse anti-otoferlin (1:500 diluted in GSDB, Cat.-No. ab53233; Abcam) and rabbit anti-α-tubulin (1:400 diluted in GSDB, Cat.-No. 302008; Synaptic Systems). Specimens were washed three times for 10 min in wash buffer at room temperature and were afterwards incubated with the following secondary antibodies for 1 h at room temperature in a light-protected wet chamber: goat anti-mouse Alexa 568 (1:200 diluted in GSDB, Cat.-No. A11004; Life technologies) and goat anti-rabbit Alexa 488 (1:200 diluted in GSDB, Cat.-No. A11008; Life technologies). Finally,

organs of Corti were washed three times in wash buffer for 10 min and once in 5 mM phosphate buffer for 5 min at room temperature before mounting the specimens in Mowiol and carefully placing a glass cover slip on top. Samples were dried and stored light-protected at 4°C.

2.3.3. Sample preparation for electron microscopy

2.3.3.1. Conventional embedding

Organs of Corti and utricles were processed from mice as explained above and fixed immediately with 4 % paraformaldehyde and 0.5 % glutaraldehyde in PBS (pH 7.4) for 1 h on ice followed by a further fixation step overnight with 2 % glutaraldehyde in 0.1 M sodium cacodylate buffer (pH 7.2) on ice. Subsequently, samples were washed in 0.1 M sodium cacodylate buffer (three times for 10 min each, on ice) and treated with 1 % osmium tetroxide (v/v in 0.1 M sodium cacodylate buffer) for 1 h on ice. After osmium tetroxide treatment, samples were washed twice in 0.1 M sodium cacodylate buffer on ice for 10 min, respectively and further in distilled water (three times for 5 min each, on ice). Next, en bloc staining with 1 % uranyl acetate (v/v in distilled water) was performed for 1 h on ice and samples were briefly washed three times in distilled water (10 min each, on ice), dehydrated in an ascending concentration series of ethanol (Table 2.5) on ice, infiltrated and embedded in flat molds using epoxy resin to get finally polymerized for 48 h at 70°C (Table 2.6).

Time (min)	Ethanol concentration (v/v)
5	30 %
5	50 %
10	70 %
10	95 %
10	95 %
12	100 %
12	100 %
12	100 %

Table 2.5.: Increasing series of ethanol concentration

Time (h)	Condition	Epon concentration (v/v)
0.5	On a rotating wheel (10-20 rpm) at room temperature	1:1 epoxy resin in ethanol
1.5		1:1 epoxy resin in ethanol
Overnight		100 % epoxy resin
3-5		100 % epoxy resin

Table 2.6.: Series of epon-ethanol infiltration

2.3.3.2. Immunogold pre-embedding

Immunogold pre-embedding labeling was performed by using the following two main protocols, whereby the Triton X protocol was adapted from Nieratschker et al. (2009).

Triton X protocol:

Samples were fixed with 2 % paraformaldehyde and 0.06 % glutaraldehyde in PEM (0.1 M PIPES, 2 mM EGTA, 1 mM $MgSO_4$ x 7 H_2O, v/v) for 45 min on ice. After fixation, the organs were washed twice in PEM for 15 min each and blocked for 1 h in 2 % bovine serum albumin (BSA)/ 3 % normal horse serum (NHS) in 0.2 % PBST (0.2 % Triton X-100 diluted in PBS, v/v). Next, samples were incubated with the primary antibody (Table 2.7, diluted in 0.1 % PBST) for 1 h at room temperature and overnight at 4°C. Subsequently, specimens were washed four times with 0.1 % PBST for 1 h each and incubated for 2 h with the 1.4 nm gold-coupled secondary antibody (Table 2.7, 1:30 diluted in 0.1 % PBST) followed by another washing step in 0.1 % PBST for 30 min at room temperature and overnight at 4°C. Further washing steps were performed in 0.1 % PBST (two times for 30 min each) until samples were post-fixated with 2 % glutaraldehyde in PBS (v/v) for 30 min and briefly washed four times in distilled water (10 min each). For silver enhancement, the HQ Silver-enhancement kit (Nanoprobes) was used for 3 min in the dark and specimens were briefly washed in distilled water for additional four times. Further fixation was obtained by the treatment with 2 % osmium tetroxide (v/v in 0.1 M cacodylate buffer) for 30 min followed by one washing step in distilled water for 1 h and two washing steps in distilled water for 30 min, respectively. Finally, samples were dehydrated and embedded in epoxy resin for further processing.

Protein	**Piccolino**	**RIBEYE**	**Myosin VI**	**Tubulin**
Primary Ab	Aczp18p19	CtBP2	Myosin VI	α-tubulin
Host	rabbit	mouse	rabbit	rabbit
Dilution	1:500	1:200	1:250	1:250
Company	Limbach et al., 2011 (kindly provided by M.W. Kilimann)	BD Biosciences	Proteus Biosciences	Synaptic Systems
Secondary Ab	Nanogold anti-rabbit	Nanogold anti-mouse	Nanogold anti-rabbit	Nanogold anti-rabbit
Dilution	1:30			
Quality	P0 (Triton X): + P2 (Triton X): + P4 (Saponin): - P9 (Triton X): ++ P9 (Triton X): + P14 (Triton X): ++ P21 (Triton X): ++	P4 (Saponin): + P4 (Triton X): - P11 (Triton X): + P12 (Saponin): ++ P14 (Saponin): ++ P14 (Triton X): +	P14 (Saponin): - P15 (Triton X): +	P11 (Triton X): -

Table 2.7.: Antibodies used for immunogold electron microscopy
All secondary antibodies used for immunogold pre-embedding in this study were from Nanoprobes, Inc. USA. (-) unspecific labeling, (+) weak specific labeling, (++) strong specific labeling.

Saponin protocol:
Here, tissues were fixed with 4 % paraformaldehyde in PBS for 45 min on ice followed by a brief washing step in PBS and a permeabilization step with 0.05 % saponin for 45 min. After washing once more in PBS, samples were first blocked with 2 % BSA/ 3 % NHS in PBS for 1 h and then incubated with the primary antibody (Table 2.7, diluted in 5 % NHS in PBS) for 1 h at room temperature and overnight at 4°C. Thereafter, specimens were washed three times in PBS for 1 h each and incubated for 2 h with the 1.4 nm gold-coupled secondary antibody (Table 2.7, 1:30 diluted in 5 % NHS in PBS). Subsequently, several washing steps were performed in PBS (for 30 min, overnight at 4°C and two times for 30 min each) until samples were post-fixated with 2 % glutaraldehyde in PBS (v/v) for 30 min and briefly washed four times in distilled water. Further processing of the samples such as the silver enhancement, osmium tetroxide treatment, dehydration and embedding in epoxy resin was performed as described in the Triton X protocol.

2.3.3.3. Enhanced en bloc staining for serial block face (SBF)- and focused ion beam (FIB)-scanning electron microscopy (SEM)

Enhanced en bloc staining was performed according to Deerinck TJ (2010). After fixation (see Section 2.3.3.1), samples were treated with 1.5 % potassium ferrocyanide and 2 % osmium tetroxide (v/v in 0.1 M sodium cacodylate buffer) for 1 h on ice. Next, specimens were briefly washed (five times for 5 min each) in distilled water and placed into a freshly prepared thiocarbohydrazide solution for 20 min followed by five additional washing steps in distilled water at room temperature. A second exposure to 2 % osmium tetroxide (v/v in 0.1 M sodium cacodylate buffer) was conducted followed by five brief washing steps in distilled water before the samples were placed in 2.5 % uranyl acetate (v/v in distilled water) overnight at room temperature in the dark. Subsequently, organs were washed in distilled water (five times for 5 min each) and contrasted with Reynold's lead citrate for 30 min at 60°C. Additional five washing steps were performed before samples were dehydrated (Table 2.5), incubated in 100 % acetone (for 10 min), infiltrated and embedded in tubes using durcupan (Table 2.8). Specimens were polymerized for 48 h at 60°C.

Time (h)	Condition	Durcupan concentration (v/v)
1	On a rotating wheel (10-20 rpm) at room temperature	25 % durcupan in acetone
1		50 % durcupan in acetone
1		75 % durcupan in acetone
Overnight		100 % durcupan
1-2		100 % durcupan

Table 2.8.: Infiltration series of durcupan

2.3.3.4. Trimming of embedded samples

Cured resin blocks (Section 2.3.3.1) of cochlea and utricle preparations were trimmed using a Diatome file in order to remove the empty resin and approach the organs. For the organ of Corti, blocks were trimmed until the tunnel of Corti (located between inner and outer hair cells) was

reached. The region of interest in the utricle was easily accessible by trimming the block until surrounding pigmented epithelium disappeared and the first HCs were detectable. Afterwards, excess of epoxy resin at the sides was removed with a file and then carefully with a razor blade whereby a small trapeze-like block face was shaped. Samples for SBF- and FIB-SEM (Section 2.3.3.3) were treated differently. First, the tube around the polymerized durcupan resin was removed by using a razor blade. Thereafter, all steps of trimming and creating a rectangular block face were conducted with the razor blade. Since organs of Corti were oriented horizontally inside the tube, organs were approached gently from the top until the upper part of the tissue was reached. For FIB-SEM, trimming was additionally performed from the outer hair cell side until the tunnel of Corti was accessed using a 90° trimming knife (Diatome). The remaining sides were straightened as well with the 90° trimming knife. Next, a razor blade was used to cut out the trimmed sample block, which was subsequently placed on a standard SEM stub (Science Services GmbH, Pin 12.7 mm $\times$ 3.1 mm) and glued with silver-filled epoxy (EPO-TEK - Epoxy Conductive Adhesive). This semiconductor needed to be cured overnight at 60°C before samples could be imaged.

2.3.3.5. Formvar coating of slot and mesh grids

Grids were first coated with 1 % formvar (w/v in water free chloroform) in order to use them later for the sections of the trimmed samples. A separatory glass funnel was filled with 1 % formvar solution and a glass object slide was placed inside. The valve was opened fast and entirely to ensure an optimal drag force. Subsequently, a thin coat of 1 % formvar (a silver/white to light yellow color represents a thickness of $\sim$80-90 nm) was applied to the glass slide. Afterwards, the glass slide was removed from the funnel and all the edges were cut on both sides of the slide using a razor blade. The glass slide was carefully immersed into a distilled water filled beaker causing the cut formvar film to detach and float on the surface of the water. Using forceps, grids were then placed with the non-shiny (rough) side facing down on the floating formvar film and were gently attached to the formvar by pressing them down. The slot grid (3.05 mm ϕ, 1 mm $\times$ 2 mm slot) covered formvar film was lifted up with parafilm, while for mesh grids (3.05 mm ϕ) only the paper of the parafilm was used. At the last step, the film was placed into a petri dish for drying and small holes were poked into the spaces between the grids to release air bubbles.

2.3.3.6. Sectioning

Prior sectioning, the surface of the trimmed samples was smoothened with a 45° trimming knife. For transmission electron microscopy, 70-75 nm ultrathin sections were cut from the samples with an Ultracut E microtome (Leica Microsystems) equipped with a 35° diamond knife (Diatome) (Figure 2.4). Next, sections were mounted on 1 % formvar-coated copper slot grids (3.05 mm ϕ, 1 mm $\times$ 2 mm slot). Whereas, for electron tomography, 250 nm semithin sections were obtained and collected on 1 % formvar-coated copper 100 mesh grids (3.05 mm ϕ).

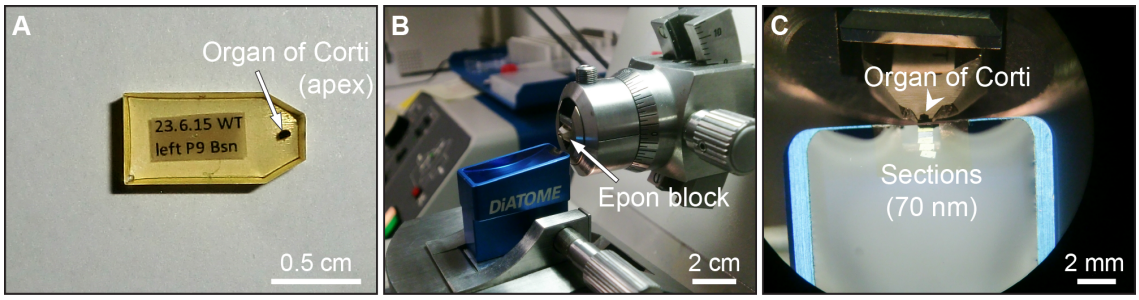

Figure 2.4.: Sectioning procedure with a diamond knife
(A) Polymerized epoxy block containing the apical turn of the organ of Corti specimen. **(B)** Side view of the sectioning procedure using the Ultracut E microtome. **(C)** Ultrathin sections float on the water surface and string together. A ribbon of sections can be collected onto formvar coated copper grids by gently touching the sections.

2.3.3.7. Section poststaining

70-75 nm ultrathin sections (placed on grids) were counterstained on droplets of 4 % uranyl acetate in water or uranyl acetate replacement solution (EMS) for 45 min and for $<$ 1 min on Reynold's lead citrate droplets. In order to prevent lead precipitates (lead carbonate), the staining was done within a closed atmosphere in the presence of NaOH pellets to reduce atmospheric CO_2. Finally, grids were washed two times (for 5-10 min each) on droplets of distilled water, which was boiled before to obtain CO_2-free water. After removing the water with filter paper, grids were dried and placed into grid boxes for later analysis. 250 nm semithin sections, used for electron tomography, were counterstained as described above but in addition 10 nm gold particles were applied after drying to both sides of the mesh grids (for 5 min each) acting as fiducial markers.

2.3.4. Microscopy imaging

2.3.4.1. Confocal microscopy

Image acquisition was performed on a laser-scanning confocal microscope (TCS SP2, Leica Microsystems) using a 63x glycerin immersion objective. Excitation was provided by a 488 nm (Argon) and a 543 nm (Helium-Neon) laser. Image stacks were acquired with the following settings: 2x or 4x zoom, 1024 $\times$ 512 image size, 4 frame averages and a step size of either 0.2 or 0.5 μm. Finally, images were processed with the ImageJ program (version 1.51k, National Institute of Health, USA).

2.3.4.2. Transmission electron microscopy (TEM)

For 2D image acquisition of random single sections as well as serial sections, a JEM-1011 (JEOL) TEM was used at 80 kV. Micrographs were acquired with a Gatan Orius 1200A camera (Gatan GmbH, using the Digital Micrograph software package) at 10,000-x magnification, unless otherwise stated.

2.3.4.3. Electron tomography

Tilt series image acquisition was conducted mainly from -60° to +60° with 1° increments at 10,000-x magnification using a JEM-2100 (JEOL) TEM at 200 kV with the Serial-EM software (Mastronarde, 2005). Few tilt series were acquired with fewer tilts because of grid bars that disturb the visual field. For tomogram alignments, the IMOD software package etomo was used with a fiducial-guided alignment mode (see Section 2.3.5.4). Tomographic reconstructions were generated using 3dmod (Kremer et al., 1996, see also Section 2.3.5.5).

2.3.4.4. Serial block face scanning electron microscopy (SBF-SEM) for 3D visualization of larger volumes

Trimmed samples were first coated with a gold layer for 300 sec using the Balzers SCD 050 sputter coater to limit charging by the electron beam during SEM imaging. The setup for SBF-SEM comprises a FEI Quanta 250 FEG scanning electron microscope (FEI) equipped with a Gatan 3View (GATAN Inc., USA) automatic microtome. The system was set to cut sections with 80 nm thickness at activated oscillator. Image acquisition was done at 30 Pa chamber pressure at 2.50 kV with spot size 3.5, a dwell time of 7 μs/pixel and an image size of 4,096 $\times$ 4,096 pixels. The magnification was set to 7x resulting in images with a pixel size of 4.9 nm.

2.3.4.5. Focused ion beam scanning electron microscopy (FIB-SEM) for 3D visualization of larger volumes

For FIB-SEM, specimens were coated with an 8 nm platinum layer using the sputter coating machine EM ACE600 (Leica) at 35 mA current. Afterwards, samples were positioned at an angle of 54° into the Crossbeam 540 focused ion beam scanning electron microscope (Carl Zeiss Microscopy GmbH). To ensure even milling and protect the surface, a 300 nm carbon layer was deposited. Atlas 3D (Atlas 5.1, Canada) software was used to collect the 3D data. Samples were exposed with a 30 nA current and a 7 nA current was used to polish the surface. Images were acquired at 1.5 kV with the ESB detector (500 V ESB grid, pixel size x/y 3 nm) in a continuous mill and acquire mode using 1.5 nA for the milling aperture (z-step 5 nm). Image alignments were done with TrackEM2 and local contrast enhancements with CLAHE, plugins of Fiji.

2.3.5. Data analysis

2.3.5.1. Quantification of 2D electron microscopic random single sections

When ribbons from random sections were attached to the AZ membrane via a presynaptic density (PD) and the AZ membrane was clearly visible, data were analyzed with the program ImageJ (version 1.51k, National Institute of Health, USA). For SVs, the first layer around the ribbon with a maximum distance of 80 nm from the vesicle membrane to the ribbon edge were counted per section (Figure 2.5A-B'). The horizontal and vertical axis were measured and averaged to calculate the mean SV diameter. For ribbon size, the height and width was measured taking the longest axis of the ribbon excluding the presynaptic density. Additionally, manual tracing of the

synaptic ribbon shape was performed to determine the ribbon area (Figure 2.5A-B'). Furthermore, the number of postsynaptic densities (PSD) per synapse was counted and the length was measured along the AZ membrane (Figure 2.5A-B').

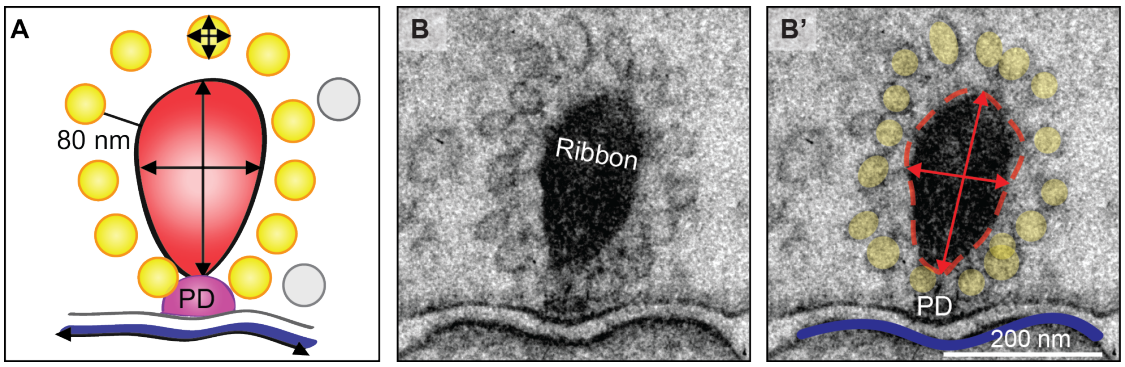

Figure 2.5.: Quantification criteria for 2D analysis of cochlear and utricular HC random sections
(A) Illustration showing the parameters for random section analysis of SV diameter and ribbon size. SVs (yellow) are determined as the first layer ($\leq$ 80 nm distance from the SV outer rim to the ribbon as displayed by the black line) around the ribbon (red). SV diameter, ribbon size (height, width and area) and PSD (blue) were measured as indicated by the black arrows. **(B, B')** Electron micrograph of a P48 cochlear IHC depicts ribbon (red lines), PSD (blue line) and SV (yellow circles) quantifications. Figure modified from (Michanski et al., 2019).

For the RIBEYE KO data, additionally two distinct morphological vesicle pools at ribbon synapses were analyzed in size and number in random 2D sections (as previously defined in Strenzke et al., 2016): (i) membrane-proximal synaptic vesicles (MP-SVs, $\leq$ 25 nm distance between SV membrane and AZ membrane and $\leq$ 80 nm from the presynaptic density); and (ii) ribbon-associated synaptic vesicles (RA-SVs, first layer of vesicles around the ribbon with a maximum distance of 80 nm from the ribbon surface to the vesicle membrane and not falling into the MP-SV pool) or in case of the KO animals presynaptic density-associated synaptic vesicles (PDA-SVs/ ribbonless AZs, vesicles within 80 nm distance of the presynaptic density excluding MP-SVs). Moreover, the length of the presynaptic density was measured in this study (Figure 2.6; Jean et al., 2018).

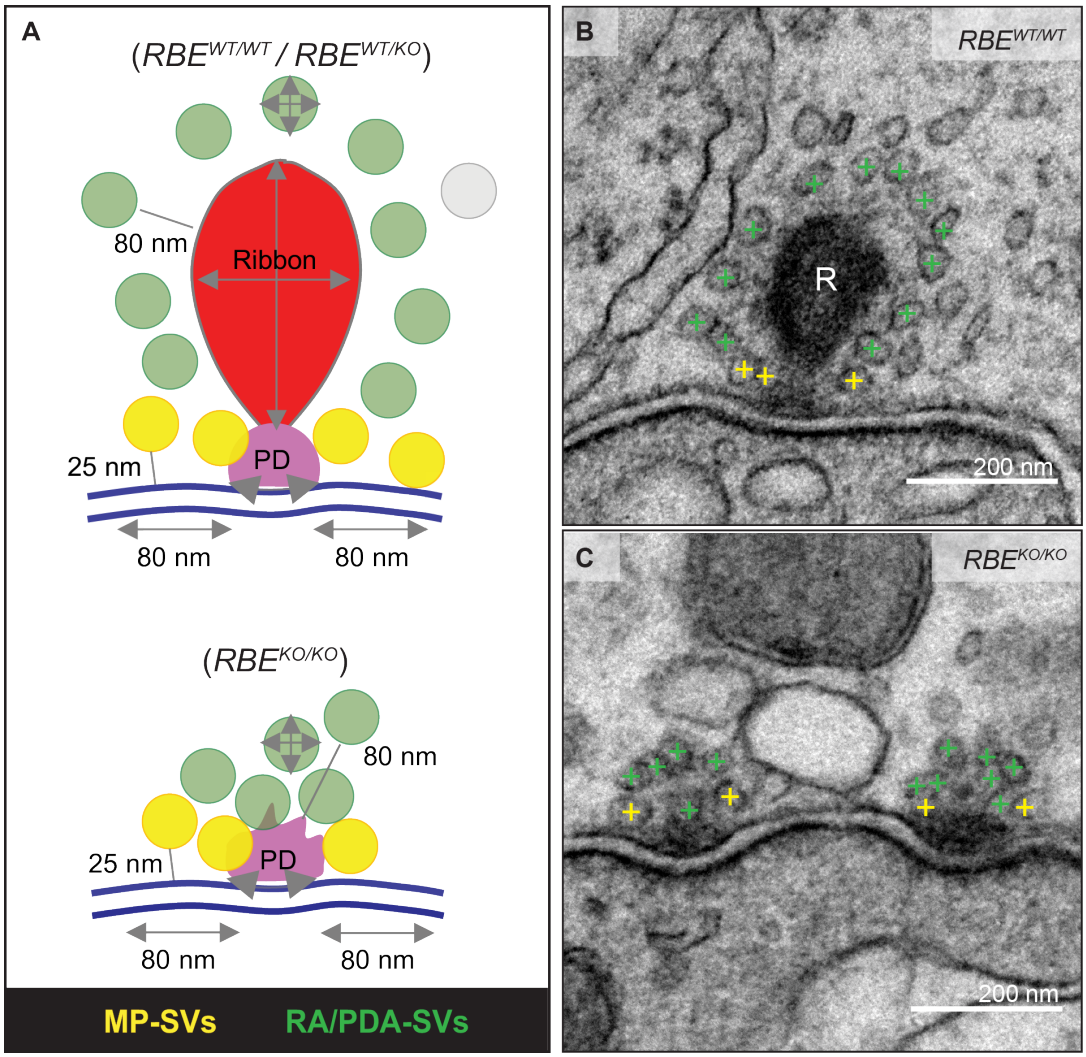

Figure 2.6.: Analysis criteria of random sections from $RBE^{WT/WT}$, $RBE^{WT/KO}$ and $RBE^{KO/KO}$ murine IHCs
(A) Schematic depicts the quantitative analysis of SV diameter, ribbon height, ribbon width and ribbon area as highlighted by the gray measurement lines. Additionally, the length of the PD was quantified along the AZ. For ribbon-occupied AZs: Membrane-proximal (MP) SVs (yellow) are defined as SV in a distance of $\leq$ 25 nm from the AZ membrane (blue) and $\leq$ 80 nm from the PD. Ribbon-associated (RA) SVs represent the first layer around the ribbon (red) with a maximum distance of 80 nm to the ribbon. For ribbonless AZs: Instead of RA-SVs, PD-associated SVs are determined (PDA-SVs: all SVs $\leq$ 80 nm around the PD not matching the MP-SV criteria, defined as for ribbon-occupied AZs). **(B, C)** Electron micrographs illustrating the quantification of MP-SVs (yellow crosses) and RA/PDA-SVs (green crosses) in $RBE^{WT/WT}$ and $RBE^{KO/KO}$ IHCs. Figure taken from Jean et al. (2018).

2.3.5.2. Semi-quantitative analysis of pre-embedding immunogold data

For quantifications of the immunogold labeling, only cross sectioned ribbons - attached to a clear visible cell membrane via a presynaptic density - were selected. Electron micrographs were adjusted to the size of the ribbon scheme without changing the ratio. Afterwards, different sized gold

particles were marked by big-, medium- or small-sized gray circles. Overlaying multiple ribbons from the same age group generated a visual map of the protein disposition.

2.3.5.3. Generation of serial 3D reconstructions with Reconstruct

For 3D reconstructions of consecutive serial sections from TEM, the program Reconstruct (version 1.1.0.0) was used (Fiala, 2005). First of all, consecutive sections from the same ribbon were aligned by the trace palette and the tool box. Therefore, recognizable positions in each section were marked with different symbols like the ribbon center, the membrane vertically below the ribbon center and one marker left and right from the first membrane marker. After aligning the sections, structures of interest were manually segmented with the *draw closed point by point* tool. Synaptic ribbons, presynaptic densities and AZ membranes were assigned as *boissonnat surface* with 32 facets. In contrast, SVs were assigned as *sphere* with 32 facets and were segmented by drawing a triangle along the outer SV membrane rim.

2.3.5.4. Generation of tomograms from tilt series using the program IMOD

As described previously (Imig, 2013; Chakrabarti, 2016), tomograms were generated from their respective tilt series (**.mrc*) using the IMOD software package (Kremer et al., 1996; Mastronarde, 2005). To provide functionality similar to Linux on Microsoft Windows, the installation of a Unix-like environment, named Cygwin, is required. First, the **.mrc* file extension was transformed into **.st* to facilitate the recognition as a single stack by eTomo (graphical user interface of IMOD). Afterwards, pre-processing steps were performed to identify and remove camera artefacts that can occur by random x-rays causing extreme high or low pixel values. These extreme pixel values were corrected by averaged neighboring values using the program *Ccderaser*. Next, a coarse-aligned image stack was generated by using the programs *Tiltxcorr*, *Xftoxg* and *Newstack* followed by creating a fiducial model based on the position of gold particles, which were applied to both sides of the grids as explained previously in Section 2.3.3.7. These gold fiducial markers were identified and tracked through the tilt series by utilizing the program *Beadtrack*. For the fine alignment step, the program *Tiltalign* was used to solve for the displacements, rotations, tilts and magnification differences between each tilted view in order to reduce the residual error mean. Moreover, a sample tomogram with a thickness of 1000 virtual sections was generated creating a reconstruction that is much thicker than the original sections. Further, three small sample reconstructions were created (top, middle and bottom of the tilt images) defining the x, y-axis angles and the z-position of the section due to boundary lines that were placed at the end of the biological material. After using the program *Tomopitch* for linear interpolation, a full-aligned stack was generated. The projections were binned three times during the procedure, leading to a final isotropic voxel size of 1.432 nm at 10,000-x magnification. The final tomogram was generated with the program *Tilt*, which uses a back projection algorithm. For a more detailed guide with further instructions on IMOD see the following webpage http://bio3d.colorado.edu/.

2.3.5.5. 3D reconstructions of electron tomograms, SBF-SEM and FIB-SEM data

Tomograms as well as SBF/FIB-SEM datasets were reconstructed semi-automatically using 3dmod of the IMOD software package (Kremer et al., 1996).
Synaptic ribbons, presynaptic densities, mitochondria, afferent fibers, efferent fibers, nuclei and IHCs were reconstructed as *closed* objects with the *sculpt* drawing tool. They were first manually segmented every 5-10 virtual sections to interpolate the volume across the z-stack with the *interpolator* tool afterwards. Subsequently, each virtual section was corrected manually. In contrast, AZ membranes were segmented in each consecutive section of the tomogram due to lots of irregularities. For the 3D model, the mentioned structures were represented by *meshing* and *fill* the contours (Helmprobst et al., 2015). Round SVs were segmented as spherical *scattered* objects with the *normal* drawing tool at its maximum projection marking the outer rim of the vesicles, which results in individually adjusted diameters for each vesicle. In addition to round SVs also flattened SVs occur. These vesicles were reconstructed in the same way as synaptic ribbons or presynaptic densities. For single virtual section image representation, tomographic stacks (**.rec*) were converted into TIFF image stacks (**.tif*) using the program *mrc2tif* in Cygwin. The TIFF image stacks were opened in ImageJ as a *sequence* considered as a *hyper-stack*. As a last step, the contrast was adapted throughout the virtual sections.
Number, volume and surface area information of objects were automatically given by using the *imodinfo* function of 3dmod. Distance measurements were performed with the *measurement* drawing tool along the x, y and z-axis.
Analysis of SBF- and FIB-SEM data additionally required a separation of the modiolar and pillar side. Therefore, cellular axes were determined as follows: (i) the IHC apical-basal axis was defined based on the tissue context, e.g. the position and orientation of adjacent IHCs and supporting cells; subsequently, (ii) to establish the pillar-modiolar axis, a line was drawn perpendicular to the apical-basal axis, starting from the center of the nucleus and ending at the most basal point of the IHC. Based on this line, the 3D-alignment of the respective IHC was performed. Finally, the positions of all synaptic ribbons and afferent nerve fibers were transposed into 2D projections for pillar-modiolar assignment and further analysis.

2.3.5.6. Statistics

Data are presented as mean $\pm$ standard error of the mean (SEM) and were analyzed using *Excel*, *Igor Pro 6* (Wavemetrics, version 6.3.7.2) and *Java*. Normality was assessed with the Jarque-Bera test and equality of variances in normally distributed data was assessed with the F-test. In order to compare two samples, the unpaired two-tailed Mann-Whitney-Wilcoxon test was used or when data were normally distributed and/or variances were equal, the Student's unpaired two-tailed t-test was used. To calculate statistical significance in multiple comparisons, the One-way ANOVA test followed by Tukey's test was used for normally distributed data or in case of non-normally distributed data the Kruskal-Wallis (KW) test followed by a non-parametric multiple comparisons test (NPMC) was used.

Employing the analysis tool based on Java Statistical Classes library (JSC) (Bertie, 2002) applied

in our previous studies (Jean et al., 2018; Chakrabarti et al., 2018), the KW test was performed for the identification of significant differences between SV diameters in cochlear and utricular HCs. In brief, due to the tied ranks of SV diameter measurements obtained for random sections, their SEM was used as a tolerance value, where two values were treated as equal if their difference was $\leq$ SEM. The non-significant difference between samples is indicated as *n.s.*, significant differences are indicated as $^{*}p < 0.05$, $^{**}p < 0.01$, $^{***}p < 0.001$ and $^{****}p < 0.0001$.

3. Results

The highly specialized active zones (AZs) of cochlear inner hair cells (IHCs) are characterized by the presence of presynaptic electron-dense projections named synaptic ribbons, which tether numerous synaptic vesicles (SVs). As mentioned in the introduction, murine IHC ribbon synapses undergo major functional and structural refinements upon maturation. These days, the time course of AZ assembly, ribbon formation as well as maturation and the involved molecular mechanisms are still poorly understood. In this part of my thesis, different 2D and 3D microscopic techniques were employed in order to address these issues by analyzing IHC AZ development on the ultrastructural level. First, I quantified a range of morphological parameters of synaptic ribbons, their corresponding postsynaptic densities (PSDs), and SVs from embryonal stages till early adulthood of cochlear IHCs. In the second part, I analyze the establishment of IHC heterogeneity by focusing on synaptic ribbon morphology. Finally, I present investigations of the potential molecular key players involved in ribbon formation. This section is based on the paper entitled: "Mapping developmental maturation of mouse inner hair cell ribbon synapses" (Michanski et al., 2019).

My second aim of the thesis was to investigate the ultrastructural consequences of deleting the main component of the IHC ribbon, which will be described in Section 3.2. Finally, Section 3.3 describes my findings on the maturation of vestibular hair cell ribbon synapses of the utricle and to what extent the processes are comparable to cochlear IHCs.

3.1. Maturation of cochlear IHC ribbon synapses from pre-hearing to hearing mice

As mentioned above, the context of this section was previously published in Michanski et al. (2019).

Mapping developmental maturation of inner hair cell ribbon synapses in the apical mouse cochlea

Susann Michanski, Katharina Smaluch[#], Anna Maria Steyer[#], Rituparna Chakrabarti, Cristian Setz, David Oestreicher, Christian Fischer, Wiebke Möbius, Tobias Moser, Christian Vogl, and Carolin Wichmann

[#] These authors contributed equally to the work
Proceedings of the National Academy of Sciences (PNAS), 2019 Mar 26;116(13):6415-6424.
doi: 10.1073/pnas.1812029116

Detailed author contribution of Susann Michanski:
The following figures in this thesis are taken from or represent modified versions from Michanski et al. (2019).
- Experimental electron microscopic work and analysis: conventional embeddings (Figure 3.1, 3.2, 3.4, 3.6, 3.7, 3.9, 3.10), pre-embedding immunogold labelings (Figure 3.15, 3.16), electron microscopy of random sections, electron microscopy tomography (Figure 3.8, 3.9), enhanced en bloc stainings followed by serial bloc face-scanning electron microscopy together with C.F. (Figure 3.11), and focused ion beam-scanning electron microscopy together with A.M.S (Figure 3.11, 3.12, 3.13)
- Preparation of the manuscript with contributions of all other authors

3.1.1. Ultrastructural refinement of IHC AZs

In order to examine in detail how an AZ is formed and how it changes upon maturation, the following age groups from C57BL/6J mice were studied to cover the whole range of AZ development: embryonic day (E)14, E16, E18, postnatal day (P)0-1, P2-4, P9, P12, P15, P19-20, and P48.
In the first step, random ultrathin sections of E14, E16 and E18 IHCs were studied and imaged using transmission electron microscopy (TEM) to determine the exact time of AZ generation. Flanked by microtubule-filled inner pillar supporting cells and outer hair cells (OHCs), mature IHCs are normally easy to distinguish by a round nucleus and abundant mitochondria. In comparison, OHCs are exposed directly to the extracellular space due to less surrounding supporting cells. Furthermore, the cylindric shaped OHCs exhibit larger nuclei than IHCs. In prenatal organs of Corti, the identification of IHCs turned out to be more difficult, because of the immature appearance of all surrounding cell types and the extremely sparse occurrence of IHCs at these ages. Intensive screening of the tissue by finding novel landmarks made the detection of IHCs possible. In Figure 3.1A-B", few and very occasionally differentiated IHCs are already present in E14 IHCs, whereas the first afferent fibers approaching IHCs were observed at E16 corroborating previous reports (Koundakjian et al., 2007, reviewed in Bulankina and Moser, 2012). These fibers were identified due to their bouton-like appearance in contact to IHCs and the less dense cytoplasm.

Interestingly, TEM data displayed neither synaptic ribbons with SVs nor electron-dense AZ and PSDs specializations of any kind prior to E18 (Figure 3.1A-B"). Clear presynaptic ribbons could be detected from E18 onwards (Figure 3.1C-C") - an observation consistent with the immunofluorescence data from Huang et al. (2012). In addition to earlier findings, my ultrastructural data of E18 IHCs reveal the presence of small ribbons floating in the cytoplasm as well as membrane-attached ribbons proximal to developing PSDs (Figure 3.1C-C").

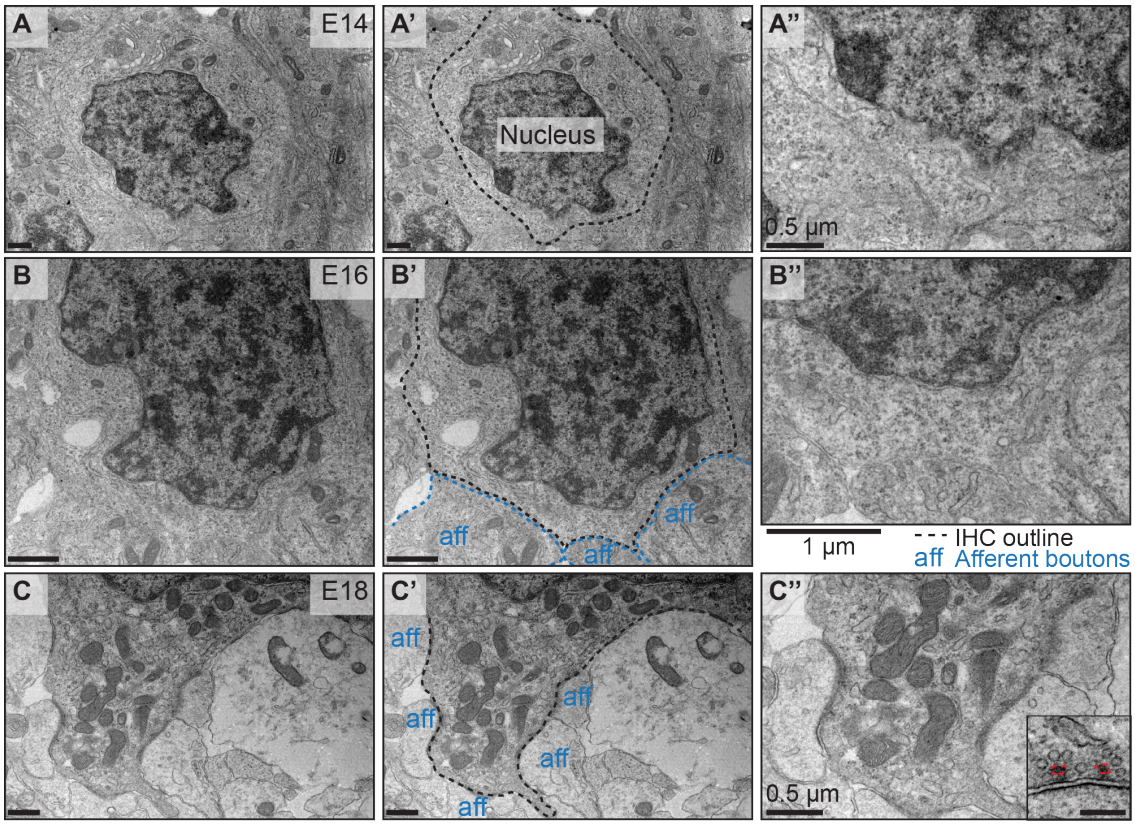

Figure 3.1.: Random section analysis showed first afferent fibers approaching IHCs at E16 (A-A") Representative electron micrograph of an E14 IHC (black dotted line). At this developmental stage, no contacts with afferent fibers can be found. **(B-B")** Afferent fibers (aff) start contacting IHCs at ∼E16 (blue dotted lines); ribbons, SVs or PSDs are not visible. **(C-C")** In E18 IHCs, afferent fibers have established synaptic contacts with morphologically distinguishable PSDs, presynaptic ribbons and SVs. Inset depicts two attached ribbons (red dashed lines) with tethered SVs (scale bar: 200 nm).

3.1.2. Upon maturation, ribbon size and SV number increases, while SV diameter and ribbon number per synapse are progressively reduced

For a comparative analysis on morphological features of the IHC presynaptic AZ upon maturation, I initially focused on parameters like ribbon size and number per synapse (Figure 3.2) as well as the SV number and diameter (Figure 3.4). Therefore, 2D TEM images of all age groups showing synaptic ribbons (E18-P48) were quantified. Per synaptic contact frequently several small spherical synaptic ribbons were observed in embryonic and early postnatal IHCs with multiple attachments (presynaptic densities) to the presynaptic plasma membrane (Figure 3.2A-C). With maturation the majority of IHC synapses comprise a single and in shape elongated ribbon with one continuous presynaptic density (Figure 3.2D-E). Furthermore, I analyzed developmental changes regarding the ribbon size. To do so, the maximal ribbon height, width and area excluding the presynaptic density were measured in random sections of cross-sectioned synaptic ribbons (Figure 3.2F-I). The overall observed increase in ribbon size implies a progressive enlargement of synaptic ribbons until they reach their mature size around the onset of hearing at ∼P12 (Figure

3.2F-H, Section A Table A1).

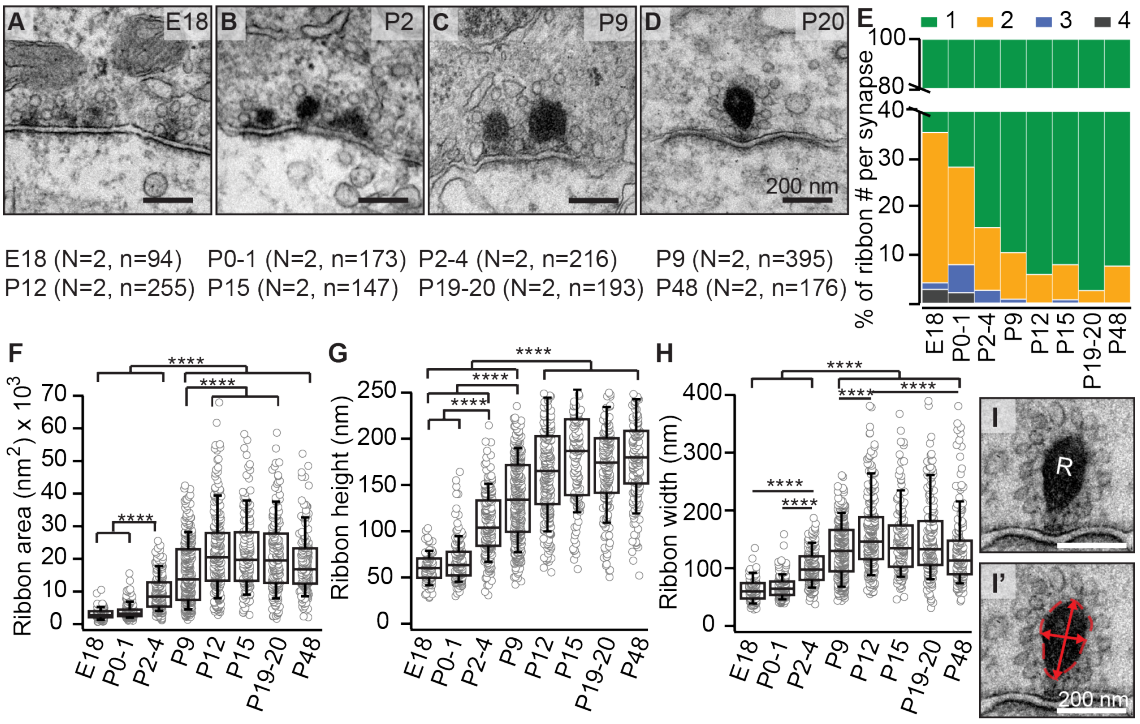

Figure 3.2.: Synaptic ribbon size steadily increases until hearing onset
(A-D) Representative electron micrographs of the indicated age groups, showing IHC presynaptic contacts either decorated with multiple or single synaptic ribbons. **(E)** In contrast to the mainly single synaptic ribbons in hearing animals, pre-hearing animals frequently display multi-ribbon synapses. **(F-H)** Random section analysis of ribbon size across all indicated age groups exhibits larger ribbons in mature animals. Ribbon size stabilizes around hearing onset and remains constant thereafter. **(I)** Electron micrograph highlighting the analysis criteria to determine the ribbon size in random sections. Ribbon size was measured in height, width and area, as indicated by the red arrows and dashed line. N = animal number, n = ribbon number. Data are presented as box plots showing 10, 25, 50, 75 and 90th percentiles with individual data points overlaid (****$p < 0.0001$). For more detailed statistical values see Section A Table A1.

3.1.2.1. Immature ribbon synapses are round in shape, while ribbons in hearing animals are more elongated

3D reconstructions of ribbon series (at least three sections of the same ribbon) enabled to get more detailed information of synaptic ribbon as well as SV number, size and shape. While one individual section might show a single synaptic ribbon, consecutive sections of the same region can reveal multiple ribbons as shown in Figure 3.3 (P12). The 3D data depicted rather round ribbons in pre-hearing animals (Figure 3.3; P9 and P12) and more elongated ribbons with predominantly droplet or wedge-like shapes in hearing animals (Figure 3.3; P19 and P48). As already described above, mature ribbon synapses were anchored to the AZ membrane via a single presynaptic density (Figure 3.3; P19 and P48). On the contrary, two rootlets could be detected for immature ribbon synapses (Figure 3.3; P12). These data corroborate my 2D random section analysis and

additionally revealed a diverse ribbon structure not only between different ages but also within the same age (Figure 3.3; P48a, b).

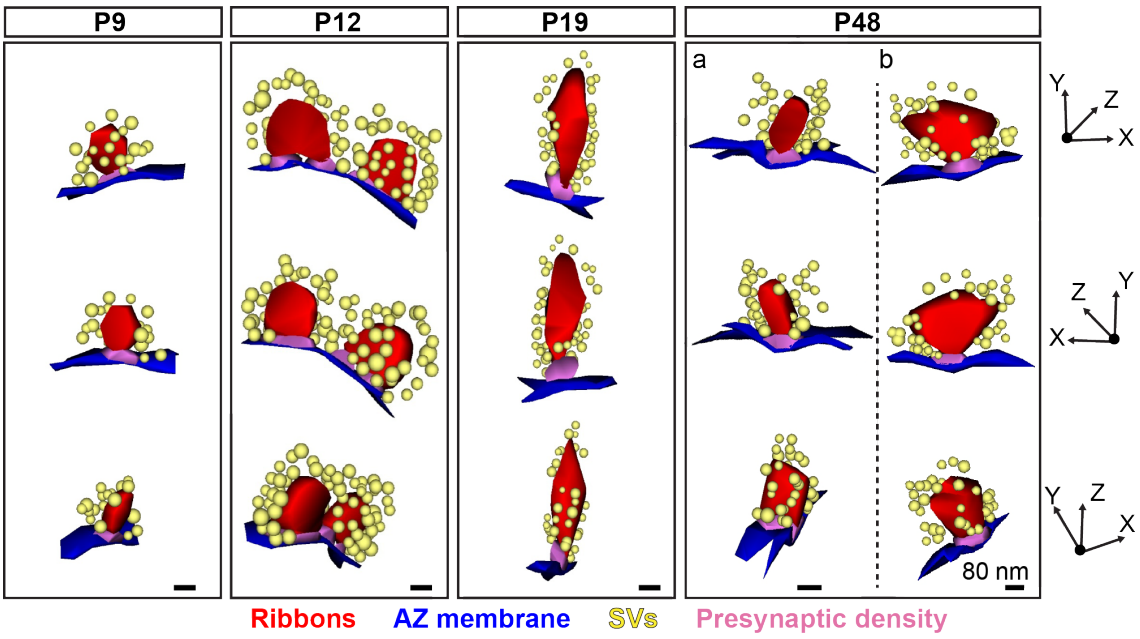

Figure 3.3.: Serial 3D reconstructions of ribbon synapses reveal a structural ribbon diversity IHC ribbon synapses develop from small and round ribbons (P9, P12) to larger and droplet or wedge-like shaped ribbons (P19, P48). However, they do not show exclusively one special form but rather occur in different structures in IHCs of the same age. For P48 two distinct synaptic ribbons are displayed.

3.1.2.2. Developmental changes of the SV number and diameter

Synaptic ribbons tether a large number of SVs close to release sites (Figure 3.4A). To check for possible changes in correlation to maturation from pre-hearing to hearing, I first counted the number of SVs in all aforementioned age groups (first layer of SVs around the ribbon within a maximum distance of 80 nm, Figure 3.4A, and Figure 2.5 for analysis criteria) and measured their diameter. Analysis of random ultrathin sections revealed a continuous increase of the SV number per ribbon during maturation (Figure 3.4B, Section A Table A2; from E18: 4.48 $\pm$ 0.16 to P48: 13.98 $\pm$ 0.36; $p < 0.0001$ NPMC test), which was positively correlated with the observed ribbon growth (Figure 3.4E). Interestingly, the opposite was found for the SV diameter, where a constant decrease until hearing onset was detected (Figure 3.4C, D, Section A Table A2; from E18: 47.00 $\pm$ 0.28 nm to P48: 34.86 $\pm$ 0.13 nm; $p = 0.0052$ KW test).

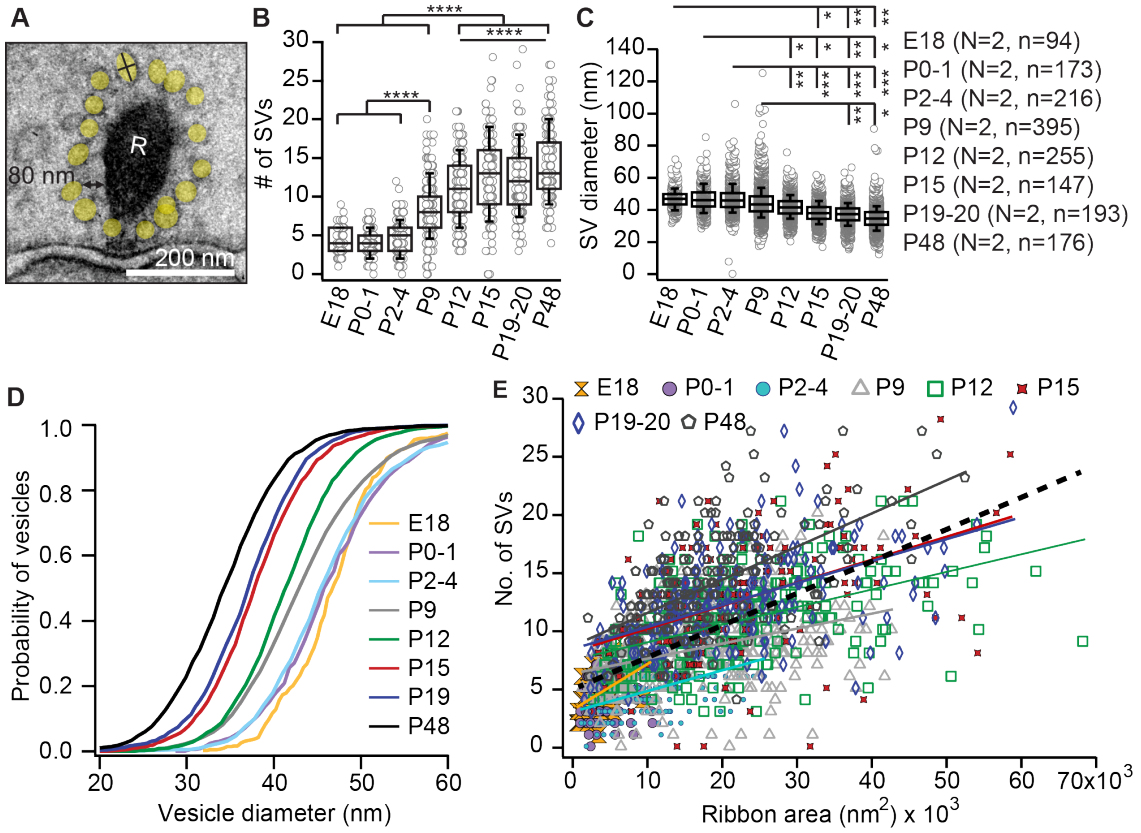

Figure 3.4.: SV maturation is accompanied by a decrease in vesicular volume
(A) Electron micrograph depicting the performed analysis routine: all SVs (yellow) were counted in the first layer ($\leq$ 80 nm) around the ribbon. The outer SV diameter was calculated by averaging the values measured for the horizontal and vertical axis. **(B)** The number of SVs significantly increases (from E18: 4.48 $\pm$ 0.16 towards P48: 13.98 $\pm$ 0.36; $p < 0.0001$ NPMC test), while the mean SV diameter decreases (from E18: 47.00 $\pm$ 0.28 nm towards P48: 34.86 $\pm$ 0.13 nm; $p = 0.0052$ KW test) upon maturation **(C)**. Data are represented as box plots showing 10, 25, 50, 75 and 90th percentiles with individual data points overlaid. For detailed statistical values see Section A Table A1 and Table A2. $^{*}p < 0.05$, $^{**}p < 0.01$, $^{***}p < 0.001$, $^{****}p < 0.0001$. **(D)** Cumulative probability distributions of SV diameters illustrating the gradual reduction in SV size between immature and mature age groups. **(E)** Number of SVs and ribbon area is positively correlated (correlation coefficient r = 0.917). N = animal number, n = ribbon number.

In summary, the electron microscopic data demonstrate a morphological refinement of IHC AZs from pre-hearing to hearing: immature synapses are mainly occupied by multiple small ribbons surrounded by large-sized SVs, while mature synapses are characterized by large, mainly single ribbons tethering a larger population of smaller-sized SVs (Figure 3.5).

3.1.3. Postsynaptic maturation is characterized by the fusion of several small PSDs into one single, continuous PSD

The electron-dense PSD, juxtaposed to the presynaptic AZ, is a multi-protein structure that is essential for localizing glutamate receptors near to the sites of neurotransmitter release. Previous work on IHC ribbon synapses described an increase in PSD length upon development from P6 to

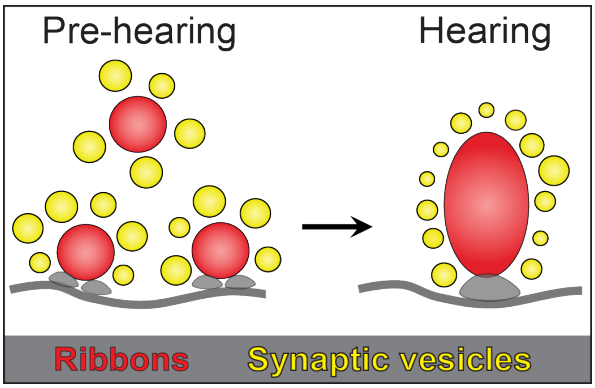

Figure 3.5.: Schematic drawing summarizing the main morphological features affected by developmental maturation
In pre-hearing mice, multiple small ribbons with large SVs dominate the presynaptic morphology, while large, mainly single ribbons with increased counts of smaller SVs are characteristic for AZs of hearing mice.

P20 IHCs (Wong et al., 2014). In order to gain a more time-resolved insight into PSD maturation, I quantitatively analyzed the number of distinguishable PSDs per synaptic contact and the individual PSD length in random ultrathin sections of all aforementioned age groups (Figure 3.6A, B). Upon maturation, I found a reduction in PSD number but an increase in length (Figure 3.6C, D, Table 3) supporting the finding from Wong et al. (2014), which states that several small PSD appositions merge into a single larger PSD (Figure 3.6D, E).

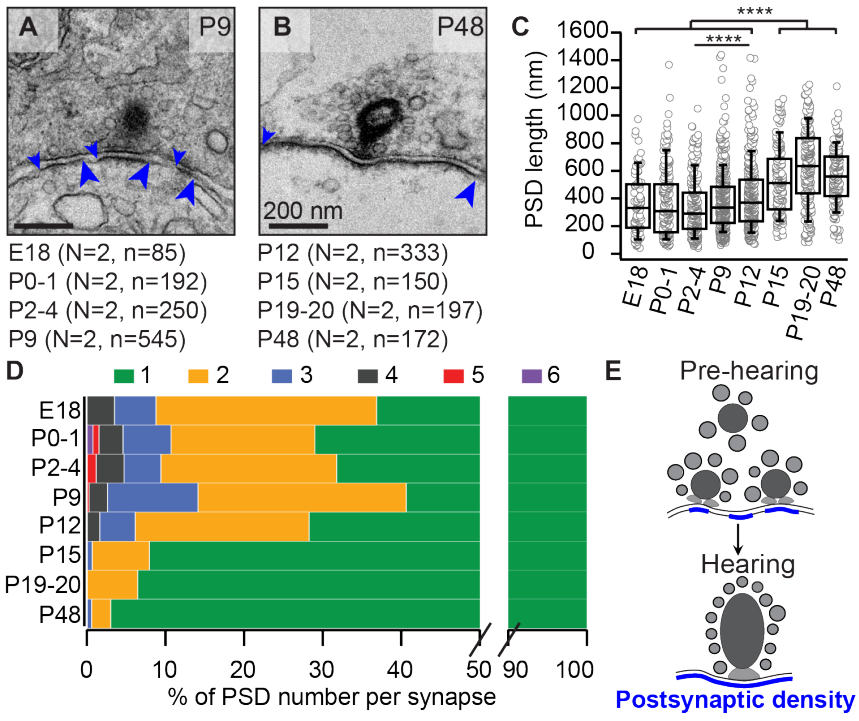

Figure 3.6.: Postsynaptic developmental refinement leads to an increase in size and

Figure 3.6 *(previous page)*: formation of a continuous, single PSD in SGN boutons.
(A, B) Example electron micrograph illustrating the analysis of the PSD length and number (starting points: small blue arrowheads from above; end points: large blue arrowheads from below) of an immature **(A)** and a mature **(B)** IHC synapse. **(C)** An increase in PSD length is shown reaching a plateau around the third postnatal week (smallest PSDs at P2-4: 330.0 $\pm$ 12.5 nm; largest PSD at P19-20: 626.3 $\pm$ 19.0 nm; $p < 0.0001$ NPMC test). Box plots depict 10, 25, 50, 75 and 90th percentiles with individual data points overlaid ($^{****}p < 0.0001$). For more detailed statistical values see Section A Table A3. **(D)** The number of PSD appositions per random section of a synaptic contact decreases during development from up to six separated PSD patches to predominantly a single PSD. N = animal number, n = PSD number. **(E)** Schematic representation of developmental changes from pre-hearing to hearing in murine cochlear IHCs.

3.1.4. Putative fusion of ribbon precursors is a critical step in presynaptic AZ maturation

As mentioned above, particularly IHCs of pre-hearing animals possess floating ribbons in close proximity to ribbon-occupied AZs. In order to evaluate the occurrence of these structures in random ultrathin sections, I followed two analysis criteria: (i) ribbons that exhibited a clearly visible membrane attachment via a presynaptic density were considered as attached ribbons (Figure 3.7H); or (ii) ribbons lacking any contact to the membrane visible in 2D were considered as floating ribbons (Figure 3.7A-C). Moreover, I measured the nearest distance between the outer edge of floating ribbons and the presynaptic plasma membrane in 2D. Changes in the floating ribbon distance might unravel important details about the localization of ribbons within the IHC. Quantifications demonstrated that floating ribbons can still be detected in mature animals, however, with a drastically reduced frequency (Figure 3.7I). The distance of floating ribbons to the cell membrane is longer in IHCs of immature mice and decreased afterwards from a mean of 900.97 $\pm$ 144.91 nm at E18 to 262.19 $\pm$ 114.93 nm at P48 (Figure 3.7J, $p = 0.017$ Tukey's Test). All observed floating ribbons were decorated with a full set of SVs. Due to the developmental decline of floating ribbons and reduced distances to the membrane in mature IHCs, I assume that they represent ribbon precursors, which undergo a maturation process due to and also after attachment to the membrane. In addition to the floating ribbon precursors, I found ribbons (attached as well as floating ones) that exhibit an electron-dense connection to neighboring ribbons (Figure 3.7D-G). Recently, a similar mechanism of highly mobile ribbon material that can exchange the ribbon component RIBEYE within a single ribbon but also between different ribbons has been described in zebrafish lateral line neuromast hair cells (Graydon et al., 2017).

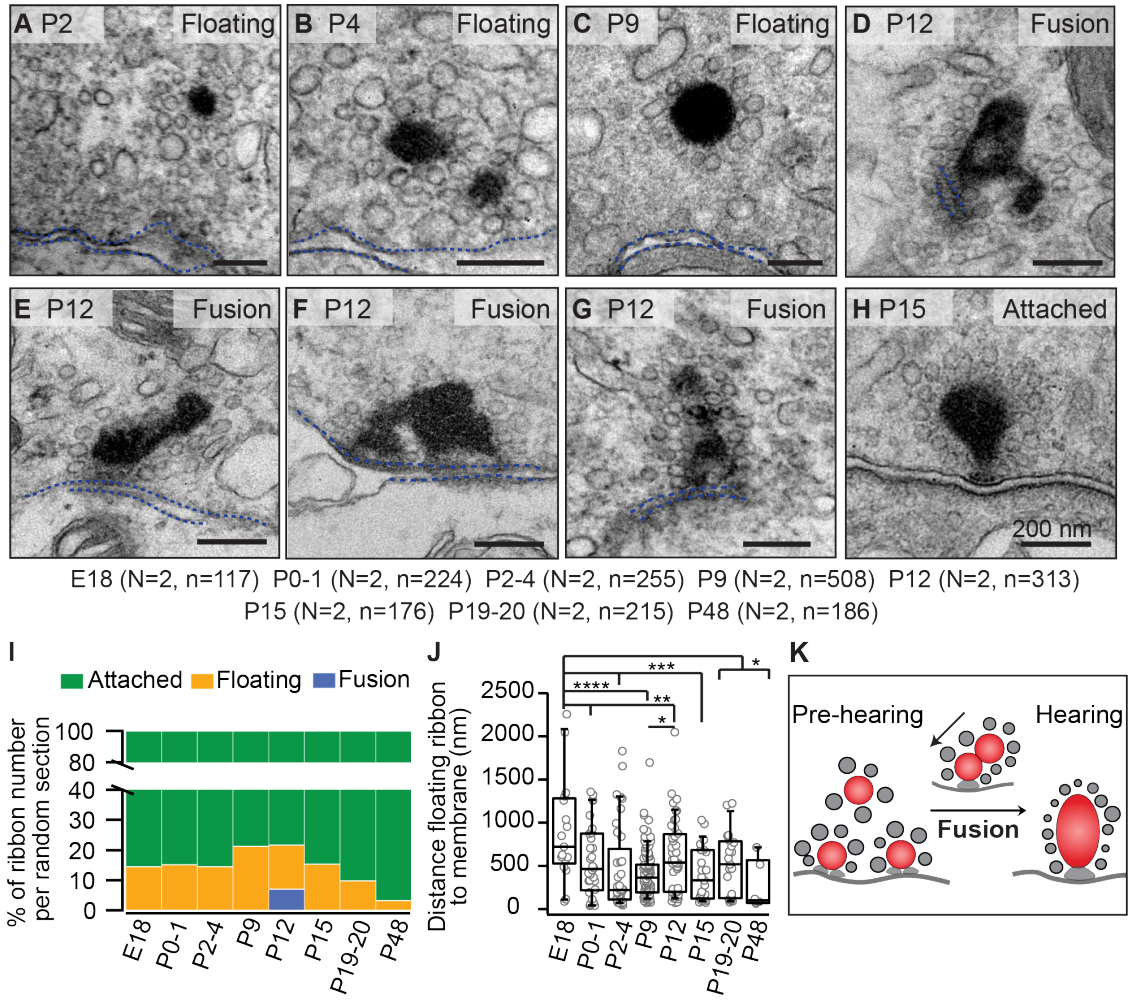

Figure 3.7.: Ribbon precursor fusion is critical for AZ maturation
(A-C) Representative electron micrographs showing cytoplasmically floating ribbon precursors in close vicinity to the IHC membrane (dashed blue lines). **(D-G)** Putative ribbon fusion events. **(H)** Depicted is a fully mature and membrane-attached ribbon synapse. **(I)** The proportion of membrane-attached ribbons increases upon maturation (from 85.47 % in E18 to 96.77 % in P48) and the number of floating ribbons decreases after P12 (from 14.53 % in E18 to 3.23 % in P48). N = animal number, n = ribbon number. **(J)** Floating ribbon distance to the IHC membrane reduces in the course of development ($^{*}p < 0.05$, $^{**}p < 0.01$, $^{***}p < 0.001$, $^{****}p < 0.0001$). **(K)** Schematic proposing ribbon synapse maturation through ribbon precursor fusion.

Two hypotheses could explain the interaction between different ribbons. Either ribbons form protrusions to get pruned (Spiwoks-Becker et al., 2004) or they represent ribbon-ribbon fusion events (Spiwoks-Becker et al., 2004; Regus-Leidig et al., 2009; Wong et al., 2014). My findings of floating ribbon precursors near attached ribbon synapses and the steadily increase in synaptic ribbon size, favor the latter scenario. In my preparations, different kinds of potential fusion events could be detected: (i) fusion of floating ribbon precursors (Figure 3.7G); (ii) fusion of small floating ribbon precursors with membrane-attached ribbons (Figure 3.7D, E); and (iii) fusion of two membrane-attached ribbons at the same synaptic contact (Figure 3.7F). These events have been predominantly observed around the onset of hearing (P12) (Figure 3.7I) pointing towards a crucial step towards ribbon maturation around hearing onset.

Investigations of random single sections allowed the morphological characterization of IHC ribbon synapses over a wide developmental range. However, it should be noted that the analysis of 2D data could have created false positives for floating ribbons depending on the individual orientation to the projection plane. A ribbon with no visible presynaptic density and some distance to the AZ membrane would have been categorized as a floating ribbon even though the ribbon might show a shorter distance to the membrane in another cutting plane with a clear presynaptic density. In order to ensure for the occurrence of floating ribbon precursors as well as putative fusion events, I utilized high-resolution 3D electron tomography in a small subset of samples (Figure 3.8). In conclusion, tomograms and their 3D models corroborated the presence of floating ribbon precursors in IHCs of pre-hearing mice (Figure 3.8A-B'). However, all ribbon synapses in mature IHCs showed a membrane attachment via a presynaptic density (Figure 3.8C, C'). Furthermore, potential ribbon fusion events were also detected in tomograms supporting the TEM observations. Here, predominantly one large AZ-anchored ribbon was connected to a smaller ribbon (Figure 3.8D-F"). In some cases, I also found an additional small attached ribbon (Figure 3.8D, D", E, E") or floating precursor ribbon (Figure 3.8F', F") next to the fusing ribbons.

3.1.5. Intracellular transport mechanisms

In several 2D electron micrographs, I observed floating ribbon precursors in close vicinity to microtubules (Figure 3.9A, B). Transport of cargos is commonly mediated by molecular motor proteins like myosin, kinesin or dynein (Alberts et al., 2002; Mallik and Gross, 2004). Cytoskeletal elements like actin and microtubules provide targeted trafficking due to interactions with the motor proteins. Suggestively, the detected microtubules may actively transport ribbon precursors towards AZs via a cytoskeletal pathway. Additional analysis with confocal microscopy and EM tomography could identify microtubules throughout the IHCs (Figure 3.9C-E'). Whether ribbon precursors are attached to microtubules needs still to be tested. However, in 2D random sections, I could observe microtubules close to AZs that appeared decorated with another cargo: I identified dense-core vesicles, which will be discussed in the next section.

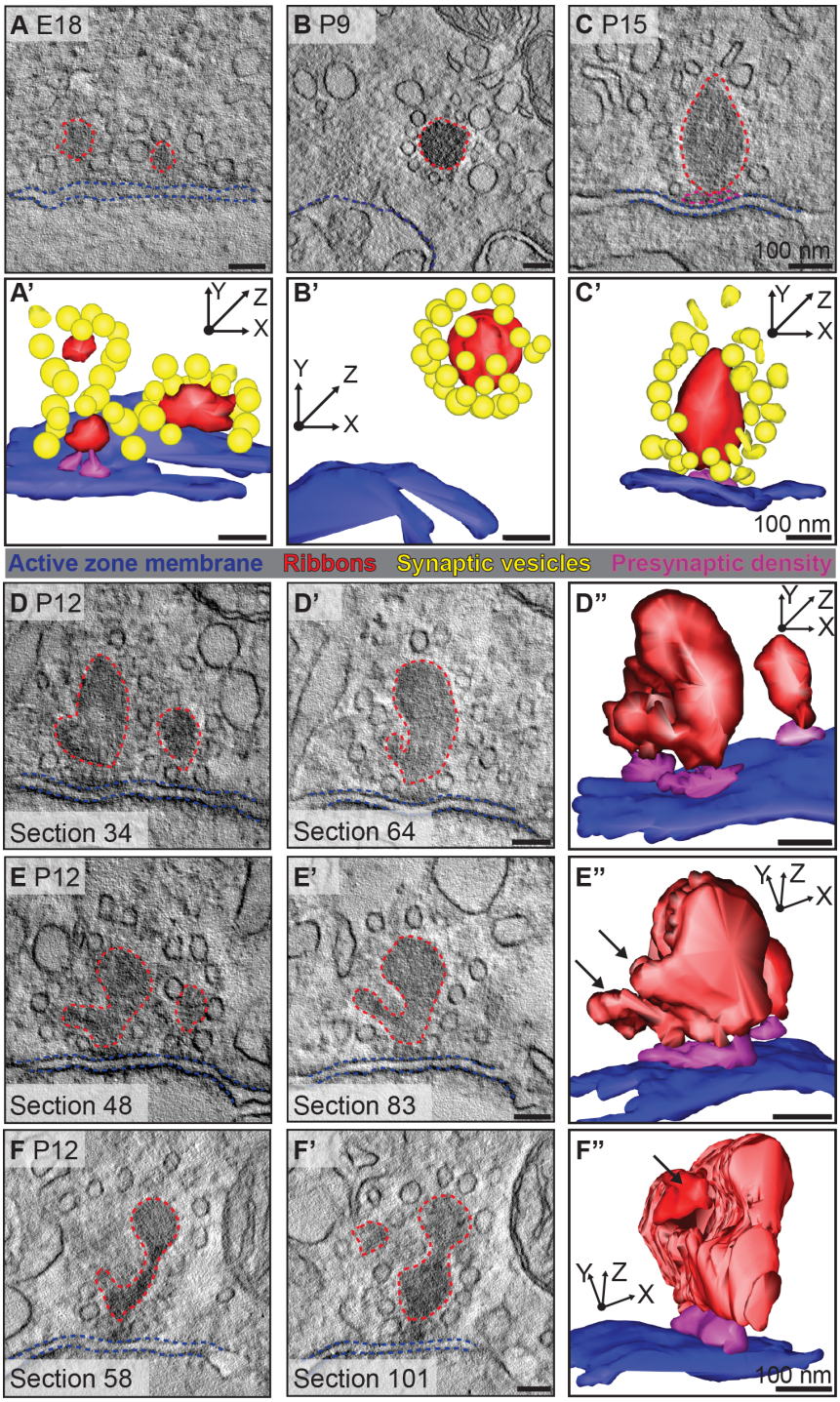

Figure 3.8.: Ribbon-fusion processes at synaptically-anchored ribbons around the onset of hearing

(A, B, C) Single tomogram virtual sections of ribbons before (E18, P9) and after (P15) the onset of hearing. Ribbons: red dashed line; AZ membrane: blue dashed line; presynaptic density: magenta dashed line. **(A', B', C')** Tomogram 3D models depicting several floating ribbons in immature IHCs **(A', B')** as well as synaptic ribbons that are attached to the AZ membrane by a presynaptic density **(A', C')**. **(D, D', E, E', F, F')** Single tomogram virtual sections and the corresponding 3D models **(D", E", F")**. For better visualization of the contacts between the ribbons, SVs are removed from the 3D models. Note, that both of the fusing ribbons in **(D")** are attached by individual single presynaptic densities. In **(E")** 'bulges' are found (arrows) and in **(F', F")** a floating ribbon is visible in close proximity to the cavity of the attached ribbon.

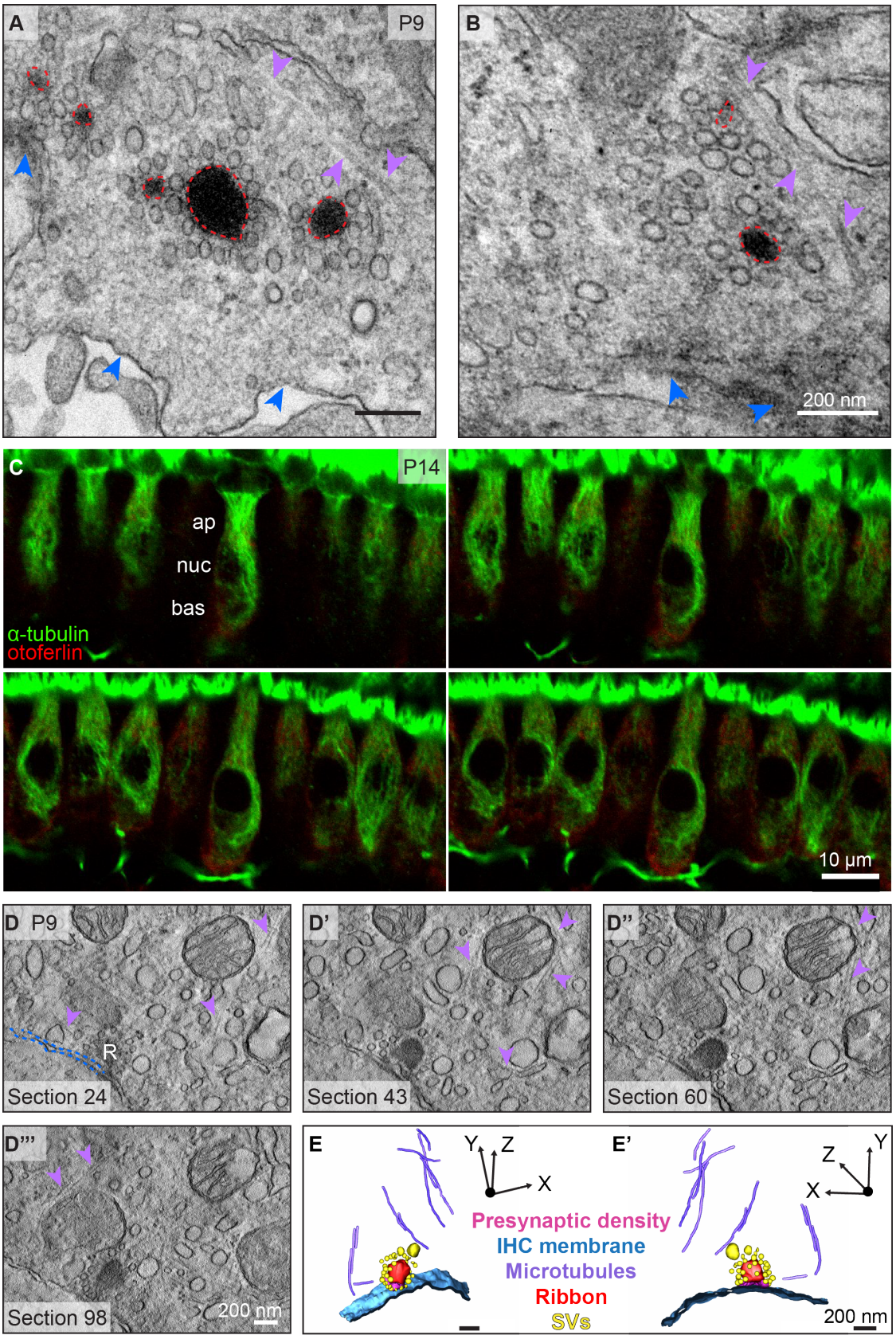

Figure 3.9.: Potential transport of ribbon precursors along microtubules
(A-B) Exemplary electron micrographs of multiple ribbon precursors (dashed red line), free floating in the cytoplasm, which are frequently observed relatively close to microtubules (purple arrowheads) and the IHC membrane (blue arrowheads) in pre-hearing mice.

Figure 3.9 ***(previous page)*****: (C)** Confocal single optical sections of IHCs immunostained for α-tubulin (green), a dimer that forms together with β-tubulin microtubules and the IHC marker otoferlin (red). Tubulin fluorescence is detected as filamentous structures throughout the IHCs (ap: apical, nuc: nucleus, bas: basal). **(D-D''')** Tomogram single virtual sections visualizing several microtubules in a P9 IHC (purple arrowheads) proximal to an attached ribbon synapse (R) and the IHC membrane (blue dashed line). **(E, E')** 3D model of the tomogram shown in **(D-D''')** from two different side views.

3.1.6. Dense-core vesicles appear in close proximity to IHC presynaptic AZs during embryonal and neonatal development (E18-P4)

Intriguingly, apart from ribbon precursors, I further detected accumulations of dense-core vesicles (DCVs) juxtapose to AZs in random single sections of E18-P4 animals (Figure 3.10A-C). Moreover, tubular structures that were reminiscent in shape and diameter to microtubules were found in close proximity to DCVs (Figure 3.10C). Quantification of the DCV diameter resulted in a high variance for all analyzed age groups (Figure 3.10D) ranging from $\sim$50 nm to $\sim$180 nm. The very low overall density and apparently temporally tightly confined developmental occurrence of these structures, limited further analysis. So far, DCVs in conventional synapses are described to be involved in the assembly of AZs by two different mechanisms: (i) DCVs containing neurotrophins that may be required for axonal pathfinding and synapse formation (Michael et al., 1997; Fariñas et al., 2001; Luo et al., 2001; Wu et al., 2004; Kersigo and Fritzsch, 2015); and (ii) DCVs that target several AZ proteins to the presynaptic membrane (e.g. piccolo and bassoon) (Huttner et al., 1995; Zhai et al., 2001; Shapira et al., 2003). In order to clarify the true nature of these DCVs in immature cochlear IHCs, I planned to do pre-embedding immunogold labelings against proteins that might be part of the DCV. I performed several labelings against the C-terminal truncated isoform of piccolo, piccolino (Aczp18p19 antibody that recognizes the short and the long piccolo isoform), but no electron-dense gold particle labeling could be detected on DCVs. Additional pre-embedding immunogold labelings against bassoon remained unspecific in IHCs of pre-hearing animals. Next, I attempt immunogold stainings against the brain-derived neurotrophic factor (Bdnf). Unfortunately, I was not able to perform this experiment in the time frame of my PhD thesis.

To summarize these findings, remarkable morphological changes of cochlear IHC ribbon-type synapses in the course of development were found: (i) the SV number as well as ribbon size increased; (ii) the SV diameter and ribbon counts per synaptic contact decreased; and finally (iii) the number of cytoplasmically floating ribbon precursors declined and their distance to the AZ reduced during maturation. Furthermore, I detected putative assembly packages of the AZ in form of DCVs and a possible intracellular trafficking pathway of AZ and ribbon material. Finally, I found the occurrences of synaptic ribbons that appear to undergo a fusion process around P12, which is consistent with the final ribbon area reached with the age of P12.

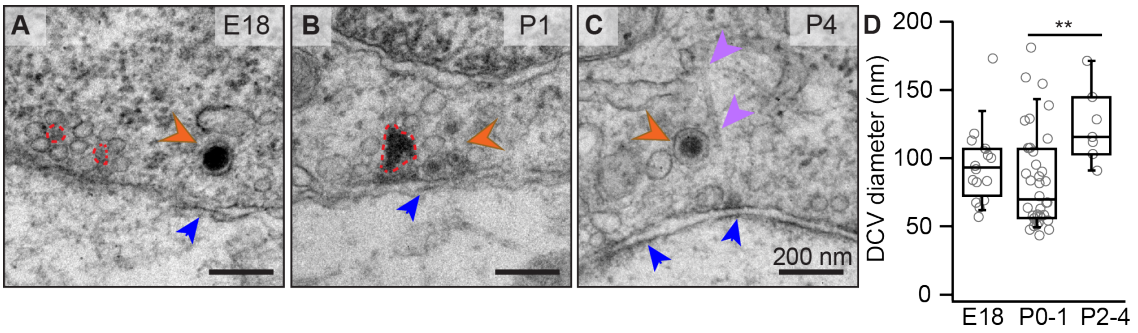

Figure 3.10.: Dense-core vesicles in immature cochlear IHCs
(A-C) In the age groups between E18 and P4, several DCVs (orange arrowheads) are present in close proximity to the AZ membrane (blue arrowheads), ribbons (red dotted lines) and microtubules (purple arrowheads). **(D)** Box plots represent a highly variable DCV diameter (mean = 91.36 nm) showing 10, 25, 50, 75 and 90th percentiles with individual data points overlaid ($^{**}p < 0.01$). For more detailed statistical values see Section A Table A3.

3.1.7. Establishing IHC ribbon synapse heterogeneity

Analysis of random and serial ultrathin sections as well as EM tomograms revealed a high diversity of ribbon shapes and sizes - even in functionally mature IHCs. Much work on the potential IHC heterogeneity has been carried out in cats and mice (Merchan-Perez and Liberman, 1996; Frank et al., 2009; Liberman et al., 2011; Kantardzhieva et al., 2013; Ohn et al., 2016) showing that the ribbon size as well as number and activation kinetics of voltage-gated Ca^{2+}-channels depend on the topographic localization within one individual IHC. Mainly large or multiple ribbons were detected at the modiolar (neural) side of IHCs. These are supposed to drive low spontaneous rate, high threshold SGNs. On the contrary, high spontaneous rate, low threshold neurons are driven by smaller ribbon synapses preferentially situated at the pillar (abneural) side.
In this section, I address the question whether in accordance to the previous studies, the number of ribbons as well as their size distributes in a certain pattern within an individual IHC and if so, whether this is already established before the onset of hearing. I utilized serial block face - scanning electron microscopy (SBF-SEM) and focused ion beam - scanning electron microscopy (FIB-SEM) to assess the morphological heterogeneity of ribbons from intact mouse IHCs of different ages. Initially, I performed SBF-SEM to standardize the protocol for cochlear IHCs and to carry out first quantitative analyses. Afterwards, I mainly employed FIB-SEM, because of the higher z-resolution allowing a more detailed quantification of ribbon size and SV numbers. SBF-SEM is based on an ultramicrotome inside the vacuum chamber of the SEM and images of the block face are acquired after the knife cuts a section. In contrary, the FIB-SEM uses a beam of ions and its sputtering capability facilitates the removal of material via nano-machining. Regardless of the precise method, both 3D EM techniques allowed the analysis of ribbon size and number depending on the localization within the IHC and their tethered SVs. I semi-automatically reconstructed the complete basolateral compartment of IHCs including ribbon synapses that were each sampled from three different age groups (P9: pre-hearing, 2 IHCs; P14 and P15: hearing, 2 IHCs; P34: mature, 2 IHCs) (Figure 3.11).

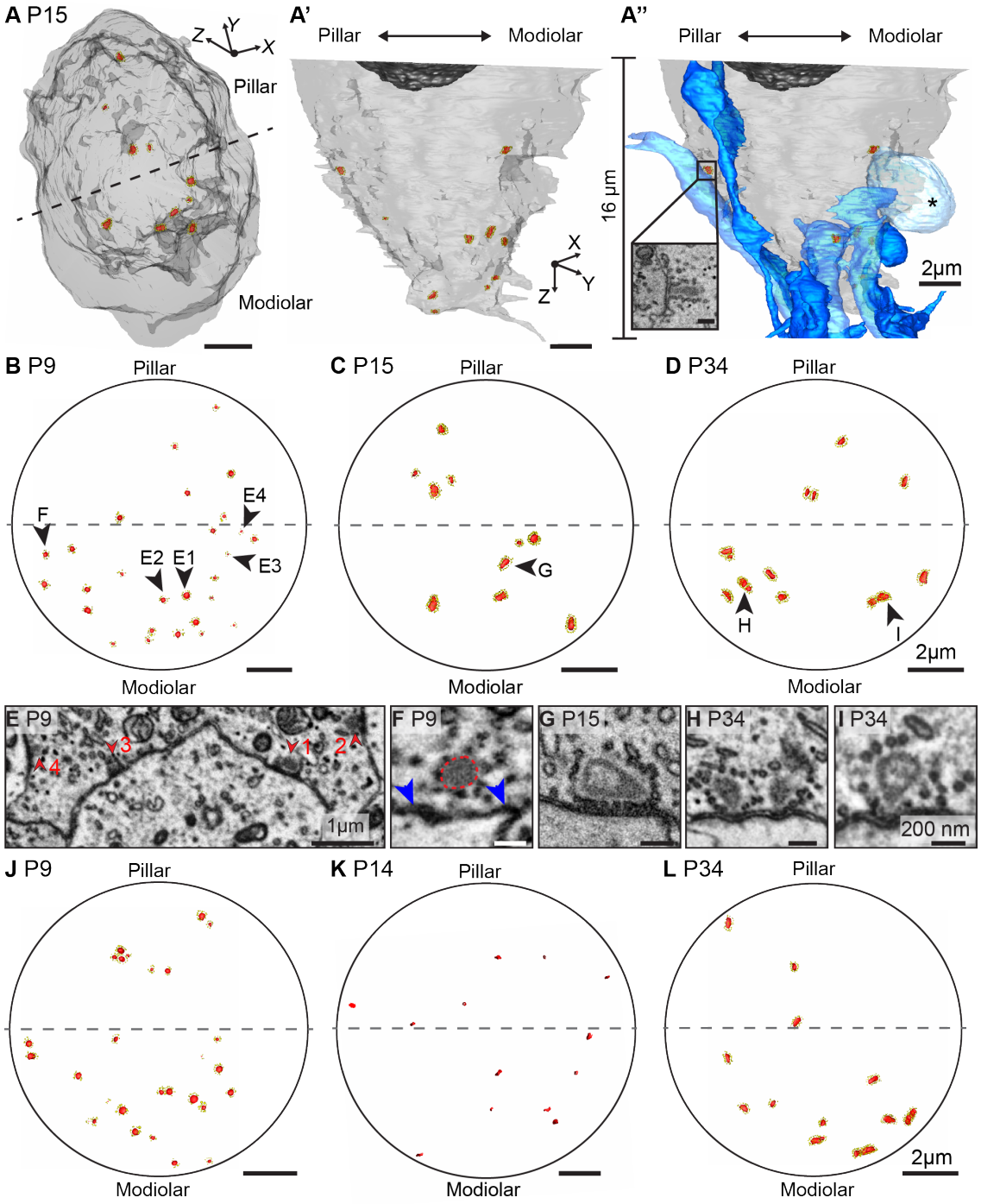

Figure 3.11.: 3D reconstructions of the basolateral IHC compartment
(A-A") 3D models of the basal part of a P15 IHC using FIB-SEM displayed either in top view **(A)**, with **(A")** or without **(A')** the afferent innervation for clarity. Small inset shows a representative section of a reconstructed ribbon. Scale bar: 100 nm. Gray: IHC membrane, black: nucleus, red: ribbons, yellow: SVs, blue: afferent fibers, asterisk: swollen afferent bouton. **(B-D)** FIB-SEM 3D models of reconstructed ribbons (red) and SVs (yellow) throughout the basal part of IHCs at different ages. Gray dashed lines hemisect the IHCs into pillar (abneural) and modiolar (neural) side (please refer to Section 2.3.5.5 for further details) and black arrowheads highlight ribbons that are shown in **(E-I)** by representative sections.

Figure 3.11 ***(previous page)*****: (E)** Red arrowheads point towards membrane-attached synaptic ribbons, blue arrowheads in **(F)** highlight the IHC plasma membrane with a floating ribbon precursor (red dashed line). In P9, all ribbons appear spherical, whereas in P15 and P34 also droplet- and wedge-like ribbon shapes are existing. Additionally, mature IHCs frequently exhibit ribbons with a bright core **(G, I)**. **(H)** Multi-ribbon synapses are still present in adult IHCs. **(J-L)** 3D model of reconstructed ribbons and SVs from the basolateral compartment of a second cochlear IHC from each age group, respectively. The P14 dataset was obtained by SBF-SEM, while P9 and P34 are FIB-SEM datasets.

Consistent with earlier findings (Stamataki et al., 2006; Huang et al., 2007; Sendin et al., 2007; Huang et al., 2012; Wong et al., 2014), an age dependent decrease in the number of synaptic ribbons per IHC was observed (Figure 3.12A). For that reason, ribbon synapses at P9 appeared close together, while ribbons in mature IHCs are more uniformly distributed (Figure 3.11B, J vs. C, D, K, L). The ribbon shape changed from mainly round in pre-hearing animals (Figure 3.11E, F) to mature wedge-like or droplet-like ribbons (Figure 3.11G-I). As reported in previous studies (Liberman, 1980; Sobkowicz et al., 1982), mature ribbons in P34 IHCs frequently exhibited a bright core (Figure 3.11G, I). In all age groups, fewer ribbons were found at the pillar side compared to the modiolar side of IHCs (Figure 3.11B-D, J-L, Figure 3.12A). With maturation SV numbers increased along with growing ribbon sizes - a result comparable to the random section analysis but independent of the subcellular location (Figure 3.12B, C). Summing up the volumes of multiple ribbons per synapse in order to examine the total volume of the ribbon material revealed comparable mean ribbon volumes per contact between P9 and P34 IHCs (Figure 3.12D, P9 pillar: $6.50 \times 10^6 \pm 1.77 \times 10^6$ nm^3, n = 14 ribbons, N = 2 IHCs vs. P34 pillar: $6.62 \times 10^6 \pm 0.80 \times 10^6$ nm^3, n = 7 ribbons, N = 2 IHCs, *n.s.*; P9 modiolar: $8.31 \times 10^6 \pm 1.40 \times 10^6$ nm^3, n = 42 ribbons, N = 2 IHCs vs. P34 modiolar: $8.52 \times 10^6 \pm 0.86 \times 10^6$ nm^3, N = 2 IHCs, *n.s.* Wilcoxon test). This result supports the hypothesis of a ribbon fusion process without losing a vast amount of ribbon material. Comparing SVs counts per synaptic contact between P9 and P34 IHCs corroborated the age-related raise in number (Figure 3.12E, P9 pillar: 31.50 ± 7.25, n = 14 ribbons, N = 2 IHCs vs. P34 pillar: 57.33 ± 5.82, n = 7 ribbons, N = 2 IHCs, $p = 0.0426$ Wilcoxon test; P9 modiolar: 35.95 ± 5.00, n = 42 ribbons, N = 2 IHCs vs. P34 modiolar: 74.44 ± 5.91, n = 24 ribbons, N = 2 IHCs, $p < 0.0001$ Wilcoxon test).

Next, I quantified the number of ribbons per synaptic contact and found multiple ribbons predominantly in P9 IHCs (Figure 3.11E, H, Figure 3.13A). However, double and triple ribbons still occur in $\sim$25 % of the synapses at P34, where the distances between these mature ribbons were shorter than those observed at multi-ribbon contacts of P9 IHCs (Figure 3.13B). In contrast, the nearest neighbor distances between single ribbons of neighboring synapses were comparable in all three age groups (Figure 3.13C). In P9 and P34, multi-ribbon synaptic contacts occurred mainly at the modiolar side of the IHCs (Figure 12D, P9 modiolar side: 42.86 % single and 57.14 % multiple ribbons vs. P9 pillar side: 62.50 % single and 37.50 % multiple ribbons, P34 modiolar side: 72.22 % single and 27.78 % multiple ribbons vs. P34 pillar side: 83.33 % single and 16.67 % multiple ribbons). Additionally, the appearance of floating ribbon precursors (Figure 3.11F) could be con-

firmed particularly in P9 with an average distance of 117.22 ± 32.51 nm to the IHC membrane (Figure 3.12A, Figure 3.13D). Some of the afferent fibers possessed ribbonless contacts with IHCs of all investigated age groups - a feature represented equally at both, pillar and modiolar sides. Interestingly, a couple of afferent fibers in P15 and P34 IHCs were subdivided into two branches or exhibited contacts to two neighboring IHCs on ribbon-occupied or ribbonless sides. More afferent fibers contacted the modiolar side of IHCs independent of the age and concurrent with the ribbon synapse allocation. Only half as many afferents showed contacts to the IHC pillar sides. For detailed 3D information see the following movie, which scans through a representative FIB-SEM z-stack of a P15 IHC: http://www.innerearlab.uni-goettingen.de/materials.html.

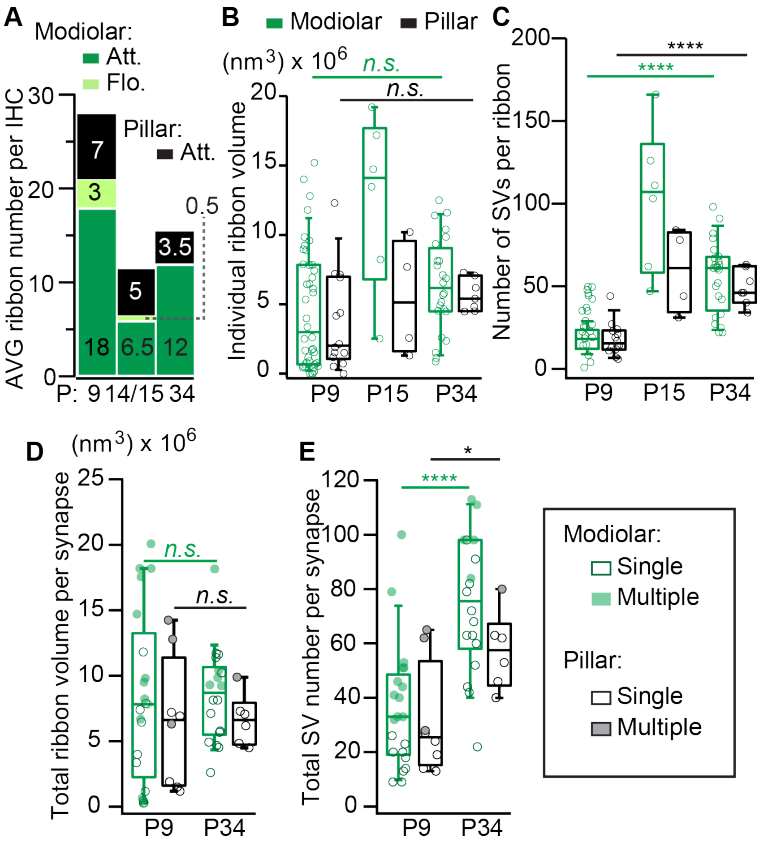

Figure 3.12.: Fewer ribbons are found at the pillar side of IHCs
(A) Absolute ribbon counts of all three age groups. Floating (Flo.) ribbons are solely present at the modiolar side of maturing IHCs, but not at P34 IHCs, where all ribbons are attached (Att.). N = 2 IHCs for each age group; P14 represents the SBF-SEM dataset. Statistical comparisons were only performed between FIB-SEM datasets. **(B)** Box plots display individual ribbon size measurement data points with 10, 25, 50, 75 and 90th percentiles (P9 modiolar: $4.65 \times 10^6 \pm 0.68 \times 10^6$ nm^3, n = 42 ribbons, N = 2 IHCs vs. P34 modiolar: $6.39 \times 10^6 \pm 0.69 \times 10^6$ nm^3, n = 24 ribbons, N = 2 IHCs, $p = 0.0758$ T-test; P9 pillar: $3.69 \times 10^6 \pm 0.95 \times 10^6$ nm^3, n = 14 ribbons, N = 2 IHCs vs. P34 pillar: $5.68 \times 10^6 \pm 0.45 \times 10^6$ nm^3, n = 7 ribbons, N = 2 IHCs, $p = 0.0610$ Wilcoxon test).

Figure 3.12 ***(previous page)*****: (C)** Individual SV counts per ribbon indicate an increase during maturation (P9 modiolar: 17.98 ± 1.13, n = 42 ribbons, N = 2 IHCs vs. P34 modiolar: 55.83 ± 4.39, n = 24 ribbons, N = 2 IHCs, $p < 0.0001$ Wilcoxon test; P9 pillar: 18.00 ± 2.61, n = 14 ribbons, N = 2 IHCs vs. P34 pillar: 49.14 ± 4.10, n = 7 ribbons, N = 2 IHCs, $p < 0.0001$ T-test). **(D)** Quantification of the combined ribbon-occupied volume per synaptic contact. Empty circles represent single ribbon synapses, filled circles the summed volume of multi-ribbon synapses. **(E)** Box plots showing the total number of SVs per synaptic contact. Higher SV counts are detected in P34 IHCs. Box plots present 10, 25, 50, 75 and 90th percentiles with individual data points overlaid ($n.s. > 0.05$, $^{*}p < 0.05$, $^{****}p < 0.0001$).

In summary, across all preparations and age groups, generally higher numbers of afferent fibers and ribbons as well as more multiple ribbons per synaptic contact could be detected on the modiolar side, thereby indicating a spatial gradient of synaptic contact sites. I could show that this distribution is already established before hearing onset.

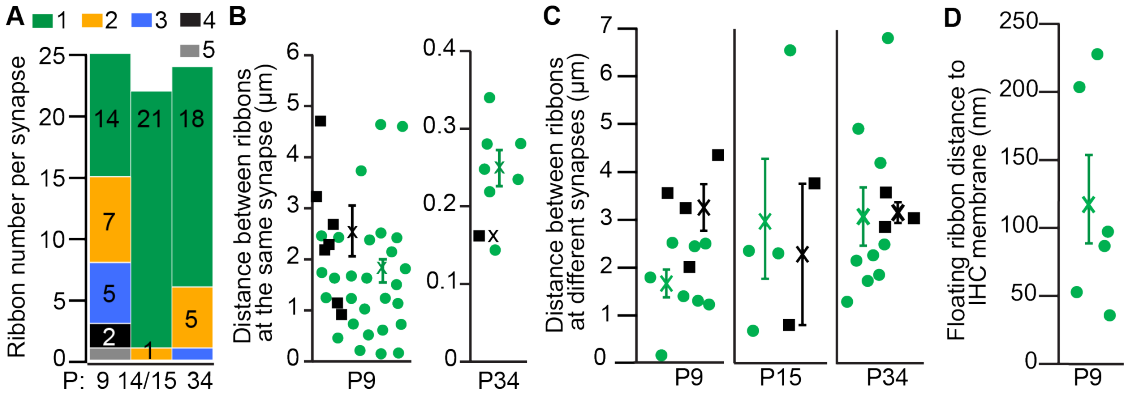

Figure 3.13.: Multiple ribbons per synaptic contact are present in immature and mature cochlear IHCs

(A) Graph represents absolute numbers of two IHCs, respectively for each age group. Note also here, that P14 depicts the SBF-SEM dataset. Immature IHCs display more frequently multiple ribbons per synaptic contact. In mature IHCs, single ribbon contacts dominate the presynaptic morphology, although also multiple ribbons are present. **(B)** Analysis of distance measurements between ribbons that are localized at the same synapse (P9: average modiolar (green X) = 1.67 ± 0.23 μm, n = 33 ribbons, N = 2 IHCs, average pillar (black X) = 2.45 ± 0.49 μm, n = 8 ribbons, N = 2 IHCs; P34: average modiolar = 0.25 ± 0.02 μm, n = 11 ribbons, N = 2 IHCs, average pillar = 0.16 μm, n = 2 ribbons, N = 2 IHCs).

Figure 3.13 ***(previous page)*****: (C)** Measurements of the shortest distance between the nearest ribbons of different synapses (P9: average modiolar (green X) = 1.62 $\pm$ 0.29 μm, SD = 0.83, n = 9 ribbons, N = 2 IHCs, average pillar (black X) = 3.23 $\pm$ 0.5 μm, SD = 0.98, n = 5 ribbons, N = 2 IHCs; P15: average modiolar = 2.97 $\pm$ 1.25 μm, SD = 2.51, n = 6 ribbons, N = 1 IHC, average pillar = 2.28 $\pm$ 1.48 μm, SD = 2.09, n = 4 ribbons, N = 1 IHC; P34: average modiolar = 3.09 $\pm$ 0.61 μm, SD = 1.82, n = 13 ribbons, N = 2 IHCs, average pillar = 3.17 $\pm$ 0.215 μm, SD = 0.37, n = 5 ribbons, N = 2 IHCs). **(D)** Distance measurements of floating precursor ribbons to the cell membrane at P9 IHCs (mean = 117.22 $\pm$ 32.51 nm, n = 6 ribbons, N = 2 IHCs).

3.1.8. Insights into the molecular constituents of developing ribbons and their intracellular transport pathway

Finally, I studied the abundance of AZ proteins upon maturation to investigate the protein composition of floating ribbon precursors and if cytoskeletal components can be found nearby. First, I performed pre-embedding immunogold labelings against cytoskeletal elements by using an α-tubulin antibody against microtubules and a specific antibody against the actin based motor protein myosin VI. This technique uses silver enhanced electron-dense gold particles as markers, which are conjugated to the secondary antibody, to identify proteins on the ultrastructural level. Unfortunately, stainings against both proteins showed an unspecific labeling pattern tested with two different protocols (Triton X and Saponin, for detailed explanations see Section 2.3.3.2) (Figure 3.14). Therefore, further experiments testing other experimental approaches (e.g. post-embedding immunogold labeling) are needed to localize their protein expression within IHCs and explore the potential transport mechanism in more detail.

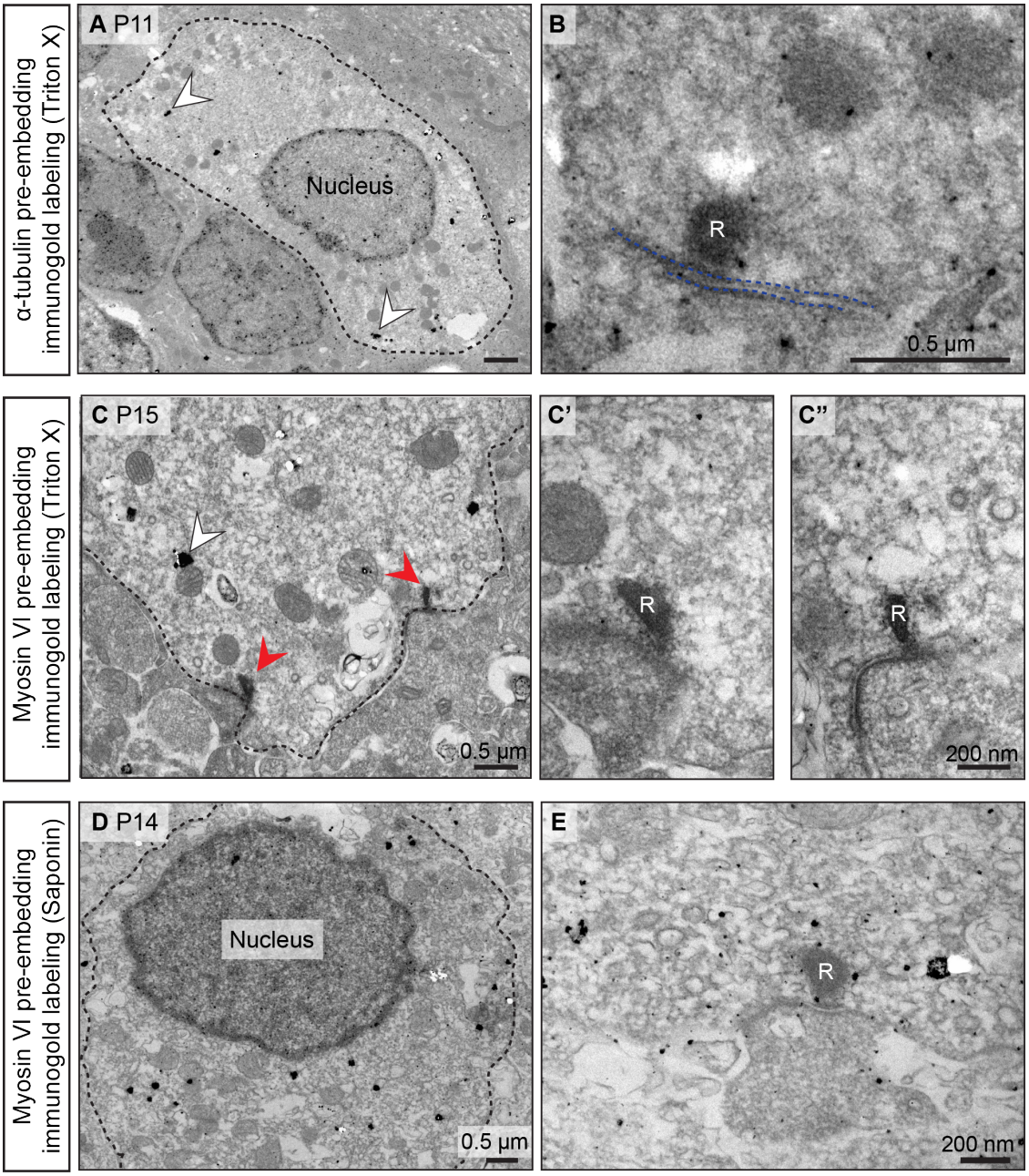

Figure 3.14.: Pre-embedding immunogold labelings against cytoskeletal proteins
(A, B) Staining against the α dimer of tubulin shows an unspecific background labeling (white arrowheads) within IHCs (IHC outline: black dashed line) and neighboring cells. A higher concentration of gold particles in the nuclei and no specific accumulation close to ribbons (R) or AZ membranes (blue dashed line) is visible. **(C-C")** The immunogold labeling against myosin VI displays a low labeling efficiency using the Triton X protocol. Red arrowheads point towards synaptic ribbons shown in higher magnification in **C'** and **C"**. When using the Saponin protocol, the labeling efficiency was higher **(D, E)**, but nevertheless both protocols resulted in an unspecific staining.

3.1.8.1. Floating ribbon precursors consist of RIBEYE and piccolino

Next, I determined the localization of the ribbon constituent RIBEYE (Schmitz et al., 2000) and the scaffolding protein piccolino on developing ribbon synapses utilizing pre-embedding immunogold labelings. As mentioned above, immunogold labelings against piccolino (Aczp18p19 antibody that recognizes the short and the long piccolo isoform) did not label DCVs. However, a clear labeling against piccolino was detected on floating ribbon precursors as well as membrane-anchored ribbons at the age of P2 and P9 (Figure 3.15A-D). In order to define the distribution of the labels in detail, I analyzed electron micrographs showing a clear cross-section of a ribbon. After defining the center of these attached ribbon synapses, I divided the ribbon into two halves (apical and basal, see illustration in Figure 3.15I). The overlay of multiple ribbons generated additionally a visual map of the protein disposition (for more details see Section 2.3.5). At ribbon-occupied synapses, large-sized silver enhanced gold clusters were found predominantly at the apical ribbon part (Figure 3.15A, C, E, F). Upon maturation, the labeling also extended towards the base of the ribbon as clearly shown for P21 (Figure 3.15G-J).

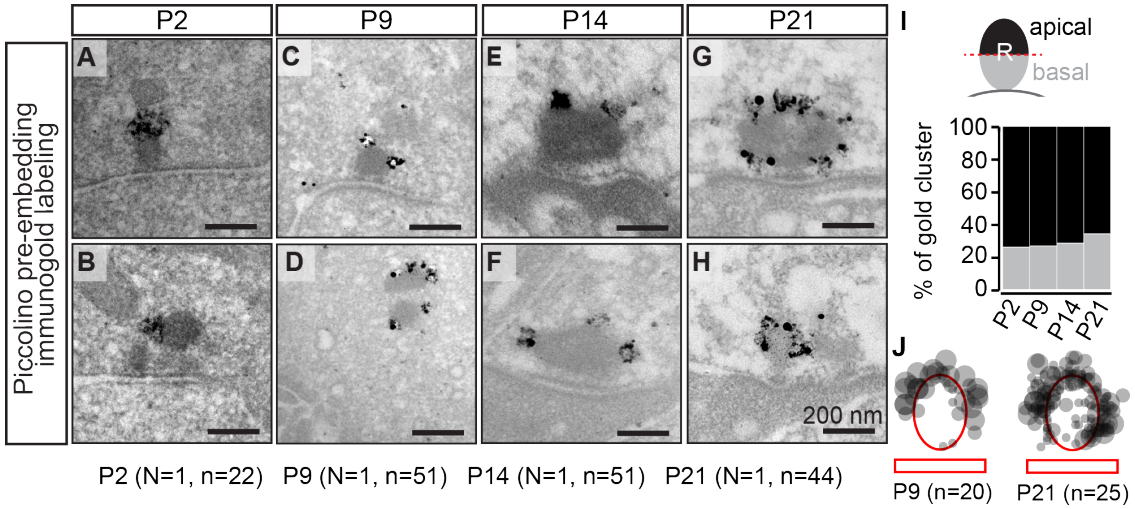

Figure 3.15.: Distribution of piccolino within maturing ribbons
(A-H) Piccolino localizes to IHC ribbons. At P2 **(A, B)**, P9 **(C)** and P14 **(E, F)**, big gold clusters are mainly found at the apical part of the ribbon. At P21 ribbons **(G, H)**, the labeling distribution is more homogeneous. **(D)** Cytoplasmic precursor ribbons are labeled for piccolino. **(I)** Graph represents the percentage of gold cluster occurrence at the apical and basal ribbon (R) half in immature and mature IHCs (N = animal number, n = ribbon number). **(J)** Schematic illustrations of the position of differently-sized anti-piccolino immunogold particles (gray circles) overlaid from several ribbons, visually highlighting the distinct piccolino distribution between P9 and P21 IHCs. The red oval-shaped circles outline the ribbon, red boxes below indicate the IHC membrane.

Immunogold labelings against the ribbon component RIBEYE, by using the CtBP2 antibody showed a label distributed over the whole ribbon surface, with no preference towards any direction in all investigated ages (Figure 3.16A-H). Despite parallel sample preparation of P9 and P21 IHCs labeled against piccolino, I discovered for both antibodies a generally less efficient labeling in younger animals as well as larger and fewer silver enhanced gold clusters compared to mature P21 animals. As expected, CtBP2 labeling was also found on floating ribbon precursors (Figure 3.16B) as well as fusing ribbons around the onset of hearing at P12 (Figure 3.15C, D). Overall these results confirm and expand the findings of photoreceptor ribbons (Dick et al., 2001; Limbach et al., 2011). Here, RIBEYE and piccolino labelings also decorated the IHC ribbon synapse, but in addition, I detected their labeling on floating ribbon precursors with a slightly different pattern for piccolino on mature synaptic ribbons.

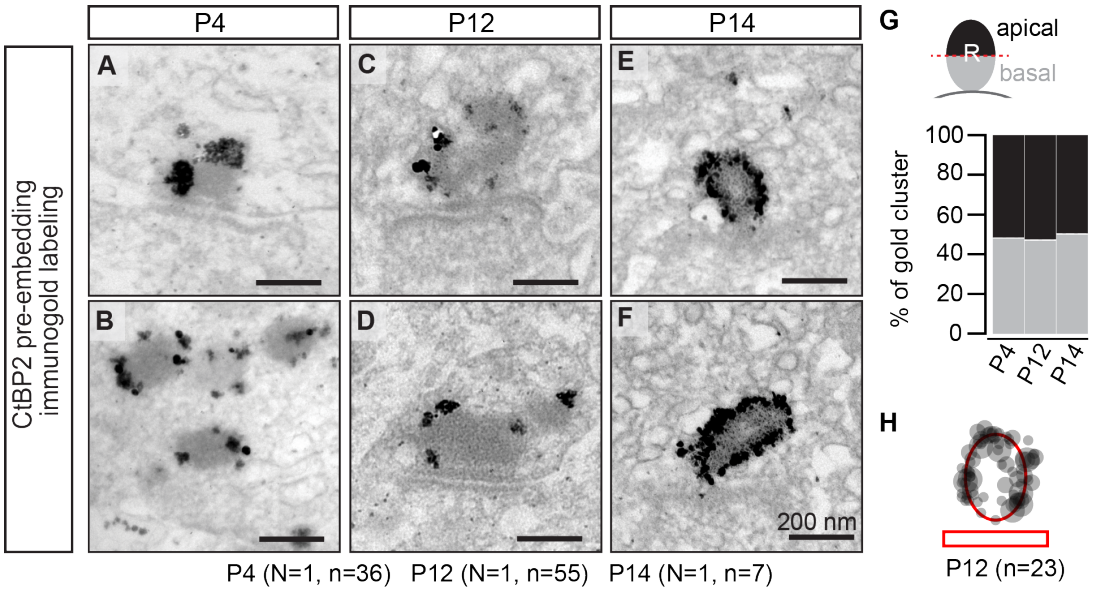

Figure 3.16.: Homogeneous labeling of CtBP2 during maturation
(A-F) The ribbon marker CtBP2 is detected over the whole ribbon surface in immature, mature and also fusing ribbons **(C, D)**. **(G)** Bar plot depicts an equal distribution of gold cluster between the apical and basal ribbon (R) half in immature and mature IHCs (N = animal number, n = ribbon number). **(H)** Representation of the CtBP2 labeling (gray circles) in P12 IHCs from various overlaid synaptic ribbons. Red oval-shaped circle outlines the ribbon, red box below indicates the IHC membrane.

3.2. Ultrastructural consequences of the disruption of RIBEYE, the main component of synaptic ribbons, in murine cochlear inner hair cells

The second aim of my thesis was to characterize the role of the synaptic ribbon for the structural integrity of cochlear IHC AZs. To do so, I investigated the morphological consequences of genetic disruption in the major constituent of the ribbon, the protein RIBEYE. Using electron microscopy of random single and serial sections enabled to assess the molecular anatomy of presynaptic AZs in mature RIBEYE knockout mice ($RBE^{KO/KO}$; Maxeiner et al., 2016). The content of this section has been previously published in Jean et al. (2018). Descriptions and figures are based on this publication.

The synaptic ribbon is critical for sound encoding at high rates and with temporal precision

Philippe Jean*, David Lopez de la Morena*, Susann Michanski*, Lina María Jaime Tobón*, Rituparna Chakrabarti, Maria Magdalena Picher, Jakob Neef, SangYong Jung, Mehmet Gültas, Stephan Maxeiner, Andreas Neef, Carolin Wichmann, Nicola Strenzke, Chad Grabner, and Tobias Moser

* These authors contributed equally to the work
eLife. 2018; 7: e29275. Published online 2018 Jan 12.
doi:10.7554/eLife.29275

Detailed author contribution of Susann Michanski:
The following figures in this thesis are taken from or represent modified versions from Jean et al. (2018).
- Experimental electron microscopic work and analysis: conventional embeddings and electron microscopy of random and serial sections (Figure 3.17, 3.18, 3.19)
- Contribution to the preparation of the manuscript

3.2.1. Ribbon loss in $RBE^{KO/KO}$ mice

To address the impact of RIBEYE deletion on IHC synapses, I used TEM on random ultrathin (70-75 nm) sections from P21, 6 weeks and 8 months old mice. As expected, I found a complete loss of synaptic ribbons in $RBE^{KO/KO}$ IHCs compared to the wild-type littermate controls $RBE^{WT/WT}$ and heterozygous $RBE^{WT/KO}$ IHCs, which both exhibited ribbon-occupied AZs (Figure 3.17A-C). Surprisingly, in $RBE^{KO/KO}$ IHCs, I frequently found several presynaptic densities (PDs) per synapse. Normally, in mature IHCs the ribbon is attached via a single continuous PD, while immature IHC ribbon synapses are predominantly attached via two PD rootlets juxtapose to multiple PSDs (Sendin et al., 2007; Wong et al., 2014, see also Section 3.1). PDs in $RBE^{KO/KO}$ IHCs clustered numerous synaptic vesicles (SVs) (Figure 3.17C) and thus from now on are assumed as individual AZs.

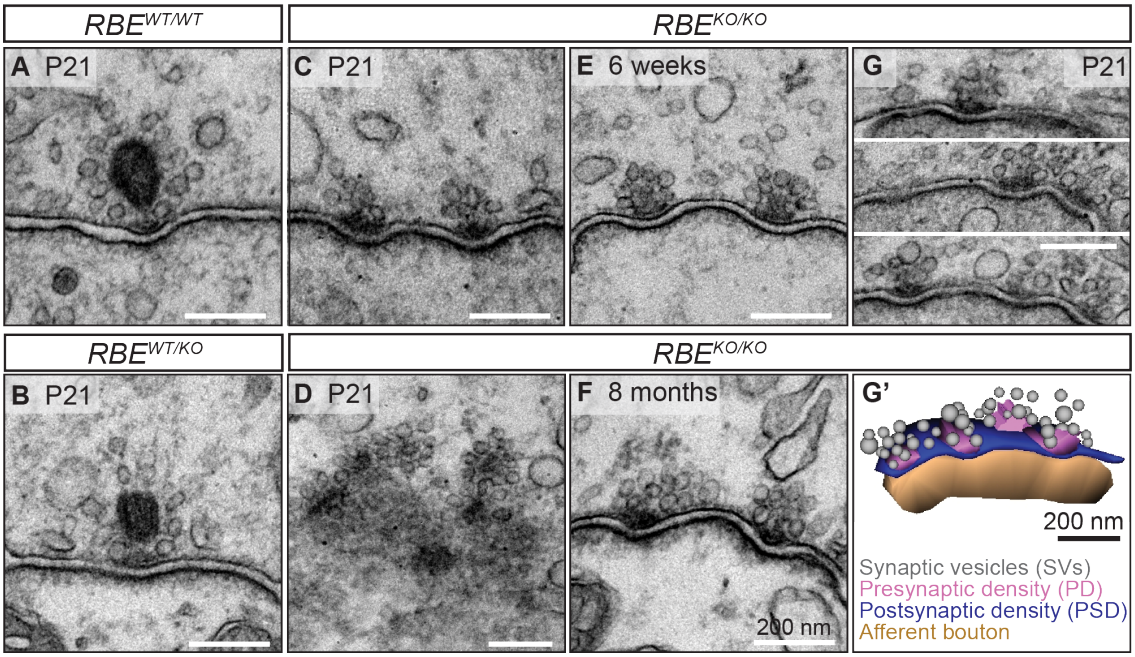

Figure 3.17.: Deletion of RIBEYE leads to the transformation of IHC synapses into multiple small ribbonless AZs
(A-C) Representative electron micrographs of IHC afferent synapses from P21 $RBE^{WT/WT}$, $RBE^{WT/KO}$ and $RBE^{KO/KO}$ mice. Ribbonless $RBE^{KO/KO}$ synapses display one or more PDs, clustering SVs. **(D)** $RBE^{KO/KO}$ IHC AZ cut tangentially, revealing multiple PDs (here six). **(E, F)** Representative electron micrographs of $RBE^{KO/KO}$ IHC synapses from mice at 6 weeks **(E)** and 8 months **(F)** of age: the presence of at least 2 AZs per contact in mature IHCs argues against a developmental arrest. **(G)** Consecutive serial sections of a typical $RBE^{KO/KO}$ P21 IHC synapse showing multiple AZs. **(G')** Corresponding 3D model of the synapse in **(G)** showing four PDs (magenta) surrounded by a total of 48 SVs (gray). Scale bars: 200 nm.

In contrast to immature wild-type IHCs, these multiple AZs mainly faced a single continuous PSD. Therefore, they are unlikely caused by a developmental delay or arrest due to a lack of RIBEYE, which is further supported by a similar AZ appearance in mature older animals. Here, multiple small ribbonless AZs at one synaptic contact were observed in 6 weeks and 8 months old $RBE^{KO/KO}$ mice (Figure 3.17E, F). This structure in $RBE^{KO/KO}$ IHCs was further confirmed by tangential cuts of the synapse (Figure 3.17D) as well as by 3D reconstructions from serial ultrathin sections (Figure 3.17G, G') suggesting a potential compensatory mechanism for the ribbon loss. In order to test this hypothesis, further quantifications regarding the number of PDs and associated SVs per synapse were required.

The evaluation of random sections from P21 old animals regarding the number of PDs/ribbons per synapse confirmed with the increased occurrence of multiple PDs in $RBE^{KO/KO}$ IHCs ($\sim$19.10 % compared to only 10.87 % of multiple ribbons in $RBE^{WT/KO}$ and 6.0 % of multiple ribbons in $RBE^{WT/WT}$ IHCs, Figure 3.18A). Also quantifications based on serial 3D reconstructions of $RBE^{KO/KO}$ synaptic contacts demonstrated a similar trend with on average 1.92 PDs $\pm$ 0.34 (n = 17 serial 3D reconstructions, N = 2) and 20.58 $\pm$ 2.98 total SVs per contact (Figure 3.18B). The lengths of individual PDs were analyzed in random sections and were comparable between

$RBE^{KO/KO}$ and $RBE^{WT/WT}$ synapses, but $RBE^{WT/KO}$ IHCs exhibited larger sized PDs (Figure 3.18C). While PSDs of $RBE^{KO/KO}$ synapses only showed a tendency towards an enlarged size compared to $RBE^{WT/WT}$ PSDs, they were significantly larger than $RBE^{WT/KO}$ PSDs (Figure 3.18D). Moreover, a reduction in the ribbon size for all three measurements (ribbon height, width and area) was found in $RBE^{WT/KO}$ IHCs in contrast to $RBE^{WT/WT}$ IHC synaptic ribbons (Figure 3.18E-G).

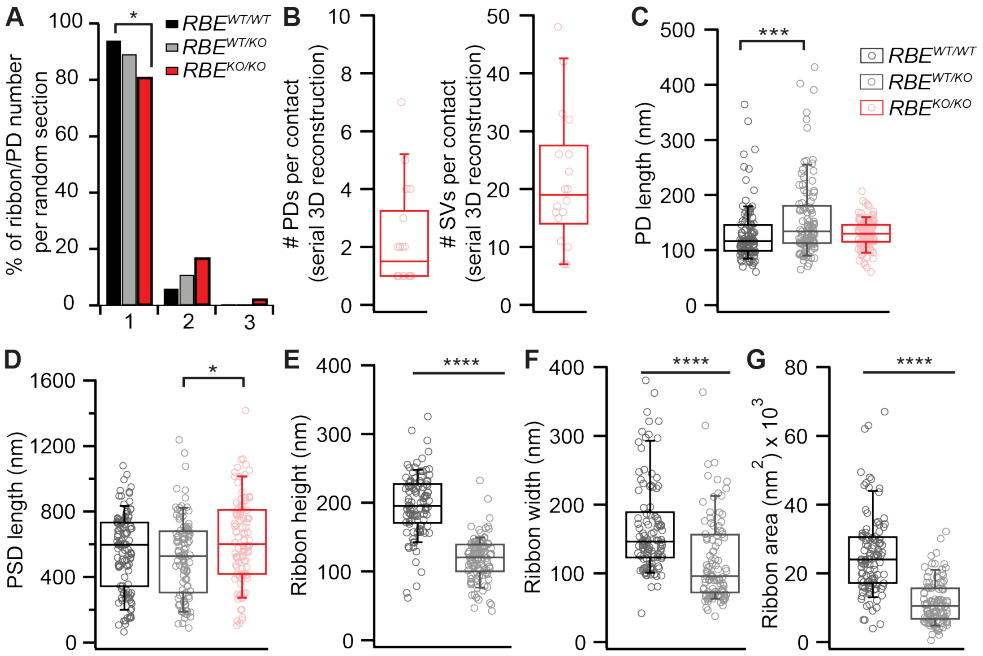

Figure 3.18.: Random section analysis showed bigger synaptic ribbons in $RBE^{WT/WT}$ mice
(A) Quantification of the number of ribbon/PD per random section. AZs with a single PD were less frequently observed in $RBE^{KO/KO}$ IHCs (0.81 ± 0.04, n = 108 AZs, N = 2 for $RBE^{KO/KO}$ vs. 0.94 ± 0.02, n = 106 AZs, N = 2 for $RBE^{WT/WT}$; $p < 0.05$, NPMC test). **(B)** Number of PDs and SVs per synaptic contact in serial 3D reconstructions of P21 $RBE^{KO/KO}$ IHCs. **(C, D)** Quantification of random IHC synapse (P21) sections reveal no significant differences between $RBE^{WT/WT}$ and $RBE^{KO/KO}$ for the PD and PSD length (PD length: 129.35 nm ± 4.89, n = 108 PDs , N = 2 for $RBE^{WT/WT}$ vs. 129.89 nm ± 2.53, n = 108 PDs, N = 2 for $RBE^{KO/KO}$; $p = 0.92$, NPMC test and PSD length: 555.91 nm ± 22.24, n = 113 PDs, N = 2 for $RBE^{WT/WT}$ vs. 623.77 nm ± 26.70, n = 98 PDs, N = 2 for $RBE^{KO/KO}$; $p = 0.11$, Tukey's test). However, in the $RBE^{WT/KO}$ IHCs, the PDs are bigger than in the WT IHCs (157.64 nm ± 7.19, n = 101 PDs, N = 2; $p = 0.0004$, NPMC test), and the PSDs are smaller than in the knockout IHCs (521.34 nm ± 24.20, n = 100 PSDs, N = 2 for $RBE^{WT/KO}$; $p = 0.01$, Tukey's test). **(E-G)** Random section analysis of P21 mice reveal smaller ribbon sizes in $RBE^{WT/KO}$ IHCs (ribbon height: 118.32 nm ± 3.17, n = 101 ribbons, N = 2 for $RBE^{WT/KO}$ vs. 197.09 nm ± 4.36, n = 106 ribbons, N = 2 for $RBE^{WT/WT}$; ribbon width: 119.80 nm ± 6.23 for $RBE^{WT/KO}$ vs. 168.34 nm ± 6.83 for $RBE^{WT/WT}$; ribbon area: 11.5e3 nm^2 ± 6.2e2 for $RBE^{WT/KO}$ vs. 25.4e3 nm^2 ± 1.1e2 for $RBE^{WT/WT}$; $p < 0.0001$, Mann-Whitney-Wilcoxon test for all).

3.2.2. Less SVs in $RBE^{KO/KO}$ IHCs

Next, I investigated two different and already described (Strenzke et al., 2016) morphologically discernable SV pools at IHC ribbon synapses in 2D random sections, membrane-proximal SVs

(MP-SVs, $\leq$ 25 nm distance between SV membrane and plasma membrane, laterally within 80 nm of the PD, yellow in Figure 2.6) and ribbon-associated SVs (RA-SVs, first layer of SVs around the ribbon within 80 nm, green in Figure 2.6). Further, for ribbonless synapses I defined an analogous pool to RA-SVs, the "PD-associated" SVs (PDA-SVs, ribbonless AZs: SVs within 80 nm distance of the PD and not falling into the MP-SV pool (see above), green in Figure 2.6). Both MP-SVs

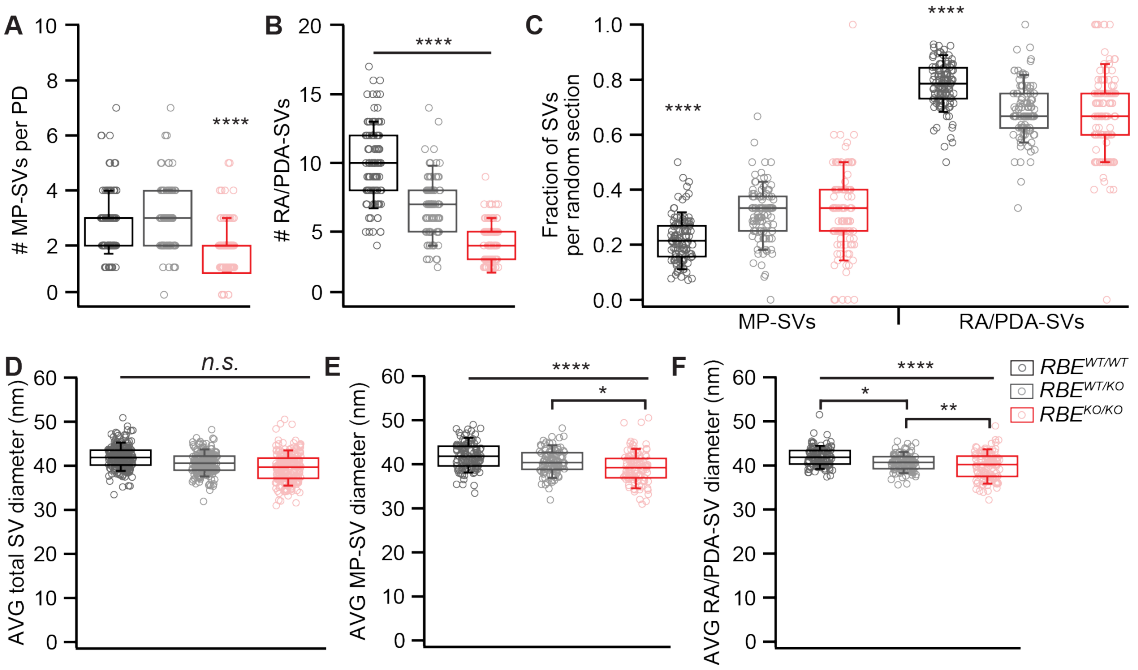

Figure 3.19.: *RBE*$^{KO/KO}$ ribbonless AZs cluster fewer SVs
(A-C) MP-SVs (1.92 $\pm$ 0.09, n = 108 AZs, N = 2 for *RBE*$^{KO/KO}$ 2.77 $\pm$ 0.12, n = 106 AZs, N = 2 for *RBE*$^{WT/WT}$; $p < 0.0001$, NPMC test) and RA/PDA-SVs (4.12 $\pm$ 0.15, n = 108 AZs, N = 2 for *RBE*$^{KO/KO}$ vs. 10.09 $\pm$ 0.27, n = 106 AZs, N = 2 for *RBE*$^{WT/WT}$; $p < 0.0001$, Tukey's test) per AZ, as well as the fraction of RA/PDA-SVs in *RBE*$^{KO/KO}$ IHCs, are significantly reduced (0.67 $\pm$ 0.02, n = 108 AZs, N = 2 for *RBE*$^{KO/KO}$ vs. 0.78 $\pm$ 0.01, n = 106 AZs, N = 2 for *RBE*$^{WT/WT}$; $p < 0.0001$, NPMC test). **(D)** The SV diameter per ribbon/PD is unaltered for all three genotypes considering all SVs (39.59 nm $\pm$ 0.21, n = 108 AZs, N = 2 for *RBE*$^{KO/KO}$ vs. 40.53 nm $\pm$ 0.14, n = 101 AZs, N =2 for *RBE*$^{WT/KO}$ vs. 41.80 nm $\pm$ 0.13, n = 106 AZs, N = 2 for *RBE*$^{WT/WT}$; $p = 0.30$, NPMC test). **(E)** However, a reduction of MP-SV diameter (39.29 nm $\pm$ 0.34, n = 108 AZs, N = 2 for *RBE*$^{KO/KO}$ vs. 41.79 nm $\pm$ 0.26, n = 106 AZs, N = 2 for *RBE*$^{WT/WT}$; $p < 0.0001$, NPMC test and 40.29 nm $\pm$ 0.25, n = 101 AZs, N = 2 for *RBE*$^{WT/KO}$ vs. *RBE*$^{KO/KO}$; $p = 0.03$, NPMC test) and RA/PDA-SV diameter (**(F)**: 39.72 nm $\pm$ 0.27, n = 108 AZs, N = 2 for *RBE*$^{KO/KO}$ vs. 41.81 nm $\pm$ 0.15, n = 106 AZs, N =2 for *RBE*$^{WT/WT}$; $p < 0.0001$, NPMC test and *RBE*$^{KO/KO}$ vs. 40.63 nm $\pm$ 0.17, n = 101 AZs, N =2 for *RBE*$^{WT/KO}$; $p = 0.003$, NPMC test and *RBE*$^{WT/KO}$ vs. *RBE*$^{WT/WT}$; $p = 0.02$, NPMC test) is observed.

(Figure 3.19A) and PDA-SVs (Figure 3.19B) significantly declined at ribbonless *RBE*$^{KO/KO}$ AZs. The calculated fraction of MP-SVs relative to the total number of SVs at *RBE*$^{KO/KO}$ AZs was higher than at *RBE*$^{WT/WT}$ AZs (Figure 3.19C). As a consequence, a reduction in the fraction of PDA-SVs was observed at *RBE*$^{KO/KO}$ AZs (Figure 3.19C). In *RBE*$^{WT/KO}$ IHCs, I found a decrease in the number of RA-SVs (Figure 3.19B), which is consistent with the reported smaller ribbon size (Figure 3.18E-G) and hence implies a partial impairment of the RIBEYE gene function upon the

loss of one allele. The SV diameter estimated for the total SV population was constant throughout all genotypes (Figure 3.19D), whereas a slight decrease of the MP-SV diameter for $RBE^{KO/KO}$ and $RBE^{WT/KO}$ (Figure 3.19E) as well as RA-/PDA-SV diameter (Figure 3.19F) was found reaching statistical significance. This significant difference between the individual SV categories could be the result of tied ranks of SV diameter measurements. However, the consideration of the total SV pool leads to the stabilization of tied ranks and thus results in the loss of significance.

Taken together, the disruption of RIBEYE causes a lack of synaptic ribbons in $RBE^{KO/KO}$ animals. Nevertheless, $RBE^{KO/KO}$ IHCs assemble several small AZs at each synaptic contact with fewer SVs. This seems not to be associated with a developmental impairment since similar results are found in older mice (6 weeks and 8 months).

3.3. Investigation of utricular hair cell ribbon synapse maturation in wild-type mice

As a part of the vestibular system, the utricle detects linear accelerations and head tilt by two types of hair cells (HCs), namely type I and type II that are morphologically different from cochlear IHCs. Type I utricular HCs are enclosed by an afferent calyceal ending and type II HCs exhibit bouton-like contacts of several afferent nerve fibers. In comparison to IHC ribbon synapses, relatively little is known about the synaptic morphology in utricular HCs and their changes upon maturation. An elaborate ultrastructural analysis of ribbon synapse development in type I and type II utricular HCs may lead to a better understanding of head motion encoding. Therefore, I investigated utricles of immature and mature age groups using TEM combined with electron tomography, and pre-embedding immunogold labelings in wild-type mice. Behavioral studies of balance reflexes in rats revealed that the vestibular system is mature at around P16 (Hård and Larsson, 1975; Lannou et al., 1979). For this reason, the following two immature (P9 and P15) and two mature (P20 and 11 months) ages from C57BL/6J mice were examined in detail. Part of this work (conventional embedding of P9 and 11 months utricles and the piccolino pre-embedding immunogold labeling) was performed by a bachelor student Timo Henneck (Bachelor thesis: "Investigating structure and development of type I & II hair cell ribbon synapses in the mouse utriculus" from 20th April 2016) under my supervision. Moreover, he prepared these samples for later TEM imaging and contributed electron micrographs for his embedded samples and added several electron micrographs for the P15 and P20 samples. Additional utricles at the age of P93 and P189 (CBA wild-type mouse) were embedded and partially trimmed and cut by Timo Henneck. I performed electron tomography and acquired serial ultrathin sections with corresponding 3D reconstructions of these two samples. Finally, both of us performed ultrastructural quantifications and statistical analyses presented in this chapter.

Similar to cochlear IHCs may structural characteristics of synaptic ribbons and SVs give some indication of functional related maturation processes. For this reason, we quantified the size and number of ribbon synapses as well as SVs. Moreover, we investigated the proportions of membrane-attached vs. floating ribbons, the latter being a signature of immaturity in cochlear IHCs as reported in Section 3.1.

3.3.1. The number of multiple attached ribbon synapses per synaptic site decreases upon maturation

In this study, we compared four different ages (P9, P15, P20, and 11 months) of utricular type I and type II HCs. How to distinguish the two HC types is explicitly described in (Figure 1.5). First, we restricted our analysis to the AZs containing ribbons with clear attachments (presynaptic densities) to the AZ membrane. In random 2D ultrathin sections, membrane-attached ribbons were quantified in number and size. Therefore, attached ribbon synapses were measured in height, width, and area excluding the presynaptic density similar to the cochlear IHC study (see Figure 2.5). Moreover, the number and diameters of SVs were determined in the first layer ($\leq$ 80 nm) around the ribbon. The results showed that both, type I and type II utricular HCs more frequently

exhibit multiple ribbons per synapse in immature ages (Figure 3.20A-G), which is similar to results obtained in cochlear IHCs (see Figure 2.5).

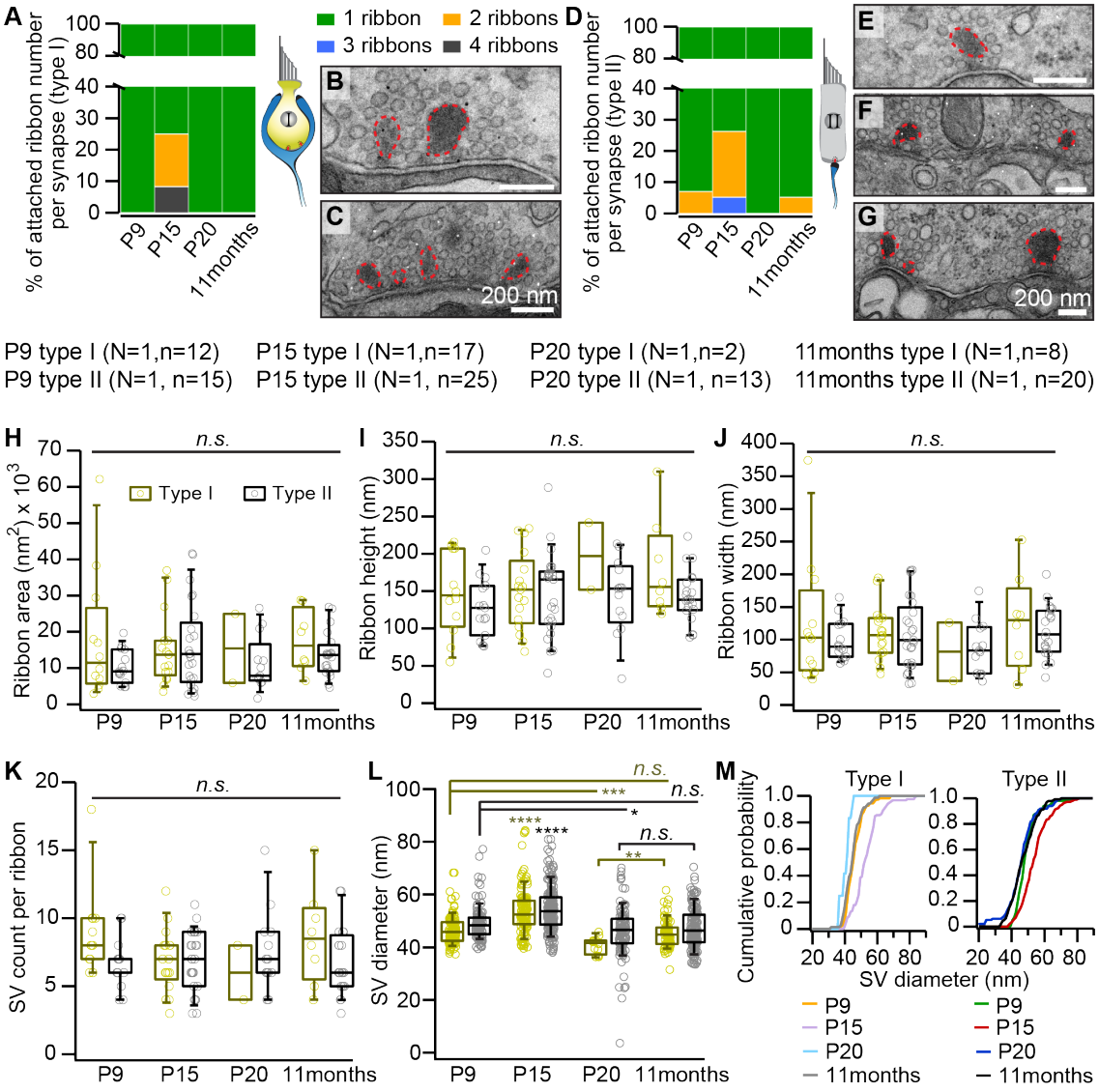

Figure 3.20.: Multiple ribbons per synaptic contact are prominent in immature ages of both HC types
(A, D) Analysis of the number of attached synaptic ribbons displays a larger quantity of multiple ribbons per synapse in immature type I **(A)** and type II **(D)** utricular HCs compared to the mature ages. **(B, C, E-G)** Exemplary electron micrographs depicting either multiple or single synaptic ribbons (highlighted with red dashed lines) in type I **(B, C)** and type II **(E-G)** HCs.

Figure 3.20 ***(previous page)*****: (C, F)** Raw images are kindly provided by Timo Henneck. **(H-J)** Box plots show random section quantifications of the ribbon size for all age groups. No significant changes regarding the ribbon area, height, and width (*n.s.* > 0.05, Tukey's test) could be observed. **(K)** While the number of SVs in both HC types remains constant (*n.s.* > 0.05, Tukey's test), the maturation of SV diameter **(L)** is fluctuating ($^{*}p < 0.05$, $^{***}p < 0.001$). **(M)** Cumulative probability distributions of SV diameters demonstrating the variation upon maturation. N = animal number, n = ribbon number. Box plots present 10, 25, 50, 75 and 90th percentiles with individual data points overlaid.

However, single synaptic ribbons clearly dominated at synaptic sites of both utricular HC types throughout the development (Figure 3.20A, D). In contrast to the increasing cochlear IHC ribbon size upon maturation (Section 3.1), the examination of the utricular ribbon size revealed neither a change in ribbon area nor in its height or width in any HC type (Figure 3.20H-J). In line with the ribbon size, a constant mean number of SVs in type I and type II HCs of all aforementioned age groups was observed (Figure 3.20K). SV diameters in utricular HCs first increase from P9 to P15 (Type I: from 46.43 $\pm$ 0.55 nm in P9 to 53.741 $\pm$ 0.811 nm in P15, $p = 5.41\text{e}{-12}$; Type II: from 49.23 $\pm$ 0.67 nm in P9 to 54.40 $\pm$ 0.67 nm in P15, $p = 5.65\text{e}{-08}$ KW test) and significantly decrease afterwards at the age of P20 (Type I: from 53.74 $\pm$ 0.81 nm in P15 to 40.75 $\pm$ 0.91 nm in P20, $p = 7.28\text{e}{-07}$; Type II: from 54.40 $\pm$ 0.67 nm in P15 to 46.08 $\pm$ 1.01 nm in P20, $p = 2.50\text{e}{-11}$ KW test). Thereafter, SV diameters in 11 months old animals again slightly increased in size of both HC types (Figure 3.20L, M; Type I: from 40.75 $\pm$ 0.91 nm in P20 to 45.11 $\pm$ 0.64 nm in 11 months, $p = 0.004$; Type II: from 46.08 $\pm$ 1.01 nm in P20 to 47.49 $\pm$ 0.66 nm in 11 months, $p = 0.525$ KW test). Additionally, no clear differences between the two utricular HC types were detected in terms of ribbon size or SV number and diameter.

3.3.2. Floating ribbons are not declining in mature HCs

A typical characteristic of immaturity in cochlear IHCs is the presence of free-floating ribbon precursors, which attach to the AZ membrane upon maturation (see Section 3.1.4). In order to investigate how the maturation of utricular HC synapses proceeds, the abundance of floating ribbons was determined in type I and II HCs. It has been found that a considerable number of floating ribbons was present in both utricular HC types. In type I utricular HCs, a higher number of floating ribbons was detected even in fully mature (11 months) HCs (Figure 3.21A-D). Intriguingly, the percentage of floating ribbons even increased during development from $\sim$60 % in P9 to nearly $\sim$90-100 % in P20 and 11 months old HCs of the type I. This stands in striking contrast to IHCs, where the number of floating ribbons progressively decreased with maturation, and ribbons are fully attached in hearing animals (Wong et al., 2014, see also Section 3.1). For type II utricular HCs, we observed a small increase of floating ribbons from $\sim$30 % at P9 to $\sim$60 % at the age of P20. Thereafter, the amount of floating ribbons reduced to P9 levels. In addition to this unexpected finding, floating ribbons formed clusters of up to eight ribbons visible per random section in type I and a maximum of three ribbons in type II utricular HCs (Figure 3.21A, B, E, F).

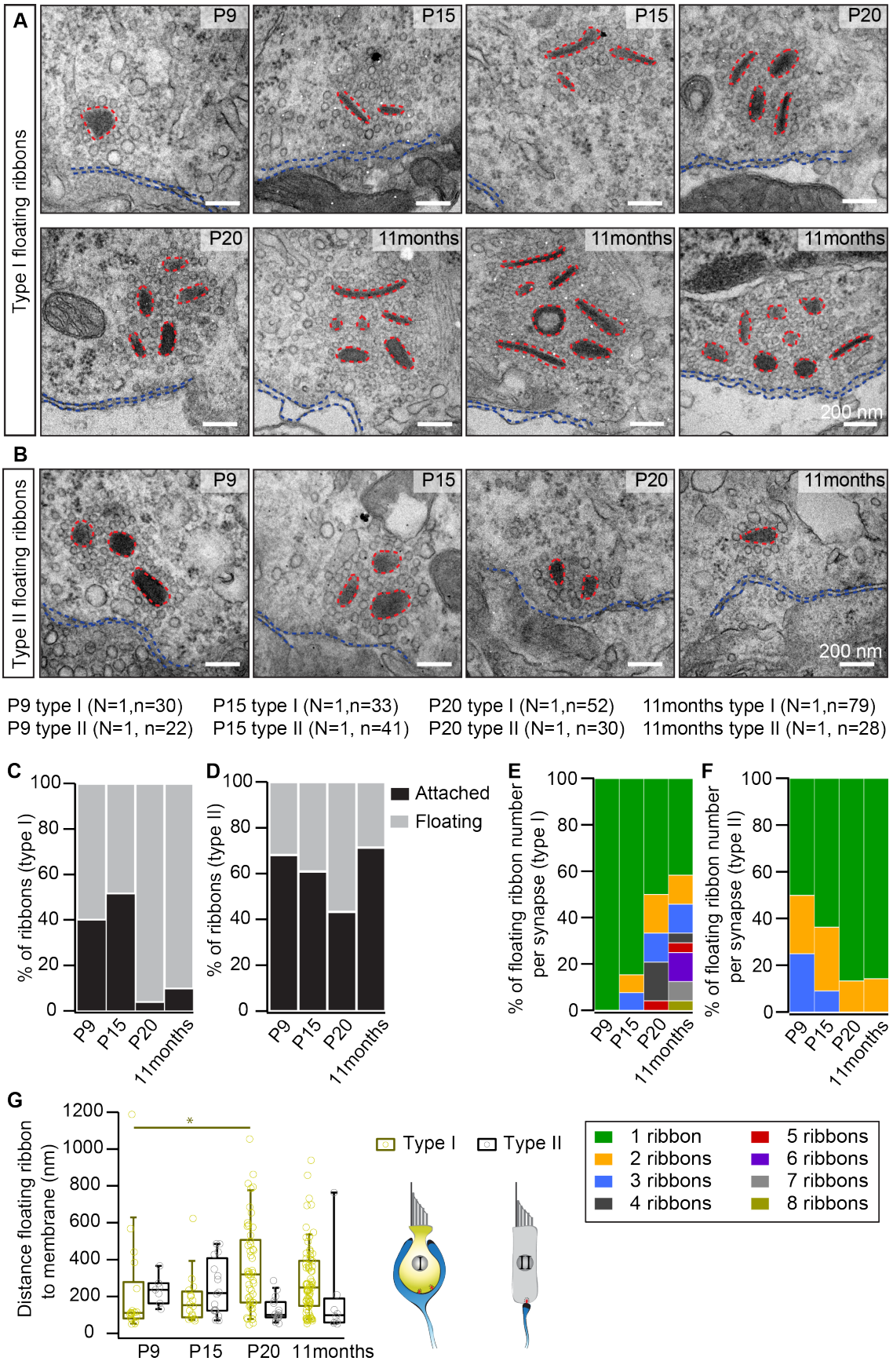

Figure 3.21.: Accumulation of floating ribbons particularly in mature type I utricular HCs
(A, B) Representative electron micrographs showing single and multiple floating ribbons (red dashed lines) in type I **(A)** and type II **(B)** HCs.

Figure 3.21 ***(previous page)*:** All ribbons lack the presynaptic contact to the HC membrane (blue dashed lines). Note, the frequent cluster formation in mature type I and immature type II HCs. Timo Henneck kindly supplied the original micrographs of **A**: P9, P15 (two floating ribbons), 11 months and **B**: P9, P20, 11 months. **(C, D)** Graphs represent the percentual distribution of floating and membrane-attached ribbons during maturation. **(C)** Mature type I utricular HCs possess predominantly floating ribbons, whereas type II cells exhibit mainly attached ribbon synapses throughout all investigated ages. **(E, F)** Quantification of the total number of floating ribbons per synapse reveals the occurrence of large ribbon clusters in both HC types. With aging, the number of multiple floating ribbons per synapse increases in type I utricular HCs **(E)** but decreases in type II HCs **(F)**. **(G)** Measurements of the nearest distance between floating ribbons and the HC membrane. Floating ribbons in immature type I cells are localized closer to the membrane than in mature ages ($^{*}p < 0.05$ NPMC test). In type II HCs, an opposite development was found, though it does not reach statistical significance. The box plot displays 10, 25, 50, 75 and 90th percentiles with individual data points overlaid. N = animal number, n = ribbon number.

Our data demonstrate an opposing ratio between type I and type II HCs regarding the number of floating ribbons per cluster. While in type I utricular HCs the number of floating ribbons in such a cluster increased during maturation (Figure 3.21E), multiple floating ribbons in type II utricular HCs appeared more frequently in immature synapses (Figure 3.21F). Comparative results have not been observed in wild-type cochlear IHCs, irrespective of the age. To determine a putative directional targeting of floating ribbons towards the AZ as known for IHC ribbons, the distances from the outer edge of floating ribbons to the HC membrane were measured. Results showed no continuous trend towards a putative decrease or increase over maturation in both HC types (Figure 3.21G).

3.3.3. Excluding genetic causes and preparation methods that could lead to a raise of floating ribbons

Surprisingly, floating ribbons mostly occur in large clusters - a phenomenon that is not known in wild-type cochlear IHCs. To exclude that the preparation method of the delicate tissue could have caused putative artifacts, we considered different treatments of the samples for embedding. So far, all utricle samples were first isolated from the inner ear and afterwards transferred into the fixation solution. During this preparation step, it is impossible to completely avoid mechanical stimulation of the tissue possibly leading to structural changes for instance by enhanced synaptic activity caused by forced stereocilia deflection. Another scenario could be that touching the organ with forceps disrupts HCs and thus the ultrastructure of the tissue is impaired. For this reason, we performed another way of preparation, where first only a small hole at the apical coil of the cochlea and above the utricle was opened without touching the sensory epithelia below. Next, the fixation solution was cautiously perfused through the oval window and the complete inner ear was fixed overnight. After several washing steps, the utricle was finally dissected. Thus, touching the utricle during the subsequent preparation cannot alter the already fixed ultrastructure. In electron tomographic 3D reconstructions of such prepared mature utricle samples, we still found floating ribbons forming large clusters (Figure 3.22), confirming our results from random sections and

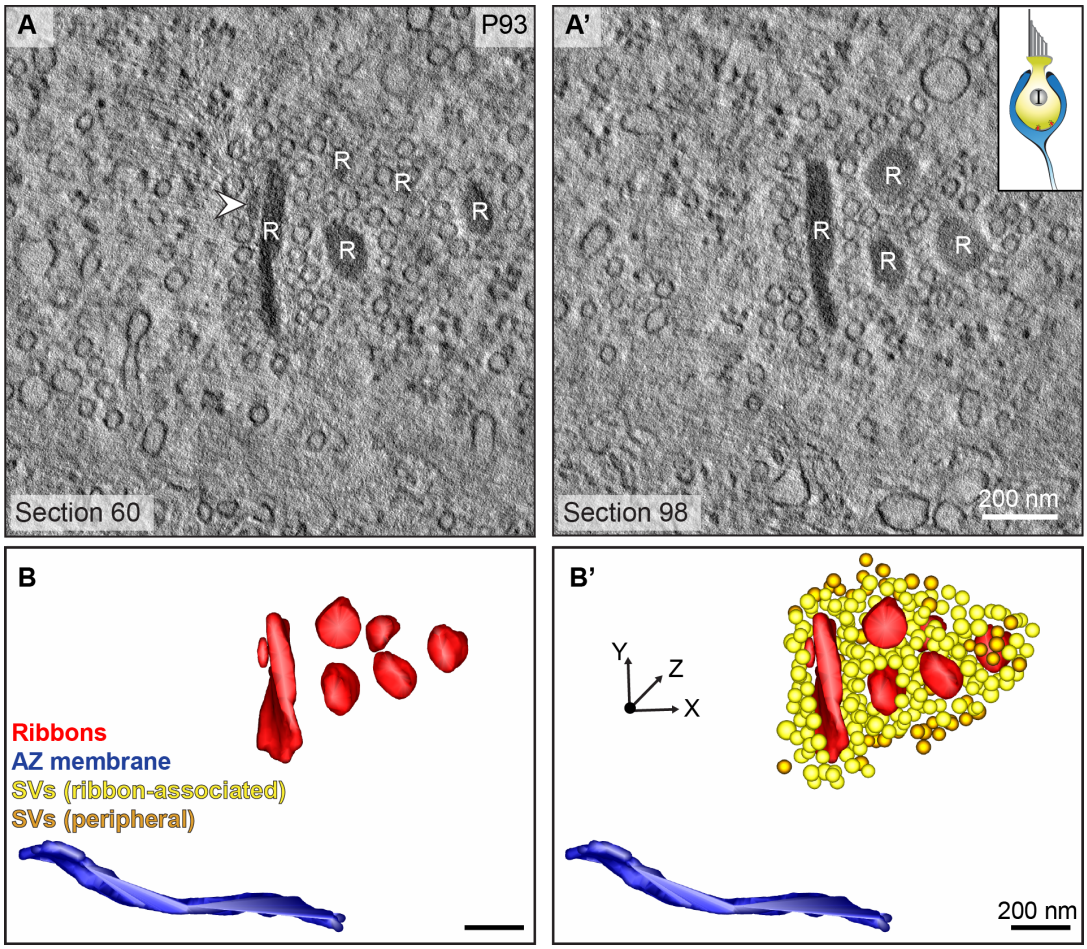

Figure 3.22.: The standard utricle preparation method is not the cause for the observed clusters of floating ribbons
(A, A') Single tomogram virtual sections of a floating ribbon (R) cluster from a mature (P93) type I utricular HC. Using here a different preparation procedure exhibit exactly the same ribbon clusters as with the previously used method. **(B, B')** Tomogram 3D model depicting several disc shaped floating ribbons. For better clarity of the cluster arrangement and ribbon appearance, SVs are not shown in **(B)**.

therefore excluding preparation artifacts. Further, the 3D information elucidated that these floating ribbons exhibit a disc-like shape (Figure 3.22B, B').

Moreover, a genetically caused age-related progressive hearing loss in C57BL/6J mice was detected by a loss of IHCs, OHCs and SGNs starting around 3-6 months of age (Mikaelian et al., 1974; Henry and Chole, 1980; Shnerson et al., 1981; Willott, 1986; Li and Borg, 1991; Johnson et al., 1997; White et al., 2000; Hequembourg and Liberman, 2001; Ison and Allen, 2003). Thus, the impairment in the organ of Corti could potentially also lead to structural artifacts in the vestibular HCs. To exclude this, we additionally started to examine the CBA adult (P189) wild-type mice strain, which maintains relatively normal hearing until the mice reach senescence (Willott, 1986; Willott et al., 1988, 988a; Shone et al., 1991; Walton et al., 1995; Spongr et al., 1997). EM micrographs of random ultrathin sections in CBA utricular HCs revealed also a higher incidence of

floating ribbons. Serial 3D reconstructions further illustrated floating ribbons that appeared flat and clustered together, comparable to HCs of C57BL/6J mice (Figure 3.23).

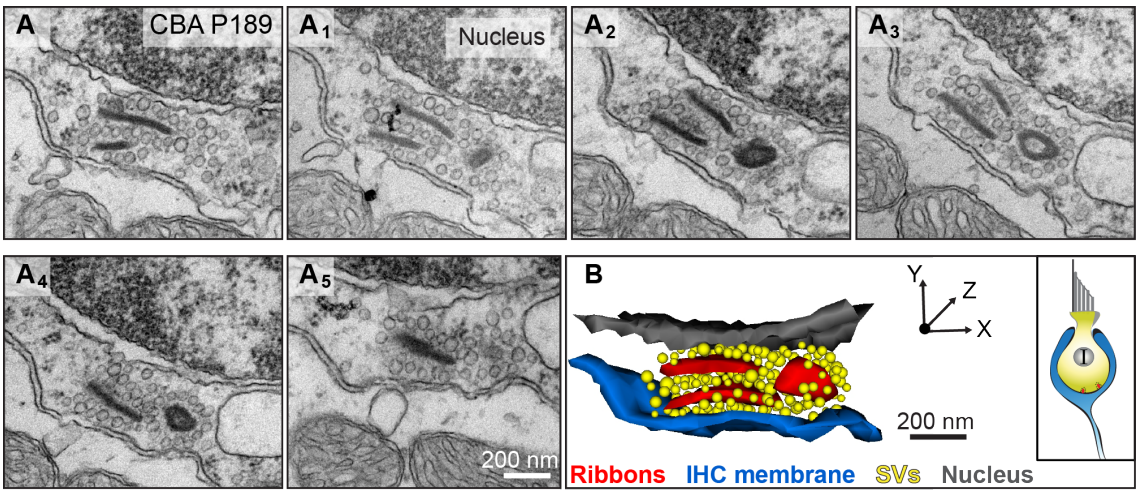

Figure 3.23.: Floating ribbon clusters are not caused by impairment of hearing and potentially balance
(A-A5) Consecutive ultrathin sections of a cluster containing three floating ribbons and the corresponding 3D model **(B)**. Electron microscopic data were obtained from a mature (P189) CBA wild-type mouse.

3.3.4. Floating ribbon clusters are composed of RIBEYE and piccolino

Finally, we investigated the presence and localization of the two scaffolding proteins RIBEYE and piccolino in the utricle using pre-embedding immunogold labelings. Both proteins are intensively studied in cochlear IHCs making them to ideal candidates for the establishment of the pre-embedding immunogold protocol in utricular HCs. The major component of ribbon synapses is RIBEYE (Schmitz et al., 2000), a protein that can be labeled by the antibody against the transcription repressor CtBP2 as mentioned previously. The antibody Aczp18p19 recognizes the long piccolo isoform but also the short isoform named piccolino, which is specific for synaptic ribbons (Regus-Leidig et al., 2013). In cochlear IHCs, pre-embedding immunogold labelings against both antibodies resulted in marked floating and attached ribbons (see Section 3.1.8).

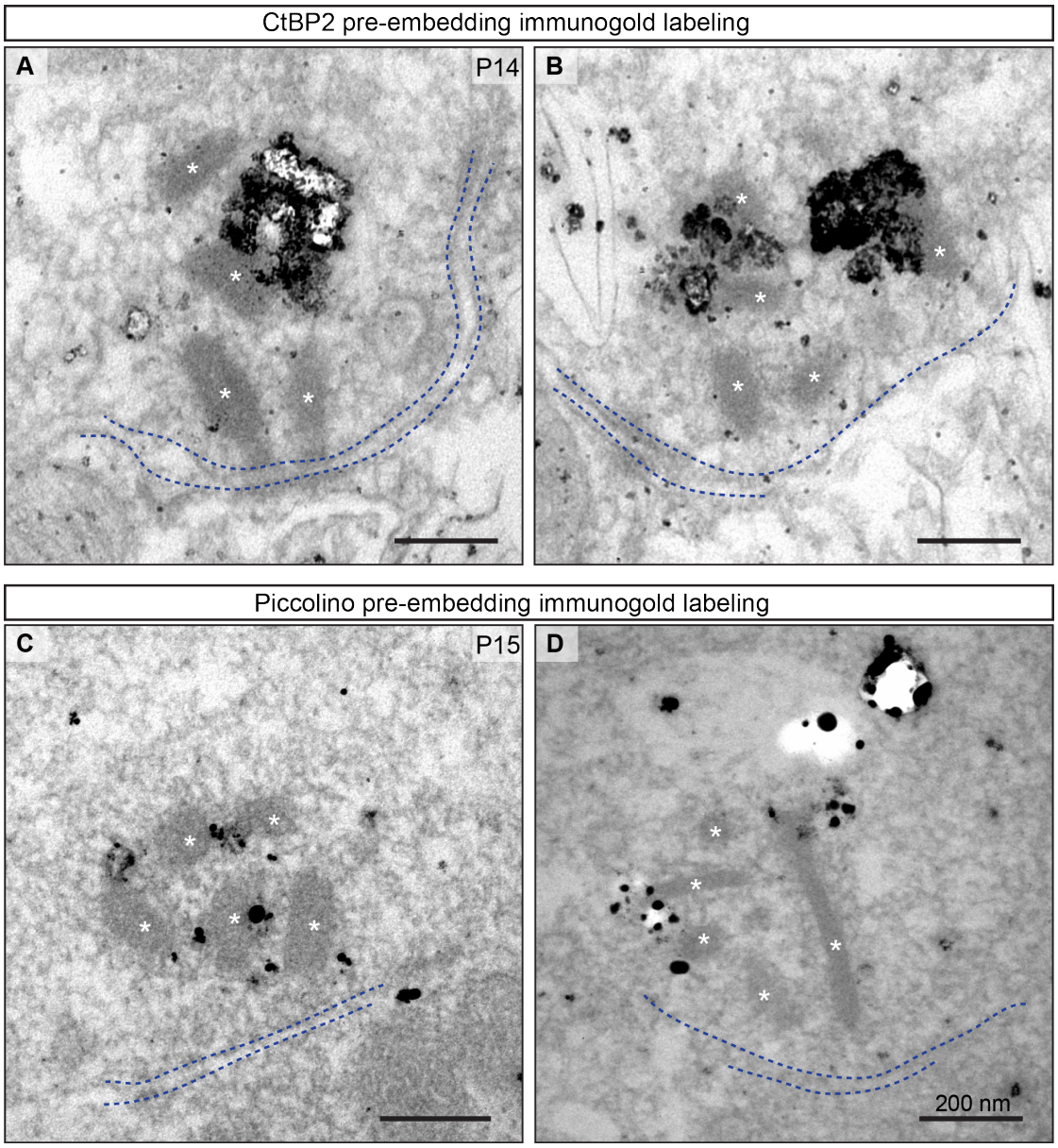

Figure 3.24.: RIBEYE and piccolino are localized at utricular HC synaptic ribbons
(A, B) The synaptic ribbon marker CtBP2 labels floating ribbon clusters with big accumulations of gold particles. **(C, D)** Piccolino appears, similar to RIBEYE, to be part of the floating ribbons that form clusters. Several small gold particles that label individual floating ribbons are visible.

Figure 3.24 ***(previous page)*****:** Both electron micrographs **(C, D)** were acquired and kindly provided by Timo Henneck. White asterisks highlight ribbons and dashed blue lines represent the HC membrane. N = 1 animal, respectively for the CtBP2 and piccolino immunogold labeling.

In utricular HCs also floating and attached ribbons were positively labeled, indicating a working pre-embedding immunogold protocol in this tissue. Focusing on the ribbon clusters, silver-enhanced gold particles against RIBEYE and piccolino marked floating ribbons that belong to clusters in both HC types (Figure 3.24). In detail, we detected some small and scattered gold particles at several floating ribbons of a single cluster (Figure 3.24C, D) but also large accumulations of gold particles at few ribbons (Figure 3.24A, B). The latter being a potential consequence of limited accessibility due to the aggregation of multiple ribbons. Hence, the presence of the synaptic proteins RIBEYE and piccolino could be confirmed in vestibular HCs comparable to the localization at IHC ribbon synapses.

To sum up, our electron microscopic findings discovered morphological alterations in HCs of the utricle upon maturation (Figure 3.25). Outstanding is the frequent appearance of floating ribbons in both HC types even at the age of 11 months. In comparison to type II HCs, exhibited type I utricular HCs more floating ribbons that increase in number upon maturation forming large and conspicuous ribbon clusters. Testing another fixation protocol as well as a wild-type mouse strain with a different genetical background supported the existence of floating ribbon clusters. Interestingly, no striking changes concerning the ribbon and SV size or SV number have been observed. As a last point, pre-embedding immunogold labelings demonstrated the expression of the synaptic proteins RIBEYE and piccolino at utricular HC ribbon synapses.

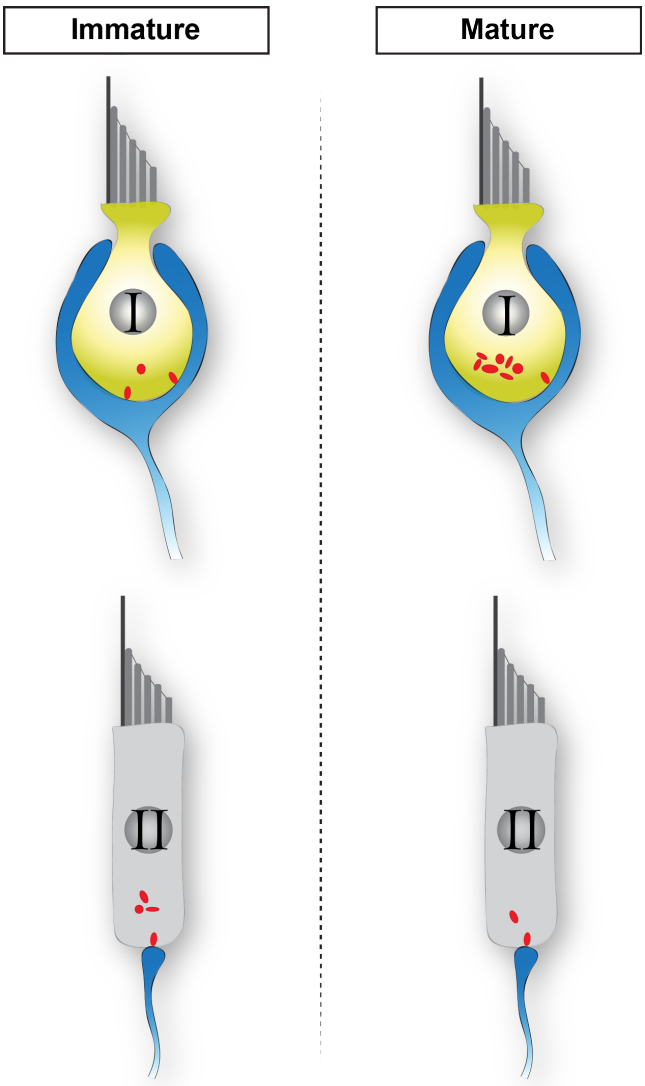

Figure 3.25.: Illustrative overview of utricular HC ribbon synapse maturation
Summary of the main morphological observations during utricle development. While type II utricular HCs show very similar developmental events as detected in cochlear IHCs, type I utricular HCs undergo a distinct maturation process. I: Type I utricular HC, II: Type II utricular HC, blue: afferent contacts, red: ribbon synapses.

4. Discussion

In this chapter, I first evaluate my developmental results of cochlear IHCs and interpret its importance on AZ formation, the commencement of a spatial gradient within IHCs and the role of AZ proteins in ribbon assembly. Afterwards, I discuss structural consequences of disrupting RIBEYE in IHCs that have been investigated in this work. Related to current hypotheses, I analyze the functional role of ribbon-type synapses. Finally, reasons for my ultrastructural findings on the maturation of vestibular HC synaptic ribbons in the utricle are addressed. Review of pertinent literature along with rating my utricle data in comparison to my developmental data of the cochlea add substantially to the understanding of the newly discovered developmental processes in vestibular HCs.

4.1. Synaptogenesis in developing cochlear IHCs

Cochlear inner hair cells (IHCs) faithfully encode acoustic information by specialized ribbon-type synapses. These synaptic ribbons are electron-dense structures that tether a halo of glutamate filled synaptic vesicles (SVs) and cluster Ca^{2+}-channels in order to carry pre-sensory and sensory signals by Ca^{2+}-dependent exocytosis at the presynaptic active zone (AZ) to spiral ganglion neurons (SGNs) (Lenzi et al., 1999; Beutner and Moser, 2001; Lenzi et al., 2002; Khimich et al., 2005; Frank et al., 2010; Wong et al., 2014; Jean et al., 2018). Ribbons are proposed to provide SVs, which are essential to maintain continuous and tonic neurotransmitter release (Buran et al., 2010; Frank et al., 2010; Becker et al., 2018; Jean et al., 2018). In mice, the onset of hearing occurs around postnatal day (P)12 (Mikaelian and Ruben, 1965) - an age associated with several structural and functional refinements of the presynaptic AZ (Sobkowicz et al., 1982; Frank et al., 2010; Huang et al., 2012; Wong et al., 2014). Despite of tremendous research in the cellular and molecular mechanisms of ribbon organization and regulation, many questions remain open such as: (i) where is ribbon assembly induced and which intracellular pathways are involved? (ii) How are floating ribbon precursors targeted to the AZ? and finally (iii) what is the procedure of ribbon synapse maintenance and maturation towards the characteristic monosynaptic connection with SGNs? To address these questions, I examined cochlear IHCs of wild-type mice in different developmental stages from pre-hearing to mature ages. Using various electron microscopic techniques, I visualized the ultrastructure of IHCs in detail to acquire new knowledge about the morphology of developing IHCs and their synaptic ribbons in particular. In this thesis, I proposed novel mechanisms of ribbon synapse maturation and maintenance, which are essential to achieve functional maturation. Parts of this chapter are based on the paper: ”Mapping developmental maturation of mouse inner hair cell ribbon synapses” (Michanski et al., 2019).

4.1.1. How and when are cochlear inner hair cell ribbon synapses generated?

Electron microscopic data from random ultrathin sections showed floating ribbon precursors and small attached immature ribbons in pre-hearing IHCs. I propose that the floating ribbon precursors attach to the presynaptic membrane after the establishment of synaptic contacts between IHCs and SGN fibers. First afferent projections approach IHCs already at the embryonal day (E)16, while synapses with attached ribbons - positioned opposite a PSD - could be observed from E18 on. These findings are consistent with previous immunohistochemical stainings (Koundakjian et al., 2007; Huang et al., 2012) and indicate that synapse establishment initiates during late embryogenesis where AZ formation, detectable by several ribbonless PSDs, precedes ribbon attachment. Investigations of mutant mice that did not experience IHC innervation due to a deletion of neurotrophin factors, which promote SGN survival (Ernfors et al., 1995; Michael et al., 1997; Fariñas et al., 2001; Luo et al., 2001; Wu et al., 2004; Kersigo and Fritzsch, 2015, reviewed in Rubel and Fritzsch, 2002), revealed a reduction in ribbon number. This result implies the necessity of SGNs for the ribbon synapse formation and maintenance (Wan et al., 2014; Kersigo and Fritzsch, 2015). The observed sequence of SGNs contacting IHCs and the occurrence of the first ribbon synapses some days later further represents the dependence of ribbon synapse establishment on the IHC innervation. Synapse formation in the vertebrate central nervous system (reviewed in McAllister, 2007) but also in neuromuscular junctions (Sanes and Lichtman, 1999) start as well after the establishment of contact sites between presynaptic and postsynaptic cells. Studies in neuromuscular junctions reported that an exchange of signals shortly after contacts are formed is important to coordinate synapse establishment and maturation (for an overview see Dennis, 1981; Hall and Sanes, 1993; Jennings and Burden, 1993). In IHCs, the overexpression of the neurotrophin Ntf-3 leads to a synaptic regeneration after acoustic trauma suggesting a potential neurotrophin based signaling pathway essential for ribbon synapse formation in general (Wan et al., 2014).

To apprehend the structural refinement of the AZ after initial ribbon synapse establishment, a systematic ultrastructural characterization of the synaptic ribbon and its SVs was performed. Since floating ribbon precursors as well as attached ribbons are found from E18 on, I will first discuss changes that occur at attached ribbons. Quantification of the ribbon size upon maturation revealed a rapid increase, which reaches a plateau shortly after the onset of hearing. The ribbon number per synapse decreases, but multi-ribbon contacts are still present in mature IHCs. Analysis of SVs tethered to attached ribbons demonstrated an increase in number, while the SV diameter successively decreases during development. I hypothesize that the observed remodeling of the AZ may reflect the structural adaptation to the specific requirements of the respective synaptic activity. In pre-hearing mice, IHCs fire spontaneous Ca^{2+}-mediated action potentials (APs) (Beutner and Moser, 2001; Marcotti et al., 2003; Johnson and Marcotti, 2008; Johnson et al., 2012) leading to the neurotransmitter release of glutamate, which drives bursting activity of SGNs (Tritsch et al., 2010). On the contrary, mature IHCs generate graded receptor potentials in response to sound stimuli (Johnson et al., 2013). In immature rat cochlear IHCs, Tritsch et al. (2007) demonstrated an ATP dependent depolarization of IHCs released periodically from supporting cells, which declines after hearing onset. These spontaneous APs are supposed to guide SGNs to the proper contact sides and drive synaptic maturation before sensory activity (Zhang and Poo, 2001). The

observed increase in synaptic ribbon size and in the number of associated SVs prior to the onset of hearing might change the Ca^{2+}-dependence by influencing the neurotransmitter release and SGN firing properties. Increasing the surface area of the ribbon facilitate more space for SVs tethered to the ribbon, which may cause the regulation of AZ strength and this way result in an optimized sound transmission for the mature auditory pathway. Investigations of neurons in the brain already demonstrated a correlation between structural changes of synaptic specializations with more releasable SVs and higher efficiency of release promoting prolonged high-frequency firing in mature synapses (Lisman and Harris, 1993; Geinisman et al., 1996; Taschenberger et al., 2002).

For the SV diameter quantification, we could already show in (Jean et al., 2018) that SVs of P21 wild-type IHCs range between 35-50 nm in size with a mean of 41.80 nm. In this study, I found a similar distribution of differently sized SVs in mature IHCs. However, immature IHCs possess larger SVs. I took into consideration that the observed morphological change in SV diameter could have been caused during sample processing. Comparing quick-freezing techniques with conventional embeddings revealed no change in the SV size of different synapses from the cochlear nucleus and zebrafish neuromuscular junctions (Tatsuoka and Reese, 1989; Helmprobst et al., 2015). Moreover, it was shown that chemical fixation, changes in activity and increasing the osmotic pressure in rat hippocampal cell cultures do not influence the SV size (Qu et al., 2009). Further, the measurement of mean SV diameters on 2D random sections might underestimate the exact size due to the variability from section to section. Nevertheless, detailed studies on serial sections of conventional synapses exhibited almost constant SV sizes with an error of less than 9 % (Feuerverger et al., 2000; Hu et al., 2008). All these studies excluded methodological artifacts. Therefore, the observed decline in size might represent another mechanism for the maturation process of the neurotransmitter release. It has to be taken into consideration that there might exist a variability between species and synapse type related to the need of the specialized synaptic function (Hu et al., 2008). For instance, fluorescence correlation spectroscopy and cryogenic EM showed a reversible enlargement of SVs in rat conventional synapses of the brain upon loading with glutamate (Budzinski et al., 2009). A similar observation was reported in *Drosophila* larvae overexpressing the vesicular glutamate transporter (Daniels et al., 2004, 2006).

Interestingly, data on developing zebrafish neuromuscular junctions and rat motor-sensory neocortex synapses exhibit also larger SVs in immature synapses that decrease in size but increase in number during maturation (Markus et al., 1987; Helmprobst et al., 2015). Large SVs of immature IHCs might contain more neurotransmitter as indicated earlier for other preparations (Daniels et al., 2004, 2006; Budzinski et al., 2009). For that reason, they can release more glutamate at one go, which might be needed in this stage to stimulate the immature auditory pathway and thus prepare and train the synaptic function for Ca^{2+} sensitivity in response to mature receptor potentials. An explanation for the developmental decline in SV size was found by a study in electromotoneurons of electric rays, where a pulse-labeling technique was used in order to trace the life cycle of SVs in vivo (Kiene and Stadler, 1987). Their results demonstrated that immature SVs lose proteoglycans during exocytosis causing a smaller SV size afterwards (Kiene and Stadler, 1987). Another study based on activity-dependent FM1-43 dye uptake assays and EM serial sections compared wild-type with *Drosophila* mutants lacking the adaptor protein AP180.

Adaptor proteins play a crucial role in the process of SV membrane retrieval and reassembly into new SVs during endocytosis (Maycox et al., 1992; Takei et al., 1996). The loss of AP180 in mutant larval body-wall muscles showed an increased SV size and impaired endocytosis indicating that AP180 is important for the regulation of SV size by a clathrin-dependent reassembly process that defines the amount of presynaptic membrane retrieved into clathrin cages during endocytosis (Zhang et al., 1998). Moreover, the HC specific protein otoferlin might play an important role in organizing the SV size. Otoferlin was proposed to localize to SVs (Roux et al., 2006), but was also observed on endosomal structures in IHCs (Strenzke et al., 2016). Mutant mice with reduced otoferlin levels revealed enlarged SV sizes in IHCs (Strenzke et al., 2016). A strong impairment in the sustained exocytosis let the authors conclude that otoferlin is required for SV reformation during replenishment (Strenzke et al., 2016). Considering that otoferlin seems not to be functionally important in early immature IHCs (Safieddine and Wenthold, 1999; Uthaiah and Hudspeth, 2010; Reisinger et al., 2011), the SV maturation towards smaller diameters might represent an increased involvement of otoferlin in the reformation of proper sized mature SVs upon development. Hence, developmental changes in the abundance of vesicle associated proteins and a concomitant membrane remodeling, which remain largely unknown in cochlear IHCs, could lead to the typical smaller SVs in mature IHCs. In conclusion, the structural maturation of the SV size and number according to the ribbon size and number might play an essential role in the functional transition of these synapses in order to control the sound evoked intrinsic activity.

In addition, I found a simultaneous maturation of the postsynaptic compartment. The postsynaptic membrane becomes electron-dense with multiple PSDs per SGN at the age of E18. As synaptic ribbons mature and increase in size, the apposed PSDs gradually enlarge as well forming mainly a single continuous AZ/PSD complex per SGN. My recent results extend our previous study (Wong et al., 2014) that additionally revealed a Ca^{2+}-channel confinement during development. Consequently, the increase in SV number that goes along with an enlargement of the ribbon synapse, together with the improved presynaptic clustering of Ca^{2+}-channels and larger PSDs shapes the properties of functionally mature synapses, which respond solely to auditory signals.

4.1.1.1. Fusion of synaptic ribbons represents an essential mechanism in the presynaptic maturation

The underlying mechanisms of synaptic ribbon/PSD reduction parallel to an increase in size are still unknown, but the following two hypotheses have been proposed: (i) targeted degradation of the AZ material (also known as pruning) (Spiwoks-Becker et al., 2004; Wong et al., 2014), where the remaining ribbons/PSDs undergo several morphological and molecular changes to evolve into mature functional synapses; or alternatively (ii) fusion of multiple small ribbons/PSDs to produce one single mature AZ/PSD complex (also known as merging) (Spiwoks-Becker et al., 2004; Regus-Leidig et al., 2009; Wong et al., 2014).

Intriguingly, I found floating ribbon precursors up to the second postnatal week, which may reflect the frequency at which new synaptic sites are formed. Analysis of 2D random sections and 3D tomography show ribbon precursors free floating in the cytosol associated with SVs, indicating that their formation occurs at a distance to the AZ. Such floating ribbon precursors have already

previously been reported in cochlear IHCs, retinal photoreceptors and zebrafish lateral line neuromast hair cells (Sobkowicz et al., 1986; Regus-Leidig et al., 2009; Wong et al., 2014; Graydon et al., 2017). The developmental reduction of floating ribbon precursors compared to an increase of attached ribbon synapses in this study suggests that these precursors are transport units for ribbon proteins forming mature synaptic ribbons. However, the site of origin remains elusive and requires more intensive studies. Surprisingly, I observed electron-dense ribbon material connecting floating ribbon precursors and attached ribbon synapses as well as two neighboring attached ribbons. While pruning is known as a general mechanism to refine SGNs (Sobkowicz et al., 1982; Sendin et al., 2007; Huang et al., 2012), my data are indicative for ribbon fusion. I propose that fusion of ribbon material facilitates the reduction in ribbon number while at the same time the ribbon size enlarges. Recent live-cell studies in zebrafish neuromasts suggest as well precursor fusion events in vivo (Graydon et al., 2017). The synaptic ribbon protein RIBEYE was shown to self-associate via five RIBEYE-RIBEYE interactions sites and even have the ability to form aggregates (Schmitz et al., 2000; Magupalli et al., 2008). Hence, synaptic ribbon assembly and fusion of ribbon material may be initiated by multiple RIBEYE-RIBEYE interactions, but also other proteins could be involved in this process. Piccolo is also present on the ribbon (Dick et al., 2001; Limbach et al., 2011, see also Section 3.1.8 in this study) and thus fusion of spherical ribbon material could imply the merging of several AZ proteins. Previous studies in murine photoreceptors revealed activity-dependent structural changes of ribbon synapses (Spiwoks-Becker et al., 2004; Fuchs et al., 2013). The authors observed that ribbons under light exposure start to form protrusions, which get released as spherical ribbons into the cytoplasm. The remaining attached ribbons show a reduction in size. The opposite occurs at temporal dark exposure during the light phase. Here, floating spherical ribbons undergo a refusion with the attached ribbons leading to an enlargement of synaptic ribbons. However, constant light or dark exposure revealed no morphological changes of ribbon synapses. Similar ribbon spheres were found in photoreceptors treated with the Ca^{2+} chelator EGTA (Regus-Leidig et al., 2010). Less intracellular Ca^{2+} results in less synaptic activity - a phase related with budding of ribbon material. As a consequence, highest synaptic activity with greatest light sensitivity in the retina exists during the dark period where synaptic ribbons are larger and possess more releasable SVs (Balkema et al., 2001).

Moreover, my 3D data of the basolateral part of IHCs demonstrated comparable ribbon volumes per synaptic contact between P9 and P34 IHCs supporting the hypothesis of ribbon fusion: while the number of ribbons per contact decreased, the ribbon size increased such that the abundance of presynaptic RIBEYE remains relatively constant during synapse maturation. It is tempting to speculate that the presence of floating ribbons and the block-wise modulation of IHC ribbon size - and concomitant SV tethering capacity - related to temporary sound exposure, may also present a form of presynaptic plasticity to provide functional adaptation. In retina, the abundance of cytosolic ribbon spheres did not reduce during illumination and no uptake by autophagosomes or disintegration of ribbon material could be found (Spiwoks-Becker et al., 2004). However, my data of cochlear IHCs revealed a decrease of floating ribbon precursors once the final ribbon size was established at hearing onset. Therefore, I do not exclude a putative mechanism of diffusional addition of individual cytosolic RIBEYE molecules, but I propose that the main mechanism for

ribbon growth during development is ribbon precursor fusion. Fusion and/or budding of SV-tethering ribbon blocks with membrane-anchored ribbons may present an efficient mechanism to rapidly modulate ribbon SV storage capacity likely exceeding the adaptive capacity provided by addition/loss of soluble RIBEYE.

4.1.2. Synaptic ribbon size and number differ along a pillar-modiolar spatial gradient

It was previously shown that the general view of a monosynaptic connection between IHCs and SGNs with a single ribbon occupying the presynaptic AZ might be too simplified, as ∼20 % of ribbon synapses analyzed in adult cats still displayed multi-ribbon contacts (Merchan-Perez and Liberman, 1996; Kantardzhieva et al., 2013). Similarly, in my study of random sections from murine IHCs a subpopulation of multi-ribbon contacts was found maintained into adulthood. This finding is likely functionally significant since the occurrence of multiple ribbons per synaptic contact strikingly increases the availability of SVs as well as presynaptic Ca^{2+}-channels. The fact that synaptic ribbons appear to reach their final dimensions already around the onset of hearing suggests that the number of ribbons per contact may offer an additional means of regulation, allowing the strengthening of individual synapses. Previous studies on the spatial gradient of cat and mice IHCs determined mainly large and/or multiple ribbons at the modiolar (neural) side of IHCs, which are innervated by low spontaneous rate, high threshold SGN fibers (Merchan-Perez and Liberman, 1996; Frank et al., 2009; Liberman et al., 2011; Kantardzhieva et al., 2013; Ohn et al., 2016). On the pillar (abneural) side, rather smaller synaptic ribbons drive high spontaneous rate, low threshold neurons (Merchan-Perez and Liberman, 1996; Frank et al., 2009; Liberman et al., 2011; Kantardzhieva et al., 2013; Ohn et al., 2016).

3D microscopy approaches to reconstruct large volumes of the basolateral part of IHCs provide new opportunities to investigate the cellular organization at multiscale resolution and to relate for instance ribbon size or number per synapse to the topographic position within an individual IHC. To find out when the IHC heterogeneity establishes, I investigated mouse IHCs at three different ages (P9, P14/15, P48) by performing serial block face (SBF)- and focused ion beam - scanning electron microscopy (FIB-SEM). Using these methods allowed the analysis of several synaptic parameters in 3D and hence majorly extends previous work on this topic (Merchan-Perez and Liberman, 1996; Taberner and Liberman, 2005; Frank et al., 2009; Liberman et al., 2011; Ohn et al., 2016). In my 3D models, the number of synaptic ribbons declines over maturation. In line with this, Schmiedt et al. (1996) reported a reduction of low spontaneous rate fibers, which might reflect a higher vulnerability of IHC synapses to drive these SGNs (Furman et al., 2013). Multi-ribbon synaptic contacts could be detected - preferentially at the modiolar side of IHCs - across all age groups. In addition, my data indicate that over the transitional period around the onset of hearing, this spatial arrangement remains unchanged. Interestingly, floating ribbon precursors could be predominantly detected on the modiolar side. The lower ribbon density at the pillar side and the fact that only two reconstructed IHCs were analyzed per age group though might have reduced the chance to detect floating ribbon precursors also at the pillar side. Consistent with my random sectioning data, ribbon size slightly increased for both, the pillar and modiolar side during

synaptic maturation, with more and larger ribbons at the modiolar side. This is in line with previous findings of larger ribbons - labeled with a fluorophore-tagged peptide or antibodies - in a study of presynaptic Ca^{2+} influx in murine IHCs (Liberman et al., 2011; Ohn et al., 2016). Together, these results support my random section data and imply that the morphological IHC heterogeneity is already present in immature IHCs before the onset of hearing, and thus partially develops independently of experience with sound intensity. How exactly IHCs interact with SGNs in order to establish the described morphological heterogeneous pattern is still extensively discussed (Koundakjian et al., 2007; Yu and Goodrich, 2014). Signaling between IHCs and SGNs is thought to be essential for normal ribbon formation. For instance, mutant mice that lack the regulator for PSD differentiation (V-maf musculoaponeurotic fibrosarcoma oncogene homolog B; short Mafb), showed disrupted PSDs on an ultrastructural level leading to an impaired SGN response to sound (Yu et al., 2013). In addition, their IHCs exhibited smaller sized ribbons in decreased number, whereas overexpression of Mafb induced faster presynaptic ribbon development.

Functionally, location-dependent release capacity might directly contribute to the observed differences in the firing properties of SGNs. The large modiolar AZs contain more Ca^{2+}-channels, likely enabling high maximal rates of release, but operate at more depolarized potentials (Ohn et al., 2016). In other words, more depolarization is required to elicit transmitter release. Therefore, despite having more Ca^{2+}-channels and SVs, modiolar AZs might release less at resting potentials and during weak stimulation offering a presynaptic hypothesis for the low spontaneous rate, high threshold SGNs. However, upon strong stimulation, their high release capacity will be recruited which, in turn, might cause their importance to hearing in noise (Costalupes et al., 1984; Furman et al., 2013) but with higher vulnerability to degeneration (Schmiedt et al., 1996; Furman et al., 2013). Moreover, larger ribbons on the modiolar side organize more Ca^{2+}-channels (Liberman et al., 2011; Ohn et al., 2016), which may facilitate uncoordinated SV release leading to multiphasic excitatory postsynaptic currents (EPSCs) of SGNs with different amplitudes and shapes. In contrast, the smaller AZs at the pillar side show a more hyperpolarized operating range of presynaptic Ca^{2+} influx, which could explain the high spontaneous rate and low threshold of the postsynaptic SGNs (Ohn et al., 2016). Here, compact AZs might span fewer and more dense glutamate receptors probably causing a more coordinated SV release with monophasic EPSCs. Another hypothesis suggests that the heterogeneity of EPSC amplitudes could be proposed by the uniquantal release model (Chapochnikov et al., 2014). Monophasic EPSCs would be generated due to the instantaneous and complete release of the whole glutamate content of a single SV, while multiphasic EPSCs represent the exocytosis of a single SVs with diverse fusion pore openings and closings also termed as fusion pore flickering (Chapochnikov et al., 2014).

Afferent fibers with multi-ribbon contacts may have the ability to sustain a prolonged high rate of large EPSC events more easily. On the other hand, larger ribbons could be capable to raise glutamate release over a wide range of sound intensities, thus elevating - in association with high sensitivity fibers - the overall dynamic range of the auditory system (Meyer and Moser, 2010). Consequently, I propose that IHCs adjust their AZs with different numbers of Ca^{2+}-channels and ribbons as well as ribbon sizes to diversify neurotransmitter release rates and drive differential intensity encoding of auditory signals (Frank et al., 2009; Ohn et al., 2016). Finally, I unexpectedly

found few SGNs that form multiple synaptic contacts with individual IHCs but also with neighboring IHCs - a phenomenon known from vestibular HCs. In my IHC 3D reconstructions, multiple contacts of a given SGN with ribbonless and ribbon-occupied IHC AZs could be observed, arguing against the assumption that SGNs do not branch and exclusively form a 1:1 relationship with the presynaptic site (Liberman, 1980). These results indicate that SGNs can receive stimulatory input from more than one AZ and offer novel insights into their firing properties. Future studies should establish the prevalence of mono- and multi-synaptic SGN-IHC connectivity.

4.1.3. The molecular architecture of ribbon synapses and precursors

Early after birth, I found in my random sections floating ribbon precursors with a full set of SVs but also dense-core vesicles (DCVs) close to IHC AZs. These DCVs could represent either piccolo-bassoon transport vesicles (PTVs) or DCVs that contain neurotrophins. PTVs, having a dense-core and a size of $\sim$80 nm were characterized at synapses of the central nervous system (Zhai et al., 2001; Shapira et al., 2003; Tao-Cheng, 2007). This kind of DCVs carries a set of presynaptic proteins and is proposed to assemble AZs by fusion with the presynaptic plasma membrane. To understand which type of DCVs is present in IHCs, I performed pre-embedding immunogold labelings against the ribbon specific presynaptic proteins piccolino and RIBEYE. Here, I did not detect piccolino (shorter piccolo variant) or CtBP2 (RIBEYE marker) labeling on DCVs of IHCs. Additionally, the observed DCVs were heterogeneous in size and their average diameter exceeds what has previously been published for PTVs (Zhai et al., 2001; Shapira et al., 2003). Hence, I favor the hypothesis that AZs in IHCs are established via membrane-attachment of floating ribbon precursors independent of PTVs.

Spherical ribbon precursors in photoreceptors are associated with cytomatrix proteins like bassoon, piccolo, RIBEYE and RIM1 (Regus-Leidig et al., 2009). Also in my study I could observe piccolino and CtBP2 labelings on floating ribbon precursors as well as on attached ribbons in IHCs of both, immature and mature age-groups. Thus, floating ribbon precursors might assemble within the cytosol prior to the translocation to the AZ due to the interaction of different proteins. However, the role of piccolino at IHCs is still under debate. At conventional synapses, the scaffolding protein piccolo plays a role in AZ assembly (Gundelfinger et al., 2016), SV trafficking and clustering (Fenster et al., 2000; Mukherjee et al., 2010; Butola et al., 2017) and in the cytoskeletal organization (Kim et al., 2003). At photoreceptors, the ribbon specific piccolino is suggested to be involved in ribbon organization (Limbach et al., 2011; Regus-Leidig et al., 2014) and in the assembly of mature ribbon synapses (Regus-Leidig et al., 2009). Loss of piccolino resulted even in severe morphological abnormalities in the retina implying a delayed and impaired developmental maturation (Regus-Leidig et al., 2014).

In order to elucidate the role of piccolino in IHCs, I further quantified the immunogold labelings at attached ribbon synapses. Interestingly, piccolino was predominantly present on the apical ribbon half throughout the development but distributed also to the base of the ribbon upon maturation. Hence, these data largely extend previous observations from retinal photoreceptors reporting piccolino expression at attached ribbons (Limbach et al., 2011; Regus-Leidig et al., 2013). Because of

an immunogold labeling pattern mostly around the ribbon, it is tempting to speculate that piccolino - besides its role in the structural organization and development of the ribbon (Spiwoks-Becker et al., 2004; Regus-Leidig et al., 2009; Limbach et al., 2011) - could be involved in the tethering of SVs. This hypothesis is supported by the following studies: (i) In conventional synapses, the long piccolo isoform was suggested to play a role in the SV movement (Fenster et al., 2000) due to its interaction with F-actin (Fenster et al., 2003). (ii) Piccolo deficient endbulbs of Held - the central auditory synapses of the cochlear nucleus - were described to have a reduced readily releasable pool (RRP) size of SVs by an impaired SV replenishment (Butola et al., 2017). (iii) Mukherjee et al. (2010) observed less SV clustering in double bassoon/piccolo-deficient synapses of cortical neurons and (iv) Chakrabarti et al. (2018) demonstrated the presence of more filaments at the apical part of IHC ribbon synapses. The distinct piccolino gold particle labeling between immature and mature ribbon synapses together with the observation that mature ribbons reveal more often a translucent center (Stamataki et al., 2006, Section 3.1 in this study) might be indications for a developmental reorganization of the protein composition according to the functional requirements. As discussed above, RIBEYE and piccolino might be potential candidates for such a restructuring of developing synaptic ribbons. Alternatively, Sobkowicz et al. (1982) suggested that the lucent ribbon center might be the evidence for a limited life span of ribbon synapses.

Still, the question arises what is the nature of these DCVs and which role do they play in the presynaptic development of E18-P4 IHCs? Since my measured DCV diameters vary from the characteristic PTV diameters, I assume that these DCVs may contain neurotrophins. Earlier investigations in neurons of the central nervous system could already demonstrate that brain-derived neurotrophic factor (Bdnf) and neurotrophin-3 (Ntf-3) are stored in large DCVs (Wu et al., 2004). In the auditory system, Bdnf was detected in IHCs as well as in outer hair cells (OHCs) until the age of $\sim$P10 and was additionally described in supporting cells at early postnatal ages (P1-P6) (Wiechers et al., 1999; Sugawara et al., 2007; Wan et al., 2014). Similarly, Ntf-3 was found in postnatal and adult cochlear IHCs as well as supporting cells (Fritzsch et al., 1999; Pirvola et al., 1992; Sugawara et al., 2007). Therefore, it is likely that the detected DCVs in this study contain neurotrophins. Nevertheless, experiments utilizing immunogold labelings against Bdnf and Ntf-3 are needed to confirm my hypothesis. In neuronal synapses, neurotrophins play an important role in developmental signaling and they have been reported to be involved in synaptic plasticity (Haubensak et al., 1998; McAllister, 1999; Wu et al., 2004). In the early postnatal organ of Corti, neurotrophic factors are essential to guide neuronal pathfinding and boost SGN survival (Fariñas et al., 1994; Ernfors et al., 1995). The maintenance of SGNs, in turn, has previously been described to be essential for supporting ribbon synapse establishment (Fritzsch et al., 2004; Ramekers et al., 2012; Zuccotti et al., 2012; Wan et al., 2014). In IHCs, Ntf-3 was shown to regulate ribbon synapse density and overexpression of Ntf-3 enabled the regeneration of ribbons after noise trauma (Wan et al., 2014). Suzuki et al. could demonstrate that the treatment with neurotrophins after noise exposure repairs or replaces destroyed ribbon synapses, which supports my theory and reveals an interesting research topic for future experiments (Suzuki et al., 2016).

Identification of DCVs by immunostainings have been demonstrated to be difficult in different kind of tissues (Luo et al., 2001). Hence, very little data exist on the molecular constituents of

DCVs. Labeling efficiency of the antibody, vulnerability to fixation and the overall low concentration of neurotrophins could represent potential reasons for a weak immunoreactivity. Only few studies in conventional synapses could show so far a successful pre-embedding immunogold labeling of Bdnf containing DCVs (Michael et al., 1997; Luo et al., 2001). In hippocampal neurons, synaptotagmin 4 have been shown to be a membrane protein of Bdnf carrying DCVs (Zhang et al., 2009). Therefore, using an antibody against synaptotagmin 4 for future experiments may help to demonstrate the localization of neurotrophins in IHCs.
Furthermore, DCVs - similar to the highly mobile PTVs - were found in close proximity to microtubules (Zhai et al., 2001; Shapira et al., 2003; Fejtova et al., 2009, Section 3.1.6 in this study) indicating a transport mechanism towards the presynaptic plasma membrane. Therefore, I favor the interpretation that DCVs traffic via the cytoskeleton to AZs, where they support synaptic ribbon formation and maintenance. We still do not know, if all DCVs deliver the same set of neurotrophins and how many DCVs are needed in order to assemble the AZ? The observed heterogeneous size could be an indicator for different neurotrophin content, which subsequently implies a putative requirement of variable DCV amounts.

4.1.3.1. Putative intracellular transport mechanism of AZ material

Independent of the analyzed age group, I could at no instance detect floating ribbon precursors in the supranuclear IHC compartment - i.e. where the Golgi apparatus is located - indicating a rather basolateral synthesis in the cytosol. While RIBEYE has previously been shown to self-assemble into aggregates within the cytoplasm via RIBEYE-RIBEYE interactions in multiple cell types (Spiwoks-Becker et al., 2004; Magupalli et al., 2008; Schmitz, 2009; Fuchs et al., 2013), the transport mechanism underlying targeted delivery of native ribbons to the presynaptic AZ remains elusive. In this study, I frequently found microtubules nearby floating ribbon precursors and immature attached ribbons. My data suggest an involvement of a cytoskeletal transport process guiding the floating precursor ribbons to their destination at the presynaptic AZ. This hypothesis is in line with previous biochemical experiments reporting a potential interaction of RIBEYE with actin and tubulin (Uthaiah and Hudspeth, 2010). In neurons of the central nervous system, it is known that synaptic material and precursor SVs are transported by microtubules (kinesin, dynein) or actin filaments (myosin) to establish synaptic terminals and facilitate activity-dependent changes during plasticity (Nakata et al., 1998; Ahmari et al., 2000; Tao-Cheng, 2007; van den Berg and Hoogenraad, 2012). Unfortunately, pre-embedding immunogold labelings for the cytoskeletal filament system using antibodies against tubulin and myosin VI revealed always unspecific stainings in this study. Cross-reactivity but also binding of immunoreagents to unsaturated aldehyde groups could have caused such negative results (Posthuma et al., 1987). Possibilities to improve the labeling efficiency for future experiments represent antibody dilution and changes in duration and/or kind of fixation to increase accessibility. Another option represents the implementation of the post-embedding protocol, which so far failed in my hands. This kind of protocol requires the application of antibodies onto ultrathin sections of the polymerized organ of Corti enabling better preservation of the ultrastructure in contrast to the incubation of the complete tissue before embedding. Immunogold labelings against tubulin, in guinea pig IHCs, depicted a positive stain-

ing with more tubulin labeling in IHCs compared to OHCs (Steyger et al., 1989; Furness et al., 1990). This labeling pattern might present the need for a more activity dependent transport in IHCs. Moreover, myosin VI pre-embedding immunogold labeling in mouse IHCs was additionally found around synaptic ribbons and was shown to be essential for the maturation of synaptic ribbons and their physiological properties (Roux et al., 2009). In conclusion, these findings corroborate the theory of a cytoskeletal transport mechanism that targets floating ribbon precursors and DCVs to the presynaptic membrane, where fusion of ribbon material and fusion of DCVs with the presynaptic membrane causes mature AZ formation. Deletion of myosin VI in IHCs (Roux et al., 2009) might have impaired these transport pathway of ribbon precursors and thus the capability of ribbon fusion stating a reason for morphologically immature ribbons in adult mice. Future studies in cochlear IHCs will have to test the cytoskeletal-based transport hypothesis in more detail and if it plays a role in the regulation of ribbon volume even after AZ maturation.

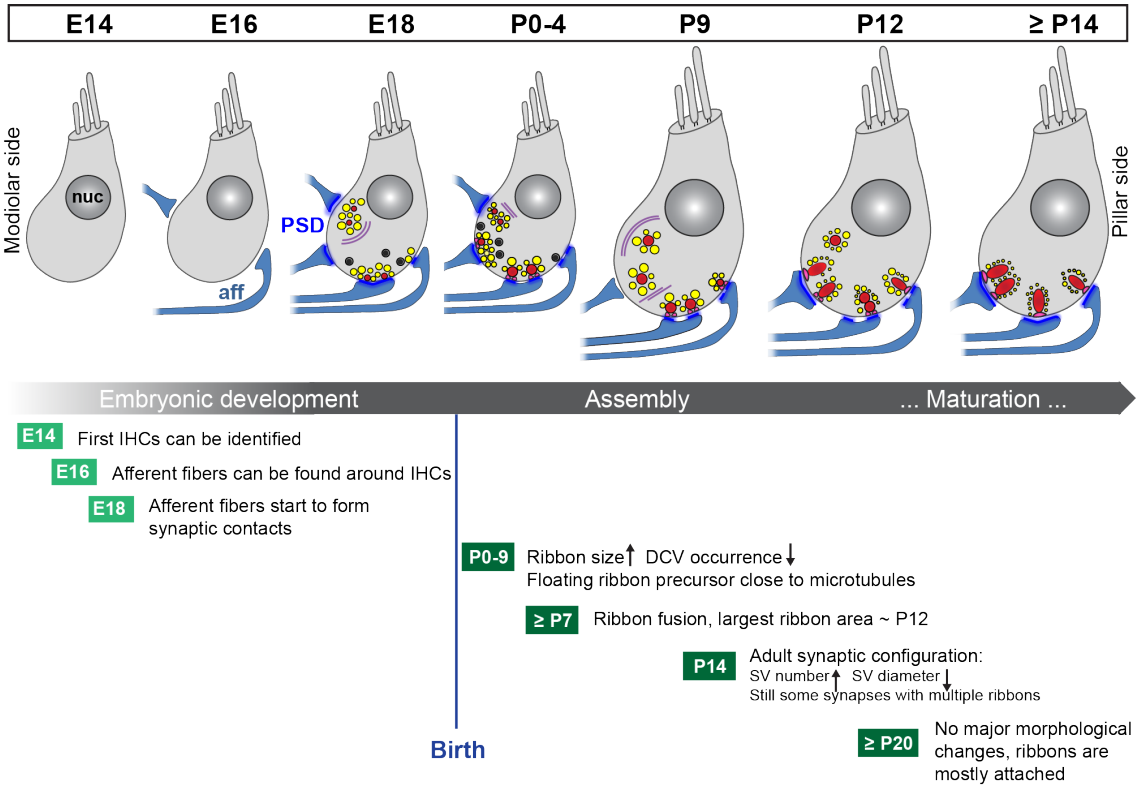

Figure 4.1.: Schematic summary of the key findings observed during developmental maturation and transition from pre-hearing to hearing in murine cochlear IHCs. Nuc: nucleus, aff: afferent fiber, PSD: postsynaptic density, light grey: IHCs, red: ribbon synapses, yellow: synaptic vesicles (SVs), magenta: presynaptic density, purple lines: microtubules, black: dense-core vesicles (DCVs).

4.2. Ultrastructure of cochlear IHC synapses in the absence of RIBEYE

As discussed in the previous section, is the protein RIBEYE an integral part of the synaptic ribbon. Ribbon synapse development likely involves fusion of ribbon material putative due to RIBEYE-RIBEYE interaction. In this part of the thesis, I focused on the structural organization of murine IHC synapses lacking the main component of the ribbon, RIBEYE. Ribbon synapses of mature RIBEYE knockout mice ($RBE^{KO/KO}$) were compared to synapses of heterozygous and control littermates ($RBE^{WT/KO}$ and $RBE^{WT/WT}$) using transmission electron microscopy on random ultrathin sections and serial sections. This section is partially based on the publication "The synaptic ribbon is critical for sound encoding at high rates and with temporal precision" (Jean, Lopez de la Morena, Michanski, Jaíme Tobón et al., 2018, elife).

4.2.1. Conventional-like synapses in $RBE^{KO/KO}$ IHCs

RIBEYE consists of two domains, a ribbon specific A domain and a B domain that compose the transcriptional repressor CtBP2 and possess binding sites for NADH (Schmitz et al., 2000). The connection between RIBEYE A and B domain induces further possible interactions of the B domain with other presynaptic components (Schmitz et al., 2000). Previous studies proposed RIBEYE as the key organizer of the ribbon whose functional role is still under debate (Schmitz et al., 2000; Magupalli et al., 2008; Schmitz, 2009; Maxeiner et al., 2016).

In this project, 3 weeks old knockout mice of the RIBEYE-specific A domain were investigated (Maxeiner et al., 2016) in order to elucidate its role in IHC synapse formation. Consistent with findings of the $RBE^{KO/KO}$ mouse in the retina (Maxeiner et al., 2016) and a companion study in IHCs published back to back with Jean et al. (2018) (Becker et al., 2018), my electron microscopic observations revealed that IHC synapses of $RBE^{KO/KO}$ mice completely lack the typical ribbon structure. Instead I found only roundish presynaptic densities (PDs) with a length of $\sim$130 nm, which is comparable to $RBE^{WT/WT}$. Interestingly, synapses of $RBE^{KO/KO}$ IHCs exhibited a multi-AZ arrangement by clustering SVs to multiple PDs - a feature resembling conventional synapses. In contrast to neuromast HCs of *ribeye* zebrafish mutants (Lv et al., 2016), I did not detect synapses with a ribbon-like but non-electron-dense structure harboring SVs around. These so-called "ghost ribbons" were smaller in size but exhibited the same shape as normal synaptic ribbons. However, residual RIBEYE putatively along with other scaffold proteins like piccolino might have caused such electron-translucent structures in the incomplete knockout in zebrafish (Lv et al., 2016).

3D models from serial sections regularly detected several PDs per synaptic contact forming AZ clusters. This was supported by tangential cuts from random sections through the presynapse that exhibited a maximum of 6 individual AZs. The frequent occurrence of multi-AZs in IHCs could be a sign for immaturity (Sobkowicz et al., 1982; Sendin et al., 2007; Huang et al., 2012; Wong et al., 2014, see Section 3.1.2 in this study). However, also in 6 weeks and 8 months old $RBE^{KO/KO}$ mice I could detect the same morphological phenotype arguing against a developmental delay. In addition to this, single highly regular PDs in $RBE^{KO/KO}$ IHCs differ from the immature PDs

with their characteristically two rootlets (Sobkowicz et al., 1982; Wong et al., 2014, see Section 3.1.2 in this study). The comparable large though not stripe-like, and continuous PSDs between $RBE^{WT/WT}$ and $RBE^{KO/KO}$ IHCs provided further evidence for the mature stage of IHC synapses of $RBE^{KO/KO}$ mice, because developing IHCs show rather several, partially interrupted smaller sized PSD appositions (Wong et al., 2014, see Section 3.1.3 in this study).
Comparison of SVs demonstrated a normal SV size but significantly fewer SVs at the individual $RBE^{KO/KO}$ AZs in comparison to $RBE^{WT/KO}$ and $RBE^{WT/KO}$ AZs. In agreement with Maxeiner et al. (2016) and Becker et al. (2018), such a reduction in number is most likely the result of the ribbon loss providing less available space for SV tethering. Surprisingly, due to the multi-AZ organization, each synaptic contact possesses comparable amounts of SVs as at ribbon-occupied wild-type synapses. Therefore, the multi-AZ arrangement might represent a mechanism to compensate for the RIBEYE deletion. Concentrating on the fraction of membrane-proximal (MP) and PD associated SVs (PDA-SVs) relative to the total SV number per random section, demonstrated that MP-SVs represent approximately one third of the total SV pool. The remaining ones belong to the category of PD associated SVs (PDA-SVs). PDA-SVs could potentially replenish the release sites once MP-SVs fused and consequently ribbonless PDs might function in a similar way as what is proposed for conventional AZs (Siksou et al., 2007; Fernăndez-Busnadiego et al., 2013; Cole et al., 2016). To sum up, the present result from $RBE^{KO/KO}$ mice confirm the essential role of RIBEYE in establishing synaptic ribbons and give further insights into the ribbon function.

4.2.2. What is the ribbon needed for?

Synaptic ribbons have been implicated to act as: (i) a structural organizer of the AZ (Schmitz et al., 2000; Khimich et al., 2005; Magupalli et al., 2008; Wong et al., 2014; Maxeiner et al., 2016); (ii) a conveyer to provide SVs for sustained release (von Gersdorff et al., 1996; Muresan et al., 1999; Lenzi et al., 2002; Frank et al., 2010; Snellman et al., 2011; Safieddine et al., 2012; Graydon et al., 2014; Maxeiner et al., 2016); and (iii) a Ca^{2+}-channel organizer (Khimich et al., 2005; Frank et al., 2010; Wong et al., 2014). The complete loss of IHC ribbons resulted in reduced spontaneous and sound-evoked SGN firing, which is indicative for an impairment sound encoding at ribbonless IHC-SGN synapses of $RBE^{KO/KO}$ mice (Jean et al., 2018; Becker et al., 2018). In line with this, damaging ribbon synapses in the mouse retina by using photodamage almost abolishes neurotransmitter release (Snellman et al., 2011). The authors observed that photolytically inactivated synaptic ribbons release only a single complement of the RRP SVs, which was already prepared for release but the replenishment of this pool is disrupted. As a consequence, both the fast and sustained components of neurotransmitter release were impaired for all following stimuli. Here, Snellman et al. (2011) proposed a role of synaptic ribbons in fast and slow signaling and in addition to its role in organizing SVs, ribbons are presumed to also prime SVs for exocytosis at AZs. Further studies of RIBEYE knockdown in the zebrafish of developing HCs resulted in a loss of Ca^{2+}-channel clusters and hence reduces the firing rate of SGNs (Sheets et al., 2011). Overexpression of RIBEYE, on the other side, colocalized Ca^{2+}-channels with ectopic aggregates of RIBEYE suggesting a crucial role of RIBEYE in the clustering of Ca^{2+}-channels during synaptogenesis (Sheets et al., 2011). RIBEYE knockout data in the retina agree with this

hypothesis because of mislocalized Ca^{2+}-channels that impair the coupling between Ca^{2+} influx and vesicular release (Maxeiner et al., 2016).

Interestingly, the multi-AZ arrangement in $RBE^{KO/KO}$ IHCs might involve the tethering of more SVs to reduce the impairment of sound encoding. It is tempting to speculate that bassoon, the major component of the PD, might be an interesting candidate for this role. The disruption of bassoon in IHCs revealed mostly synapses lacking anchored ribbons and increased the proportion of floating ribbons (Khimich et al., 2005; Frank et al., 2010; Jing et al., 2013). Compared to bassoon deficient IHCs (Khimich et al., 2005; Frank et al., 2010; Jing et al., 2013), Ca^{2+}-channels were not reduced in $RBE^{KO/KO}$ IHCs and the exocytic membrane capacitance (C_m) changes were only mildly reduced for weak depolarizations (Jean et al., 2018). Exocytic C_m changes were unchanged for strong depolarizations, whereas in the bassoon mutant, the fast and sustained exocytosis was significantly reduced (Frank et al., 2010). The decline in Ca^{2+}-channels as well as reduced Ca^{2+}-currents indicate an important role of bassoon in the spatial organization of Ca^{2+}-channels (Khimich et al., 2005; Frank et al., 2010; Jing et al., 2013). $RBE^{KO/KO}$ IHCs depicted more frequently small and round Ca^{2+}-channels forming several clusters per synaptic contact, whereas the size and number of SVs per synaptic contact were unchanged (Jean et al., 2018). Furthermore, the colocalization of bassoon and Ca^{2+}-channels in STED (stimulated emission depletion) microscopy immunofluorescence stainings (Jean et al., 2018) supported the hypothesis that bassoon might play a role in positioning Ca^{2+}-channels in $RBE^{KO/KO}$ IHCs to provide normal vesicular release. Immunohistochemical stainings additionally demonstrated a loss of piccolino fluorescence (the ribbon specific short splice variant of piccolo) in the presynapse of $RBE^{KO/KO}$ IHCs (Jean et al., 2018). Thus, the possibility of a piccolino based compensatory mechanism can be ruled out. Nevertheless, also other proteins like otoferlin, the scaffolding protein RIM2 or the RIM-binding protein could be involved in this process due to potential interaction with bassoon. This can be corroborated by the localization of the RIM-binding protein 2 and RIM2 at the base of the ribbon indicating that they might be a part of the bassoon-positive PD (Jung et al., 2015b; Krinner et al., 2017). The reason behind the striking difference in C_m measurements of bassoon mutants could be the concomitant impairment of the synaptic ribbon and the presynaptic density preventing most likely a functional compensation to such an extent as in $RBE^{KO/KO}$.
Further functional analysis of $RBE^{KO/KO}$ IHCs exhibited a reduced SV replenishment and a small depolarized shift of Ca^{2+}-channel activation, resulting in the observed reduced spontaneous and evoked firing rates as well as in the elevated thresholds of $RBE^{KO/KO}$ SGNs (Jean et al., 2018).
In conclusion, these data corroborate the role of ribbon synapses in maintaining large SV numbers, in SV replenishment and in Ca^{2+}-channel organization and regulation (Jean et al., 2018; Becker et al., 2018). Whereby, other AZ proteins might have the ability to partially take over some functional parts of the ribbon, making it difficult to unravel the true synaptic ribbon function.

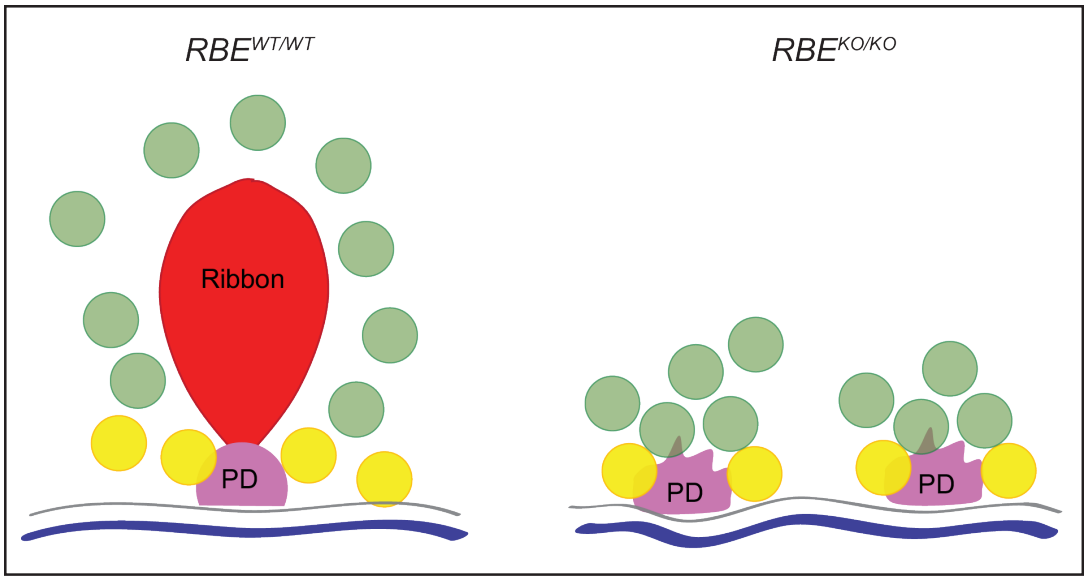

Figure 4.2.: Illustration of morphological distinctions between wild-type and RIBEYE knockout IHC AZs. PD: presynaptic density, yellow: membrane-proximal SVs, green PD associated SVs, grey: presynaptic membrane, blue: postsynaptic density.

4.3. Morphological changes of utricular HC ribbon synapses during postnatal development

The vestibular system is localized in the inner ear, where it detects head motions and along with sensory inputs from the visual system and proprioreceptors maintains the sense of balance. Like cochlear IHCs, vestibular HCs transduce their stereocilia displacements into receptor potentials. Vestibular HCs are categorized into two distinct types: type I and type II cells, which are defined by the differences in the afferent innervation characteristics. While one or more type I HCs are engulfed by a large calyx-shaped afferent terminal, type II HCs make synaptic contacts with multiple bouton-like afferent terminals (Wersall, 1956). Behavioral experiments testing the presence of balance required reflexes in rodents propose that the vestibular system is mature around P16 (Schönfelder and Schwartze, 1970; Hård and Larsson, 1975).
The human balance deteriorates with aging, which results in a postural instability (Konrad et al., 1999; Abrahamova and Hlavačka, 2008). To address the underlying reasons, I examined developmental changes of murine vestibular AZs by concentrating on the utricle, which is responsible for linear acceleration and horizontal head movements. This project aimed to analyze the so far mainly unknown morphological characteristics of type I and type II utricular HC ribbon synapses and their associated SVs in terms of number, size and localization upon maturation. In order to identify possible variations between type I and type II cells as well as between utricular and cochlear HCs, electron microscopy on random ultrathin sections combined with electron tomography were utilized at immature and mature ages. Finally, to test also for potential differences in the protein composition between utricular and cochlear HCs, pre-embedding immunogold labelings were performed for the well-known scaffolding proteins of cochlear IHC synaptic ribbons - RIBEYE and piccolo/piccolino.

4.3.1. Membrane-attached utricular HC synaptic ribbons show only mild developmental changes

As explicitly described in Section 3.1, cochlear IHC AZs undergo a morphological change from often containing multiple small synaptic ribbons per synapse to fewer but larger ribbons with more smaller SVs in mature mice. My analysis of random section data from utricles revealed that also immature utricular HCs possess membrane-attached multi-ribbon synaptic contacts, which decline in number after P15 to form mainly a single ribbon per synapse. However, this phenomenon in utricular HCs is less pronounced compared to cochlear IHCs. Interestingly, the ribbon size stays unaltered in type I and type II cells of the utricle. Thus, it is not surprising that similar amounts of SVs were observed at all ages. Nevertheless, the SV diameter significantly increases from P9 to P15 utricular HCs and similar to cochlear IHCs decreases afterwards. Similar to what was already discussed in Section 4.1.1, a potential reason for such a change in SV size during development could represent the maturation of SV reformation. In cochlear IHCs, otoferlin was reported to be important for the replenishment of SVs and the regulation of their sizes (Strenzke et al., 2016). Differences in otoferlin expression over IHC development implies that the process of SV reformation undergoes a maturational change possibly causing distinct SV sizes. In otoferlin knockout

utricular HCs, the existence of another potential Ca^{2+} sensor was implied besides to otoferlin (Dulon et al., 2009). Because of this, I speculate that the abundance of otoferlin in utricular HCs might increase or decrease depending on the developmental stage and HC type, which might influence SV diameters. Next to developmental changes in the protein abundance or composition also changes in the neurotransmitter amount may demonstrate a substantiated explanation (for more detailed descriptions see Section 4.1.1). Murine neuromuscular synapses with a 70 % reduced expression of the vesicular acetylcholine transporter showed smaller SVs, which were flat in shape (Rodrigues et al., 2013). The same ultrastructural result could be observed with a pharmacological blocking of acetylcholine uptake in wild-type mice suggesting that the transmitter amount and protein levels of vesicular neurotransmitter transporter regulate the appearance of SVs (Rodrigues et al., 2013). Therefore, immature utricular HCs may require more neurotransmitter to activate the vestibular system compared to matured HCs as explicitly discussed above for cochlear IHCs.
In conclusion, the relatively minor structural changes of membrane-attached synaptic ribbons and corresponding SVs in type I and type II HCs contradict what has been found in the cochlea and present an unexpected difference. HCs in the utricle might undergo another kind of developmental reorganization, which will be further discussed in the following sections.

4.3.2. Mature type I utricular HCs form floating ribbon clusters

One important finding was the enhanced occurrence of floating ribbons in both utricular HC types even in 11 months old HCs. After the age of P15 nearly all detected ribbons in type I cells were floating. This observation stands in striking contrast to cochlear IHCs, where the number of floating ribbons reduces in older animals until they are all attached to the IHC membrane. The appearance of floating ribbons in type II cells remains constant at all investigated ages. With a floating ribbon proportion of approximately 30 %, type II utricular HCs also exceed what has been found in cochlear IHCs (see Section 3.1.4). Measurements of the floating ribbon distance to the membrane though revealed no particular developmental trend. Moreover, floating ribbons in the utricle accumulate to form clusters. In type I HCs, the amount of floating ribbons per cluster increases continuously upon maturation, whereas in type II HCs a decrease was detected.
The reasons for such ribbon cluster perhaps lie in the regeneration capability of type II HCs (Burns and Stone, 2017). Non-attached ribbons could be a sign of the immature stage of the newly formed type II cells as known from cochlear IHCs (Wong et al., 2014, see Section 3.1.4). But this could not explain the floating ribbons in type I utricular HCs, as these do not regenerate (Burns and Stone, 2017), possibly also a reason why the sense of balance deteriorates so fast with aging. Here, spatial differences might cause the morphological findings. The utricle consists of a central (striolar) and a peripheral (extrastriolar) region. While in the striolar zone more type I than type II cells are present, both types of HCs are equally present in the extrastriolar (Lindeman, 1969; Eatock and Lysakowski, 2006). Thus, depending on the region of the utricle ribbon features might vary as well. Another hypothesis for increased floating ribbons might be a developmental reorganization or even loss of AZ components. For instance, deletion of bassoon (the main component of the presynaptic density) in the retina and cochlea resulted in ribbons lacking any attachment to the AZ membrane (Dick et al., 2003; Khimich et al., 2005). Electron micrographs of random sections

from photoreceptors exhibited a similar cluster formation of floating ribbons as detected in the utricle (Dick et al., 2003). Another reason could be the morphology of the calyx enclosing type I HCs. Due to this structure, the postsynapse receives sensory input from several AZs and in case of dimorphic afferents, even from two or three cells. In contrast, the afferent bouton contact at type II HCs receives input mainly from a single ribbon. Thus, ribbon-occupied synapses might be more required in type II utricular HCs to facilitate synaptic transmission by a large pool of SVs at each AZ. Moreover, synaptic ribbons could develop to floating ones due to a secondary detachment from the AZs. As described above (Section 4.1.1.1), the detachment of ribbon material in the visual system is correlated with illumination (Spiwoks-Becker et al., 2004; Regus-Leidig et al., 2010; Fuchs et al., 2013). Similar to my observations in the utricle, pinealocytes from guinea pigs under constant light exposure demonstrate a formation of ribbon clusters (Jastrow et al., 2004). It is known that different light/darkness conditions influence the functional state of the pineal gland where light has an inhibitory impact on activity (Kappers, 1976). Electron microscopic images revealed that the constant illumination caused irregular ribbon shapes of spheres or plates that accumulated to ribbon clusters (Jastrow et al., 2004). According to this, synaptic activity is essential for ribbon maintenance in pinealocytes. Hence, a potential dynamic process in type I utricular HCs could cause the establishment of floating ribbon clusters. In this scenario, activity dependent synaptic modifications could represent a mechanism of plasticity in order to provide adaptation to changes in the equilibrium. The ribbon cluster may function as a reservoir of ribbons waiting to be recruited to the plasma membrane until they are required.

The presence of the largest floating ribbon clusters in the 11 months old utricle suggests rather a continuous detachment - maybe by constant ribbon material replacement - than a degradation process. On the other hand, ribbon synapses in cochlear OHCs are described to diminish during maturation due to the retraction of afferent fibers (Spoendlin, 1972; Sobkowicz et al., 1986; Simmons and Liberman, 1988). So far, no raise in the number of floating ribbons were described in mature OHCs indicating the ability of at least some HC types to degrade ribbon material. Due to the small sample size in this study, more data are needed in order to figure out the role of increasing floating ribbon clusters in type I HCs.

Ultrastructural studies from Ross (1993, 2000) support this assumption for the adult rat vestibular system. Here, rats were flown in a space shuttle and utricles were processed shortly after landing. Intriguingly, flight animals displayed an increase between 41 % (type I) and 55 % (type II) in ribbon density. Detection of ribbon clusters let Ross also come to the conclusion that utricular HCs are adaptive to changes, which would clarify the ability of astronauts to quickly recover from vestibular problems after space flights (Hallgren et al., 2016). However, it has to be taken into consideration that floating ribbon clusters were only found in type II utricular HCs contradicting my developmental study, where they are predominantly present in type I utricular HCs. Ross (1993) proposes that ribbon clusters develop by forming new ribbons in close proximity to already existing ones and that the accumulation of synapses enhances the total SV pool size, which might improve the probability of neurotransmitter release (Ross, 1993). Nonetheless, it does not explain the reduction in the membrane-attached synaptic ribbons. HC type specific differences between the present and Ross' study could be the result of variations in the examined species, its age and

environmental conditions. The effect of microgravity on the vestibular system still needs further investigations to decipher its exact impact on the HC morphology.

4.3.3. 3D reconstructions confirm the presence of floating ribbon clusters and visualize the ribbon shape

It is well described that C57BL/6J mice undergo an age-dependent, progressive decline in hearing function (Henry and Chole, 1980; Shnerson et al., 1981; Willott, 1986; Li and Borg, 1991; White et al., 2000; Hequembourg and Liberman, 2001; Ison and Allen, 2003). To ensure that the vestibular system is not affected by this impairment, another wild-type strain was investigated. The CBA wild-type mouse exhibits no significant changes in the auditory anatomy and function until the end of its average span of life (Willott, 1986; Willott et al., 1988, 988a; Shone et al., 1991; Li and Borg, 1991; Walton et al., 1995; Spongr et al., 1997). Tomograms from CBA IHCs as well as serial sections from a differently processed utricle ruled out the possibility of genetical and methodical reasons that could influence the HC ultrastructure. 3D reconstructions of type I utricular HCs showed elongated disc-like shaped ribbons, a shape rather known from retinal photoreceptors and bipolar cells (Sterling and Matthews, 2005; Matthews and Fuchs, 2010; Wichmann and Moser, 2015). In IHCs, abnormally thin and elongated ribbon synapses can be found in mutant mice of the vesicular glutamate transporter 3 (Vglut3). Essential for loading SVs with glutamate, its absence is associated with deafness due to the lack of glutamate release (Seal et al., 2008).

Similar to IHC synaptic ribbons, functional differences in the utricle could be related to the observed ultrastructural variations and developmental alterations. For instance, ribbon synapse localization, ribbon number or HC position within the utricle could partially lead to the described different exocytosis rates (Dulon et al., 2009), K^+ conductance (Rusch and Eatock, 1996; Rüsch et al., 1998; Frank et al., 2009) or firing pattern (Eatock and Songer, 2011) between type I and type II HCs but also between cochlear and utricular HCs. Baird et al. (1988) reported only a threefold more powerful HC input onto the calyx (Baird et al., 1988). They are suggesting a weaker transmission at type I ribbon synapses reducing the gain, which may serve to expand the stimulus range at calyx afferents because they will not saturate at large velocities of head motions. Importantly, type I saccular HCs lose gain during rat development (Songer and Eatock, 2013). Increased floating ribbon clusters over maturation acting potentially as a temporary deposit would support Baird's hypothesis.

Functional differences were also described in terms of the region in the frog utricle, where the central striolar zone facilitates high frequency-signaling (Baird, 1994a,b, reviewed in Eatock and Lysakowski, 2006). Here, the large transduction and conductance reduce the membrane time constant (the product of the membrane resistance and membrane capacitance) possibly enhancing signal transmission (reviewed in Eatock and Lysakowski, 2006). Morphological characteristics of large synaptic contacts and calyceal afferent fiber diameters facilitate fast signaling (reviewed in Eatock and Lysakowski, 2006). In agreement with the present observations of this study, immunohistochemical stainings in the rat crista ampullaris (located in the ampullae of semicircular canals to sense head rotation) revealed that synaptic ribbons and postsynaptic glutamate receptor appositions are frequently not juxtaposed in type I HCs (Sadeghi et al., 2014). Postsynaptic membrane

potentials and calyx AP firing rates, furthermore, show evidence for glutamate accumulation and spillover leading to a slow depolarization of the postsynapse (Sadeghi et al., 2014). This result might explain the high frequency-signaling with highly irregular spiking and phase locking of type I HC afferents (Sadeghi et al., 2007, 2014). Such a spillover at high frequencies has also been reported in the hippocampus, where increased glutamate concentrations in the synaptic cleft can remain for hundreds of milliseconds (Hires et al., 2008). Aggregations of floating ribbons provide an immense SV pool that may supply the glutamate content required for a spillover.

I propose two opportunities for the increased occurrence of ribbon clusters with age: either it has a regional background or developmental processes cause the accumulation of floating ribbons to ensure mature synaptic transmission. Utricle processing so far made it impossible to distinguish between the striolar and extrastriolar zone. Thus, the investigated regions within the utricle might differ for each animal, wherefore we have to be careful with interpretations favoring a developmental origin solely. Studies stating a different developmental time course of the two utricular zones (Sans and Chat, 1982; Rüsch et al., 1998) and the ability of type II HCs to regenerate (Burns and Stone, 2017; Bucks et al., 2017) corroborate my consideration about the uncertain developmental stage of HCs present in adult utricles.

4.3.4. RIBEYE and piccolino are structural components of utricular HC ribbon synapses

The molecular physiology of the vestibular HC synapse has so far remained fundamentally unknown. To gain insight into their molecular anatomy, I investigated the expression of two known scaffolding proteins from cochlear IHCs using pre-embedding immunogold labelings combined with transmission electron microscopy. Mice at the age of P14 and P15 proved the presence of RIBEYE (the central ribbon protein) and piccolino (the ribbon specific piccolo variant) in the utricle. Gold particles demonstrated their localization on floating ribbons as well as on attached ribbons in both HC types. The examined staining patterns for RIBEYE and piccolino are similar to immunogold labelings of IHC ribbon synapses indicating a comparable protein position for these two scaffolding proteins. However, indications for a distinct AZ composition exist. The loss of $Ca_v1.3$ channels leads to deafness, but no vestibular impairments have been described (Dou et al., 2004). Hence, vestibular HCs are proposed to additionally possess the T-type Ca^{2+}-channel $Ca_v3.1$ (Nie et al., 2008). No vestibular defects were also reported for the loss of Vglut3 suggesting the presence of other vesicular glutamate transporters (Seal et al., 2008). Immunohistochemical stainings in rat vestibular HCs, provide evidence for the expression of Vglut1 by colocalization of Vglut1 with Vglut3 (Zhang et al., 2011), whereas in the mouse a ring-like Vglut1 and Vglut2 staining was observed at the necks of HCs.

Further investigations comparing neonatal with mature mice might reveal how developmental changes influence the molecular composition of utricular HC synapses. Moreover, stainings against other proteins of the exocytosis machinery could help to understand the accumulation of floating ribbons in adult type I utricular hair cells. The next most interesting candidate would be the major component of the synaptic ribbon anchor, bassoon (Khimich et al., 2005; Frank et al., 2010; Wong et al., 2014). It would be interesting to see, if bassoon disappears with the rise of

floating ribbons or if bassoon remains as an integral part of ribbon clusters to facilitate ribbon attachment at any time.

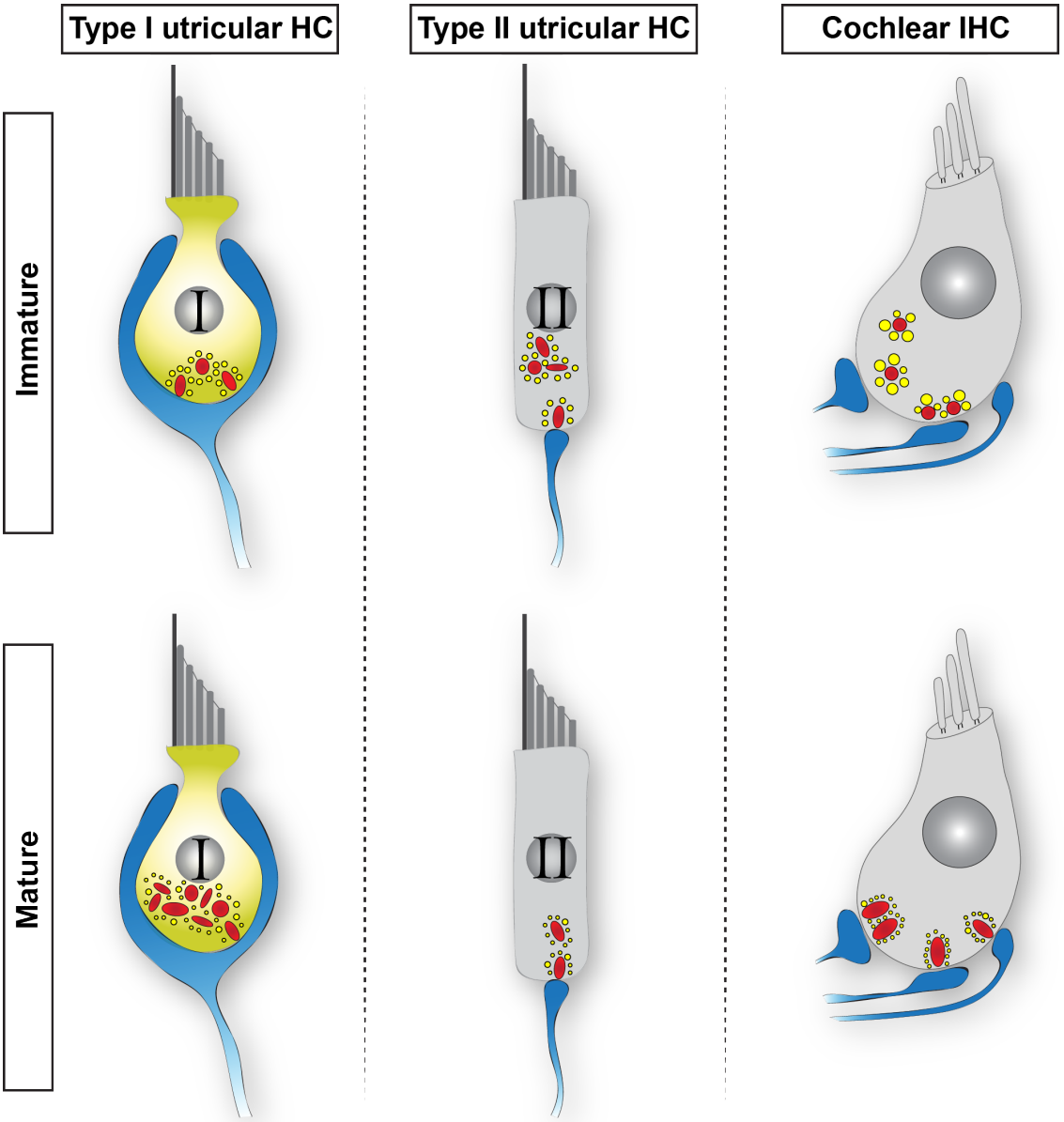

Figure 4.3.: Schematic representation of the main differences between utricular and cochlear HCs upon maturation. Blue: afferent innervation, red: ribbon synapses, yellow: synaptic vesicles (SVs), magenta: presynaptic density

5. Conclusion and outlook

In this thesis, I reported how ribbon synapses mature during development by investigating ascending ages of two organs of the inner ear. Ultrastructural data from cochlear IHCs (responsible for auditory signal transmission) and utricular HCs (mediating the sense of balance) reveal indications for a functional ribbon synapse plasticity.

Remarkably, I found first evidence of ribbon-ribbon fusion events in developing IHCs. This discovery elucidates how several small ribbons establish the final mature - predominantly single and larger sized - synaptic ribbon with increased capability of SV tethering. In contrast, a putative secondary detachment of ribbons in utricular HCs might lead to floating ribbon clusters. As previously shown for photoreceptors (Regus-Leidig et al., 2009; Spiwoks-Becker et al., 2004), these results might represent mechanisms to lose or gain AZ material in correlation to the functional need. Moreover, clear hints for a neurotrophin-based AZ assembly was detected in form of dense-core vesicles in pre-hearing cochlear IHCs that were found in close proximity to developing AZs. To figure out the proteinaceous composition of these dense-core vesicles, more immunogold labelings using different protocols should be performed. Additional ultrastructural investigations of IHCs that lack the expression of neurotrophins throughout their development might clarify if neurotrophins are at all involved in AZ formation. Furthermore, my cochlear IHC data highlight a possible microtubule based trafficking pathway of dense-core vesicles as well as floating ribbon precursors.

In the last few years, immense progress has been made in apprehending how ribbon-type synapses functionally develop. However, the picture of how molecular mechanisms control such developmental processes and in particular ribbon assembly in cochlear and utricular HCs is still far from complete. Until now we do not understand which signals trigger the anchorage of ribbons along with the PSD assembly and how the ribbon size as well as the highly variable ribbon shape is determined. Further, questions like: (i) how fast and how much synaptic material is being transported via floating ribbon precursors to the AZ; and (ii) how are they coordinated depending on the pillar-modiolar gradient requires more experimental data. Future work, which takes activity dependent block-wise addition/removal of ribbon material into account, will need to be carried out by performing for instance live-cell confocal imaging or time-lapse stimulated emission depletion (STED) imaging of fluorescently-labeled ribbons and cytoskeletal filaments. Pharmacological blocking of microtubule polymerization would present another promising topic to identify the intracellular transport pathway in IHCs and explore if microtubule inhibition causes precursor ribbons to remain floating. But also an optogenetic approach could serve as a base for future studies by using a precise optical stimulation of IHCs at different ages followed by rapid high-pressure freezing of the organ of Corti. Thus, the fast stimulation and immediate near to native

state of structural preservation allows to capture dynamic processes within milliseconds. Regarding the heterogeneity of IHCs, further tests focusing on multiple afferent and efferent contacts on cochlear IHCs might help to gain new knowledge about the distinct neuron firing properties. It would be interesting to analyze for example their respective fiber diameter and mitochondria content in 3D. In order to corroborate the hypothesis that piccolino - the only expressed piccolo isoform in IHCs - is involved in SV tethering, it would be interesting to quantify piccolo knockout rats (available in the lab of Prof. Dr. Craig Garner; generated by F. Kent Hamra), affecting also the short piccolino isoform, on an ultrastructural level.

Maturation of utricular HCs differs in many aspects from cochlear IHCs. Although the utricle results are encouraging, they should be validated by a larger sample size. To figure out the role of floating ribbon clusters in adult type I utricular HCs, future studies should first target the two different zones (striolar and extrastriolar zone) of the utricle for morphological distinctions. Secondly, the examination of the presence and localization of the protein bassoon (major component of the presynaptic density) by using immunohistochemistry and immunogold labelings in different ages might give new insights into the increase of floating ribbon numbers in type I HCs with increased age. Is bassoon degraded or can it still be found on AZs or on floating ribbons? Further experiments will also look into plasticity related structural changes by comparing utricular HCs of adult mice that were raised in a standard cage with mice that experienced an enriched environment. In an enriched environment, mice are able to move more extensively compared to standard laboratory conditions, which induces plasticity by increased neural activity (Praag et al., 2000). Thus, it can be investigated if features of the AZ can be influenced by adaptations to changes in the activity. Additionally, ultrastructural investigations of mutant mice with a significant vestibular dysfunction like the usher syndrome mouse model should be performed in the future focusing on the localization and appearance of ribbon synapses in utricular HCs.

Moreover, I addressed the role of synaptic ribbons in cochlear IHCs by examining ultrastructural consequences of RIBEYE deletion, the main ribbon constituent. I found a complete loss of synaptic ribbons but multiple ribbonless AZs per synapse tethering vesicles to the presynaptic density seem to present a compensatory mechanism for this loss. Therefore, it raises the questions which additional proteins are needed to facilitate proper synapse function and enable such a compensation in mature RIBEYE knockout mice. Here, double knockout experiments of bassoon and RIBEYE but also a developmental characterization of RIBEYE knockout IHCs represent a promising future research.

In conclusion, a detailed developmental map of cochlear and utricular ribbon synapse synaptogenesis was created providing the framework for a better understanding of the functional role of ribbon-type synapses and serve as a substantial basis for future studies. Novel knowledge about fundamental developmental events like ribbon synapse assembly and transport as well as ribbon dynamics and its heterogeneity within a single IHC represent important information in terms of hearing or balance related problems, also in humans.

Bibliography

Abrahamova, D. and F. Hlavačka

2008. Age-related changes of human balance during quiet stance. *Physiological Research*, 57(6).

Ahmari, S. E., J. Buchanan, and S. J. Smith

2000. Assembly of presynaptic active zones from cytoplasmic transport packets. *Nature Neuroscience*, 3(5):445–451.

Alberts, J. L., M. Saling, and G. E. Stelmach

2002. Alterations in transport path differentially affect temporal and spatial movement parameters. *Experimental Brain Research*, 143(4):417–425.

Altrock, W. D., S. tom Dieck, M. Sokolov, A. C. Meyer, A. Sigler, C. Brakebusch, R. Fässler, K. Richter, T. M. Boeckers, H. Potschka, C. Brandt, W. Löscher, D. Grimberg, T. Dresbach, A. Hempelmann, H. Hassan, D. Balschun, J. U. Frey, J. H. Brandstätter, C. C. Garner, C. Rosenmund, and E. D. Gundelfinger

2003. Functional inactivation of a fraction of excitatory synapses in mice deficient for the active zone protein bassoon. *Neuron*, 37(5):787–800.

Appler, J. M. and L. V. Goodrich

2011. Connecting the ear to the brain: Molecular mechanisms of auditory circuit assembly. *Progress in Neurobiology*, 93(4):488–508.

Ashmore, J.

2008. Cochlear Outer Hair Cell Motility. *Physiological Reviews*, 88(1):173–210.

Baird, R. A.

1994a. Comparative transduction mechanisms of hair cells in the bullfrog utriculus. i. responses to intracellular current. *Journal of Neurophysiology*, 71(2):666–684. PMID: 7909840.

Baird, R. A.

1994b. Comparative transduction mechanisms of hair cells in the bullfrog utriculus. ii. sensitivity and response dynamics to hair bundle displacement. *Journal of Neurophysiology*, 71(2):685–705. PMID: 7909841.

Baird, R. A., G. Desmadryl, C. Fernandez, and J. M. Goldberg

1988. The vestibular nerve of the chinchilla. ii. relation between afferent response properties and peripheral innervation patterns in the semicircular canals. *Journal of Neurophysiology*, 60(1):182–203. PMID: 3404216.

Balkema, G. W., K. Cusick, and T.-H. Nguyen
2001. Diurnal variation in synaptic ribbon length and visual threshold. *Visual Neuroscience*, 18(5):789–797.

Bao, H., W. H. Wong, J. M. Goldberg, and R. A. Eatock
2003. Voltage-Gated Calcium Channel Currents in Type I and Type II Hair Cells Isolated From the Rat Crista. *Journal of Neurophysiology*, 90(1):155–164.

Bartoletti, T. M., S. L. Jackman, N. Babai, A. J. Mercer, R. H. Kramer, and W. B. Thoreson
2011. Release from the cone ribbon synapse under bright light conditions can be controlled by the opening of only a few Ca^{2+} channels. *Journal of Neurophysiology*, 106(6):2922–2935.

Becker, L., M. E. Schnee, M. Niwa, W. Sun, S. Maxeiner, S. Talaei, B. Kachar, M. A. Rutherford, and A. J. Ricci
2018. The presynaptic ribbon maintains vesicle populations at the hair cell afferent fiber synapse. *eLife*, 7:e30241.

Bertie, A.
2002. Java applications for teaching statistics. *MSOR Connections*, 2(3):78–81.

Beurg, M., N. Michalski, S. Safieddine, Y. Bouleau, R. Schneggenburger, E. R. Chapman, C. Petit, and D. Dulon
2010. Control of exocytosis by synaptotagmins and otoferlin in auditory hair cells. *The Journal of Neuroscience: The Official Journal of the Society for Neuroscience*, 30(40):13281–13290.

Beutner, D. and T. Moser
2001. The presynaptic function of mouse cochlear inner hair cells during development of hearing. *The Journal of Neuroscience*, 21(13):4593. 00125.

Bharadwaj, H. M., S. Verhulst, L. Shaheen, M. C. Liberman, and B. G. Shinn-Cunningham
2014. Cochlear neuropathy and the coding of supra-threshold sound. *Frontiers in Systems Neuroscience*, 8:26.

Blankenship, A. G. and M. B. Feller
2010. Mechanisms underlying spontaneous patterned activity in developing neural circuits. *Nature Reviews Neuroscience*, 11(1):18–29.

Brandt, A., D. Khimich, and T. Moser
2005. Few $Ca_v1.3$ channels regulate the exocytosis of a synaptic vesicle at the hair cell ribbon synapse. *The Journal of Neuroscience*, 25(50):11577. 00135.

Brandt, A., J. Striessnig, and T. Moser
2003. $Ca_v1.3$ channels are essential for development and presynaptic activity of cochlear inner hair cells. *The Journal of neuroscience*, 23(34):10832–10840. 00164.

Bucks, S. A., B. C. Cox, B. A. Vlosich, J. P. Manning, T. B. Nguyen, and J. S. Stone
2017. Supporting cells remove and replace sensory receptor hair cells in a balance organ of adult mice. *eLife*, 6.

Budzinski, K. L., R. W. Allen, B. S. Fujimoto, P. Kensel-Hammes, D. M. Belnap, S. M. Bajjalieh, and D. T. Chiu

2009. Large Structural Change in Isolated Synaptic Vesicles upon Loading with Neurotransmitter. *Biophysical Journal*, 97(9):2577–2584.

Bulankina, A. V. and T. Moser

2012. Neural circuit development in the mammalian cochlea. *Physiology*, 27(2):100–112.

Buran, B. N., N. Strenzke, A. Neef, E. D. Gundelfinger, T. Moser, and M. C. Liberman

2010. Onset coding is degraded in auditory nerve fibers from mutant mice lacking synaptic ribbons. *The Journal of Neuroscience: The Official Journal of the Society for Neuroscience*, 30(22):7587–7597.

Burda, H. and M. Branis

1988. Postnatal development of the organ of Corti in the wild house mouse, laboratory mouse, and their hybrid. *Hearing Research*, 36(1):97–105.

Burns, J. C. and J. S. Stone

2017. Development and regeneration of vestibular hair cells in mammals. *Seminars in Cell & Developmental Biology*, 65:96–105.

Butola, T., C. Wichmann, and T. Moser

2017. Piccolo promotes vesicle replenishment at a fast central auditory synapse. *Frontiers in Synaptic Neuroscience*, 9.

Catterall, W. A.

2011. Voltage-gated calcium channels. *Cold Spring Harbor perspectives in biology*, 3(8):a003947.

Chabbert, C., I. Mechaly, V. Sieso, P. Giraud, A. Brugeaud, J. Lehouelleur, F. Couraud, J. Valmier, and A. Sans

2003. Voltage-gated na+ channel activation induces both action potentials in utricular hair cells and brain-derived neurotrophic factor release in the rat utricle during a restricted period of development. *The Journal of Physiology*, 553(1):113–123.

Chakrabarti, R.

2016. *Investigation of Vesicle Pool Dynamics at Activity Modulated Inner Hair Cell Ribbon Synapses*. PhD thesis, Georg-August-University of Göttingen.

Chakrabarti, R., S. Michanski, and C. Wichmann

2018. Vesicle sub-pool organization at inner hair cell ribbon synapses. *EMBO reports*, P. 60.

Chapochnikov, N. M., H. Takago, C.-H. Huang, T. Pangršič, D. Khimich, J. Neef, E. Auge, F. Göttfert, S. W. Hell, C. Wichmann, F. Wolf, and T. Moser

2014. Uniquantal Release through a Dynamic Fusion Pore Is a Candidate Mechanism of Hair Cell Exocytosis. *Neuron*, 17(83):1389–1403.

Chen, J. W. Y. and R. A. Eatock

2000. Major potassium conductance in type i hair cells from rat semicircular canals: Characterization and modulation by nitric oxide. *Journal of Neurophysiology*, 84(1):139–151. PMID: 10899192.

Chen, Z., S. G. Kujawa, and W. F. Sewell

2007. Auditory sensitivity regulation via rapid changes in expression of surface AMPA receptors. *Nature Neuroscience*, 10(10):1238–1240.

Cole, A. A., X. Chen, and T. S. Reese

2016. A Network of Three Types of Filaments Organizes Synaptic Vesicles for Storage, Mobilization, and Docking. *Journal of Neuroscience*, 36(11):3222–3230.

Corey, D. P. and A. J. Hudspeth

1979. Ionic basis of the receptor potential in a vertebrate hair cell. *Nature*, 281(5733):675–677.

Correia, M. J. and D. G. Lang

1990. An electrophysiological comparison of solitary type I and type II vestibular hair cells. *Neuroscience Letters*, 116(1):106–111.

Costalupes, J. A., E. D. Young, and D. J. Gibson

1984. Effects of continuous noise backgrounds on rate response of auditory nerve fibers in cat. *Journal of Neurophysiology*, 51(6):1326–1344.

Dallos, P.

2008. Cochlear amplification, outer hair cells and prestin. *Current opinion in neurobiology*, 18(4):370–376.

Daniels, R. W., C. A. Collins, K. Chen, M. V. Gelfand, D. E. Featherstone, and A. DiAntonio

2006. A Single Vesicular Glutamate Transporter Is Sufficient to Fill a Synaptic Vesicle. *Neuron*, 49(1):11–16.

Daniels, R. W., C. A. Collins, M. V. Gelfand, J. Dant, E. S. Brooks, D. E. Krantz, and A. DiAntonio

2004. Increased expression of the drosophila vesicular glutamate transporter leads to excess glutamate release and a compensatory decrease in quantal content. *Journal of Neuroscience*, 24(46):10466–10474.

Deerinck TJ, Bushong E, T. A. E. M.

2010. Ncmir methods for 3d em: A new protocol for preparation of biological specimens for serial block-face sem. microscopy. Pp. 6–8.

Delacroix, L. and B. Malgrange

2015. Cochlear afferent innervation development. *Hearing Research*, 330:157–169.

Dennis, M. J.

1981. Development of the neuromuscular junction: Inductive interactions between cells. *Annual Review of Neuroscience*, 4(1):43–68. PMID: 7013639.

Dick, O., I. Hack, W. D. Altrock, C. C. Garner, E. D. Gundelfinger, and J. H. Brandstätter
2001. Localization of the presynaptic cytomatrix protein Piccolo at ribbon and conventional synapses in the rat retina: Comparison with Bassoon. *The Journal of Comparative Neurology*, 439(2):224–234.

Dick, O., S. tom Dieck, W. D. Altrock, J. Ammermüller, R. Weiler, C. C. Garner, E. D. Gundelfinger, and J. H. Brandstätter
2003. The Presynaptic Active Zone Protein Bassoon Is Essential for Photoreceptor Ribbon Synapse Formation in the Retina. *Neuron*, 37(5):775–786.

Dou, H., A. E. Vazquez, Y. Namkung, H. Chu, E. L. Cardell, L. Nie, S. Parson, H.-S. Shin, and E. N. Yamoah
2004. Null mutation of alpha1d Ca^{2+} channel gene results in deafness but no vestibular defect in mice. *Journal of the Association for Research in Otolaryngology: JARO*, 5(2):215–226.

Driver, E. C. and M. W. Kelley
2010. Transfection of mouse cochlear explants by electroporation. *Current Protocols in Neuroscience*, 51(1):4.34.1–4.34.10.

Dulon, D., S. Safieddine, S. M. Jones, and C. Petit
2009. Otoferlin Is Critical for a Highly Sensitive and Linear Calcium-Dependent Exocytosis at Vestibular Hair Cell Ribbon Synapses. *The Journal of Neuroscience*, 29(34):10474 –10487.

Eatock, R. A. and K. M. Hurley
2003. Functional development of hair cells. volume 57 of *Current Topics in Developmental Biology*, Pp. 389 – 448. Academic Press.

Eatock, R. A. and M. J. Hutzler
1992. Ionic currents of mammalian vestibular hair cells. *Annals of the New York Academy of Sciences*, 656:58–74.

Eatock, R. A. and A. Lysakowski
2006. Mammalian Vestibular Hair Cells. In *Vertebrate Hair Cells*, R. A. Eatock, R. R. Fay, and A. N. Popper, eds., Springer Handbook of Auditory Research, Pp. 348–442. New York, NY: Springer New York.

Eatock, R. A. and J. E. Songer
2011. Vestibular Hair Cells and Afferents: Two Channels for Head Motion Signals. *Annual Review of Neuroscience*, 34(1):501–534.

Ernfors, P., T. Van De Water, J. Loring, and R. Jaenisch
1995. Complementary roles of BDNF and NT-3 in vestibular and auditory development. *Neuron*, 14(6):1153–1164.

Fariñas, I., K. R. Jones, C. Backus, X.-Y. Wang, and L. F. Reichardt
1994. Severe sensory and sympathetic deficits in mice lacking neurotrophin-3. *Nature*, 369(6482):658–661.

Fariñas, I., K. R. Jones, L. Tessarollo, A. J. Vigers, E. Huang, M. Kirstein, D. C. de Caprona, V. Coppola, C. Backus, L. F. Reichardt, and B. Fritzsch
2001. Spatial shaping of cochlear innervation by temporally regulated neurotrophin expression. *The Journal of Neuroscience: The Official Journal of the Society for Neuroscience*, 21(16):6170–6180.

Favre, D. and A. Sans
1979. Morphological changes in afferent vestibular hair cell synapses during the postnatal development of the cat. *Journal of Neurocytology*, 8(6):765–775.

Fejtova, A., D. Davydova, F. Bischof, V. Lazarevic, W. D. Altrock, S. Romorini, C. Schöne, W. Zuschratter, M. R. Kreutz, C. C. Garner, N. E. Ziv, and E. D. Gundelfinger
2009. Dynein light chain regulates axonal trafficking and synaptic levels of bassoon. *The Journal of Cell Biology*, 185(2):341–355.

Fenster, S. D., W. J. Chung, R. Zhai, C. Cases-Langhoff, B. Voss, A. M. Garner, U. Kaempf, S. Kindler, E. D. Gundelfinger, and C. C. Garner
2000. Piccolo, a Presynaptic Zinc Finger Protein Structurally Related to Bassoon. *Neuron*, 25(1):203–214.

Fenster, S. D., M. M. Kessels, B. Qualmann, W. J. Chung, J. Nash, E. D. Gundelfinger, and C. C. Garner
2003. Interactions between Piccolo and the Actin/Dynamin-binding Protein Abp1 Link Vesicle Endocytosis to Presynaptic Active Zones. *Journal of Biological Chemistry*, 278(22):20268 – 20277.

Fernăndez-Busnadiego, R., S. Asano, A.-M. Oprisoreanu, E. Sakata, M. Doengi, Z. Kochovski, M. Zürner, V. Stein, S. Schoch, W. Baumeister, and V. Lucič
2013. Cryo-electron tomography reveals a critical role of RIM1α in synaptic vesicle tethering. *The Journal of Cell Biology*, 201(5):725–740.

Feuerverger, A., M. Menzinger, H. L. Atwood, and R. L. Cooper
2000. Statistical methods for assessing the dimensions of synaptic vesicles in nerve terminals. *Journal of Neuroscience Methods*, 103(2):181–190.

Fiala, J. C.
2005. Reconstruct: a free editor for serial section microscopy. *Journal of Microscopy*, 218(1):52–61.

Frank, T., D. Khimich, A. Neef, and T. Moser
2009. Mechanisms contributing to synaptic Ca^{2+} signals and their heterogeneity in hair cells. *Proceedings of the National Academy of Sciences*, 106(11):4483. 00045.

Frank, T., M. A. Rutherford, N. Strenzke, A. Neef, T. Pangršič, D. Khimich, A. Fejtova, E. D. Gundelfinger, M. C. Liberman, B. Harke, K. E. Bryan, A. Lee, A. Egner, D. Riedel, and T. Moser
2010. Bassoon and the synaptic ribbon organize Ca^{2+} channels and vesicles to add release sites and promote refilling. *Neuron*, 68(4):724–738. 00000.

Friauf, E., C. Aragón, S. Löhrke, B. Westenfelder, and F. Zafra
1999. Developmental expression of the glycine transporter glyt2 in the auditory system of rats suggests involvement in synapse maturation. *Journal of Comparative Neurology*, 412(1):17–37.

Fritzsch, B., N. Pan, I. Jahan, and K. L. Elliott
2015. Inner ear development: building a spiral ganglion and an organ of Corti out of unspecified ectoderm. *Cell and Tissue Research*, 361(1):7–24.

Fritzsch, B., U. Pirvola, and J. Ylikoski
1999. Making and breaking the innervation of the ear: neurotrophic support during ear development and its clinical implications. *Cell and Tissue Research*, 295(3):369–382.

Fritzsch, B., L. Tessarollo, E. Coppola, and L. F. Reichardt
2004. Neurotrophins in the ear: their roles in sensory neuron survival and fiber guidance. volume 146 of *NGF and Related Molecules in Health and Disease*, Pp. 265–278. Elsevier.

Fuchs, M., A. Sendelbeck, J. Atorf, J. Kremers, and J. H. Brandstätter
2013. Strain differences in illumination-dependent structural changes at mouse photoreceptor ribbon synapses. *The Journal of Comparative Neurology*, 521(1):69–78.

Fuchs, P. A., E. Glowatzki, and T. Moser
2003. The afferent synapse of cochlear hair cells. *Current Opinion in Neurobiology*, 13(4):452–458. 00081.

Furman, A. C., S. G. Kujawa, and M. C. Liberman
2013. Noise-induced cochlear neuropathy is selective for fibers with low spontaneous rates. *Journal of Neurophysiology*, 110(3):577–586.

Furness, D. N., C. M. Hackney, and P. S. Steyger
1990. Organization of microtubules in cochlear hair cells. *Journal of Electron Microscopy Technique*, 15(3):261–279.

Geinisman, Y., L. Detoledoa-Morrell, F. Morrell, I. S. Persina, and M. A. Beatty
1996. Synapse restructuring associated with the maintenance phase of hippocampal long-term potentiation. *Journal of Comparative Neurology*, 368(3):413–423.

Géléoc, G. S. G. and J. R. Holt
2003. Developmental acquisition of sensory transduction in hair cells of the mouse inner ear. *Nature Neuroscience*, 6:1019.

Géléoc, G. S. G., J. R. Risner, and J. R. Holt
2004. Developmental acquisition of voltage-dependent conductances and sensory signaling in hair cells of the embryonic mouse inner ear. *Journal of Neuroscience*, 24(49):11148–11159.

Glowatzki, E. and P. A. Fuchs
2002. Transmitter release at the hair cell ribbon synapse. *Nature Neuroscience*, 5(2):147–154.

Grant, L., E. Yi, and E. Glowatzki
2010. Two Modes of Release Shape the Postsynaptic Response at the Inner Hair Cell Ribbon Synapse. *The Journal of Neuroscience*, 30(12):4210–4220.

Graydon, C. W., S. Cho, G.-L. Li, B. Kachar, and H. v. Gersdorff
2011. Sharp Ca^{2+} Nanodomains beneath the Ribbon Promote Highly Synchronous Multivesicular Release at Hair Cell Synapses. *The Journal of Neuroscience*, 31(46):16637–16650.

Graydon, C. W., U. Manor, and K. S. Kindt
2017. In vivo ribbon mobility and turnover of ribeye at zebrafish hair cell synapses. *Scientific Reports*, 7(1):2045–2322.

Graydon, C. W., J. Zhang, N. W. Oesch, A. A. Sousa, R. D. Leapman, and J. S. Diamond
2014. Passive Diffusion as a Mechanism Underlying Ribbon Synapse Vesicle Release and Resupply. *The Journal of Neuroscience*, 34(27):8948–8962.

Gundelfinger, E. D. and A. Fejtova
2012. Molecular organization and plasticity of the cytomatrix at the active zone. *Current Opinion in Neurobiology*.

Gundelfinger, E. D., C. Reissner, and C. C. Garner
2016. Role of Bassoon and Piccolo in Assembly and Molecular Organization of the Active Zone. *Frontiers in Synaptic Neuroscience*, 7.

Hall, Z. W. and J. R. Sanes
1993. Synaptic structure and development: The neuromuscular junction. *Cell*, 72:99–121.

Hallermann, S., A. Fejtova, H. Schmidt, A. Weyhersmüller, R. A. Silver, E. D. Gundelfinger, and J. Eilers
2010. Bassoon Speeds Vesicle Reloading at a Central Excitatory Synapse. *Neuron*, 68(4):710–723.

Hallgren, E., L. Kornilova, E. Fransen, D. Glukhikh, S. T. Moore, G. Clément, A. Van Ombergen, H. MacDougall, I. Naumov, and F. L. Wuyts
2016. Decreased otolith-mediated vestibular response in 25 astronauts induced by long-duration spaceflight. *Journal of Neurophysiology*, 115(6):3045–3051. PMID: 27009158.

Haubensak, W., F. Narz, R. Heumann, and V. Lessmann
1998. BDNF-GFP containing secretory granules are localized in the vicinity of synaptic junctions of cultured cortical neurons. *Journal of Cell Science*, 111(11):1483–1493.

Heidrych, P., U. Zimmermann, S. Kuhn, C. Franz, J. Engel, S. V. Duncker, B. Hirt, C. M. Pusch, P. Ruth, M. Pfister, W. Marcotti, N. Blin, and M. Knipper
2009. Otoferlin interacts with myosin VI: implications for maintenance of the basolateral synaptic structure of the inner hair cell. *Human Molecular Genetics*, 18(15):2779–2790.

Helmprobst, F., M. Frank, and C. Stigloher

2015. Presynaptic architecture of the larval zebrafish neuromuscular junction. *The Journal of Comparative Neurology*, 523(13):1984–1997.

Henry, K. R. and R. A. Chole

1980. Genotypic differences in behavioral, physiological and anatomical expressions of age-related hearing loss in the laboratory mouse. *Audiology: Official Organ of the International Society of Audiology*, 19(5):369–383.

Hequembourg, S. and M. C. Liberman

2001. Spiral Ligament Pathology: A Major Aspect of Age-Related Cochlear Degeneration in C57bl/6 Mice. *JARO: Journal of the Association for Research in Otolaryngology*, 2(2):118–129.

Hires, S. A., Y. Zhu, and R. Y. Tsien

2008. Optical measurement of synaptic glutamate spillover and reuptake by linker optimized glutamate-sensitive fluorescent reporters. *Proceedings of the National Academy of Sciences*, 105(11):4411–4416.

Holstein, G. R., R. D. Rabbitt, G. P. Martinelli, V. L. Friedrich, Jr, R. D. Boyle, and S. M. Highstein

2004. Convergence of excitatory and inhibitory hair cell transmitters shapes vestibular afferent responses. *Proceedings of the National Academy of Sciences of the United States of America*, 101(44):15766–15771.

Holt, J. R., D. P. Corey, and R. A. Eatock

1997. Mechanoelectrical transduction and adaptation in hair cells of the mouse utricle, a low-frequency vestibular organ. *Journal of Neuroscience*, 17(22):8739–8748.

Hopsu, V. K. and A. U. Arstila

1965. AN APPARENT SOMATO-SOMATIC SYNAPTIC STRUCTURE IN THE PINEAL GLAND OF THE RAT. *Experimental Cell Research*, 37:484–487.

Hård, E. and K. Larsson

1975. Development of Air Righting in Rats. *Brain, Behavior and Evolution*, 11(1):53–59.

Hu, Y., L. Qu, and T. Schikorski

2008. Mean synaptic vesicle size varies among individual excitatory hippocampal synapses. *Synapse (New York, N.Y.)*, 62(12):953–957.

Huang, L.-C., M. Barclay, K. Lee, S. Peter, G. D. Housley, P. R. Thorne, and J. M. Montgomery

2012. Synaptic profiles during neurite extension, refinement and retraction in the developing cochlea. *Neural development*, 7(1):1–17.

Huang, L.-C., P. R. Thorne, G. D. Housley, and J. M. Montgomery

2007. Spatiotemporal definition of neurite outgrowth, refinement and retraction in the developing mouse cochlea. *Development (Cambridge, England)*, 134(16):2925–2933.

Hull, C., K. Studholme, S. Yazulla, and H. von Gersdorff
2006. Diurnal changes in exocytosis and the number of synaptic ribbons at active zones of an ON-type bipolar cell terminal. *Journal of Neurophysiology*, 96(4):2025–2033.

Huterer, M. and K. E. Cullen
2002. Vestibuloocular reflex dynamics during high-frequency and high-acceleration rotations of the head on body in rhesus monkey. *Journal of Neurophysiology*, 88(1):13–28. PMID: 12091529.

Huttner, W. B., M. Ohashi, R. H. Kehlenbach, F. A. Barr, R. Bauerfeind, O. Bräunling, D. Corbeil, M. Hannah, H. A. Pasolli, and A. Schmidt
1995. Biogenesis of neurosecretory vesicles. *Cold Spring Harbor Symposia on Quantitative Biology*, 60:315–327.

Imig, C.
2013. *Molecular and Morphological Correlates of Synaptic Vesicle Priming*. PhD thesis, Georg-August-University of Göttingen.

Ison, J. R. and P. D. Allen
2003. Low-Frequency Tone Pips Elicit Exaggerated Startle Reflexes in C57bl/6j Mice with Hearing Loss. *JARO: Journal of the Association for Research in Otolaryngology*, 4(4):495–504.

Jastrow, H., D. Schmanke, and J. Weinert
2004. Bizarre alterations of the morphology of pineal synaptic bodies under constant light and an evaluation of suitable 3d-reconstruction software. *Micron*, 35(8):655–670.

Jean, P., D. Lopez de la Morena, S. Michanski, L. M. Jaime Tobón, R. Chakrabarti, M. M. Picher, J. Neef, S. Jung, M. Gültas, S. Maxeiner, A. Neef, C. Wichmann, N. Strenzke, C. Grabner, and T. Moser
2018. The synaptic ribbon is critical for sound encoding at high rates and with temporal precision. *eLife*, 7.

Jennings, C. G. and S. J. Burden
1993. Development of the neuromuscular synapse. *Current Opinion in Neurobiology*, 3(1):75–81.

Jing, Z., M. A. Rutherford, H. Takago, T. Frank, A. Fejtova, D. Khimich, T. Moser, and N. Strenzke
2013. Disruption of the presynaptic cytomatrix protein bassoon degrades ribbon anchorage, multiquantal release, and sound encoding at the hair cell afferent synapse. *The Journal of Neuroscience*, 33(10):4456–4467. 00001.

Johnson, C. P. and E. R. Chapman
2010. Otoferlin is a calcium sensor that directly regulates SNARE-mediated membrane fusion. *The Journal of Cell Biology*, 191(1):187–197.

Johnson, K. R., L. C. Erway, S. A. Cook, J. F. Willott, and Q. Y. Zheng
1997. A major gene affecting age-related hearing loss in C57bl/6j mice. *Hearing Research*, 114(1):83–92.

Johnson, S. L., T. Eckrich, S. Kuhn, V. Zampini, C. Franz, K. M. Ranatunga, T. P. Roberts, S. Masetto, M. Knipper, C. J. Kros, and W. Marcotti
2011. Position-dependent patterning of spontaneous action potentials in immature cochlear inner hair cells. *Nat Neurosci*, 14(6):711–717.

Johnson, S. L., C. Franz, M. Knipper, and W. Marcotti
2009. Functional maturation of the exocytotic machinery at gerbil hair cell ribbon synapses. *The Journal of Physiology*, 587(Pt 8):1715–1726.

Johnson, S. L., H. J. Kennedy, M. C. Holley, R. Fettiplace, and W. Marcotti
2012. The resting transducer current drives spontaneous activity in prehearing mammalian cochlear inner hair cells. *Journal of Neuroscience*, 32(31):10479–10483.

Johnson, S. L., S. Kuhn, C. Franz, N. Ingham, D. N. Furness, M. Knipper, K. P. Steel, J. P. Adelman, M. C. Holley, and W. Marcotti
2013. Presynaptic maturation in auditory hair cells requires a critical period of sensory-independent spiking activity. *Proceedings of the National Academy of Sciences of the United States of America*, 110(21):8720–8725.

Johnson, S. L. and W. Marcotti
2008. Biophysical properties of $Ca_v1.3$ calcium channels in gerbil inner hair cells. *The Journal of Physiology*, 586(4):1029–1042.

Johnson, S. L., W. Marcotti, and C. J. Kros
2005. Increase in efficiency and reduction in Ca^{2+} dependence of exocytosis during development of mouse inner hair cells. *The Journal of Physiology*, 563(1):177–191.

Johnson, S. L., J. Olt, S. Cho, H. v. Gersdorff, and W. Marcotti
2017. The Coupling between Ca^{2+} Channels and the Exocytotic Ca^{2+} Sensor at Hair Cell Ribbon Synapses Varies Tonotopically along the Mature Cochlea. *Journal of Neuroscience*, 37(9):2471–2484.

Jung, S., T. Maritzen, C. Wichmann, Z. Jing, A. Neef, N. H. Revelo, H. Al-Moyed, S. Meese, S. M. Wojcik, I. Panou, et al.
2015a. Disruption of adaptor protein 2μ (ap-2μ) in cochlear hair cells impairs vesicle reloading of synaptic release sites and hearing. *The EMBO journal*, 34(21):2686–2702.

Jung, S., T. Oshima-Takago, R. Chakrabarti, A. B. Wong, Z. Jing, G. Yamanbaeva, M. M. Picher, S. M. Wojcik, F. Göttfert, F. Predoehl, K. Michel, S. W. Hell, S. Schoch, N. Strenzke, C. Wichmann, and T. Moser
2015b. Rab3-interacting molecules 2α and 2β promote the abundance of voltage-gated $Ca_v1.3$

Ca^{2+} channels at hair cell active zones. *Proceedings of the National Academy of Sciences*, 112(24):E3141–E3149.

Kandel, E. R., J. H. Schwartz, and T. Jessell
2012. *Principles of Neural Science*. New York: McGraw-Hill Medical.

Kandler, K., A. Clause, and J. Noh
2009. Tonotopic reorganization of developing auditory brainstem circuits. *Nature Neuroscience*, 12(6):711–717.

Kantardzhieva, A., M. C. Liberman, and W. F. Sewell
2013. Quantitative analysis of ribbons, vesicles, and cisterns at the cat inner hair cell synapse: correlations with spontaneous rate. *The Journal of Comparative Neurology*, 521(14):3260–3271.

Kappers, J. A.
1976. The mammalian pineal gland, a survey. *Acta Neurochirurgica*, 34(1-4):109–149.

Kawase, T. and M. C. Liberman
1992. Spatial organization of the auditory nerve according to spontaneous discharge rate. *Journal of Comparative Neurology*, 319(2):312–318.

Keithley, E. M. and M. L. Feldman
1982. Hair cell counts in an age-graded series of rat cochleas. *Hearing Research*, 8(3):249–262.

Kennedy, H. J.
2012. New Developments in Understanding the Mechanisms and Function of Spontaneous Electrical Activity in the Developing Mammalian Auditory System. *Journal of the Association for Research in Otolaryngology*.

Kersigo, J. and B. Fritzsch
2015. Inner ear hair cells deteriorate in mice engineered to have no or diminished innervation. *Frontiers in Aging Neuroscience*, 7:33.

Khimich, D., R. Nouvian, R. Pujol, S. tom Dieck, A. Egner, E. D. Gundelfinger, and T. Moser
2005. Hair cell synaptic ribbons are essential for synchronous auditory signalling. *Nature*, 434(7035):889–894. 00209.

Kiene, M. L. and H. Stadler
1987. Synaptic vesicles in electromotoneurones. I. Axonal transport, site of transmitter uptake and processing of a core proteoglycan during maturation. *The EMBO Journal*, 6(8):2209–2215.

Kikuchi, K. and D. Hilding
1965. The development of the organ of Corti in the mouse. *Acta Oto-Laryngologica*, 60(3):207–222.

Kim, S., J. Ko, H. Shin, J.-R. Lee, C. Lim, J.-H. Han, W. D. Altrock, C. C. Garner, E. D. Gundelfinger, R. T. Premont, B.-K. Kaang, and E. Kim
2003. The GIT family of proteins forms multimers and associates with the presynaptic cytomatrix protein Piccolo. *The Journal of Biological Chemistry*, 278(8):6291–6300.

Konrad, H. R., M. Girardi, and R. Helfert
1999. Balance and aging. *The Laryngoscope*, 109(9):1454–1460.

Kopecky, B. J., R. DeCook, and B. Fritzsch
2012. N-myc and l-myc are essential for hair cell formation but not maintenance. *Brain Research*, 1484:1 – 14.

Koundakjian, E. J., J. L. Appler, and L. V. Goodrich
2007. Auditory neurons make stereotyped wiring decisions before maturation of their targets. *The Journal of Neuroscience: The Official Journal of the Society for Neuroscience*, 27(51):14078–14088.

Kremer, J. R., D. N. Mastronarde, and J. R. McIntosh
1996. Computer visualization of three-dimensional image data using IMOD. *Journal of Structural Biology*, 116(1):71–76.

Krinner, S., T. Butola, S. Jung, C. Wichmann, and T. Moser
2017. RIM-binding protein 2 promotes a large number of Ca_v Ca^{2+}-channels and contributes to fast synaptic vesicle replenishment at hair cell active zones.

Kros, C. J., J. P. Ruppersberg, and A. Rüsch
1998. Expression of a potassium current in inner hair cells during development of hearing in mice. *Nature*, 394(6690):281–284.

Lannou, J., W. Precht, and L. Cazin
1979. The postnatal development of functional properties of central vestibular neurons in the rat. *Brain Research*, 175(2):219–232.

Lenoir, M., A. Shnerson, and R. Pujol
1980. Cochlear receptor development in the rat with emphasis on synaptogenesis. *Anatomy and Embryology*, 160(3):253–262.

Lenzi, D., J. Crum, M. H. Ellisman, and W. M. Roberts
2002. Depolarization redistributes synaptic membrane and creates a gradient of vesicles on the synaptic body at a ribbon synapse. *Neuron*, 36(4):649–659.

Lenzi, D., J. W. Runyeon, J. Crum, M. H. Ellisman, and W. M. Roberts
1999. Synaptic Vesicle Populations in Saccular Hair Cells Reconstructed by Electron Tomography. *The Journal of Neuroscience*, 19(1):119–132.

Lenzi, D. and H. von Gersdorff
2001. Structure suggests function: the case for synaptic ribbons as exocytotic nanomachines. *Bioessays*, 23(9):831–840.

Li, H. S. and E. Borg

1991. Age-related loss of auditory sensitivity in two mouse genotypes. *Acta Oto-Laryngologica*, 111(5):827–834.

Liberman, L. D., H. Wang, and M. C. Liberman

2011. Opposing Gradients of Ribbon Size and AMPA Receptor Expression Underlie Sensitivity Differences among Cochlear-Nerve/Hair-Cell Synapses. *The Journal of Neuroscience*, 31(3):801–808.

Liberman, M. C.

1980. Morphological differences among radial afferent fibers in the cat cochlea: an electron-microscopic study of serial sections. *Hearing Research*, 3(1):45–63.

Liberman, M. C.

1982. The cochlear frequency map for the cat: labeling auditory-nerve fibers of known characteristic frequency. *The Journal of the Acoustical Society of America*, 72(5):1441–1449.

Liberman, M. C.

2017. Noise-induced and age-related hearing loss: new perspectives and potential therapies. *F1000Research*, 6.

Limbach, C., M. M. Laue, X. Wang, B. Hu, N. Thiede, G. Hultqvist, and M. W. Kilimann

2011. Molecular in situ topology of Aczonin/Piccolo and associated proteins at the mammalian neurotransmitter release site. *Proceedings of the National Academy of Sciences*, 108(31):E392 –E401.

Lindeman, H. H.

1969. Regional differences in structure of the vestibular sensory regions. *The Journal of Laryngology and Otology*, 83(1):1–17.

Lisman, J. E. and K. M. Harris

1993. Quantal analysis and synaptic anatomy – integrating two views of hippocampal plasticity. *Trends in Neurosciences*, 16(4):141–147.

LoGiudice, L., P. Sterling, and G. Matthews

2008. Mobility and turnover of vesicles at the synaptic ribbon. *The Journal of Neuroscience*, 28(12):3150.

Luo, X.-G., R. A. Rush, and X.-F. Zhou

2001. Ultrastructural localization of brain-derived neurotrophic factor in rat primary sensory neurons. *Neuroscience Research*, 39(4):377 – 384.

Lv, C., W. J. Stewart, O. Akanyeti, C. Frederick, J. Zhu, J. Santos-Sacchi, L. Sheets, J. C. Liao, and D. Zenisek

2016. Synaptic Ribbons Require Ribeye for Electron Density, Proper Synaptic Localization, and Recruitment of Calcium Channels. *Cell Reports*, 15(12):2784–2795.

Lysakowski, A. and J. M. Goldberg

1997. A regional ultrastructural analysis of the cellular and synaptic architecture in the chinchilla cristae ampullares. *The Journal of comparative neurology*, 389(3):419–443.

Magupalli, V. G., K. Schwarz, K. Alpadi, S. Natarajan, G. M. Seigel, and F. Schmitz

2008. Multiple RIBEYE-RIBEYE interactions create a dynamic scaffold for the formation of synaptic ribbons. *The Journal of Neuroscience: The Official Journal of the Society for Neuroscience*, 28(32):7954–7967.

Mallik, R. and S. P. Gross

2004. Molecular Motors: Strategies to Get Along. *Current Biology*, 14(22):R971–R982.

Marcotti, W., S. L. Johnson, M. C. Holley, and C. J. Kros

2003. Developmental changes in the expression of potassium currents of embryonic, neonatal and mature mouse inner hair cells. *The Journal of Physiology*, 548(Pt 2):383–400.

Markus, E. J., T. L. Petit, and J. C. LeBoutillier

1987. Synaptic structural changes during development and aging. *Brain Research*, 432(2):239–248.

Mastronarde, D. N.

2005. Automated electron microscope tomography using robust prediction of specimen movements. *Journal of Structural Biology*, 152(1):36 – 51.

Matthews, G. and P. Fuchs

2010. The diverse roles of ribbon synapses in sensory neurotransmission. *Nature Reviews Neuroscience*, 11(12):812–822.

Maxeiner, S., F. Luo, A. Tan, F. Schmitz, and T. C. Südhof

2016. How to make a synaptic ribbon: RIBEYE deletion abolishes ribbons in retinal synapses and disrupts neurotransmitter release. *The EMBO Journal*, 35(10):1098–1114.

Maycox, P. R., E. Link, A. Reetz, S. A. Morris, and R. Jahn

1992. Clathrin-coated vesicles in nervous tissue are involved primarily in synaptic vesicle recycling. *The Journal of Cell Biology*, 118(6):1379–1388.

McAllister, A. K.

1999. Subplate neurons: A missing link among neurotrophins, activity, and ocular dominance plasticity? *Proceedings of the National Academy of Sciences*, 96(24):13600–13602.

McAllister, A. K.

2007. Dynamic aspects of cns synapse formation. *Annual Review of Neuroscience*, 30(1):425–450.

Melchionda, S., N. Ahituv, L. Bisceglia, T. Sobe, F. Glaser, R. Rabionet, M. L. Arbones, A. Notarangelo, E. Di Iorio, M. Carella, L. Zelante, X. Estivill, K. B. Avraham, and P. Gasparini

2001. MYO6, the human homologue of the gene responsible for deafness in Snell's waltzer

mice, is mutated in autosomal dominant nonsyndromic hearing loss. *American Journal of Human Genetics*, 69(3):635–640.

Mendoza Schulz, A., Z. Jing, J. M. Sănchez Caro, F. Wetzel, T. Dresbach, N. Strenzke, C. Wichmann, and T. Moser
2014. Bassoon-disruption slows vesicle replenishment and induces homeostatic plasticity at a CNS synapse. *The EMBO journal*, 33(5):512–527.

Merchan-Perez, A. and M. C. Liberman
1996. Ultrastructural differences among afferent synapses on cochlear hair cells: correlations with spontaneous discharge rate. *The Journal of Comparative Neurology*, 371(2):208–221.

Meyer, A. C., T. Frank, D. Khimich, G. Hoch, D. Riedel, N. M. Chapochnikov, Y. M. Yarin, B. Harke, S. W. Hell, A. Egner, and T. Moser
2009. Tuning of synapse number, structure and function in the cochlea. *Nature Neuroscience*, 12(4):444–453. 00084.

Meyer, A. C. and T. Moser
2010. Structure and function of cochlear afferent innervation. *Current Opinion in Otolaryngology & Head and Neck Surgery*, 18(5):441–446. 00016.

Michael, G. J., S. Averill, A. Nitkunan, M. Rattray, D. L. H. Bennett, Q. Yan, and J. V. Priestley
1997. Nerve growth factor treatment increases brain-derived neurotrophic factor selectively in trka-expressing dorsal root ganglion cells and in their central terminations within the spinal cord. *Journal of Neuroscience*, 17(21):8476–8490.

Michalski, N., J. D. Goutman, S. M. Auclair, J. B. d. Monvel, M. Tertrais, A. Emptoz, A. Parrin, S. Nouaille, M. Guillon, M. Sachse, D. Ciric, A. Bahloul, J.-P. Hardelin, R. B. Sutton, P. Avan, S. S. Krishnakumar, J. E. Rothman, D. Dulon, S. Safieddine, and C. Petit
2017. Otoferlin acts as a Ca^{2+} sensor for vesicle fusion and vesicle pool replenishment at auditory hair cell ribbon synapses. *eLife*, 6:e31013.

Michanski, S., K. Smaluch, A. M. Steyer, R. Chakrabarti, C. Setz, D. Oestreicher, C. Fischer, W. Möbius, T. Moser, C. Vogl, and C. Wichmann
2019. Mapping developmental maturation of inner hair cell ribbon synapses in the apical mouse cochlea. *Proceedings of the National Academy of Sciences*, 116(13):6415–6424.

Mikaelian, D. and R. J. Ruben
1965. Development of Hearing in the Normal Cba-J Mouse: Correlation of Physiological Observations with Behavioral Responses and with Cochlear Anatomy. *Acta Oto-laryngologica*, 59(2-6):451–461.

Mikaelian, D. O.
1979. Development and degeneration of hearing in the c57/b16 mouse: Relation of electrophysiologic responses from the round window and cochlear nucleus to cochlear anatomy and behavioral responses. *The Laryngoscope*, 89(1):1–15.

Mikaelian, D. O., D. Warfield, and O. Norris
1974. Genetic progressive hearing loss in the C57-b16 mouse. Relation of behavioral responses to chochlear anatomy. *Acta Oto-Laryngologica*, 77(5):327–334.

Moller, A. R.
2006. *Hearing: Anatomy, Physiolgy, and Disorders of the Auditory System*, 2 edition. Academic Press.

Moser, T. and D. Beutner
2000. Kinetics of exocytosis and endocytosis at the cochlear inner hair cell afferent synapse of the mouse. *Proceedings of the National Academy of Sciences of the United States of America*, 97(2):883–888. 00245.

Moser, T., A. Brandt, and A. Lysakowski
2006. Hair cell ribbon synapses. *Cell and Tissue Research*, 326(2):347–359. 00049.

Moser, T. and A. Starr
2016. Auditory neuropathy–neural and synaptic mechanisms. *Nature Reviews Neurology*, 12(3):135–149.

Mukherjee, K., X. Yang, S. H. Gerber, H.-B. Kwon, A. Ho, P. E. Castillo, X. Liu, and T. C. Südhof
2010. Piccolo and bassoon maintain synaptic vesicle clustering without directly participating in vesicle exocytosis. *Proceedings of the National Academy of Sciences of the United States of America*, 107(14):6504–6509.

Müller, U.
2008. Cadherins and mechanotransduction by hair cells. *Current Opinion in Cell Biology*, 20(5):557–566.

Muresan, V., A. Lyass, and B. J. Schnapp
1999. The Kinesin Motor KIF3a Is a Component of the Presynaptic Ribbon in Vertebrate Photoreceptors. *The Journal of Neuroscience*, 19(3):1027–1037.

Nakata, T., S. Terada, and N. Hirokawa
1998. Visualization of the dynamics of synaptic vesicle and plasma membrane proteins in living axons. *The Journal of Cell Biology*, 140(3):659–674.

Neef, A., C. Heinemann, and T. Moser
2007. Measurements of membrane patch capacitance using a software-based lock-in system. *Pflügers Archiv - European Journal of Physiology*, 454(2):335–344. 00007.

Nie, L., J. Zhu, M. A. Gratton, A. Liao, K. J. Mu, W. Nonner, G. P. Richardson, and E. N. Yamoah
2008. Molecular Identity and Functional Properties of a Novel T-Type Ca^{2+} Channel Cloned From the Sensory Epithelia of the Mouse Inner Ear. *Journal of Neurophysiology*, 100(4):2287–2299.

Nieratschker, V., A. Schubert, M. Jauch, N. Bock, D. Bucher, S. Dippacher, G. Krohne, E. Asan, S. Buchner, and E. Buchner
2009. Bruchpilot in ribbon-like axonal agglomerates, behavioral defects, and early death in srpk79d kinase mutants of drosophila. *PLOS Genetics*, 5(10):1–16.

Niparko, J. K.
1993. Pathology of the ear. *Head & Neck*, 16(3):298–298.

Nouvian, R., D. Beutner, T. D. Parsons, and T. Moser
2006. Structure and function of the hair cell ribbon synapse. *The Journal of membrane biology*, 209(2-3):153–165.

Nouvian, R., J. Neef, A. V. Bulankina, E. Reisinger, T. Pangršič, T. Frank, S. Sikorra, N. Brose, T. Binz, and T. Moser
2011. Exocytosis at the hair cell ribbon synapse apparently operates without neuronal SNARE proteins. *Nature Neuroscience*, 14(4):411–413. 00021.

Oghalai, J. S.
2004. The cochlear amplifier: augmentation of the traveling wave within the inner ear. *Current opinion in otolaryngology & head and neck surgery*, 12(5):431–438.

Ohn, T.-L., M. A. Rutherford, Z. Jing, S. Jung, C. J. Duque-Afonso, G. Hoch, M. M. Picher, A. Scharinger, N. Strenzke, and T. Moser
2016. Hair cells use active zones with different voltage dependence of Ca^{2+} influx to decompose sounds into complementary neural codes. *Proceedings of the National Academy of Sciences*, 113(32):201605737.

Pangršič, T., M. Gabrielaitis, S. Michanski, B. Schwaller, F. Wolf, N. Strenzke, and T. Moser
2015. EF-hand protein Ca^{2+} buffers regulate Ca^{2+} influx and exocytosis in sensory hair cells. *Proceedings of the National Academy of Sciences*, 112(9):E1028–E1037.

Pangršič, T., L. Lasarow, K. Reuter, H. Takago, M. Schwander, D. Riedel, T. Frank, L. M. Tarantino, J. S. Bailey, N. Strenzke, N. Brose, U. Müller, E. Reisinger, and T. Moser
2010. Hearing requires otoferlin-dependent efficient replenishment of synaptic vesicles in hair cells. *Nature Neuroscience*, 13(7):869–876.

Pangršič, T., E. Reisinger, and T. Moser
2012. Otoferlin: a multi-C2 domain protein essential for hearing. *Trends in Neurosciences*, 35(11):671–680.

Parsons, T. D. and P. Sterling
2003. Synaptic Ribbon. *Neuron*, 37(3):379–382.

Peter Dallos, Arthur N. Popper, and Richard R. Fay
1996. *The Cochlea*, volume 8 of *IV*. Springer Verlag, New York, Inc.

Pirvola, U., J. Ylikoski, J. Palgi, E. Lehtonen, U. Arumae, and M. Saarma
1992. Brain-derived neurotrophic factor and neurotrophin 3 mRNAs in the peripheral target fields of developing inner ear ganglia. *Proceedings of the National Academy of Sciences*, 89(20):9915–9919.

Platzer, J., J. Engel, A. Schrott-Fischer, K. Stephan, S. Bova, H. Chen, H. Zheng, and J. Striessnig
2000. Congenital deafness and sinoatrial node dysfunction in mice lacking class D L-type Ca^{2+} channels. *Cell*, 102(1):89–97.

Posthuma, G., J. W. Slot, and H. J. Geuze
1987. Usefulness of the immunogold technique in quantitation of a soluble protein in ultra-thin sections. *Journal of Histochemistry & Cytochemistry*, 35(4):405–410. PMID: 2434559.

Praag, H. v., G. Kempermann, and F. H. Gage
2000. Neural consequences of enviromental enrichment. *Nature Reviews Neuroscience*, 1(3):191–198.

Pujol, R., M. Lavigne-Rebillard, and M. Lenoir
1998. Development of sensory and neural structures in the mammalian cochlea. In *Development of the auditory system*, Pp. 146–192. Springer-Verlag New York Inc.

Purves, D., ed.
2004. *Neuroscience*, 3rd ed edition. Sunderland, Mass: Sinauer Associates, Publishers.

Qu, L., Y. Akbergenova, Y. Hu, and T. Schikorski
2009. Synapse-to-synapse variation in mean synaptic vesicle size and its relationship with synaptic morphology and function. *Journal of Comparative Neurology*, 514(4):343–352.

Rabl, K., L. Cadetti, and W. B. Thoreson
2005. Kinetics of Exocytosis Is Faster in Cones Than in Rods. *The Journal of Neuroscience*, 25(18):4633 –4640.

Ramakrishnan, N. A., M. J. Drescher, and D. G. Drescher
2009. Direct interaction of otoferlin with syntaxin 1a, SNAP-25, and the L-type voltage-gated calcium channel $ca_v1.3$. *The Journal of Biological Chemistry*, 284(3):1364–1372.

Ramekers, D., H. Versnel, W. Grolman, and S. F. L. Klis
2012. Neurotrophins and their role in the cochlea. *Hearing Research*, 288(1):19–33.

Ramrírez-Camacho, R., J. R. García-Berrocal, A. Trinidad, J. A. González-García, J. M. Verdaguer, A. Ibáñez, A. Rodríguez, and R. Sanz
2006. Central role of supporting cells in cochlear homeostasis and pathology. *Medical Hypotheses*, 67(3):550–555.

Regus-Leidig, H., M. Fuchs, M. Löhner, S. R. Leist, S. Leal-Ortiz, V. A. Chiodo, W. W. Hauswirth, C. C. Garner, and J. H. Brandstätter
2014. In vivo knockdown of Piccolino disrupts presynaptic ribbon morphology in mouse photoreceptor synapses. *Frontiers in Cellular Neuroscience*, 8:259.

Regus-Leidig, H., C. Ott, M. Löhner, J. Atorf, M. Fuchs, T. Sedmak, J. Kremers, A. Fejtová, E. D. Gundelfinger, and J. H. Brandstätter
2013. Identification and Immunocytochemical Characterization of Piccolino, a Novel Piccolo Splice Variant Selectively Expressed at Sensory Ribbon Synapses of the Eye and Ear. *PLoS ONE*, 8(8):e70373.

Regus-Leidig, H., D. Specht, S. Tom Dieck, and J. H. Brandstätter
2010. Stability of active zone components at the photoreceptor ribbon complex. *Molecular Vision*, 16:2690–2700.

Regus-Leidig, H., S. Tom Dieck, D. Specht, L. Meyer, and J. H. Brandstätter
2009. Early steps in the assembly of photoreceptor ribbon synapses in the mouse retina: the involvement of precursor spheres. *The Journal of Comparative Neurology*, 512(6):814–824.

Reisinger, E., C. Bresee, J. Neef, R. Nair, K. Reuter, A. Bulankina, R. Nouvian, M. Koch, J. Bückers, L. Kastrup, I. Roux, C. Petit, S. W. Hell, N. Brose, J.-S. Rhee, S. Kügler, J. V. Brigande, and T. Moser
2011. Probing the functional equivalence of otoferlin and synaptotagmin 1 in exocytosis. *The Journal of neuroscience: the official journal of the Society for Neuroscience*, 31(13):4886–4895. 00017.

Rennie, K. J. and M. J. Correia
1994. Potassium currents in mammalian and avian isolated type I semicircular canal hair cells. *Journal of Neurophysiology*, 71(1):317–329. PMID: 8158233.

Rodrigues, H. A., M. d. C. Fonseca, W. L. Camargo, P. M. A. Lima, P. M. Martinelli, L. A. Naves, V. F. Prado, M. A. M. Prado, and C. Guatimosim
2013. Reduced expression of the vesicular acetylcholine transporter and neurotransmitter content affects synaptic vesicle distribution and shape in mouse neuromuscular junction. *PloS One*, 8(11):e78342.

Ross, M. D.
1993. Morphological changes in rat vestibular system following weightlessness. *Journal of Vestibular Research: Equilibrium & Orientation*, 3(3):241–251.

Ross, M. D.
2000. Changes in ribbon synapses and rough endoplasmic reticulum of rat utricular macular hair cells in weightlessness. *Acta Oto-Laryngologica*, 120(4):490–499.

Roux, I., S. Hosie, S. L. Johnson, A. Bahloul, N. Cayet, S. Nouaille, C. J. Kros, C. Petit, and S. Safieddine
2009. Myosin VI is required for the proper maturation and function of inner hair cell ribbon synapses. *Human Molecular Genetics*, 18(23):4615–4628.

Roux, I., S. Safieddine, R. Nouvian, M. Grati, M.-C. Simmler, A. Bahloul, I. Perfettini, M. Le Gall, P. Rostaing, G. Hamard, A. Triller, P. Avan, T. Moser, and C. Petit
2006. Otoferlin, defective in a human deafness form, is essential for exocytosis at the auditory ribbon synapse. *Cell*, 127(2):277–289. 00205.

Rubel, E. W. and B. Fritzsch
2002. AUDITORY SYSTEM DEVELOPMENT: Primary Auditory Neurons and Their Targets. *Annual Review of Neuroscience*, 25(1):51–101.

Rusch, A. and R. A. Eatock
1996. A delayed rectifier conductance in type i hair cells of the mouse utricle. *Journal of Neurophysiology*, 76(2):995–1004. PMID: 8871214.

Rüsch, A., A. Lysakowski, and R. A. Eatock
1998. Postnatal Development of Type I and Type II Hair Cells in the Mouse Utricle: Acquisition of Voltage-Gated Conductances and Differentiated Morphology. *The Journal of Neuroscience*, 18(18):7487–7501.

Russell, I. J. and M. Kössl
1992. Modulation of hair cell voltage responses to tones by low-frequency biasing of the basilar membrane in the guinea pig cochlea. *The Journal of Neuroscience: The Official Journal of the Society for Neuroscience*, 12(5):1587–1601.

Rutherford, M. A. and T. Pangršič
2012. Molecular anatomy and physiology of exocytosis in sensory hair cells. *Cell calcium*, 52:327–37.

Sadeghi, S. G., M. J. Chacron, M. C. Taylor, and K. E. Cullen
2007. Neural Variability, Detection Thresholds, and Information Transmission in the Vestibular System. *The Journal of Neuroscience*, 27(4):771–781.

Sadeghi, S. G., S. J. Pyott, Z. Yu, and E. Glowatzki
2014. Glutamatergic signaling at the vestibular hair cell calyx synapse. *Journal of Neuroscience*, 34(44):14536–14550.

Safieddine, S., A. El-Amraoui, and C. Petit
2012. The auditory hair cell ribbon synapse: from assembly to function. *Annual Review of Neuroscience*, 35(1):509–528.

Safieddine, S. and R. J. Wenthold
1999. SNARE complex at the ribbon synapses of cochlear hair cells: analysis of synaptic vesicle- and synaptic membrane-associated proteins. *European Journal of Neuroscience*, 11(3):803–812.

Sanes, J. R. and J. W. Lichtman
1999. Development of the vertebrate neuromuscular junction. *Annual Review of Neuroscience*, 22(1):389–442. PMID: 10202544.

Sans, A. and M. Chat

1982. Analysis of temporal and spatial patterns of rat vestibular hair cell differentiation by tritiated thymidine radioautography. *Journal of Comparative Neurology*, 206(1):1–8.

Schmiedt, R. A., J. H. Mills, and F. A. Boettcher

1996. Age-related loss of activity of auditory-nerve fibers. *Journal of Neurophysiology*, 76(4):2799–2803.

Schmitz, F.

2009. The Making of Synaptic Ribbons: How They Are Built and What They Do. *The Neuroscientist*, 15(6):611–624.

Schmitz, F., A. Königstorfer, and T. C. Südhof

2000. RIBEYE, a component of synaptic ribbons: a protein's journey through evolution provides insight into synaptic ribbon function. *Neuron*, 28(3):857–872.

Schönfelder, J. and P. Schwartze

1970. Development of the falling flip-over reflex in the ontogenesis of rabbits. *Acta Biologica Et Medica Germanica*, 25(1):109–114.

Schwarz, K., S. Natarajan, N. Kassas, N. Vitale, and F. Schmitz

2011. The Synaptic Ribbon Is a Site of Phosphatidic Acid Generation in Ribbon Synapses. *The Journal of Neuroscience*, 31(44):15996–16011.

Seal, R. P., O. Akil, E. Yi, C. M. Weber, L. Grant, J. Yoo, A. Clause, K. Kandler, J. L. Noebels, E. Glowatzki, L. R. Lustig, and R. H. Edwards

2008. Sensorineural Deafness and Seizures in Mice Lacking Vesicular Glutamate Transporter 3. *Neuron*, 57(2):263–275.

Sendin, G., A. V. Bulankina, D. Riedel, and T. Moser

2007. Maturation of ribbon synapses in hair cells is driven by thyroid hormone. *The Journal of Neuroscience: The Official Journal of the Society for Neuroscience*, 27(12):3163–3173.

Shapira, M., R. Zhai, T. Dresbach, T. Bresler, V. I. Torres, E. D. Gundelfinger, N. E. Ziv, and C. C. Garner

2003. Unitary assembly of presynaptic active zones from Piccolo-Bassoon transport vesicles. *Neuron*, 38(2):237–252.

Sheets, L., J. G. Trapani, W. Mo, N. Obholzer, and T. Nicolson

2011. Ribeye is required for presynaptic $Ca_v1.3a$ channel localization and afferent innervation of sensory hair cells. *Development*, 138(7):1309 –1319.

Shnerson, A., C. Devigne, and R. Pujol

1981. Age-related changes in the C57bl/6j mouse cochlea. II. Ultrastructural findings. *Brain Research*, 254(1):77–88.

Shone, G., R. A. Altschuler, J. M. Miller, and A. L. Nuttall
1991. The effect of noise exposure on the aging ear. *Hearing Research*, 56(1):173–178.

Siksou, L., P. Rostaing, J.-P. Lechaire, T. Boudier, T. Ohtsuka, A. Fejtová, H.-T. Kao, P. Greengard, E. D. Gundelfinger, A. Triller, and S. Marty
2007. Three-dimensional architecture of presynaptic terminal cytomatrix. *The Journal of Neuroscience*, 27(26):6868 –6877.

Simmons, D. D. and M. C. Liberman
1988. Afferent innervation of outer hair cells in adult cats: I. light microscopic analysis of fibers labeled with horseradish peroxidase. *Journal of Comparative Neurology*, 270(1):132–144.

Snellman, J., B. Mehta, N. Babai, T. M. Bartoletti, W. Akmentin, A. Francis, G. Matthews, W. Thoreson, and D. Zenisek
2011. Acute destruction of the synaptic ribbon reveals a role for the ribbon in vesicle priming. *Nature Neuroscience*, 14(9):1135–1141.

Sobkowicz, H. M., J. E. Rose, G. E. Scott, and S. M. Slapnick
1982. Ribbon synapses in the developing intact and cultured organ of Corti in the mouse. *The Journal of Neuroscience*, 2(7):942–957.

Sobkowicz, H. M., J. E. Rose, G. L. Scott, and C. V. Levenick
1986. Distribution of synaptic ribbons in the developing organ of Corti. *Journal of Neurocytology*, 15(6):693–714.

Songer, J. E. and R. A. Eatock
2013. Tuning and Timing in Mammalian Type I Hair Cells and Calyceal Synapses. *The Journal of Neuroscience*, 33(8):3706–3724.

Spassova, M. A., M. Avissar, A. C. Furman, M. A. Crumling, J. C. Saunders, and T. D. Parsons
2004. Evidence that rapid vesicle replenishment of the synaptic ribbon mediates recovery from short-term adaptation at the hair cell afferent synapse. *Journal of the Association for Research in Otolaryngology: JARO*, 5(4):376–390.

Spiwoks-Becker, I., M. Glas, I. Lasarzik, and L. Vollrath
2004. Mouse photoreceptor synaptic ribbons lose and regain material in response to illumination changes. *European Journal of Neuroscience*, 19(6):1559–1571.

Spoendlin, H.
1969. Innervation patterns in the organ of corti of the cat. *Acta Oto-Laryngologica*, 67(2):239–254.

Spoendlin, H.
1972. Innervation densities of the cochlea. *Acta oto-laryngologica*, 73(2):235–248.

Spongr, V. P., D. G. Flood, R. D. Frisina, and R. J. Salvi
1997. Quantitative measures of hair cell loss in CBA and C57bl/6 mice throughout their life spans. *The Journal of the Acoustical Society of America*, 101(6):3546–3553.

Stamataki, S., H. W. Francis, M. Lehar, B. J. May, and D. K. Ryugo
2006. Synaptic alterations at inner hair cells precede spiral ganglion cell loss in aging C57bl/6j mice. *Hearing Research*, 221(1-2):104–118.

Sterling, P. and G. Matthews
2005. Structure and function of ribbon synapses. *Trends in Neurosciences*, 28(1):20–29.

Steyger, P. S., D. N. Furness, C. M. Hackney, and G. P. Richardson
1989. Tubulin and microtubules in cochlear hair cells: comparative immunocytochemistry and ultrastructure. *Hearing Research*, 42(1):1–16.

Strenzke, N., R. Chakrabarti, H. Al-Moyed, A. Müller, G. Hoch, T. Pangršič, G. Yamanbaeva, C. Lenz, K.-T. Pan, E. Auge, R. Geiss-Friedlander, H. Urlaub, N. Brose, C. Wichmann, and E. Reisinger
2016. Hair cell synaptic dysfunction, auditory fatigue and thermal sensitivity in otoferlin Ile515thr mutants. *The EMBO journal*, 35(23):2519–2535.

Strenzke, N., S. Chanda, C. Kopp-Scheinpflug, D. Khimich, K. Reim, A. V. Bulankina, A. Neef, F. Wolf, N. Brose, M. A. Xu-Friedman, and T. Moser
2009. Complexin-I Is Required for High-Fidelity Transmission at the Endbulb of Held Auditory Synapse. *The Journal of Neuroscience*, 29(25):7991–8004.

Südhof, T. C.
2012. The presynaptic active zone. *Neuron*, 75(1):11–25.

Sugawara, M., J. C. Murtie, K. M. Stankovic, M. C. Liberman, and G. Corfas
2007. Dynamic patterns of neurotrophin 3 expression in the postnatal mouse inner ear. *The Journal of Comparative Neurology*, 501(1):30–37.

Suzuki, J., G. Corfas, and M. C. Liberman
2016. Round-window delivery of neurotrophin 3 regenerates cochlear synapses after acoustic overexposure. *Scientific Reports*, 6:24907.

Taberner, A. M. and M. C. Liberman
2005. Response Properties of Single Auditory Nerve Fibers in the Mouse. *Journal of Neurophysiology*, 93(1):557–569.

Takei, K., O. Mundigl, L. Daniell, and P. De Camilli
1996. The synaptic vesicle cycle: a single vesicle budding step involving clathrin and dynamin. *The Journal of Cell Biology*, 133(6):1237–1250.

Tao-Cheng, J.-H.
2007. Ultrastructural localization of active zone and synaptic vesicle proteins in a preassembled multi-vesicle transport aggregate. *Neuroscience*, 150(3):575–584.

Taschenberger, H., R. M. Leão, K. C. Rowland, G. A. Spirou, and H. von Gersdorff
2002. Optimizing synaptic architecture and efficiency for high-frequency transmission. *Neuron*, 36(6):1127–1143.

Tatsuoka, H. and T. S. Reese
1989. New structural features of synapses in the anteroventral cochlear nucleus prepared by direct freezing and freeze-substitution. *The Journal of comparative neurology*, 290(3):343–357.

tom Dieck, S., W. D. Altrock, M. M. Kessels, B. Qualmann, H. Regus, D. Brauner, A. Fejtová, O. Bracko, E. D. Gundelfinger, and J. H. Brandstätter
2005. Molecular dissection of the photoreceptor ribbon synapse: physical interaction of Bassoon and RIBEYE is essential for the assembly of the ribbon complex. *The Journal of Cell Biology*, 168(5):825–836.

tom Dieck, S., L. Sanmartí-Vila, K. Langnaese, K. Richter, S. Kindler, A. Soyke, H. Wex, K. H. Smalla, U. Kämpf, J. T. Fränzer, M. Stumm, C. C. Garner, and E. D. Gundelfinger
1998. Bassoon, a novel zinc-finger CAG/glutamine-repeat protein selectively localized at the active zone of presynaptic nerve terminals. *The Journal of Cell Biology*, 142(2):499–509.

Torres, V. I., D. Vallejo, and N. C. Inestrosa
2017. Emerging Synaptic Molecules as Candidates in the Etiology of Neurological Disorders. *Neural Plasticity*, 2017.

Tritsch, N. X. and D. E. Bergles
2010. Developmental regulation of spontaneous activity in the Mammalian cochlea. *The Journal of Neuroscience: The Official Journal of the Society for Neuroscience*, 30(4):1539–1550.

Tritsch, N. X., A. Rodríguez-Contreras, T. T. H. Crins, H. C. Wang, J. G. G. Borst, and D. E. Bergles
2010. Calcium action potentials in hair cells pattern auditory neuron activity before hearing onset. *Nature Neuroscience*, 13(9):1050–1052.

Tritsch, N. X., E. Yi, J. E. Gale, E. Glowatzki, and D. E. Bergles
2007. The origin of spontaneous activity in the developing auditory system. *Nature*, 450(7166):50–55.

Uthaiah, R. C. and A. J. Hudspeth
2010. Molecular Anatomy of the Hair Cell's Ribbon Synapse. *The Journal of Neuroscience*, 30(37):12387–12399.

van den Berg, R. and C. C. Hoogenraad
2012. *Molecular Motors in Cargo Trafficking and Synapse Assembly*, Pp. 173–196. Vienna: Springer Vienna.

Vogl, C., B. H. Cooper, J. Neef, S. M. Wojcik, K. Reim, E. Reisinger, N. Brose, J.-S. Rhee, T. Moser, and C. Wichmann
2015. Unconventional molecular regulation of synaptic vesicle replenishment in cochlear inner hair cells. *Journal of Cell Science*, 128(4):638–644.

von Gersdorff, H. and G. Matthews

1997. Depletion and replenishment of vesicle pools at a ribbon-type synaptic terminal. *The Journal of neuroscience*, 17(6):1919.

von Gersdorff, H., E. Vardi, G. Matthews, and P. Sterling

1996. Evidence that vesicles on the synaptic ribbon of retinal bipolar neurons can be rapidly released. *Neuron*, 16(6):1221–1227.

Wagh, D., R. Terry-Lorenzo, C. L. Waites, S. A. Leal-Ortiz, C. Maas, R. J. Reimer, and C. C. Garner

2015. Piccolo Directs Activity Dependent F-Actin Assembly from Presynaptic Active Zones via Daam1. *PloS One*, 10(4):e0120093.

Waites, C. L., S. A. Leal-Ortiz, T. F. M. Andlauer, S. J. Sigrist, and C. C. Garner

2011. Piccolo Regulates the Dynamic Assembly of Presynaptic F-Actin. *The Journal of Neuroscience*, 31(40):14250 –14263.

Walton, J. P., R. D. Frisina, and L. R. Meierhans

1995. Sensorineural hearing loss alters recovery from short-term adaptation in the C57bl/6 mouse - ScienceDirect.

Wan, G., G. Corfas, and J. S. Stone

2013. Inner ear supporting cells: Rethinking the silent majority. *Seminars in cell & developmental biology*, 24(5):448–459.

Wan, G., M. E. Gómez-Casati, A. R. Gigliello, M. C. Liberman, and G. Corfas

2014. Neurotrophin-3 regulates ribbon synapse density in the cochlea and induces synapse regeneration after acoustic trauma. *eLife*, 3.

Wang, X., M. Kibschull, M. M. Laue, B. Lichte, E. Petrasch-Parwez, and M. W. Kilimann

1999. Aczonin, a 550-Kd Putative Scaffolding Protein of Presynaptic Active Zones, Shares Homology Regions with Rim and Bassoon and Binds Profilin. *The Journal of Cell Biology*, 147(1):151 –162.

Wersall, J.

1956. Studies on the structure and innervation of the sensory epithelium of the cristae ampulares in the guinea pig; a light and electron microscopic investigation. *Acta Oto-Laryngologica. Supplementum*, 126:1–85.

White, J. A., B. J. Burgess, R. D. Hall, and J. B. Nadol

2000. Pattern of degeneration of the spiral ganglion cell and its processes in the C57bl/6j mouse. *Hearing Research*, 141(1-2):12–18.

Wichmann, C.

2015. Molecularly and structurally distinct synapses mediate reliable encoding and processing of auditory information. *Hearing Research*, 330(Pt B):178–190.

Wichmann, C. and T. Moser

2015. Relating structure and function of inner hair cell ribbon synapses. *Cell and Tissue Research*.

Wiechers, B., G. Gestwa, A. Mack, P. Carroll, H.-P. Zenner, and M. Knipper

1999. A Changing Pattern of Brain-Derived Neurotrophic Factor Expression Correlates with the Rearrangement of Fibers during Cochlear Development of Rats and Mice. P. 10.

Willott, J. F.

1986. Effects of aging, hearing loss, and anatomical location on thresholds of inferior colliculus neurons in C57bl/6 and CBA mice. *Journal of neurophysiology*, 56(2):391–408.

Willott, J. F., K. Parham, and K. P. Hunter

1988. Response properties of inferior colliculus neurons in young and very old CBA/J mice. *Hearing Research*, 37(1):1–14.

Willott, J. F., K. Parham, and K. P. Hunter

1988a. Response properties of inferior colliculus neurons in middle-aged C57bl/6j mice with presbycusis. *Hearing Research*, 37(1):15–27.

Winter, I. M., A. R. Palmer, and R. Meddis

1993. The response of guinea pig auditory-nerve fibers with high spontaneous discharge rates to increments in intensity. *Brain Research*, 618(1):167–170.

Wong, A. B., Z. Jing, M. A. Rutherford, T. Frank, N. Strenzke, and T. Moser

2013. Concurrent Maturation of Inner Hair Cell Synaptic Ca^{2+} Influx and Auditory Nerve Spontaneous Activity around Hearing Onset in Mice. *The Journal of Neuroscience*, 33(26):10661–10666. 00000.

Wong, A. B., M. A. Rutherford, M. Gabrielaitis, T. Pangršič, F. Göttfert, T. Frank, S. Michanski, S. Hell, F. Wolf, C. Wichmann, and T. Moser

2014. Developmental refinement of hair cell synapses tightens the coupling of Ca^{2+} influx to exocytosis. *The EMBO Journal*, 33(3):247–264.

Wu, Y., A. Krüttgen, J. Möller, D. Shine, J. Chan, E. Shooter, and J. Cosgaya

2004. Nerve growth factor, brain-derived neurotrophic factor, and neurotrophin-3 are sorted to dense-core vesicles and released via the regulated pathway in primary rat cortical neurons. *Journal of Neuroscience Research*, 75(6):825–834.

Yasunaga, S., M. Grati, M. Cohen-Salmon, A. El-Amraoui, M. Mustapha, N. Salem, E. El-Zir, J. Loiselet, and C. Petit

1999. A mutation in OTOF, encoding otoferlin, a FER-1-like protein, causes DFNB9, a non-syndromic form of deafness. *Nature genetics*, 21(4):363.

Yu, W.-M., J. M. Appler, Y.-H. Kim, A. M. Nishitani, J. R. Holt, and L. V. Goodrich

2013. A Gata3-Mafb transcriptional network directs post-synaptic differentiation in synapses specialized for hearing. *eLife*.

Yu, W.-M. and L. V. Goodrich
2014. Morphological and physiological development of auditory synapses. *Hearing Research*, 311:3–16.

Zampini, V., S. L. Johnson, C. Franz, N. D. Lawrence, S. Münkner, J. Engel, M. Knipper, J. Magistretti, S. Masetto, and W. Marcotti
2010. Elementary properties of $Ca_v1.3$ Ca^{2+} channels expressed in mouse cochlear inner hair cells. *The Journal of Physiology*, 588(Pt 1):187–199.

Zhai, R., H. Vardinon-Friedman, C. Cases-Langhoff, B. Becker, E. D. Gundelfinger, N. E. Ziv, and C. C. Garner
2001. Assembling the presynaptic active zone: a characterization of an active one precursor vesicle. *Neuron*, 29(1):131–143.

Zhang, B., Y. H. Koh, R. B. Beckstead, V. Budnik, B. Ganetzky, and H. J. Bellen
1998. Synaptic vesicle size and number are regulated by a clathrin adaptor protein required for endocytosis. *Neuron*, 21(6):1465–1475.

Zhang, F., Y. Pang, M. Zhang, T. Zhang, Y. Dong, C. Lai, D. Shum, Y. Chan, J. Li, and Y. Li
2011. Expression of vesicular glutamate transporters in peripheral vestibular structures and vestibular nuclear complex of rat. *Neuroscience*, 173:179–189.

Zhang, L. I. and M.-m. Poo
2001. Electrical activity and development of neural circuits. *Nature Neuroscience*, 4(11s):1207–1214.

Zhang, Z., A. Bhalla, C. Dean, E. R. Chapman, and M. B. Jackson
2009. Synaptotagmin IV: a multifunctional regulator of peptidergic nerve terminals. *Nature Neuroscience*, 12(2):163–171.

Zheng, J., W. Shen, D. Z. He, K. B. Long, L. D. Madison, and P. Dallos
2000. Prestin is the motor protein of cochlear outer hair cells. *Nature*, 405(6783):149–155.

Zuccotti, A., S. Kuhn, S. L. Johnson, C. Franz, W. Singer, D. Hecker, H.-S. Geisler, I. Köpschall, K. Rohbock, K. Gutsche, J. Dlugaiczyk, B. Schick, W. Marcotti, L. Rüttiger, T. Schimmang, and M. Knipper
2012. Lack of brain-derived neurotrophic factor hampers inner hair cell synapse physiology, but protects against noise-induced hearing loss. *The Journal of Neuroscience*, 32(25):8545–8553.

A. Appendix

Table A1: Detailed list of ribbon synapse parameters demonstrating mean ± SEM values, SD, n, *p*-values and statistical tests of all examined age groups.

Table A2: Detailed list of SV parameters showing mean ± SEM values, SD, n, *p*-values and statistical tests of all examined age groups.

Table A3: Detailed list of further ultrastructural parameters displaying mean ± SEM values, SD, n, *p*-values and statistical tests of all examined age groups.

Ribbon height (nm) (Supplement figure 2B)	Ribbon area (nm^2) (Figure 1F)	Parameter
60.395 ± 1.621 (SD: 15.716, n = 94 ribbons)	3166.470 ± 176.923 (SD: 1715.335, n = 94 ribbons)	**E18** N = 2 animals
67.660 ± 1.732 (SD: 22.778, n = 173 ribbons)	3867.459 ± 170.981 (SD: 2248.908, n = 173 ribbons)	**P0-1** N = 2 animals
108.362 ± 2.319 (SD: 34.083, n = 216 ribbons)	9561.487 ± 353.313 (SD: 5192.612, n = 216 ribbons)	**P2-4** N = 2 animals
134.565 ± 2.128 (SD: 42.284, n = 395 ribbons)	15721.596 ± 474.389 (SD: 9428.290, n = 395 ribbons)	**P9** N = 2 animals
169.164 ± 3.584 (SD: 57.235, n = 255 ribbons)	22148.861 ± 756.488 (SD: 12080.148, n = 255 ribbons)	**P12** N = 2 animals
184.686 ± 4.752 (SD: 57.620, n = 147 ribbons)	22035.334 ± 1.176 (SD: 11.646, n = 147 ribbons)	**P15** N = 2 animals
172.986 ± 3.362 (SD: 46.702, n = 193 ribbons)	20981.119 ± 799.735 (SD: 11110.284, n = 193 ribbons)	**P19-20** N = 2 animals
181.395 ± 4.234 (SD: 56.173, n = 176 ribbons)	18566.445 ± 710.224 (SD: 9422.192, n = 176 ribbons)	**P48** N = 2 animals
$p < 0.0001$ (P48 vs. E18) $p < 0.0001$ (P48 vs. P0-1) $p < 0.0001$ (P48 vs. P2-4) $p < 0.0001$ (P48 vs. P9) $p < 0.0001$ (P15 vs. E18) $p < 0.0001$ (P15 vs. P0-1) $p < 0.0001$ (P15 vs. P2-4) $p < 0.0001$ (P15 vs. p9) $p < 0.0001$ (P19-20 vs. E18) $p < 0.0001$ (P19-20 vs. P0-1) $p < 0.0001$ (P19-20 vs. P2-4) $p < 0.0001$ (P19-20 vs. p9) $p < 0.0001$ (P12 vs. E18) $p < 0.0001$ (P12 vs. P0-1) $p < 0.0001$ (P12 vs. P2-4) $p < 0.0001$ (P12 vs. p9) $p < 0.0001$ (P9 vs. E18) $p < 0.0001$ (P9 vs. P0-1) $p < 0.0001$ (P9 vs. P2-4) $p < 0.0001$ (P2-4 vs. E18) $p < 0.0001$ (P2-4 vs. P0-1)	$p < 0.0001$ (P15 vs. E18) $p < 0.0001$ (P15 vs. P0-1) $p < 0.0001$ (P15 vs. P2-4) $p < 0.0001$ (P15 vs. P9) $p < 0.0001$ (P12 vs. E18) $p < 0.0001$ (P12 vs. P0-1) $p < 0.0001$ (P12 vs. P2-4) $p < 0.0001$ (P12 vs. P9) $p < 0.0001$ (P19-20 vs. E18) $p < 0.0001$ (P19-20 vs. P0-1) $p < 0.0001$ (P19-20 vs. P2-4) $p < 0.0001$ (P19-20 vs. P9) $p < 0.0001$ (P48 vs. E18) $p < 0.0001$ (P48 vs. P0-1) $p < 0.0001$ (P48 vs. P2-4) $p < 0.0001$ (P48 vs. P9) $p < 0.0001$ (P9 vs. E18) $p < 0.0001$ (P9 vs. P0-1) $p < 0.0001$ (P9 vs. P2-4) $p < 0.0001$ (P2-4 vs. E18) $p < 0.0001$ (P2-4 vs. P0-1)	***p*-value**
NPMC test	NPMC test	**Statistical test**

Ribbon width (nm) (Supplement figure 2C)	63.136 ± 2.087 (SD: 20.234, n = 94 ribbons)	66.906 ± 1.415 (SD: 18.616, n = 173 ribbons)	101.788 ± 1.971 (SD: 28.962, n = 216 ribbons)	131.427 ± 2.354 (SD: 46.779, n = 395 ribbons)	160.240 ± 4.227 (SD: 67.496, n = 255 ribbons)	148.017 ± 6.201 (SD: 61.390, n = 147 ribbons)	149.290 ± 4.680 (SD: 65.022, n = 193 ribbons)	130.885 ± 4.981 (SD: 66.079, n = 176 ribbons)	$p < 0.0001$ (P12 vs. E18) $p < 0.0001$ (P12 vs. P0-1) $p < 0.0001$ (P12 vs. P2-4) $p < 0.0001$ (P12 vs. P9) $p < 0.0001$ (P12 vs. P48) $p < 0.0001$ (P15 vs. E18) $p < 0.0001$ (P15 vs. P0-1) $p < 0.0001$ (P15 vs. P2-4) $p < 0.0001$ (P19-20 vs. E18) $p < 0.0001$ (P19-20 vs. P0-1) $p < 0.0001$ (P19-20 vs. P2-4) $p < 0.0001$ (P9 vs. E18) $p < 0.0001$ (P9 vs. P0-1) $p < 0.0001$ (P9 vs. P2-4) $p < 0.0001$ (P48 vs. E18) $p < 0.0001$ (P48 vs. P0-1) $p < 0.0001$ (P48 vs. P2-4) $p < 0.0001$ (P2-4 vs. E18) $p < 0.0001$ (P2-4 vs. P0-1)	NPMC test

Table A1: Detailed list of ribbon synapse parameters demonstrating mean ± SEM values, SD, n, *p*-values and statistical tests of all examined age groups.

Parameter	**E18** N = 2 animals	**P0-1** N = 2 animals	**P2-4** N = 2 animals	**P9** N = 2 animals	**P12** N = 2 animals	**P15** N = 2 animals	**P19-20** N = 2 animals	**P48** N = 2 animals	***p*-value**	**Statistical test**
Number of SVs (Figure 1G)	4.479 **±** 0.156 (SD: 1.508, n = 94 ribbons)	4.214 **±** 0.111 (SD: 1.457, n = 173 ribbons)	4.796 **±** 0.130 (SD: 1.906, n = 216 ribbons)	8.380 **±** 0.164 (SD: 3.268, n = 395 ribbons)	10.867 **±** 0.244 (SD: 3.896, n = 255 ribbons)	12.571 **±** 0.416 (SD: 5.040, n = 147 ribbons)	12.415 **±** 0.291 (SD: 4.040, n = 193 ribbons)	13.977 **±** 0.359 (SD: 4.757, n = 176 ribbons)	*p* < 0.0001 (P48 vs. P0-1) *p* < 0.0001 (P48 vs. E18) *p* < 0.0001 (P48 vs. P2-4) *p* < 0.0001 (P48 vs. P9) *p* < 0.0001 (P48 vs. P12) *p* < 0.0001 (P19-20 vs. P0-1) *p* < 0.0001 (P19-20 vs. E18) *p* < 0.0001 (P19-20 vs. P2-4) *p* < 0.0001 (P19-20 vs. P9) *p* < 0.0001 (P15 vs. P0-1) *p* < 0.0001 (P15 vs. E18) *p* < 0.0001 (P15 vs. P2-4) *p* < 0.0001 (P15 vs. P9) *p* < 0.0001 (P12 vs. P0-1) *p* < 0.0001 (P12 vs. E18) *p* < 0.0001 (P12 vs. P2-4) *p* < 0.0001 (P12 vs. P9) *p* < 0.0001 (P9 vs. P0-1) *p* < 0.0001 (P9 vs. E18) *p* < 0.0001 (P9 vs. P2-4)	NPMC test
SV diameter (nm) (Figure 1H)	46.998 **±** 0.278 (SD: 5.701, n = 94 ribbons)	46.758 **±** 0.265 (SD: 7.149, n = 173 ribbons)	46.850 **±** 0.243 (SD: 7.824, n = 216 ribbons)	44.245 **±** 0.143 (SD: 8.252, n = 395 ribbons)	41.777 **±** 0.113 (SD: 5.955, n = 255 ribbons)	38.262 **±** 0.137 (SD: 5.920, n = 147 ribbons)	37.320 **±** 0.123 (SD: 6.019, n = 193 ribbons)	34.861 **±** 0.125 (SD: 6.214, n = 176 ribbons)	*p* = 0.0321 (E18 vs.P15) *p* = 0.0321 (P0-1 vs.P12) *p* = 0.0321 (P0-1 vs.P15) *p* = 0.0298 (P9 vs.P48) *p* = 0.0052 (E18 vs.P48) *p* = 0.0220 (P0-1 vs.P48) *p* = 0.0043 (P2-4 vs.P12) *p* = 0.0014 (E18 vs.P19) *p* = 0.0020 (P0-1 vs.P19) *p* = 0.0007 (P2-4 vs.P15) *p* = 0.0005 (P2-4 vs.P19) *p* = 0.0005 (P2-4 vs.P48) *p* = 0.0020 (P9 vs.P19)	KW test

Table A2: Detailed list of SV parameters showing mean ± SEM values, SD, n, *p*-values and statistical tests of all examined age groups.

Parameter	**E18** N = 2 animals	**P0-1** N = 2 animals	**P2-4** N = 2 animals	**P9** N = 2 animals	**P12** N = 2 animals	**P15** N = 2 animals	**P19-20** N = 2 animals	**P48** N = 2 animals	***p*-value**	**Statistical test**
PSD length (nm) (Figure 2C)	354.804 ± 23.229 (SD: 214.165, n = 85 PSDs)	366.433 ± 17.501 (SD: 242.500, n = 192 PSDs)	330.004 ± 12.519 (SD: 197.950, n = 250 PSDs)	376.430 ± 8.856 (SD: 206.739, n = 545 PSDs)	418.382 ± 13.209 (SD: 241.048, n = 333 PSDs)	531.106 ± 20.087 (SD: 246.015, n = 150 PSDs)	626.265 ± 18.974 (SD: 266.319, n = 197 PSDs)	555.363 ± 15.382 (SD: 201.734, n = 172 PSDs)	$p < 0.0001$ (P19 vs. P2-4) $p < 0.0001$ (P19-20 vs. E18) $p < 0.0001$ (P19-20 vs. P0-1) $p < 0.0001$ (P19-20 vs. P9) $p < 0.0001$ (P19-20 vs. P12) $p < 0.0001$ (P48 vs. P2-4) $p < 0.0001$ (P48 vs. E18) $p < 0.0001$ (P48 vs. P0-1) $p < 0.0001$ (P48 vs. P9) $p < 0.0001$ (P48 vs. P12) $p < 0.0001$ (P15 vs. P2-4) $p < 0.0001$ (P15 vs. E18) $p < 0.0001$ (P15 vs. P0-1) $p < 0.0001$ (P15 vs. P9) $p < 0.0001$ (P15 vs. P12) $p < 0.0001$ (P12 vs. P2-4)	NPMC test
DCV diameter (nm) (Supplement figure 4D)	94.513 ± 6.933 (SD: 27.732, n = 16 DCVs)	83.670 ± 5.946 (SD: 35.676, n = 36 DCVs)	123.661 ± 10.286 (SD: 27.215, n = 7 DCVs)	–	–	–	–	–	$p = 0.0150$ (P2-4 vs. P0-1)	KW test

Table A3: Detailed list of further ultrastructural parameters displaying mean ± SEM values, SD, n, *p*-values and statistical tests of all examined age groups.

Acknowledgements

I would like to thank the following people for their support during my studies, without whose help this work would never have been possible:

To start I would like to gratefully acknowledge my supervisor Prof. Dr. Carolin Wichmann for introducing me to this field and for patiently teaching me the electron microscopic techniques. I am thankful for her guidance, inspirations and valuable suggestions she provided throughout my projects and I really appreciate being a member (”EMler”) of her lab.

Next, I wish to thank my thesis committee advisors, Prof. Dr. Tobias Moser and Prof. Dr. André Fiala, for all their constructive comments, ideas and great advice during the entire research.

I am particularly grateful to Dr. Christian Fischer, Dr. Wiebke Möbius and Dr. Anna Maria Steyer for their expertise and help with serial block face- and focused ion beam-scanning electron microscopy. I owe very special thanks to Dr. Anna Maria Steyer for her constant help in handling large 3D volume data.

Moreover, I thank Dr. Rituparna Chakrabarti for always offering her help no matter whether day or night, for all the long scientific and non-scientific discussions as well as her company at never-ending data analysis nights.

Among many people who have helped me during my work, there are some particular persons I would like to take the opportunity to express my deep gratitude. Many thanks to PD Dr. Michael Hoppert for his excellent technical support whenever a problem emerged with the microscopes; Christiane Senger-Freitag, Sandra Gerke and Anna Goldak for their professional technical assistance in the experimental work; Gerhard Hoch and Omar Lautaro Diaz for solving all computer problems; Dr. Jakob Neef for troubleshooting scientific and technical problems at any time; Timo Henneck for the great teamwork on the utricle project; Dr. Christian Vogl, Dr. Tina Pangršič Vilfan and Dr. Rituparna Chakrabarti for their critical comments and helpful suggestions to improve the quality of this thesis.

Furthermore, I acknowledge all members of the Institute for Auditory Neuroscience and InnerEarLab that I could not mention by name individually but provided a great and supportive work environment. All of you helped me directly or indirectly during the last years.

I would also like to extend my thanks to Dr. Mehmet Gültas, who always supported me in general scientific and advanced statistical questions. To the last moment, his advice, helpful comments and suggestions positively contributed to my work. You are not only my partner but also my best friend and mentor.

Finally and most importantly, I want to thank all of you for your time and input!